Investigation of Thermodynamic and Transport Properties of Proton-Exchange Membranes in Fuel Cell Applications

By
Pyoungho Choi

A Dissertation

Submitted to the Faculty of

WORCESTER POLYTECHNIC INSTITUTE

In partial fulfillment of the requirement for the

Degree of Doctor of Philosophy

In

Chemical Engineering

by

_____

April 2004

APPROVED:

_____
Prof. Ravindra Datta, Advisor
Head of Chemical Engineering Dept.

_____
Prof. Nikolaos K. Kazantzis

_____
Prof. Alfred A. Scala

Abstract

Proton exchange membrane (PEM) fuel cells are at the forefront among different types of fuel cells and are likely to be important power sources in the near future. PEM is a key component of the PEM fuel cells. The objective of this research is to investigate the fundamental aspects of PEM in terms of thermodynamics and proton transport in the membrane, so that the new proton conducting materials may be developed based on the detailed understanding. Since the proton conductivity increases dramatically with the amount of water in PEM, it is important to maintain a high humidification during the fuel cell operation. Therefore, the water uptake characteristics of the membrane are very important in developing fuel cell systems.

Thermodynamic models are developed to describe sorption in proton-exchange membranes (PEMs), which can predict the complete isotherm as well as provide a plausible explanation for the long unresolved phenomenon termed Schroeder's paradox, namely the difference between the amounts sorbed from a liquid solvent versus from its saturated vapor. The sorption isotherm is a result of equilibrium established in the polymer-solvent system when the swelling pressure due to the uptake of solvent is balanced by the surface and elastic deformation pressures that restrain further stretching of the polymer network.

The transport of protons in PEMs is intriguing. It requires knowledge of the PEM structure, water sorption thermodynamics in PEM, proton distribution in PEM, interactions between the protons and PEM, and proton transport in aqueous solution. Even proton conduction in water is anomalous that has received considerable attention for over a century because of its paramount importance in chemical, biological, and electrochemical systems. A pore transport model is proposed to describe proton diffusion at various hydration levels within Nafion® by incorporating structural effect upon water uptake and various proton transport mechanisms, namely proton hopping on pore surface, Grotthuss

diffusion in pore bulk, and ordinary mass diffusion of hydronium ions. A comprehensive random walk basis that relates the molecular details of proton transfer to the continuum diffusion coefficients has been applied to provide the transport details in the molecular scale within the pores of PEM. The proton conductivity in contact with water vapor is accurately predicted as a function of relative humidity without any fitted parameters. This theoretical model is quite insightful and provides design variables for developing high proton conducting PEMs.

The proton transport model has been extended to the nanocomposite membranes being designed for higher temperature operation which are prepared via modification of polymer (host membrane) by the incorporation of inorganics such as SiO_2 and ZrO_2. The operation of fuel cells at high temperature provides many advantages, especially for CO poisoning. A proton transport model is proposed to describe proton diffusion in nanocomposite Nafion®/(ZrO_2/SO_4^{2-}) membranes. This model adequately accounts for the acidity, surface acid density, particle size, and the amount of loading of the inorganics. The higher proton conductivity of the composite membrane compared with that of Nafion is observed experimentally and also predicted by the model.

Finally, some applications of PEM fuel cells are considered including direct methanol fuel cells, palladium barrier anode, and water electrolysis in regenerative fuel cells.

Acknowledgement

I would like to thank Professor Ravindra Datta for his guidance, support, and advice throughout my thesis work. I have learned so many invaluable things from him. I only hope that a small part of his intuition, breadth of knowledge, and depth of understanding has rubbed off on me.

I would also like to thank my committee members, Professor Nikolaos K. Kazantzis and Professor Alfred A. Scala, for their time and advice to complete this thesis.

I would also like to thank all the professors and staffs of chemical engineering department. They helped me in many ways that I cannot state here all the assistances I have got from them.

I would also like to thank my parents for their unconditional love and affection that I have been receiving. I cannot possibly state how much they mean to me.

I would also like to thank my wife, Misook, for her devotion and love through all the hard times during my study.

I would also like to thank my lovely kids, Youngdoo and Mark, who serve as an inspiration for me to move on against all odds on my way.

Finally, I would like to thank God for all your help.

He gives his harness bells a shake
To ask if there is some mistake.
The only other sound's the sweep
Of easy wind and downy flake.

The woods are lovely, dark and deep.
But I have promises to keep,
And miles to go before I sleep.
And miles to go before I sleep.

From "Stopping By Woods on a Snowy Evening" by Robert Frost.

Table of Contents

Abstract i

Acknowledgement iii

List of Figures viii

List of Tables xiv

PART I: Introduction and Background 1-82

Chapter 1. Introduction 1

1-1. Fuel Cell Fundamentals 1
i). Definition 1
ii). A brief history of fuel cells 1
iii). Rationale behind fuel cell research and development 5
iv). Principles of fuel cells 5
v). Hardware of fuel cells 16
1-2. Proton Exchange Membranes (PEMs) 20
i). Significance of thermodynamics and transport in fuel cells 20
ii). PEM materials 23
References 27

Chapter 2. Thermodynamics and Transport in Nafion®: Literature Review 29

2-1. Properties and Structures of Nafion® 29
2-1-1. Properties 29
2-1-1. Structure models 29
i). Eisenberg's model 34
ii). Gierke et al.'s model 36
iii). Mauritz et al.'s model 36
iv). Yeager et al.'s model 36
v). Recent models 39
2-2. Thermodynamics of Sorption 45
2-2-1. Models 46
i). Gregor's model 46
ii). Mauritz et al.'s model 50
iii). Recent models 53
2-2-2. Schroeder's Paradox 54
2-3. Transport of Protons 60

2-3-1. Proton transport in aqueous solutions 60
i). Grotthuss mechanism 61
ii). Huckel's mechanism 61
iii). Bernal et al.'s mechanism 61
iv). Conway et al.'s mechanism 64
v). Recent molecular dynamic simulations 68
2-3-2. Proton transport in PEM 70
References 78

PART II: Thermodynamics and Transport in PEMs 83-191

Chapter 3. Thermodynamics of Sorption in PEMs: An Explanation of Schroeder's Paradox 83

Abstract 83
3-1. Introduction 83
3-2. Model description 86
3-3. Theoretical model 89
3-4. Results and Discussions 99
3-5. Conclusions 108
References 109

Chapter 4. Thermodynamics of Sorption in PEMs: A predictive Model Based on Flory-Huggins Model and Membrane Elasticity 113

Abstract 113
4-1. Introduction 113
4-2. Theory 115
4-3. Experiments 124
4-4. Results and Discussions 125
4-5. Conclusions 134
References 135

Chapter 5. Transport of Protons in Nafion 138

Abstract 138
5-1. Introduction 138
5-2. Experiment 140
5-3. Theory 140
5-4. Simulations 159
5-5. Conclusions 165
References 167

Chapter 6. Proton Transport in Nafion/Sulfated ZrO_2 Nanocomposite 171
Abstract 171
6-1. Introduction 171
6-2. Experiment 174
6-3. Theory 175
6-4. Results and Discussions 184
6-5. Conclusions 198
References 199

PART III: Fuel Cell Systems 202-267

Chapter 7. Direct Methanol Fuel Cells 202
7-1. Introduction 202
7-2. Experiment 202
7-3. Results and discussions 206
7-4. Modeling of DMFC 214
7-5. Current oscillation during DMFC operation 223
7-6. Dynamic feed operation of DMFC 226
7-7. Impermeable PEM for DMFC 229
References 235

Chapter 8. Fuel Cell with Pd Nonporous Anode 237
8-1. Introduction 237
8-2. The Model 237
References 250

Chapter 9. Water Electrolysis in Regenerative Fuel Cells 251
9-1. Introduction 251
9-2. The Model 252
9-3. Simulation 257
9-4. Conclusions 262
References 266

PART IV: Conclusions and Recommendation for Future Work 268-278

Chapter 10. Conclusions and Recommendation for Future Work 268
10-1. Conclusions 268
10-2. Recommendations for future work 271
10-2-1. Proton transport in PEM below freezing temperature 271
10-2-2 Thermodynamics of hydrogen sorption in Pd 273
10-2-3. Others 276

References 277
Appendix 279

List of Figures

1-1	Grove's original H_2/O_2 fuel cell (ref. 1).	2
1-2.	A schematic representation of PEM fuel cell where fuel is hydrogen (ref. 21).	7
1-3.	Fuel cells view as a series of resistance.	14
1-4.	A schematic of single fuel cell and stack.	19
2-1.	Chemical structure of proton exchanged form of Nafion®.	30
2-2.	Simple structural conceptulization of cross-linked polyelectrolyte and clustered ionomeric system with anionic side chain.	35
2-3.	Schematic representation of cluster-network model by Gierke.	37
2-4.	Schematic representation of ionic clusters in phase separated domain of Nafion® by Mauritz et al.	38
2-5.	Three-phase structural model for Nafion®: A, fluorocarbon; B, interfacial zone; and C, ionic clusters.	40
2-6.	Schematic representation of structural changes with water content in perfluorosulfonated ionomer membranes, i.e., Nafion®.	41
2-7.	Schematic representation of sandwich-like structure elements proposed by Haubold et al.	43
2-8.	Schematic representation of water-filled channels of Nafion®.	44
2-9.	Gregor's mechanical model of ion exchange membrane.	47
2-10.	Equivalent volume of ion exchanger and swelling pressure (ref. 22).	49
2-11.	Mauritz's model of single spherical ionic cluster illustrating the dry radius (r_0), equilibrium swollen radius (r), and polymer matrix resistive pressure (Π) for a membrane in contact with pure water.	51
2-12.	Two state model of hydration-mediated equilibrium between unbound counterions and counterions bound in an outer sphere complex.	52

2-13. A schematic representation of Schroeder's Paradox. 58

2-14. The Grotthuss mechanism of proton transfer in aqueous solution. 62

2-15. Schematic representation of successive steps in an H_3O^+ rotation (Huckel's mechanism). 63

2-16. Schematic representation of tunneling and water rotation steps (Bernal and Fowler). 65

2-17. Schematic representation of the favorable and unfavorable configurations between H_3O^+ ion and proton accepting H_2O molecule. 66

2-18. Schematic diagram of the proton transfer with tunneling and field induced reorientation. 67

2-19. The quantum-mechanical probability distribution function P(Roo, δ) for (a) three hydrogen bonds of the H_3O^+ complex in water (b) most active of three hydrogen bonds characterized by the smallest value of δ. 69

2-20. Schematics of proton transfer by *ab-initio* MD simulation. 71

2-21. Optimized conformation of $CF_3SO_3H + nH_2O$. 73

2-22. The structure of proton exchange membrane in its hydrated state (two types of waters are distinguished). 76

3-1. Schematic representation of an ion-exchange membrane in its (a) unswollen, and (b) swollen state. The fixed and counter-ions in the membrane are represented by open (○) and filled (●) circles, respectively. 88

3-2. The two types of sorbed water molecules in the proton exchange membrane: five strongly bound water molecules in the primary hydration shell, akin to chemisorption and eight free water molecules, akin to physisorption. 90

3-3. Schematic representation of absorbed solvent in the pore when membrane contacts with vapor phase environment. 93

3-4. Prediction of the water sorption in Nafion®(EW=1100) by the model 103

(Eq. 30) taken ν = 5 together with experimental observations: solid line (model prediction), triangle (ref. 12), square (ref. 14), circle (ref. 16), and star (ref. 18).

3-5. Prediction of water loading from the liquid immersion with different equilibrium steps varying from 4 to 6 (Eq. 32). 106

3-6. Prediction of water loading from the vapor sorption with different equilibrium steps varying from 4 to 6 (Eq. 33). 107

4-1. The normalized swelling pressure from different models (1: Phantom model, Gusler-Cohen's model, 3: Affine model, and 4: Freger's model). 120

4-2. A schematic of equilibrium steps forming hydration sheath around sulfonic acid in Nafion®. 122

4-3. The solvent loading vs. activity of water vapor for Nafion® (EW=1100) (triangle: ref. 51, square: ref. 52, diamond: ref. 53, circle: ref.54, and star: this work). 127

4-4. The interaction parameter χ as a function of activity of water vapor (triangle:ref. 51, square: ref. 52, diamond: ref. 53, circle: ref. 54, and star: this work). 129

4-5. The predicted solvent loading with the changes of the dissociation constant. 131

4-6. The predicted solvent loading with the changes of Young's modulus. 132

4-7. Effect of EW on water vapor sorption for different relative humidity conditions at room temperature (triangle: EW=960, square: EW=1100, and circle: EW=1200). 133

5-1. A simplified picture of structure and proton transfer in Nafion® in fully hydrated state (a), and electrical analog of the proton transport in Nafion® (b). 142

5-2. A schematic representation of the first proton hopping at the surface of Nafion® (a: before and b: after the first jump). 146

5-3.	The hydrodynamic model of Grotthuss diffusion mechanism of protons in the pore bulk.	149
5-4.	The Grotthuss hopping time for the variations of rotation angle of the proton accepting water molecule.	153
5-5.	Proton conductivity of Nafion® of EW = 1100 (circle: ref. 79, triangle: ref. 80, star: this work, and solid line: model predictions).	160
5-6.	Comparison of proton conductivity data of Nafion® of EW = 960 with the model.	163
6-1.	A schematic representation of Nafion®/(ZrO_2/SO_4^{2-}) nanocomposite membrane.	176
6-2.	Structure of ZrO_2/SO_4^{2-} solid acid.	186
6-3.	The effect of acid site density on the surface diffusion coefficient.	187
6-4.	The effect of water vapor activity on the en masse diffusion coefficient.	190
6-5.	The effect of water vapor activity on the porosity/tortuosity ratio (from the top: 90ºC composite, 25ºC composite, 90ºC Nafion, 25ºC Nafion).	191
6-6.	Proton conductivity of Nafion® at 25ºC.	192
6-7.	Proton conductivity of Nafion® at 90ºC.	193
6-8.	Proton conductivity of Nafion®/(ZrO_2/SO_4^{2-}) at 25ºC.	195
6-9.	Proton conductivity of Nafion®/(ZrO_2/SO_4^{2-}) at 90ºC.	196
6-10.	The effect of temperature on the proton conductivity.	197
7-1.	A schematic diagram of cross-section of DMFC.	205
7-2.	DMFC performance at 0 atm (gauge), 1M methanol 1ml/min, and O_2 40 ml/min.	207
7-3.	DMFC performance at 1 atm (gauge), 1M methanol 1ml/min, and O_2 40 ml/min.	208
7-4.	DMFC performance at 2 atm (gauge), 1 M methanol 1ml/min, and O_2 40 ml/min.	209
7-5.	Effect of flow rate of methanol solution at 2 atm, 1 M methanol	210

and O_2 40 ml/min.

7-6. The change of OCV after a load is removed from 0.1 V at 25ºC and 0 atm. 212

7-7. Current oscillations in DMFC (60ºC, 0 psig O_2, 1 M Methanol, and 0.5ml/min) 224

7-8. Period and amplitude of the oscillations. 225

7-9. Dynamic feeding of anode feed. 228

7-10. The performance of Pd plated Nafion® membrane (0 atm, 1M methanol, and 1 ml/min). 231

7-11. The performance of Pd plated Nafion® membrane (1 atm, 1M methanol, and 1ml/min). 232

8-1. Schematic diagram of Pd nonporous anode fuel cells. 239

8-2. Schematic diagram of the concentration of hydrogen atom in Pd layer of hydrogen diffusion anode fuel cells. 245

9-1. Cross-section of SPE water electrolyzer. 253

9-2. Equivalent circuit for the electrolysis process: $V_\circ$ = internal power supply, R_A = anode resistance, R_{SPE} = membrane resistance, R_C = cathode resistance and R_I = interface resistance. 256

9-3. Comparison of the model with experiments at 80ºC (symbols: experimental data, 1: equilibrium voltage, 2: ohmic drop, 3: cathode overpotential, 4: anode overpotential on Pt-IrO_2, and 5: anode overpotential on Pt). 258

9-4. Differential resistances for water electrolysis: star = total differential resistance, circle = anode differential resistance, square = membrane differential resistance and triangle = cathode differential resistance. 263

9-5. Energy input *vs.* current density: star = energy supply due to Pt-IrO_2 anode overpotential, circle = energy supply due to cathode overpotential, 264

square = energy supply due to ohmic drop and triangle = inherent energy supply.

List of Tables

1-1. Development of proton exchange membrane. 24

2-1. Properties of Nafion® perfluorinated Membrane. 31

2-2. The uptake of water by gelatin in liquid water. 56

2-3. The release of water in gelatin by placing it in a space saturated with water vapor. 57

2-4. Structural distances of SO_2O-H and SO_2OH-OH_2 of $CF_3SO_3H + nH_2Os$. 74

3-1. The amount of water sorption in Nafion® by liquid water and its saturated vapor about room temperature. 85

3-2. Parameters employed in the model for the sorption of water in Nafion®. 102

4-1. Parameter values employed in the model for the sorption of water in Nafion®. 128

5-1. The mean step time and distance of the three diffusion mechanisms in Einstein-Smoluchowski equation. 156

5-2. Parameter values employed in the model for proton conductivity in Nafion® at room temperature. 161

5-3. Comparison of the theoretical and experimental values of proton conductivity for various EWs of Nafion®. 164

6-1. Data for water sorption in Nafion and Nafion/(ZrO_2/SO_4^{2-}) composite Membrane. 185

6-2. Parameter values employed in the model at room temperature. 188

7-1. Potential applications of DMFCs (ref. 6). 203

7-2. Open circuit voltage of DMFC (1M methanol 0.5ml/min and O_2 40 ml/min). 213

7-3. Conductivity of methanol solution. 215

7-4. Open circuit voltage of modified MEAs. 234

8-1. Diffusion coefficients in α and β phase Pd at different temperature. 247

8-2. Data for hydrogen concentration [g H/cc Pd] where C_o is the concentration of hydrogen atom in the β phase in equilibrium with 1 atm of H_2 and C_1 is the concentration of β phase in equilibrium with C_2 in the α phase. 248

8-3. Limiting current density (A/cm^2) at different temperatures for the variation of thickness of commercial Pd foil (1 atm). 249

9-1. Model parameters for water electrolysis for Pt coated anode and cathode electrodes on Nafion® electrolyte. 259

PART I.

Introduction and Background

Chapter 1. Introduction

Chapter 2. Thermodynamics and Transport in Nafion®: Literature Review

"It is difficult to say what is impossible, for the dream of yesterday is the hope of today and the reality of tomorrow." *- Robert H. Goddard -*

Chapter 1. Introduction

1-1. Fuel Cell Fundamentals

i). Definition

A fuel cell is defined as an electrochemical device in which the chemical energy of a *fuel* is converted *directly* into electrical energy. The *fuel* is typically an alcohol or a hydrocarbon or a substance derivable from it, e.g., hydrogen, which can be supplied continuously. Excluded are fuels such as atomic fuel, i.e., uranium, and metals such as zinc or sodium, the latter being used in batteries. The term *directly* implies that the device has an anode at which the fuel is electrocatalytically oxidized with the production of electrons and a cathode at which the oxygen is reduced.

ii). A brief history of fuel cells

The invention of "fuel cell" is credited to W. R. Grove.[1] However, the "fuel cell effect" was first discovered by Christian Friedrich Schoenbein who was in close contact with him. Grove was studying the electrolysis of water using electrodes made of thin platinum foil, immersed in dilute sulfuric acid solution. Hydrogen and oxygen gases were collected in the small tubes holding the electrodes. When the electric charge was stopped, Grove found that a current in the reverse direction was observed due to the recombination of the gases on the platinum electrodes. In order to prove this, Grove built a 50-cell "gaseous voltaic battery" shown in Figure 1-1 where hydrogen and oxygen react on platinum electrodes in sulfuric acid solution to form water in the tubes over the lower reservoirs. The electrons produced electrolyze water to oxygen and hydrogen in the upper tube. He proposed three requirements on which the principles of fuel cell technology have since been built: i) the platinum electrodes acted as current collectors as well as catalyst for

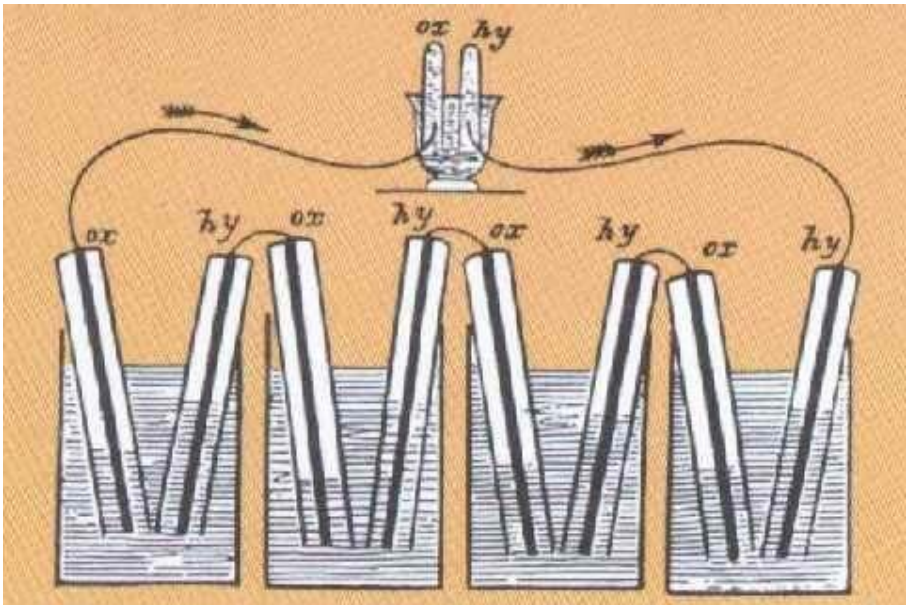

Figure 1-1. Grove's original H_2/O_2 fuel cell (ref. 1).

the gas recombinationreaction, ii) the reaction took place at the three phase interface of gas-liquid-solid, and iii) a substantial three-phase interface of the electrode was needed to produce a current of any magnitude.

In 1889, the term 'fuel cell' was coined by Mond and Langer,[2] who tried to turn the Grove's invention into a practical device by applying three-dimensional porous electrode structure. In 1896, W. W. Jacques[3] suggested fuel cell powered train and identified the potential of fuel cells for household and marine applications. From the early 1930s, Bacon has researched fuel cells for potentials as energy storage devices.[4] He also demonstrated a forklift truck and energized other devices in 1959. Based on Bacon's development, United Technologies (UTC) produced fuel cells for Apollo Lunar Mission that served as power sources for on-board applications. In the early 1950s, General Electric (GE) started to work on fuel cells and developed the first fuel cell based on a proton-exchange membrane (PEM). The space race in the 1960s stimulated interests in fuel cell since the cost was not a critical factor in this application. The PEMs used were blends of inert polymer with highly cross-linked polystyrene-based ionomer, sulfonated phenol-formaldehyde, and heterogeneous sulfonated divinylbenzene-cross-linked polystyrene. These materials were, however, chemically degraded during the operation of fuel cells. Extensive efforts to reduce the degradation was carried out which included the use of antioxidant, and addition of Teflon to electrode materials.

A solution came in mid-1960s through the collaborative efforts of GE and Du Pont. This work resulted in the development of what is still today the PEM of choice, namely, DuPont's ubiquitous Nafion® membrane. In August 1965, Gemini 5 spacecraft used GE's PEM fuel cell as a source of electrical power. In the late 1970s, Ballard entered the fuel cell area and applied novel materials and engineering techniques. In the middle of 1980s, Ballard developed fuel cell that used their proton exchange membrane as electrolyte and operated on either air or pure oxygen with either pure hydrogen or synthetic reformate fuel.

Ballard was able to achieve efficient proton-exchange membrane fuel cell operation using synthetic reformate fuel by "cleaning" the gas mixture of CO through a process of selective oxidation.[5] In 1986, Los Alamos National Laboratory (LANL) demonstrated a high active surface area electrocatalyst including ionomer gel for increasing the three-phase interface and provided opportunity for reduction of catalyst loading without loss of performance.[6] In 1991, Ballard developed "serpentine" flow field design to facilitate water removal from the cathode, thereby improving performance through enhanced oxidant gas distribution to the electrocatalysts.

Since the 1990s significant number of fuel cell programs has evolved. For example, almost all the major auto-makers i.e., General Motors (GM), Toyota, Daimler-Benz, Honda, Nissan and Ford, etc, who are seeking ways to eliminate CO, HC, and NOx emissions from vehicles and increase their efficiency have made substantial investments into fuel cell research and development. Ballard demonstrated a fuel cell powered bus in 1993, and a later 200 kW unit fuel cell powered bus. After a Ballard/Daimler-Benz alliance, Ford, followed by Toyota, made aggressive R & D efforts to produce fuel cell vehicles. A number of consortia and OEMs have now developed in the world. However, fuel cell powered vehicles have significant technical challenges remaining to be addressed, i.e., choice of fuels, hydrogen storage on vehicles, and on-board reforming. The use of pure hydrogen may not a realistic choice for widespread consumer applications, based on the current state of art of hydrogen production and storage. Methanol based on-board reforming has been demonstrated by Daimler Chrysler in their prototype NECAR3 vehicle. Fuel cells have also been tested for stationary applications and 250 kW units in distributed power system are well established. Many review articles on the fuel cell technology and its applications are available.[7-20]

The fuel cell technology is already adequately developed for commercialization except the cost of the technology. The most critical issue is to reduce the cost and improve the

fuel cell performance. Of all the areas for cost reduction and performance enhancement, PEMs are considered to be one of the key important elements. Today, there is only one commercial membrane type, namely, perfluorosulfonic acid PEMs, despite significant research and development activities throughout the world. These efforts are focused on addressing improved conductivity, dramatic cost reduction, ease of manufacture, optimization for use in specific applications, operation under reduced or zero external humidification, high-temperature operation, and low methanol crossover. A key stumbling block right now is the development of compact and efficient fuel reformers for distributed hydrogen production.

iii). Rationale behind fuel cell research and development[17]

The recent intensive interest in fuel cells has arisen as a result of the promise and the technical challenges of viable power generation systems. In addition, increasing concern on the environmental consequences of fossil fuel use in the production of electricity has also stimulated the fuel cell research worldwide. PEM fuel cells can be utilized in a wide range of power generation from watts to hundreds of kilowatts and readily scaleable to meet the need of this broad range of power generation. PEM fuel cells have no moving parts and require less maintenance than conventional engines and generators. They also provide power directly at the site of use and avoid costly losses through energy distribution from a centralized power plant. In addition, their use for home and office are ideally suited to the highly energy efficient co-generation of electricity and heat. Recent rapid progress in reducing the costs and improving the performance of fuel cells promises that in the near future fuel cell based power systems will be ideal power generation systems that are reliable, clean and environmentally friendly.

iv). Principles of fuel cells

Overall Process – A schematic diagram of fuel cell is shown in Figure 1-2.[21] In a proton-exchange membrane (PEM) fuel cell, fuels are fed continuously to the anode and an oxidant is fed continuously to the cathode. At the surface of the anode catalyst, fuels are converted into protons (H^+) and electrons (e^-). The protons travel through a PEM, which prohibits electrons, to the cathode side. The electrons (e^-) are forced to travel through an external wire and deliver part of their energy to a 'load' on their way to the cathode. At the cathode, the transferred protons and the energy depleted electron combine with oxygen to produce water. Theoretically, any substance capable of chemical oxidation that can be supplied continuously can be used as a fuel at the anode of fuel cell. Similarly, the oxidant can be any fluid that can be reduced at a sufficient rate. However, cost, availability, and reactivity are the key issues in their selection. Hydrogen and methanol are usually chosen as fuels for most PEM fuel cell applications because of their relatively high activity at low temperatures. Gaseous oxygen or air is the most common choice for the oxidant because it is readily and economically available. The electrochemical reaction takes place at the surface of the electrodes that are attached to a carbon paper or carbon cloth. The carbon is conductive and porous that allows the flow of gases and electrons through it. The membrane in a PEM cell is typically a solid electrolyte called Nafion®, a perfluorosulfonic acid polymer made by Dupont. This membrane allows protons to travel through but inhibits the electrons from passing through it. The proton transfers through the membrane by virtue of the electric field created across the membrane.

The PEM fuel cells can be either a hydrogen fuel cell or a methanol fuel cell, depending upon the fuel used. The hydrogen fuel cell uses H_2 gas as the fuel and provides very high fuel cell performance and efficiency for pure hydrogen, while methanol fuel cell uses liquid methanol as a fuel that provides relatively low performance and efficiency, but precludes the use of a reformer.

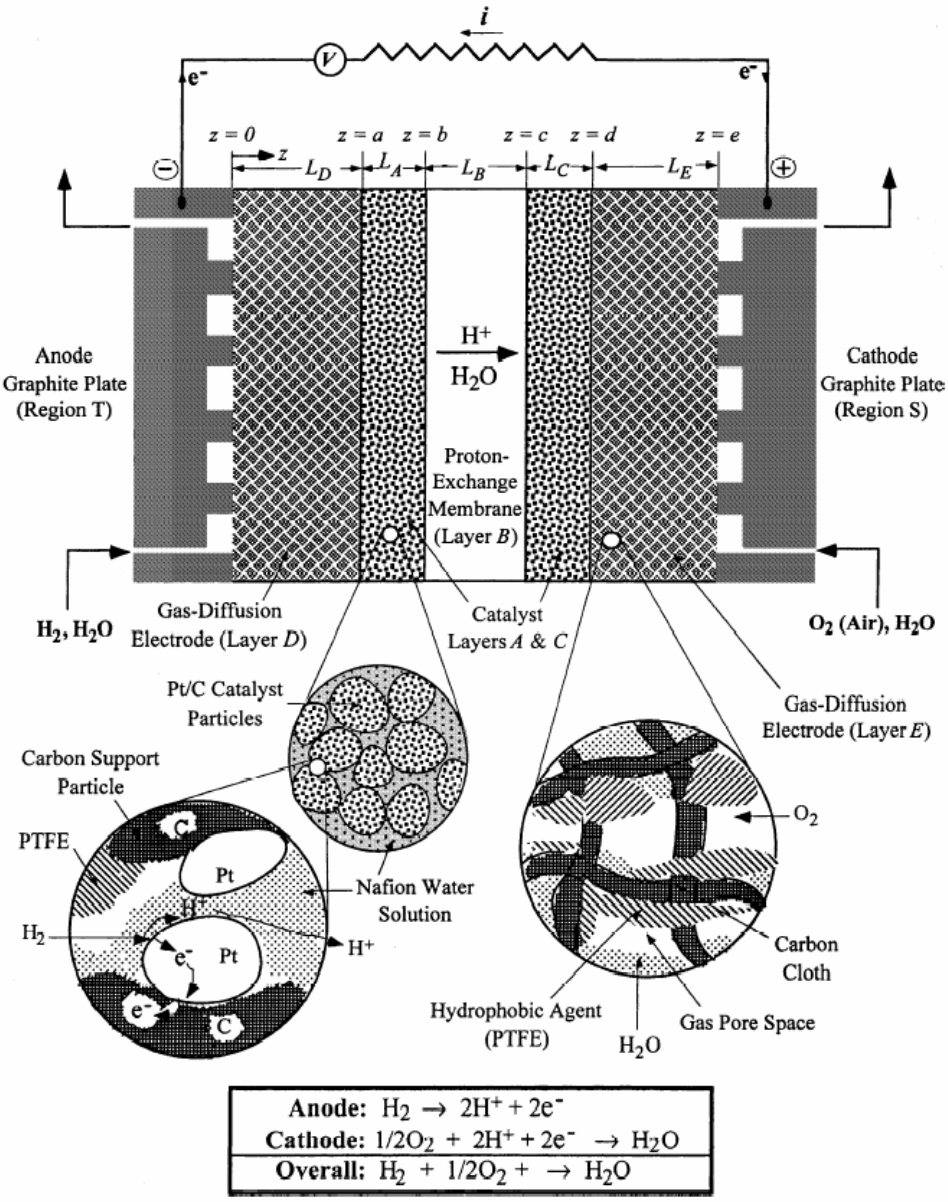

Figure 1-2. A schematic representation of PEM fuel cell where fuel is hydrogen (ref. 21).

The half-cell reactions of hydrogen fuel cell and methanol fuel cells are as follows:

Hydrogen fuel cell

Anode: $H_2 \leftrightarrows 2H^+ + 2e^-$ $\Delta G^0 = 0.00$ [1]

Cathode: $\frac{1}{2} O_2 + 2H^+ + 2e^- \leftrightarrows H_2O$ $\Delta G^0 = -237$ kJ/mol [2]

Overall: $H_2 + \frac{1}{2} O_2 = H_2O$ $\Delta G^0 = -237$ kJ/mol [3]

while for *methanol fuel cell*

Anode: $CH_3OH + H_2O \leftrightarrows CO_2 + 6H^+ + 6e^-$ $\Delta G^0 = 9.3$ kJ/mol [4]

Cathode: $\frac{3}{2} O_2 + 6H^+ + 6e^- \leftrightarrows 3H_2O$ $\Delta G^0 = -237$ kJ/mol [5]

Overall: $CH_3OH + \frac{3}{2} O_2 \leftrightarrows 2\ H_2O + CO_2$ $\Delta G^0 = -227.7$ kJ/mol [6]

Efficiency – Thermodynamic analysis provides the relationship between the chemical energy and electrical energy. The application of first law of thermodynamics a fuel cell system provides the relation of enthalpy change to heat added to the system and work done by the system as, in the absence of kinetic and potential energy changes,

$$\Delta H = Q - W \quad [7]$$

The work done W, in general, can be divided into work associated with mechanical changes and work associated with other forces, e.g., surface, friction, or electrical. For the case of fuel cells, only electrical work W is involved. For determining maximum useful electric work possible, Eq. 7 is applied to a reversible process

$$-W_{E,rev} = \Delta H - Q_{rev} \quad [8]$$

For a reversible change at constant temperature and pressure, the heat transferred to the system is given by the second law of thermodynamics

$$Q_{rev} = T\Delta S \quad [9]$$

Further, a relevant thermodynamic relation is

$$\Delta G = \Delta H - T\Delta S \quad [10]$$

Combining Eqs. 8 -10 gives

$$W_{E,rev} = -\Delta G \quad [11]$$

In order words, the change of Gibbs free energy of a reversible system is equal to the maximum electrical work obtainable from systems at constant temperature and pressure. The maximum electric work is equal to the number of charges multiplied by maximum potential difference, which is reversible cell potential

$$W_{E,rev} = -nFV_0 \quad [12]$$

where n is the number of charges, F is Faraday's constant (=96,487 C/equiv.), and V_0 is reversible cell potential. Thus

$$V_0 = -\frac{\Delta G}{nF} \quad [13]$$

The maximum efficiency of fuel cell, thus

$$\varepsilon_{rev} = -\frac{W_{E,rev}}{\Delta H} = -\frac{\Delta G}{\Delta H} \quad [14]$$

Since the actual electrical work, $W_E = nFV$, where V is the actual fuel cell voltage, the actual efficiency

$$\varepsilon = -\frac{W_E}{\Delta H} \quad [15]$$

Therefore

$$\frac{\varepsilon}{\varepsilon_{rev}} = -\frac{V}{V_0} \quad [16]$$

which shows the importance of maximizing the cell operating potential at a desired current density.

Applying Eq. 14 into hydrogen fuel cell provides $V_{0,anode}$ = 0 and $V_{0,cathode}$ = 1.229 V, while methanol fuel cell $V_{0,anode}$ = - 0.016 V and $V_{0,cathode}$ = 1.229 V. Thus, the open circuit potentials for hydrogen and methanol fuel cells are 1.229 V and 1.213 V, respectively. This calculation is based on the standard temperature and pressure with liquid phase water and methanol.

Reaction Mechanism – The catalytic hydrogen oxidation reaction occurs on Pt-based catalyst in fuel cell and has been much studied. One of the most common proposed mechanisms is the so-called Tafel–Volmer mechanism, which consists of two steps: a Tafel step, namely, the dissociative chemisorption of hydrogen, and a Volmer step, the dissociated hydrogen atom on the catalyst forming a proton and an electron by electrochemical reaction as follows:

$$2Pt_{(S)} + H_2 \leftrightarrows Pt - H_{ads} + Pt - H_{ads} \qquad \text{Tafel Step} \qquad [17]$$

$$Pt - H_{ads} \leftrightarrows Pt + H^+ + e^- \qquad \text{Volmer Step} \qquad [18]$$

where $Pt_{(S)}$ is a free surface site on Pt and $Pt - H_{ads}$ is an adsorbed H-atom on the Pt active site. The overpotential for the hydrogen oxidation reaction (HOR) is relatively small at most practical current densities. However, for reformed hydrocarbons, anode feed may contain roughly 100 ppm CO even after gas clean up in the fuel reforming section of a fuel cell power plant. Even at this small level of CO, it adsorbs strongly on Pt surface occupying the majority of sites and is thus considered as the most abundant surface species. For reformate gas containing CO, Pt alloys usually Pt-Ru are more effective for the anode HOR reaction.

For methanol oxidation reaction (MOR), many mechanisms have been suggested which may be simplified as follows;[22]

i) Electrosorption of methanol onto the catalyst

ii) Stepwise dehydrogenation to eventually form adsorbed CO, and

iii) Addition of oxygen from OH (resulting from water) to adsorbed CO to generate CO_2.

The thermodynamic equilibrium potential for MOR reaction 4 is 0.02 V. The electro-oxidation is considered to take place through the following steps:[22]

$$Pt + CH_3OH \leftrightarrows Pt\text{-}(CH_3OH)_{ads} \quad [19]$$

$$Pt\text{-}(CH_3OH)_{ads} \leftrightarrows Pt\text{-}(CH_2OH)_{ads} + H^+ + e^- \quad [20]$$

$$Pt\text{-}(CH_2OH)_{ads} \leftrightarrows Pt\text{-}(CHOH)_{ads} + H^+ + e^- \quad [21]$$

$$Pt\text{-}(CHOH)_{ads} \leftrightarrows Pt\text{-}(CHO)_{ads} + H^+ + e^- \quad [22]$$

$$Pt\text{-}(CHO)_{ads} \leftrightarrows Pt\text{-}(CO)_{ads} + H^+ + e^- \quad [23]$$

$$Pt(s) + H_2O \leftrightarrows Pt\text{-}(OH)_{ads} + H^+ + e^- \quad [24]$$

$$Pt\text{-}(CO)_{ads} + Pt\text{-}(OH)_{ads} \leftrightarrow Pt\text{-}(COOH)_{ads} \quad [25]$$

or

$$Pt\text{-}(CO)_{ads} + H_2O \leftrightarrows Pt\text{-}(COOH)_{ads} + H^+ + e^- \quad [26]$$

$$Pt\text{-}(COOH)_{ads} \leftrightarrows Pt(s) + CO_2 + H^+ + e^- \quad [27]$$

The electro-sorption of methanol on bulk platinum shows activation energy of 35 kJ/mol and the abundant surface species is linearly bonded CO at higher concentration and Pt-CHO at lower methanol concentrations.[22]

There has been an intensive search for other active materials because platinum is not sufficiently active for methanol oxidation. Most studies are concentrated on finding materials that can provide oxygen in active form from water to facilitate oxidation of chemisorbed CO. Even though various theories[23-25] have been suggested to explain the promoting effect of the additional elements, the subject remains controversial. Transition metal promoters and adatoms are seen as a means to improve the electro-catalytic behavior of electrode either by minimizing the CO adsorption or by enhancing the CO oxidation

reaction. Based on the electronic and bifunctional theories expounded it is considered that the role of the second element is to increase OH adsorption on the catalyst surface and to decrease the adsorption strength of the poisoning methanolic residues.

Many binary and ternary Pt alloys using different metals such as Pt-Ru,[26] Pt-Sn,[27] Pt-Ru-W,[28] Pt-Ru-Mo[29] and Pt-Ru-Sn[30] are proposed. Among many binary catalysts, Pt-Ru is reported as having largest promotional effect and has potential as electro-catalysts for methanol oxidation. Methanol is oxidized according to bifunctional mechanism on Pt-Ru alloy catalysts. The Pt-$(CO)_{ads}$ is removed via an oxygen-transfer step from electro-generated Ru-OH.

$$Ru + H_2O \leftrightarrows Ru\text{-}(OH)_{ads} + H^+ + e^- \quad [28]$$

$$Ru\text{-}(OH)_{ads} + Pt\text{-}(CO)_{ads} \leftrightarrows Ru + Pt + CO_2 + H^+ + e^- \quad [29]$$

Pt-Ru oxidizes CO more effectively than Pt alone owing to the ability of Ru to oxidatively adsorb water at smaller positive potentials. Pt is responsible for catalyzing the dehydrogenation of methanol and the reaction is poisoned by the formation of Pt-$(CO)_{ads}$ after complete dehydrogenation reaction. The removal of CO is facilitated by Ru, which may also act by weakening the Pt-CO bond, and/or by promoting the oxidation of CO to CO_2 via activation of water in an adjacent site to facilitate the formation of the second C-O bond. The onset potential of forming CO_2 on Pt-Ru (0.220 V vs RHE) is lower than that on Pt-black (0.325 V vs RHE). The alloying of Ru and Pt has been postulated to give rise to an electronic effect whereby electrons are transferred between Ru and Pt, though there are controversies on the direction of electron transfer in Pt-Ru alloy catalysts. The alloying Ru on Pt changes the structure of surface electrons and adsorbs CO less strongly compared with pure Pt, rendering it more liable to nucleophilic attack by water and thereby permitting oxidation of CO at lower potential. The most widely used electro-catalysts for oxygen reduction are based on platinum.[18] In DMFC, unreacted methanol from anode also

diffuses across the membrane to the cathode. Therefore, methanol oxidation and oxygen reduction in cathode compartment compete for the same sites producing a mixed potential which reduces the cell open circuit potential coupled with slower kinetics of oxygen reduction.

Kinetics, Resistances, and Polarization – The reaction kinetics on the anode and cathodes may be obtained from Butler-Volmer equation

$$i = i_0\left[\exp(\alpha_A F\eta / RT) - \exp(-\alpha_C F\eta / RT)\right] \quad [30]$$

where i_0 is the exchange current density, α_A and α_C is the transfer coefficients for the anodic and cathodic reaction, respectively, and η is the overpotential to derive the reaction. The fuel cell can be viewed as it has a number of resistances as shown in Figure 1-3. Then, based on Ohm's law, the voltage-current relationship can be written as

$$V = V_0 - iR_A - iR_M - iR_C - iR_I \quad [31]$$

where specific anode resistance is a combination of diffusion and kinetic resistance, $R_A = R_{D,A} + R_{K,A}$, and similarly cathode resistances $R_C = R_{D,C} + R_{K,C}$, R_M is the membrane resistance and R_I is the interfacial resistances in the cell. The current drawn, i, depends upon the load in the external current. In a "reversible" fuel cell, there are no irreversibilities (losses), and thus the cell voltage $V = V_0$ regardless of current "*i*" drawn. In reality, however, it drops due to the various diffusions, kinetic and ohmic resistances as

$$V = V_0 - |\eta_A| - |\eta_M| - |\eta_C| - |\eta_I| \quad [32]$$

where V_0 is the equilibrium open circuit potential, η_A, η_C, η_M and η_I represent the overpotential due to anode, membrane, cathode and interfaces, respectively. These overpotentials can be obtained as

$$\eta_A = \frac{RT}{\alpha_A F}\sinh^{-1}\left\{\frac{1}{2}\left[\frac{i_A / i_{A,0}}{1 - i_A / i_{A,L}}\right]\right\} = \eta_{D,A} + \eta_{K.A} \quad [33]$$

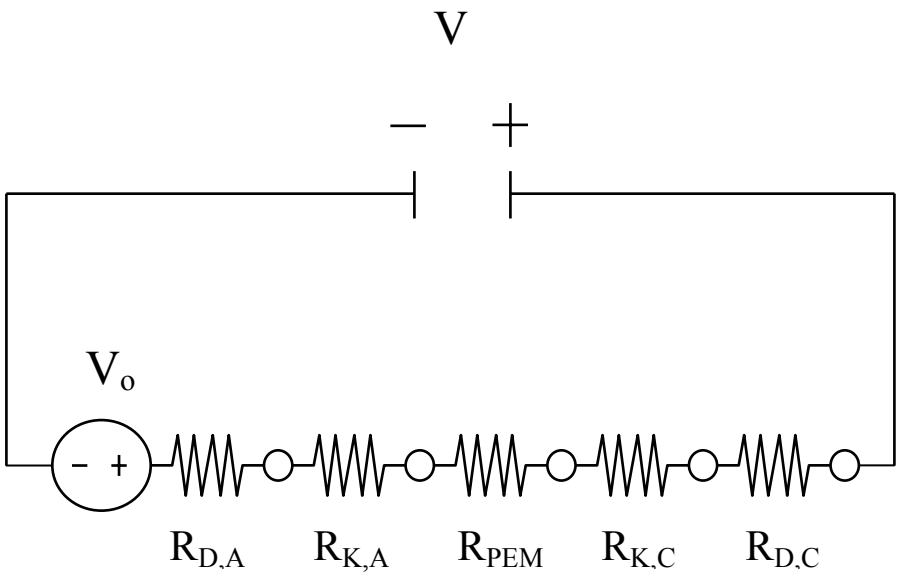

Figure 1-3. Fuel cells view as a series of resistances.

where i_A is the current density at anode, $i_{A,0}$ is the exchange current density at anode, $i_{A,L}$ is the limiting current density at anode, $\eta_{D,A}$ is the overpotential due to the diffusion of hydrogen at anode, and $\eta_{K,A}$ is the overpotential due to the kinetics at anode surface. Similarly, the cathode overpotential is

$$-\eta_C = \frac{RT}{\alpha_C F}\sinh^{-1}\left\{\frac{1}{2}\left[\frac{i_C / i_{C,0}}{1 - i_C / i_{C,L}}\right]\right\} = \eta_{D,C} + \eta_{K.C} \qquad [34]$$

The above two expressions between current density and potential loss are non-linear. For PEM, however, Ohm's law is applicable

$$i = -\sigma_B \frac{d\Phi_B}{dz} \qquad [35]$$

Integrating this over the membrane thickness for constant *i* provides

$$\eta_M = i\left(\frac{L_B}{\sigma_B}\right) \qquad [36]$$

where L_B and σ_B are the thickness and the conductivity of PEM. Thus, the current-voltage relation can be written[21] with $i_A = i_C = i$,

$$V = V_0 - \frac{RT}{\alpha_A F}\sinh^{-1}\left\{\frac{1}{2}\left[\frac{i / i_{A,0}}{1 - i / i_{A,L}}\right]\right\} - \frac{RT}{\alpha_C F}\sinh^{-1}\left\{\frac{1}{2}\left[\frac{i / i_{C,0}}{1 - i / i_{C,L}}\right]\right\} - i\left(\frac{L_B}{\sigma_B}\right) - iR_I \qquad [37]$$

Typically, anode overpotential is low, i.e., $\eta_A \approx 0.05$ V, but the cathode overpotential is highest, i.e., $\eta_C \approx$-0.4 V in normal H_2/O_2 fuel cells. The membrane overpotential increases with the thickness but decreases with the conductivity of the membrane. The power density can be obtained by multiplying *i* in Eq. 45, i.e., $P = Vi$.

In analogy to the linear Ohm's law, it is useful to define a *differential* resistance for non-linear potential-current relations by

$$R \equiv \frac{\partial(\Delta\Phi)}{\partial I} \qquad [38]$$

For a fuel cell, the overall MEA specific resistance can be defined as

$$R \equiv \frac{d(V_0 - V)}{di} \qquad [39]$$

Using this in Eq. 32 gives

$$R = -\frac{d\eta_C}{di} + \frac{d\eta_A}{di} + \frac{d\eta_M}{di} + \frac{d\eta_I}{di} \qquad [40]$$

Substitution of each overpotential and differentiation with respect to *i* give the differential resistances as follows:

$$R_A = \frac{RT}{(2\alpha_A F i_{A,0})(1 - i/i_{A,L})^2 \left[1 + \frac{1}{4}\left(\frac{i/i_{A,0}}{1 - i/i_{A,L}}\right)^2\right]^{1/2}} \qquad [41]$$

$$R_C = \frac{RT}{(2\alpha_C F i_{C,0})(1 - i/i_{C,L})^2 \left[1 + \frac{1}{4}\left(\frac{i/i_{C,0}}{1 - i/i_{C,L}}\right)^2\right]^{1/2}} \qquad [42]$$

$R_M = L_M / \sigma_M$ and, of course $R_I = R_I$. The kinetic resistance, especially cathode resistance, is dominating at low *i*. At intermediate *i*, the membrane resistance R_M dominates. At high *i*, the diffusional limitation (limiting current density) dominates the resistance. For these non-Ohmic resistance, of course, Eq. 31 is replaced by

$$V_0 - V = \int_0^i R_A di + \int_0^i R_C di + iR_M + iR_i \qquad [43$$

v). Hardware of fuel cells

Electrode (catalyst) – As described above, two separate electrochemical reactions take place on the surface of the electrodes: an oxidation half-reaction occurring at the anode and a reduction half-reaction at the cathode. The anode and cathode are separated from each other by the electrolytes, the proton-exchange membrane. Pt (or Pt-Ru) supported on carbon is typically used in PEMFC and the loading of the catalyst is about 0.4 mg/cm^2 for hydrogen fuel cell and 2 – 4 mg/cm^2 for DMFC.

Proton-Exchange Membrane – The electrolyte commonly used in a PEM fuel cell is solid polymer materials referred to Nafion® produced by DuPont. The facile transfer of protons from the anode to the cathode is the most important property of the membrane. The electrons produced at anode are forced to travel through an external wire to the cathode to complete the circuit. It is during their passage through the circuitry external to the fuel cell that the electrons provide external power to run a car or a power plant. Although the membrane is thin, 50 – 185 μm, it is an effective gas separator as well.

Gas-Diffusion Backing Layer – The backing layers, one next to the anode, and the other next to the cathode are usually made of a porous carbon paper or carbon cloth, typically 100 to 300 μm thick. The porous nature of the backing layer ensures effective diffusion of feed and product components to and from the catalyst on the MEA. The correct balance of hydrophobicity in the backing material allows the right amount of water vapor to reach the MEA to keep the membrane humidified while allowing the liquid water produced at the cathode to leave the cell.

Flow Field/Current Collector – Two plates in a single cell provide flow field for feed stream and collect current in fuel cells. The plates are made of a lightweight, strong, gas impermeable, electron-conducting material; graphite or metals are commonly used. The pattern of the flow field in plate as well as the width and depth of the channels are very important for the efficiency of fuel cells. The design of flow field also influences water supply to the membrane and water removal from the cathode. By adding a load-containing

external circuit, the PEM fuel cell is now complete. Figure 1-4 shows each component of single cell and the fuel cell stack. The connection of single cells and stacks can be in series or parallel depending on the voltage and current requirements for specific applications.

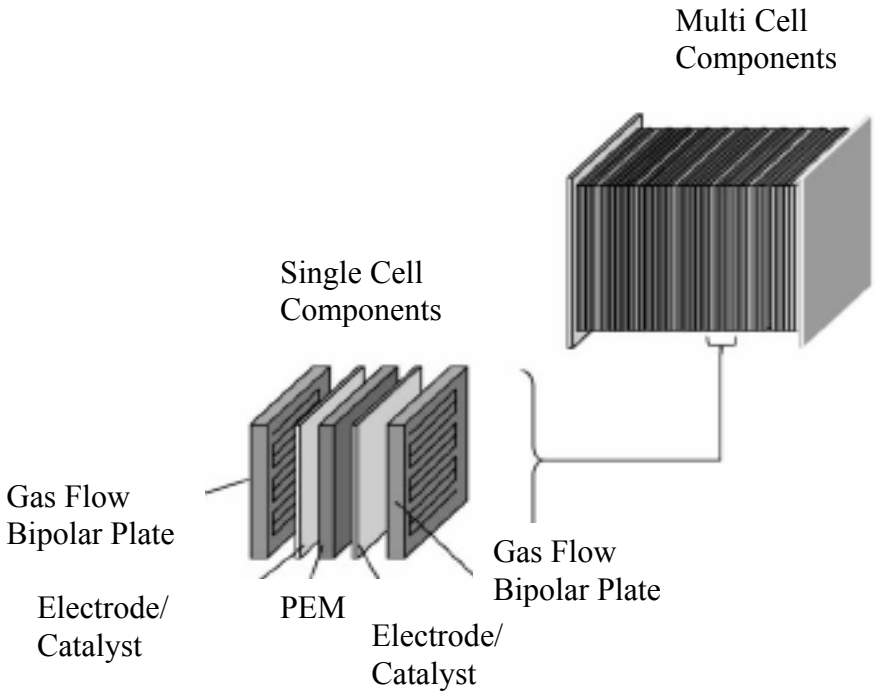

Figure 1-4. A schematic of single fuel cell and stack (ref. 7).

1-2. Proton Exchange Membranes (PEMs)

i). Significance of thermodynamics and transport in fuel cells

The proton conduction in most PEMs is directly related to the extent of hydration of the membranes due to the water-assisted proton transport mechanism in PEMs. Since the conductivity of PEMs increases strongly with the water content of the membrane,[31] it is desirable to maintain maximum attainable amount of water in the membranes to obtain highest conductivity for a given PEM. In PEM fuel cells, water is supplied to the membranes by humidified gases entering into the fuel cell, and is, of course, also provided within the cell. Thus, the water uptake characteristics of the membrane are important in understanding and developing fuel cell systems. One of the reasons limiting fuel cell operating temperature to below 100°C is that water content of the membrane is low at high temperature or low relative humidity (RH), which results in low conductivity of protons. In view of the industrial and technological importance of fuel cells, a study of the relationship between the water content and proton conductivity of PEMs can provide useful information leading to performance optimization.

The water uptake in PEMs, especially Nafion®, has been widely reported. It has been found that there are significant differences in water uptake by PEM from liquid and its saturated vapor. The water uptake depends on temperature, equivalent weight (EW), elastic properties, type of cations, and pretreatments of the membranes. PEMs of low EW show high water uptake. However, lower EWs are difficult to utilize because of ionomer stability. When PEMs are swollen aggressively at high temperature in the presence of glycerol, it also changes the water uptake characteristics substantially. For example, Nafion® 117 takes in typically 22 water molecules per sulfonic group in liquid water at room temperature, while Nafion 117 after being treated in glycerol at 225º C takes in up to 80 water molecules per sulfonic acid group. Water uptake of PEMs in vapor phase

depends on the relative humidity (RH) or activity of the water vapor. The comparison of water uptake by Nafion® from the liquid and its saturated vapor reveals an interesting apparent paradox. The water content of the membrane in equilibrium with saturated vapor is not the same as that of the same membrane in contact with liquid water. This phenomenon is called "Schroeder's Paradox"[32] and has not been clearly explained. The hydrophobic nature of vapor-equilibrated membrane surfaces may provide clues for the explanation.

The most important property of PEMs is their high proton conductivity under humidified conditions. This high proton conductivity provides the basis for the high power densities in hydrogen-oxygen fuel cells. The dependence of proton conductivity in PEMs on the water content is quite critical, and demands effective cell and stack design to maintain a high level of water during the fuel cell operation. The conductivity of Nafion® increases with the water content and reaches to 0.05-0.07 S/cm under saturated conditions at room temperature. The dependence of proton conductivity on water content has been empirically approximated by Bruggeman-type relation[33]

$$\sigma = 0.54\ \sigma_e \left(1 - V_p\right)^{1.5} \qquad [44]$$

where σ is the membrane conductivity, σ_e is the conductivity of sulfuric acid solution of equal concentration to that of sulfonic acid, and V_p is the volume fraction of polymer in the water-polymer composite. This shows that the proton conductivity is lower in a PEM as compared with same proton concentration in sulfuric acid solution. A random network model[34] has been developed to describe the proton conductivity in Nafion®. In this model, two types of pore were proposed: wet pores have high water content and thus high proton conductivity and dry pores have minimal water and low conductivity. The swelling and structural changes that occur within the membrane with water uptake were described in the following equations:

$$n(w) = n_0(1+\alpha w) \quad [45]$$

$$v(w) = v_0(1+\beta w)^3 \quad [46]$$

where $n(w)$ is the number of sulfonic acid groups in an average pore, n_0 is the number of sulfonic acid groups in the average pore of a dry membrane, $v(w)$ is the average volume of the pore, v_0 is the pore volume in the dry membrane, w is the water content of the membrane in weight percent, and the parameter α and β are used to describe the extent of the swelling and reorganization in the membrane. The fraction of wet pores is written as

$$x(w) = \frac{\gamma w}{(1+\beta w)^3 - \gamma w^2 \alpha} \quad [47]$$

where γ is a scaling factor. The conductivity of membrane is the weighted average of the conductivities of the wet and dry pores

$$\sigma = x(w)\sigma_{wet} + (1-x(w))\sigma_{dry} \quad [48]$$

The parameters α, β, and γ were fitted to the experimental data.

Another model fundamental model developed by our group is based on the dusty-gas model, dissociation equilibrium of protons in the membrane, and porosity and tortuosity considerations[35]

$$\sigma = (\varepsilon - \varepsilon_0)^q \left(\frac{\lambda_i^0}{1+\delta}\right) C_{HA,o}\alpha \quad [49]$$

where ε is the porosity ε_0 is the porosity corresponding to the percolation threshold, q is a fitted constant, $C_{HA,0}$ is the concentration of sulfonic acid groups, δ is the ratio of diffusion coefficients of hydronium ion in water to membrane matrix, λ_i^0 is the equivalent conductance at infinite dilution in water, and α is the fractional dissociation of the sulfonic acid in the membrane, which is a function of water content of the membrane. The parameter δ was used as a fitted parameter. According to this model, proton conductivity

depends upon i) ε, water content, ii) ε_0 the percolation threshold volume fraction of water in hydrated membrane, iii) q, critical or Bruggeman exponent, iv) $C_{HA,0}$, concentration of sulfonic acid, and v) α, degree of dissociation of sulfonic acid groups. Although this model captures important components for proton transport, it is not entirely predictive.

In this thesis, thermodynamics of sorption and proton transport mechanism in PEMs have been studied. Considering the fact that Nafion®, which was developed about forty years ago, is still the best and only commercial membrane so far in PEM fuel cells, it is quite necessary to investigate Nafion® in terms of its thermodynamics and proton transport characteristics in order to develop better membranes than Nafion®. This study provides an understanding of thermodynamic and proton transport of PEMs and also proposes a design strategy for proton-conducting PEMs for higher temperature fuel cell applications.

ii). PEM materials

The suitable materials for PEM should meet certain requirements such as stability (chemical, thermal, and mechanical) and low gas permeability over fuel cell operating conditions in addition to excellent proton conductivity and low cost. Historically, a variety of membrane materials have been employed in fuel cells, i.e., i) phenolic membranes, ii) partially sulfonated polystyrene sulfonic acid, and iii) interpolymer of cross-linked polystyrene-divinylbenzene sulfonic acid in an inter matrix. A critical breakthrough was achieved with the introduction of Nafion®, a perfluorosulfonic acid (PFSA) polymer in late 1960s. Table 1-1 shows the history of the PEM development along with their power density and lifetime.[7] Nafion® and its other PFSA relatives meet the basic key requirements and have exclusively used PEM materials due to their stability and good performance. Nafion® provided dramatically improved specific conductivity and lifetime. Typically, the thickness of PFSA membranes ranges between 50 and 175 μm. Other

Table 1-1. Development of proton exchange membrane (ref. 7).

Time	Membrane	Power density (kW m^{-2})	Life time (thousand of hours)
1959-1961	Phenol sulfonic	0.05-0.1	0.3-1
1962-1965	Polystyrene sulfonic	0.4-0.6	0.3-2
1966-1967	Polytrifluorostyrene sulfonic	0.75-0.8	1-10
1968-1970	Nafion® experimental	0.8-1	1-100
1971-1980	Nafion® commercial	6-8	10-100

sources of PSFA membranes have been Dow Chemical, Asahi Glass, Asahi chemicals, and W. L. Gore. W. L. Gore and Associate has designed a PEM to reduce the crossover of gases and increase mechanical strength of Nafion by incorporation of Nafion® in a fine-mesh Teflon support.

PSFA membranes consists of three regions: i) a polytetrafluoroethylene (PTFE) backbone, ii) side chains which connect the molecular backbone to ionic cluster, and iii) ionic clusters consisting of sulfonic acid ion. However, there are several disadvantages to the practical use of PSFA membranes in fuel cell applications. In addition to the high cost of production, the membrane properties degrade at high temperature (>111ºC) and even release toxic gases at temperature above 150° C. Since PSFA membrane should be kept hydrated to retain proton conductivity, the fuel cell operating temperature must be kept below the boiling point of water. Some increase in operating temperature, up to 120ºC, may be possible at the expense of operation under pressurized stream. This alternative will however shorten the life of the membranes. Because of the disadvantages of PFSA membranes, extensive research effort to find alternative materials to PSFA is being made worldwide. The PEMs developed so far can be can be classified into three categories: i) perfluorinated polymers, *e.g.*, Nafion®, Flemion®, Gore-Select® and Dow membranes; ii) partially fluorinated polymers, *e.g.*, poly-α, β, β-trifluorostyrene and Ballard Advanced Materials 3rd Generations (BAM3G) polymers; and iii) hydrocarbon polymers, *e.g.*, poly(phenylene oxide) PPO, poly(ether ether ketone) PEEK, poly(phosphazine) PP, poly(imides) PI, poly(benzimidazole) PBI. The hydrocarbon polymers have been proposed because of the high cost of perfluorinated membranes although their lifetime and mechanical strength is much inferior to PFSA. In addition to this classification, polymer/inorganic composite membranes can be identified as a newe family of PEMs.[36] The polymer/inorganic membranes can be developed via modification of polymer (host

membrane) by the incorporation of inorganics such as SiO_2, ZrO_2/SO_4^{2-}, heteropoly acids to increase proton conductivity and mechanical properties of host membranes.

Although some of the host polymers possess attractive thermo-mechanical properties, none of these alternatives have so far proved to be superior to Nafion®. Nafion® and its close relatives continue to be the electrolyte of choice because of their high conductivity and adequate mechanical properties. As the production cost of PEMs comes down, applications for PEM fuel cells will emerge.

References

1. W. Grove, *Phil. Mag.* **14** (1839) 127.
2. L. Mond and C. Langer, *Proc.R.Soc.Lond*. **46** 144 (1889).
3. W. W. Jacques, *Elec. Eng.*, **21**, 497 (1986).
4. F. T. Bacon, *Int. J. Hydrogen Energy*, **10**, 423 (1985).
5. D. Watkins, K. Dircks, D. Epp, and A. Harkness, *Proc. 32nd International Power Source Symposium*, IEEE Publications, Piscataway, NJ, p. 590, (1986).
6. I. D. Raistrick, in: R. E.White, K. Konishita, J. W. Van Zee, H. S. Burney (Eds.), *Proc. Symposium on Diapharms, Separators and Ion Exchange Membranes*, vol. **86-13**, p. 172 (1986).
7. P. Costamagna and S. Srinivasan, *J. Power Sources*, **102**, 242 (2001).
8. C. Stone and A. E. Morrison, *Solid State Ionics*, **152-152**, 1 (2002).
9. A.B. Satambouli and E. Traversa, *Renewable and Sustainable Energy Reviews*, **6**, 297 (2002).
10. M. L. Perrt and T. F. Fuller, *J. Electrochem. Soc,* **149** S59 (2002).
11. D. Voss, *Science,* **285**, 683 (1999).
12. S. M. Haile, *Acta Materials*, **51**, 5081 (2003).
13. B. C. H. Steele, *J. Material Sci.*, **36**, 1053 (2001).
14. D. P. Wilkinson, *Interface,* Spring, 22 (2001).
15. G. Halpert, H. Frank and S. Surampudi, *Interface*, **Fall**, 25 (1999).
16. G. J. K. Acres, *J. Power Sources*, **100**, 60 (2001).
17. L. Carrette, K. A. Friedrich, and U. Stimming, *Fuel Cells*, **1**, 5 (2001).
18. A. S. Arico, S. Srinivasan, and V. Antonucci, *Fuel Cells*, **1**, 133 (2001).
19. F. Preli, *Fuel Cells*, **2**, 5 (2002).
20. M. Arita, *Fuel Cells*, **2**, 10 (2002).
21. T. Thampan, S. Malhotra, J. Zhang, and D. Datta, *Catalysis Today,* **67**, 15 (2001).

22. A. Hamnett, *Catalysis Today*, **38**, 445 (1997).

23. M. M. P. Janseen and J. Moolhuysen, *Electrochim. Acta,* **21**, 861 (1976).

24. M. Watanabe and S. Motoo, *J. Electroanal. Chem*. **60**, 275 (1975).

25. A. B. Anderson, E. Grantcharova and S. Seong, *J. Electrochem. Soc.*, **143**, 2075 (1996).

26. E. Ticianelli, J. G. Berry, M. T. Paffet and S. Gottesfeld, *J. Electroanal. Chem.*, **81**, 229 (1977).

27. A. N. Haner and R. N. Ross, *J. Phys. Chem.*, **95**, 3740 (1991).

28. K. Y. Chen, Z. Sun and A. C. C. Tseung, *Electrochem. Solid State Lett.*, **3**, 10 (2000).

29. J. O'M. Bockris and S. Srinvasan, *Fuel Cell: Their Electrochemistry*, McGraw Hill Book Company, New York, 1969.

30. M. Gotz and W. Wendt, *Electrochem. Acta*, **43**, 3637 (1998).

31. P. Commer, A. G. Cherstvy, E. Spohr, and A. A. Kornshev, *Fuel Cells*, **2**, 127 (2001).

32. P. V. Schroeder, *Z. Phys. Chem.,* **45**, 75 (1903).

33. R. S. Yeo and H. L. Yeager, *Modern Aspect of Electrochemistry*, **16**, 437 (1985).

34. M. Eikerling, A. A. Kornshev, and U. Stimming, *J. Phys. Chem. B*, **101**, 10807 (1997).

35. T. Thampan, S. Malhotra, H. Tang, and R. Datta, *J. Electrochem. Soc.*, **147**, 3242 (2000).

36. G. Alberti and M. Casciola, *Annu. Rev. Mater. Res.*, **33**, 129 (2003).

Chapter 2. Thermodynamics and Transport Properties in Nafion®: Literature Review

2-1. Properties and Structure of Nafion®

2-1-1. Properties

The proton exchange-membrane (PEM) constitutes a crucial part of PEM fuel cells and warrants a careful study. It serves as a solid electrolyte that conducts protons from anode to cathode as well as a separator of reactant gases. The concept of employing an ion-exchange membrane as a solid electrolyte was first introduced by Grubb[1] in 1959. Extensive research was conducted by General Electric (GE) and others in the early 1960s.[2-4] In the 1960s, the perfluorinated ion exchange membrane called Nafion® was synthesized by Du Pont[2], which has become the standard membrane for fuel cells. Nafion® is composed of a chemically inert hydrophobic backbone ($-CF_2-CF_2-$) with hydrophilic ionic group ($-SO_3H^+$), which allow water sorption and proton conductivity.[5] Nafion® provides a high ionic conductivity, high mechanical, thermal and chemical stability, and has been used in many industrial applications including energy-related fields such as fuel cells,[6] water electrolyzer[7] and solar cell systems.[8] The chemical structure of Nafion® and its properties are given in Figure 2-1 and Table 2-1, respectively.[9]

2-1-2. Structure Models

It is necessary to understand the structure of Nafion® and resulting structure-property relationship for designing better or less expensive proton-exchange membranes for fuel cell application. There is right now a great deal of effort devoted in this direction for alternate and higher temperature PEMs. In fact, transport of protons and sorption of

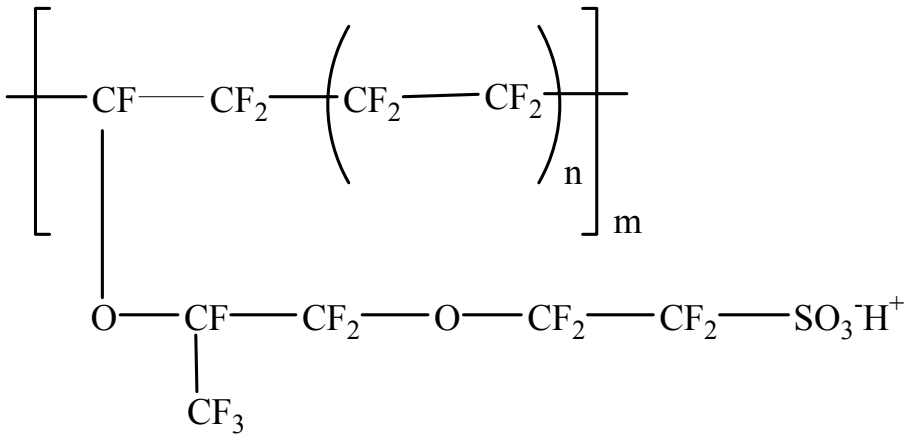

Figure 2-1. Chemical structure of proton exchanged form of Nafion®.

Table 2-1. Properties of Nafion® Perfluorinated Membrane (ref. 9).

1. Thickness and Weight[1]

Membrane Type	Typical Thickness (μm)	Basis Weight (g/m^2)
NE-112	51	100
NE1135	89	190
N-115	127	250
N-117	183	360

[1] Measurements taken with membrane conditioned to 23ºC and 50% RH.

2. Physical Properties

Properties[2]	Typical Value	Test Method
Tensile Modulus, Mpa (Kpsi)		
50 RH, 23^{0}C	249 (36)	ASTM D 882
water soaked, 23^{0}C	114 (16)	ASTM D 882
water soaked, 100^{0}C	64 (9.4)	ASTM D 882
Tensile Strength, Maximum, Mpa (Kpsi)		
50 RH, 23^{0}C	43 (6.2) in MD, 32 (4.6) in TD	ASTM D 882
water soaked, 23^{0}C	34 (4.9) in MD, 26 (3.8) in TD	ASTM D 882
water soaked, 100^{0}C	25 (3.6) in MD, 24 (3.5) in TD	ASTM D 882
Specific Gravity	1.98	-
Conductivity (S/cm)	0.083	See footnote[3]
Acid Capacity (meq/g)	0.89	See footnote[4]

[2] Where specified, MD –machine direction, TD – transverse direction. Conditioning state of membrane given. Measurements taken at 23ºC, 50 % RH.

[3] Conductivity measurement as described by Zawodzinski, et al., *J. Phys. Chem*., 95, 6040 (1991). Membrane conditioned in 100ºC water for 1 hour. Measurement cell submersed in 25ºC D.I. water during experiment.

[4] A base titration procedure measures the equivalents of sulfonic acid in the polymer, and uses the measurement to calculate the acid capacity or equivalent weight of the membrane.

Properties	Typical Value	Test Method
Water content, % water[5]	5	ASTM D 570
Water uptake, % water[6]	38	ASTM D 570
Thickness change, % increase[7]		
from 50 % RH, 23ºC to water soaked, 23^0C	10	ASTM D 756
from 50 % RH, 23ºC to water soaked, 100^0C	14	ASTM D 756
Linear expansion, % increase		
from 50 % RH, 23ºC to water soaked, 23ºC	10	ASTM D 756
from 50 % RH, 23ºC to water soaked, 100ºC	15	ASTM D 756

[5] Water content of membrane conditioned to 23ºC, 50% relative humidity (RH), compared to by dry weight basis.
[6] Water uptake taken from dry membrane to water soaked at 100ºC for 1 hour (dry weight basis).
[7] Average of MD and TD. MD expansion is slightly less than TD.

solvent molecules in a PEM are determined by the nanostructure of the membrane. Although the exact nano-structure of Nafion® is still not precisely known, several models describing its nanostructures have been suggested since early 1970s. Here, a short review of the progress made in the elucidation of ionomeric structure of Nafion® is provided.

i). Eisenberg's Model[10]

In the late 1960s, the concept of ionic clusters in organic polymers was postulated by a series of studies. The term "ionic clusters" means any ionic aggregates in an ionomer. Perfluorinated ion-exchange membranes are classified as ionomers, which are different from the conventional ion-exchange membranes in that they are not cross-linked polyelectrolytes but thermoelastic polymers with pendant acid groups that may be partially or completely neutralized to form salts. Figure 2-2 shows a simple structural conceptualization of crosslinked polyelecrolytes and clustered polyelectrolyes, *i.e.,* Nafion®.

In 1970, Eisenberg developed a theory of ionomer structure that includes the formation of ionic clusters in organic polymer. The association of ions was considered and two basic types of ion aggregates were postulated. One is small aggregates containing few ion pairs, termed multiplets, and the other is large aggregates, termed clusters, which are composed of a nonionic backbone material as well as many ion pairs. The nano-structure of the ionomer in organic polymer can be described as that of a nanophase-separated system in which a matrix of low ion content (multiplet) is interdispersed with ion-rich domain (clusters). The formation of ionic domain or clusters is considered as being a consequence of thermodynamic incompatibility of ionic groups with the low dielectric constant organic matrix. The distances between clusters and the cluster sizes are determined by work done to stretch the polymer chains in cluster formation, electrostatic energy released when multiplets aggregate to form a cluster, and threshold temperature where the elastic and

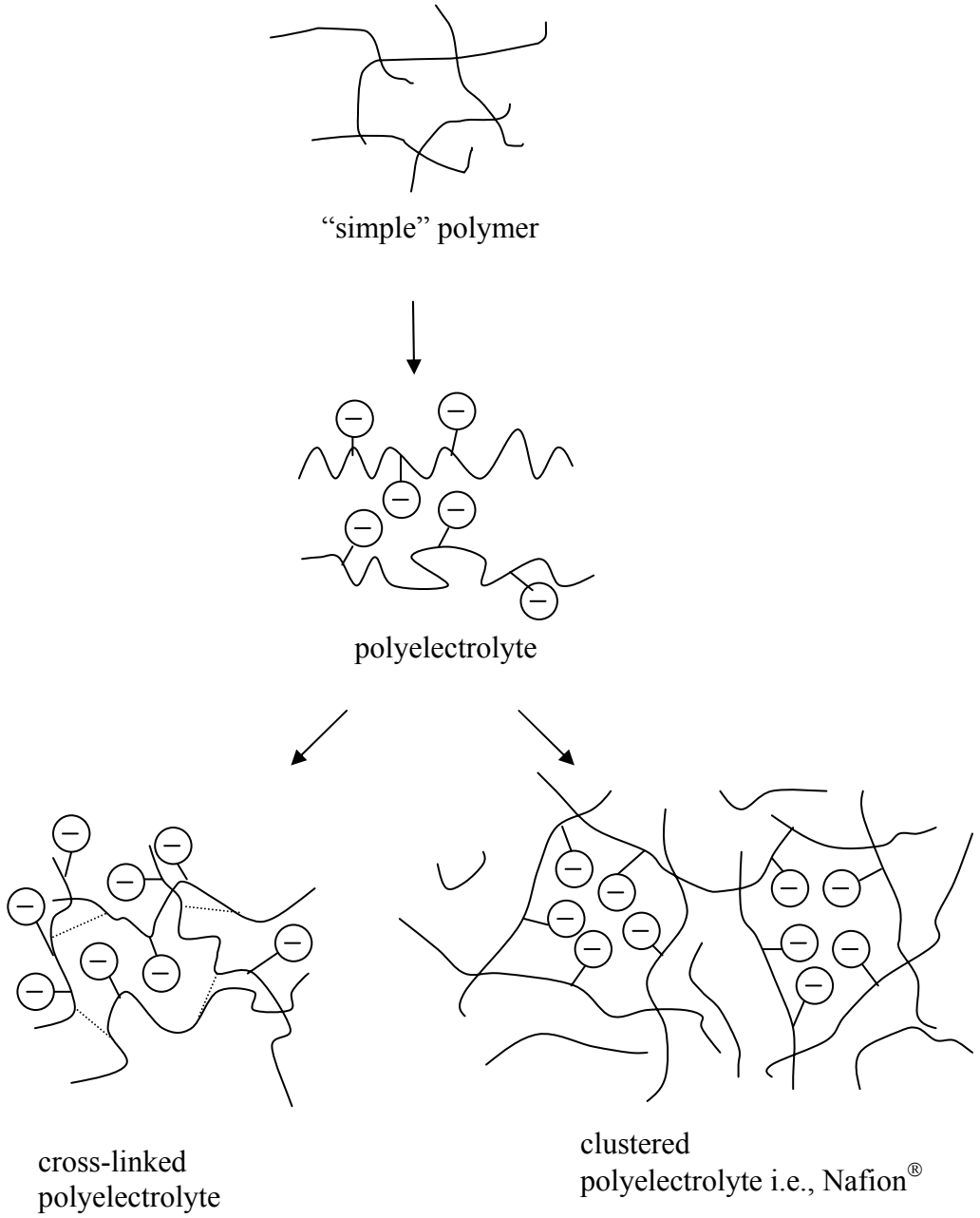

Figure 2-2. Simple structural conceptulization of cross-linked polyelectrolyte and clustered ionomeric system with anionic side chain.

electrostatic forces balance each other. The clusters are not expected to form if the attractive forces between multiplets are smaller than the elastic forces that prevent the multiplets from approaching each other.

ii). Gierke et al's Cluster-Network Model[11,12]

In 1977, Gierke[11] proposed a phenomenological cluster network model. The model adopts the concept of clusters, except that both ions and the absorbed solvent molecules are with in the clusters. Figure 2-3 shows the cluster-network model as applied to Nafion®. In this model, the phase-separated domains are assumed to be spherical inverted micellar structures connected by short narrow channels. If the clusters are indeed approximately spherical, the size of clusters can be obtained from the solvent absorption data in swollen polymer by simple calculation. In 1982, Hsu and Gierke[12] proposed a semi-phenomenological elastic theory for ion clustering which can correctly describe the experimental variation in cluster diameter with cation form of the membrane, equivalent weight, and water content. They have also showed that short channels connecting adjacent clusters are thermodynamically stable.

iii). **Mauritz et. al's Model**[13]

In 1978, Mauritz et. al described the structural organization of Nafion® under different physicochemical conditions. The model considers the balance in energy between the elastic deformation of polymer matrix and various molecular interactions that exist in the polymer. Figure 2-4 shows the schematic representation of Nafion® as developed by Mauritz. The model semi-quantitatively reproduces water absorption, polymer density, and number of waters per exchange site.

iv). Yeager et al.'s Model[14]

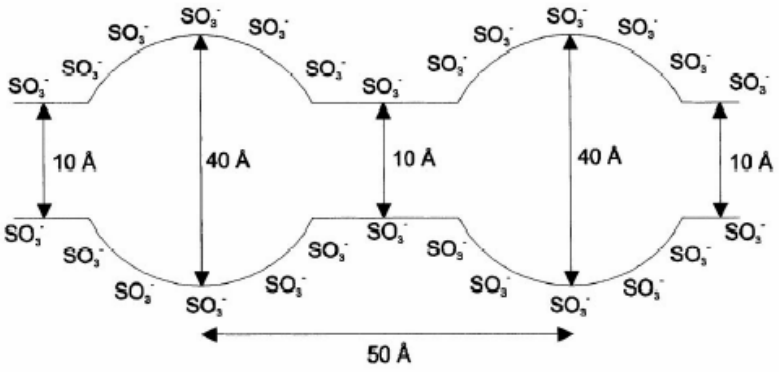

Figure 2-3. Schematic representation of cluster-network model by Gierke.

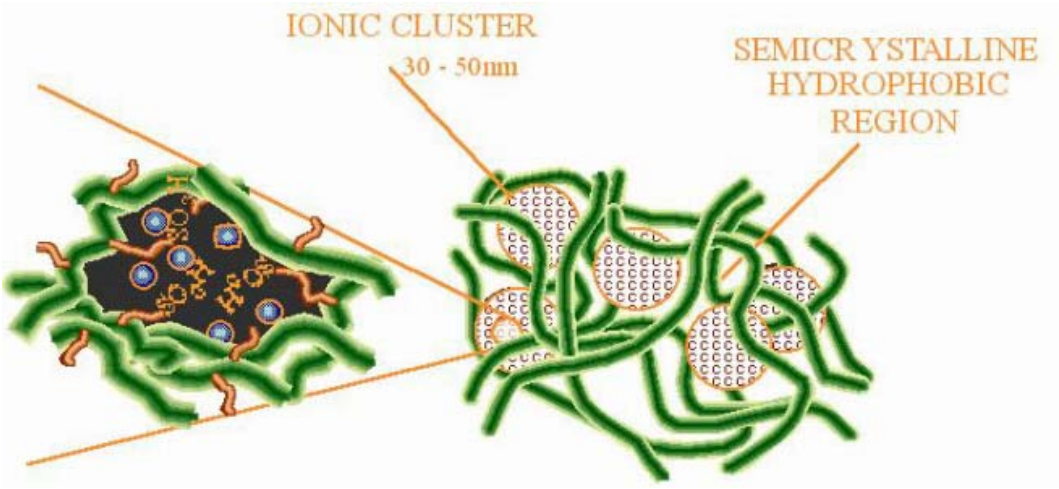

Figure 2-4. Schematic representation of ionic clusters in phase separated domain of Nafion® by Mauritz et.al.

In 1981, Yeager and Steck[14] postulated three-region structural model that correlates various spectroscopic and ionic diffusion results. Figure 2-5 represents a schematic diagram of the model in which the three phases are shown. Region A consists of the hydrophobic fluorocarbon backbone material, some of which is in crystalline form. Region B is an interfacial zone containing pendant side chain material, a small amount of water, some sulfonate exchange sites that have not been incorporated into clusters, and a corresponding fraction of counterions. Region C is hydrophilic where ionic clusters are formed, in which the majority of sulfonate exchange sites, counterions, and absorbed water exist.

v). Recent Models[15-21]

In 1997, Eikerling et al.[15] extended Gierke's cluster-network model further by assuming the existence of channels and two different types of pores in membrane: one containing surface hydration water and the other containing bulk-like water. More recently, many structural studies using small angle X-ray scattering (SAXS), small angle neuron scattering (SANS), and Atomic Force Microscopy (AFM) have been reported. In 1997, Gebel[16] confirmed the phase separation between water pools and the perfluorinated matrix by comparing the SAXS and SANS spectra combined with the analysis. In 2000[17], he proposed a structural evolution of Nafion® when the membrane changes from a dry state to the highly swollen state. Figure 2-6 shows the schematic representation of such structural evolution with water contents in the membrane. In the dry state, isolated spherical ionic clusters are formed with a diameter close to 15 Å and an inner-cluster distance close to 27 Å. The absorption of water molecules induces a modification of the cluster structure that becomes spherical water pools with the ionic groups at the polymer-water interface in order to minimize the interfacial energy. The diameter of water pool is about 20 Å and the inter-aggregate distance is roughly 30 Å, indicating that they are still

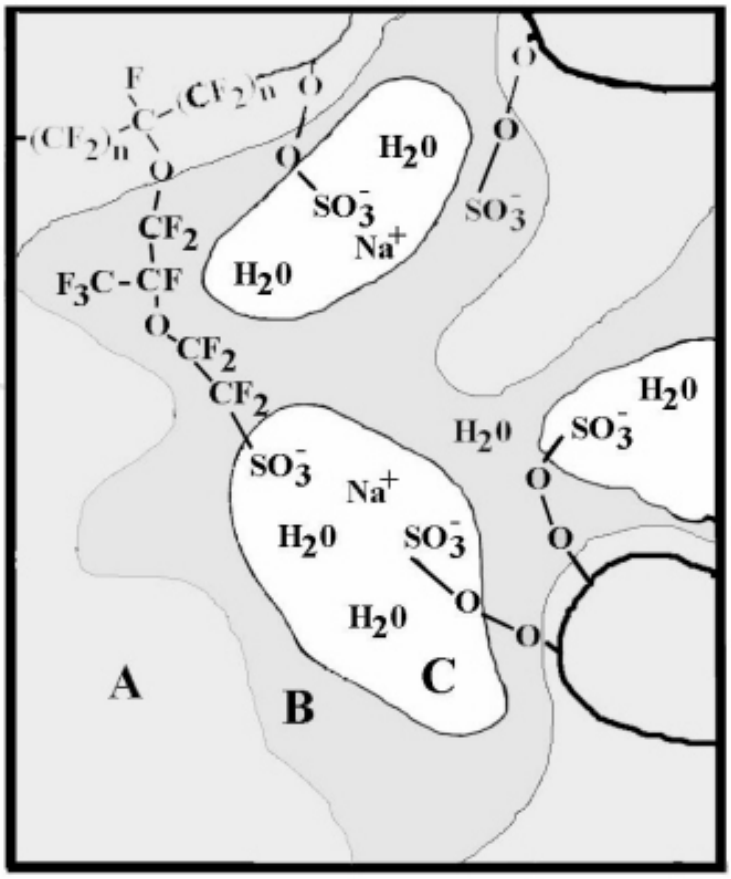

Figure 2-5. Three-phase structural model for Nafion®:
A, fluorocarbon; B, interfacial zone; and C, ionic clusters.

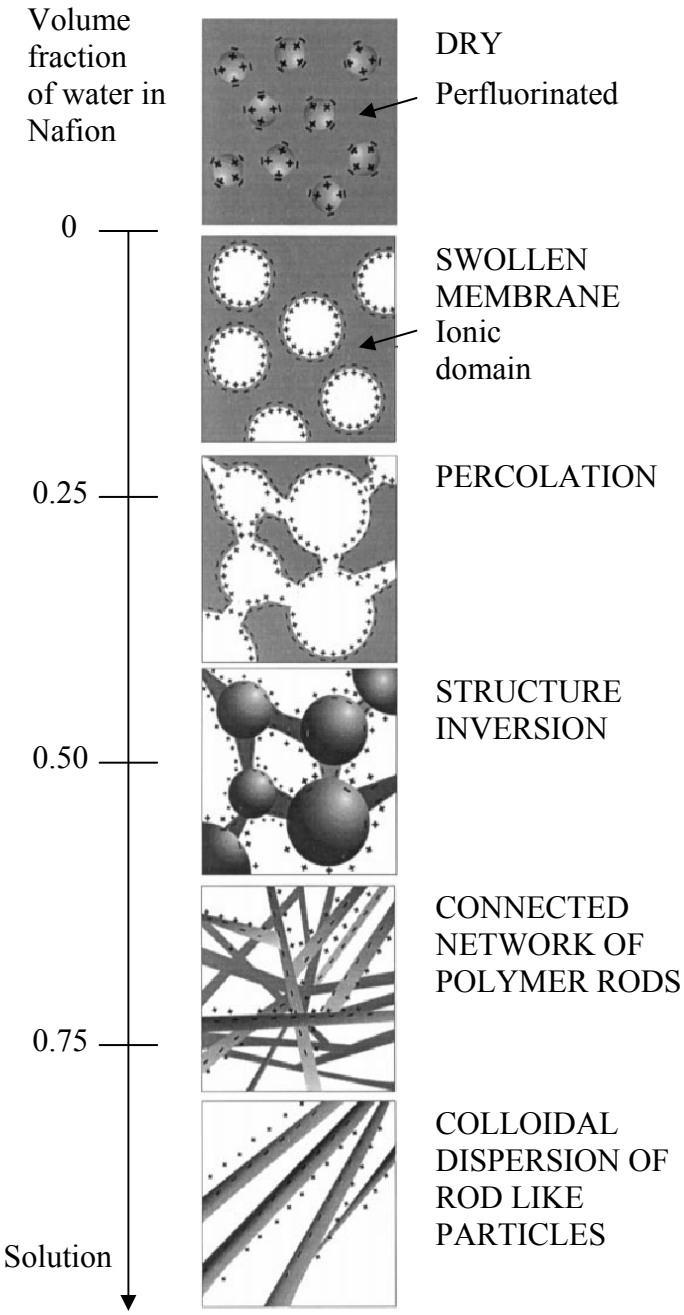

Figure 2-6. Schematic representation of structural changes with water content in perfluorosulfonated ionomer membranes, i.e., Nafion®.

isolated as revealed by the low value of ionic conductivity. As membrane absorbs more water, the cluster swells and the diameter of it increases from 20 Å to 40 Å but relatively small increase in the inter-cluster distance leads to percolation. In this process, the number of ionic groups per cluster increases, and consequently the total number of clusters in membrane decreases. The high increase in ionic conductivity for a water volume fraction larger than ϕ_w = 0.2 reveals the percolation of the ionic aggregates in the membrane. When the water volume fraction is in between ϕ_w = 0.2 and ϕ_w = 0.5, the structure is formed of spherical ionic domains connected with cylinders of water dispersed in the polymer matrix. The diameter of ionic domain increases from 40 Å to 50 Å. At ϕ_w larger than 0.5, a structural inversion occurs and the membranes correspond to a connected network of rod-like polymer aggregates. For ϕ_w = 0.5 to ϕ_w = 0.9, the rod-like network swells and the radius of the rod is about 25 Å. The structure of the highly swollen membrane would be very close to that of the Nafion solution. In 2002, Young et al.[18] confirmed the structural changes proposed by Gebel from their SANS investigation. In 2001, Haubold et al.[19] proposed a model with sandwich-like unit cells composed of polymer-pendant ionic groups-solvent molecules-pendant ionic groups-polymer as shown in Figure 2-7. The water filled wide channels Nafion® are also depicted in Figure 2-8.[20] The formation of clusters is also confirmed by atomic force microscopy (AFM) studies.[21,22]

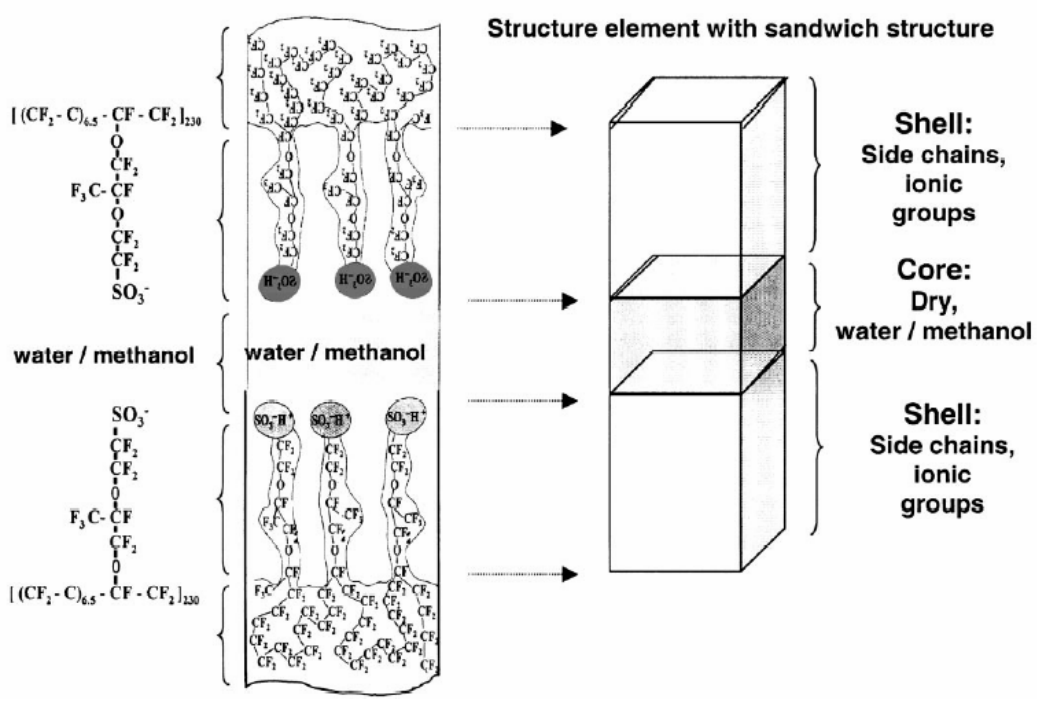

Figure 2-7. Schematic representation of sandwich-like structure elements proposed by Haubold et. al.

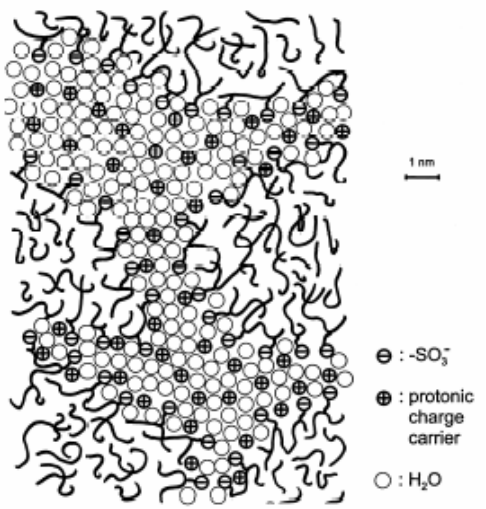

Figure 2-8. Schematic representation of the microstructure of Nafion® (ref. 20).

2-2. Thermodynamics of Sorption

The sorption of water molecules, and their interactions with membranes, and their relation with transport properties of protons in the membranes constitute the heart of the membrane research for fuel cell application. In its dry state, the membrane possesses little porosity and the counter-ions are strongly bound by the electrostatic forces in contact ion pairs. As the membrane imbibes water, it swells and water molecules penetrate into the pore regions of the membranes.[23]

The thermodynamic treatment of sorption phenomena is straightforward.[23,24] At equilibrium, the chemical potential of the solvent inside of the membrane μ_{iM} should be the same as that of the solvent outside of the membrane μ_{iL}

$$\mu_{iL} = \mu_{iM} \qquad [1]$$

In the absence of interactions or external forces

$$\mu_i = \mu_i^0\left(T, P^0\right) + \int_{P^0}^{P} \overline{V}_i dP + \mathrm{RTln}a_i \qquad [2]$$

where P^0 is reference pressure and $\overline{V}_i$ is the partial molar volume of solvent.

Eq. 1 and 2 provide

$$\mu_i^0\left(T, P^0\right) + \int_{P^0}^{P_M} \overline{V}_{iM} dP + \mathrm{RTln}a_{iM} = \mu_i^0\left(T, P^0\right) + \int_{P^0}^{P_L} \overline{V}_{iL} dP + \mathrm{RTln}a_{iL} \qquad [3]$$

where $\overline{V}_{iM}$ and $\overline{V}_{iL}$ represent the partial molar volume of solvent in the membrane and external liquid phases, respectively. Assuming the partial molar volume of the internal solvent is the same as the bulk solvent

$$\int_{P_L}^{P_M} \overline{V}_{iM} dP = -\mathrm{RTln}\frac{a_{iM}}{a_{iL}} \qquad [4]$$

Further, assuming $\overline{V}_i$ is independent of pressure

$$\overline{V}_i \ \Pi = -\mathrm{RTln}\frac{a_{iM}}{a_{iL}} \qquad [5]$$

where $\Pi = P_M - P_L$ is the swelling pressure of the membrane. For the sorption of pure solvent, a_{iL} = 1.0, Eq. 5 becomes

$$\overline{V}_i \ \Pi = -\mathrm{RTln}a_{iM} \qquad [6]$$

The activity difference of solvent inside (a_{iM}) and outside (a_{iL} = 1.0) of the membrane gives rise to a membrane internal pressure leading a deformation of polymer chain network. It should be noted here that the partial molar volume of the sorbed liquid may, in reality, not be the same as for external solvent, nor may it be uniform through the membrane because of local interaction effects. The sorbed liquid molecules interact with the membrane: *e.g.,* some of the solvent molecules close to the ion may be trapped and oriented in the electrostatic field, and others, far away from the ion, are not influenced by electrostatic field and keep their normal structure of bulk solvent molecules. The deformation of polymer chain network and swelling will depend upon the dissociation constant of the ionic group in the imbibed solvent, the number density of the ionic groups, the nature of counterions, etc.[23] Provided below is a literature review on the sorption related to ion-exchange equilibria and swelling of polymer electrolyte membranes.

2-2-1. Models

i). Gregor's Model[25-27]

In 1948, Gregor[25] initiated a general thermodynamic theory of ion-exchange equilibria in terms of a structural mechanism, which can apply to the ion-exchange membranes as well as non-aqueous systems. In his later papers,[26,27] he developed a mechanical model that can explain electrolyte sorption, swelling, and ion-exchange equilibria. Figure 2-9 represents the model treating the ion-exchange membrane as a cylinder of variable volume,

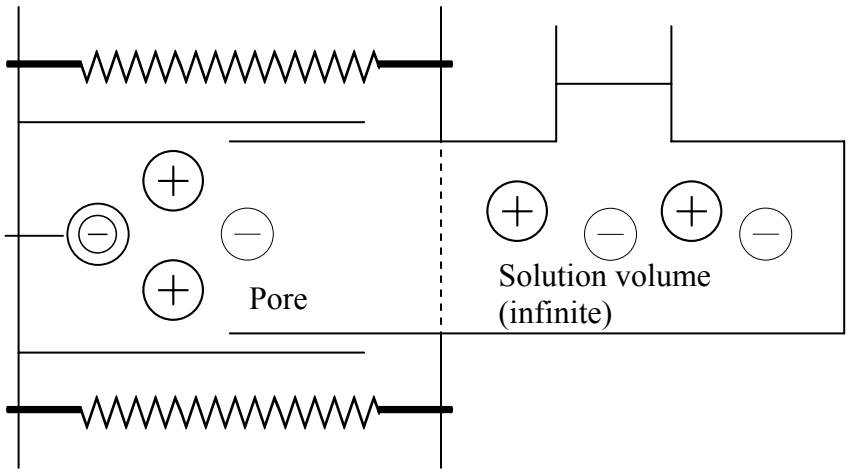

Figure 2-9. Gregor's mechanical model of ion exchange membrane.

held under pressure by springs under tension. The inner solution volume V_i is the total external volume V_e of the membrane minus the volume of incompressible polymer network including the hydrated ionogenic groups appended to the inner wall. The inner solution phase is in direct contact with the external solution, which is infinite in volume and under atmospheric pressure. At equilibrium, the polymer matrix stretches due to an internal osmotic pressure Π, which results from the effort of the external solution to dilute the polymer network. The inner solution volume V_i would vary with the pressure Π, and a simple linear relationship was postulated

$$V_i = m\Pi + b' \qquad [7]$$

or

$$V_e = m\Pi + b \qquad [8]$$

where the values of *m*, akin to an elastic modulus, and *b*, the volume of the unstrained polymer, would depend on the specific system considered. Eq. 8 has been proved experimentally as shown in Figure 2-10.[28] Thus, as more water is imbibed, it meets increased resistance from the stretched polymer chains resulting in higher internal osmotic pressure. The water within the membrane is divided into free water and water bound tightly in the hydration shells around the ions. From Eq. 6, the pressure can be written as

$$\Pi = -\frac{RT}{V_w}\ln\left(\frac{q_w}{q_w + 1}\right) \qquad [9]$$

where q_w is the number of moles of free water per equivalent of polymer. For a monovalent counterion, the total volume V_e can be written as

$$V_e = q_w\overline{V}_w + \overline{V}_c + \overline{V}_R \qquad [10]$$

where $\overline{V}_w$ is the partial molar volume of water, V_c is the solvated counterion molar volume and V_R is the equivalent volume of polymer. From the empirical constants *m*, *b* and V_R, which are invariant for all ionic salts, the degree of swelling and water uptake can

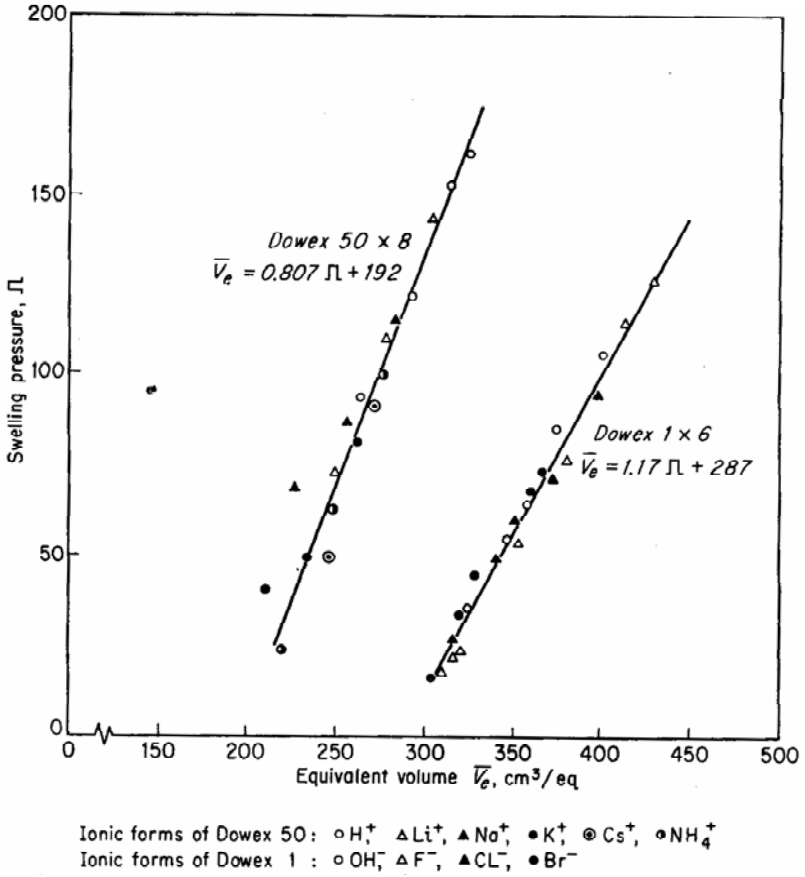

Figure 2-10. Equivalent volume of ion exchanger and swelling pressure (ref. 22).

be predicted from Eqs. 8, 9 and 10.

ii). Mauritz et al.'s Model

In 1985, Mauritz et al.[29] proposed a sorption model accounting for the equilibrium hydration states of water molecules in Nafion®. It is based on the assumptions that all the sorption water molecules are confined in the spherical ionic clusters and that all clusters are equivalent chemically and equal in size. Figure 2-11 shows a spherical ionic cluster illustrating the dry radius (r_0), equivalent swollen radius (r), and polymer matrix resistive pressure for a membrane in contact with water. The driving force for cluster expansion, which results in swelling of the membrane, is the tendency for external water to dilute the ion-containing polymer matrix prior to equilibrium. The internal osmotic pressure is resisted by a pressure due to the restoring force of the expanding polymer matrix. The basic thermodynamic formulation is used as before and the swelling pressure is taken as a pressure needed for a spherical hole to stretches its radius from the initial radius r_0 to r in an infinite block of elastic material

$$\Pi = \frac{E}{6}\left(5 - 4\delta^{-1} - \delta^{-4}\right) \qquad [11]$$

where $\delta = r/r_0$, the extension ratio for cluster, and E is Young's modulus of the material. The sorption equilibrium in Li^+ (and Na^+, K^+) exchanged Nafion® is based on the two-state model of equilibrium between unbounded counterions and counterions in an outer sphere complex. Figure 2-12 shows the equilibrium between i) a totally dissociated and fully hydrated cationic (+) species and a fixed and totally hydrated anionic (-) species, and ii) a (+) (-) ion pair that is an outer sphere complex formed at the expense of ejecting water molecules from the hydration shells in between the free ions. Then, the activity of water inside of membrane is written as

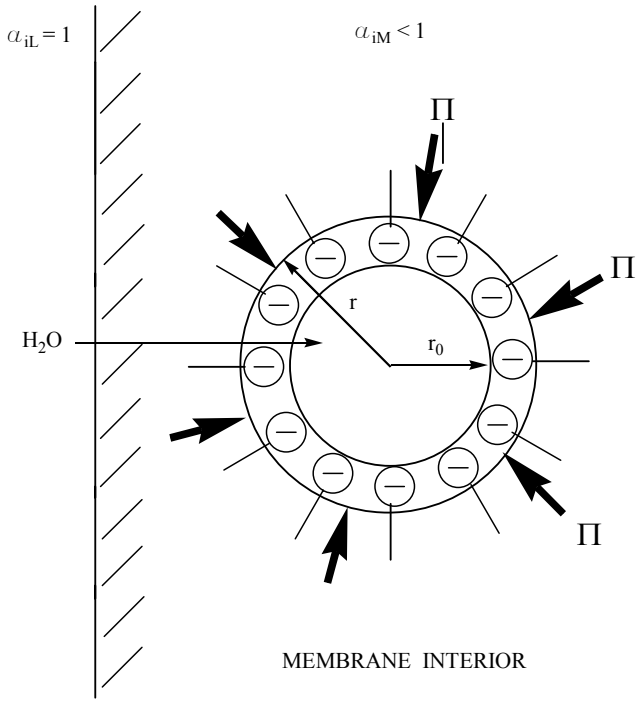

2-11. Mauritz's model of single spherical ionic cluster illustrating the dry radius (r_0), equilibrium swollen radius (r), and polymer matrix resistive pressure (Π) for a membrane in contact with pure water.

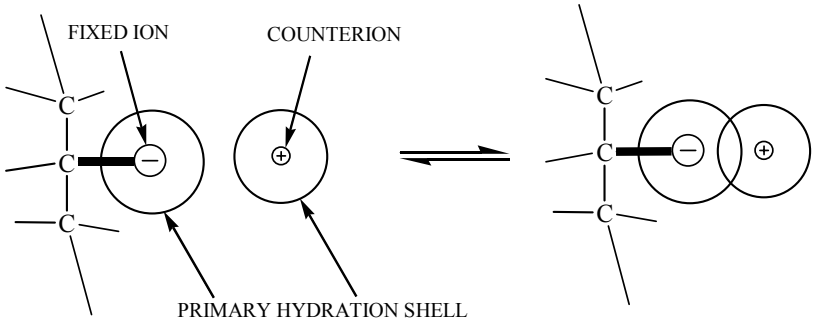

Figure 2-12. Two state model of hydration-mediated equilibrium between unbound counterions and counterions bound in an outer sphere complex.

$$a_w = \frac{n - n_+ - n_-}{n - n_+ - n_- + 1} \quad [12]$$

where n, n_+ and n_- represent the total number of water molecules per ion exchange site, the number of water molecules in the hydration shell around counterion, and around fixed anion, respectively. The extension ratio δ is the ocube root of the volume ratio of the extension volume to initial volume, and the initial volume for Eq. 11 is taken as the volume of water molecules in the hydration shell. For Na^+ exchanged Nafion® (EW=1200), the number of water molecules in hydration shell is taken to be 7, i.e., 4 for H_2O/Na^+ and 3 for H_2O/SO_3^-. The model predicts reasonable value of n, i.e., n_{pred} = 12.2, while the experimental n_{exp} was found to be 18 for liquid water sorption at 25^0C.

iii). Recent Models

Recently, many empirical models such as polynomial,[30] GAB,[31] Zimm and Lundberg,[31] and multilayer BET[32] models have been proposed to describe the amount of water uptake in perfluorinted membranes. The phase equilibrium for water-methanol mixtures in perfluorosulfonic acid membranes has been reported using Gibbs free energy with Margules[33] and Wohl[34] expansion of nonideality

$$G = \sum_i n_i \mu_i^0 + RT \sum_i n_i \ln z_i + \frac{1}{2} \sum_i \sum_j A_{ij} n_i q_i z_j + \frac{1}{3} \sum_i \sum_j \sum_k B_{ijk} n_i q_i z_j z_i \quad [13]$$

with

$$z_i = \frac{x_i q_i}{\sum_l x_l q_l} \quad [14]$$

where G is the Gibbs energy of a phase, either the liquid and the membrane phase, μ_i^0 is the standard-state chemical potential of component i, n_i is the number of moles of component i, and x_i is the mole fraction of component i in the phase of interest. The q_i,

A_{ij}, and B_{ijk} are fitting parameters that depend on the temperature and pressure. The parameters were determined experimentally for water-methanol system at temperature range of 298-333 K.

Flory-Huggins model has also been applied for the sorption of water in Nafion®

$$a_w = (1-\phi_p)\exp[(1-1/r)\phi_p + \chi\phi_p^2] \quad [15]$$

where a_w is the activity of water, ϕ_p is the volume fraction of polymer, r is the ratio of partial molar volume of polymer membrane $\overline{V}_M$ and solvent $\overline{V}_i$, *or* $r = \overline{V}_M / \overline{V}_i$, and χ is the polymer-solvent interaction parameter. The volume fraction of polymer was taken as[31] $\phi_p = r/(r+\lambda)$ where r is the without considering the chemical interaction of some of water molecules with the polymer matrix, or $\phi_p = (r+\lambda_C)/(r+\lambda)$,[35] taking the strong chemical bonding between some of water molecule and polymer matrix into consideration. The interaction parameter χ was adjusted as a function of activity of water vapor to fit the experimental sorption data of water in vapor phase. The effect of sorption pressure was not included in the chemical potential expressions.

2-2-2. Schroeder's Paradox

One of the more interesting phenomena observed in sorption of proton-exchange membranes is that the amount of sorbed from liquid versus its saturated vapor are different, which may be expected to be the same. The difference in sorption amount between liquid and its saturated vapor, the so-called "Schroeder's paradox", remains a somewhat mysterious phenomenon in polymer science that hasn't yet been satisfactorily explained. In 1903,[36] von Schroeder in Ostwald's laboratory reported very interesting phenomenon that a piece of gelation apparently did not reach the same equilibrium point in the presence of saturated vapor that it did when immersed in liquid water. Some gelatin was liquefied

and then allowed to solidify in the form of a plate.[36,37] The solidified mass, composed of 0.679 g gelatin and 0.122 g water, was immersed in liquid water and the sorption was monitored as a function of time, as shown in Table 2-2. The amount of water absorbed increased with time and the experiment was stopped after 48 hours.

Another gelatin plate, composed of 0.433 g gelatin and 4.659 g of water, i.e., containing a large amount of water was placed in a space saturated with water vapor at the same temperature as the preceding experiment. Surprisingly, the gelatin plate lost a large portion of the absorbed water. Table 2-3 shows the decrease of the water content in the gelatin plate with time. After fourteen days in saturated water vapor condition, the gelatin went down to a water concentration which fairly dry gelatin would have had after five minutes in the liquid at the same temperature. When gelatin plate was placed vertically with the lower part in water and the upper part in saturated vapor, the lower part swelled much more than the upper part and the dividing line was quite sharp. In other words, when the gelatin, which is in equilibrium with liquid water, is taken from the liquid and placed in a closed space containing the saturated water vapor, it loses a part of the absorbed liquid. As a consequence of this, a cyclic process may be devised if the gelatin gives up liquid in vapor form and takes up liquid again from the solvent as shown in Figure 2-13.[38] This is an apparent contradiction of the second law of thermodynamics and has, hence, been called a paradox.[39] There have been a number of different views as to whether the phenomenon really exists, or whether the phenomenon constitutes a violation of the second law of thermodynamics. The phenomenon has been variously attributed to the failure of achieving the same temperature in the saturated vapor as in the liquid phase,[37,40,41] the low permeation rate of vapor phase adsorption,[42,43] the existence of the meta-stable state only that is sensitive to slight changes in experimental conditions,[38] the structure and rigidity effects of solid substances,[44] the insufficient time of vapor adsorption[40,44] and the poor wetting of the condensates on solid substances.[45] However, these disparate interpretations

Table 2-2. The uptake of water by gelatin in liquid water.

Time of immersion	Water content of gelatin	
	Grams	Percent absorbed
0 min	0.122	17.0
5 min	2.282	336.1
10 min	2.934	432.1
20 min	3.559	540.3
30 min	4.072	599.7
40 min	4.300	633.3
50 min	4.415	650.2
60 min	4.506	663.6
2 hours	6.911	1018.0
48 hours	7.734	1139.0

Table 2-3. The release of water in gelatin by placing it in a space saturated with water vapor.

Time in vapor phase	Water content of gelatin	
	Grams	Percent absorbed
0 day	4.659	1076
1 day	4.400	1016
2 days	4.322	998
3 days	4.276	988
4 days	4.241	979
5 days	3.730	861
7 days	3.346	759
9 days	2.687	621
11 days	2.088	482
14 days	1.484	343

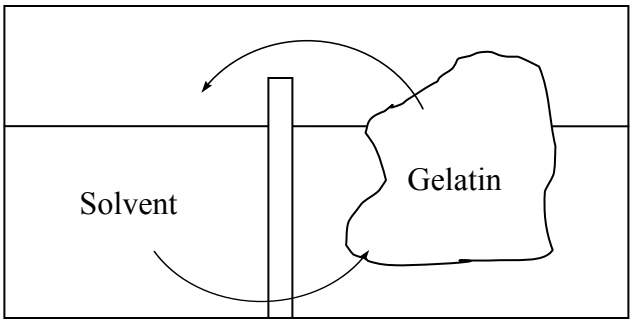

Figure 2-13. A schematic representation of Schroeder's Paradox.

do not provide a general explanation of the phenomenon. One[44] of the interesting explanations based on independent experimental system is that the 'Schroeder's Paradox' only occur in polymers with developed pore structures, which neither swell nor change their structure upon absorption. Liquid sorption is considered to take place by diffusion through large pores, while the vapor sorption is much more complex. It needs several steps of sorption into the wall of pores, formation of poly-molecular layers, meniscus formation and then condensation of vapors. This condensation mostly proceeds in small pores rather than large pores because of the smaller vapor pressure in the small pores (Kelvin effect). It also favors the short distances between walls in small pores. Therefore, the phenomenon is explained as being caused by the difficulty in filling large pores in polymer from vapor adsorption. Clearly, the permeation rate depends on the nature of solid substance such as structure and interactions with solvent. Since the sorption from vapor phase needs several steps including condensation, the permeation rate is much faster when the solid is in direct contact with liquid than in a saturated vapor environment. Thus, it may simply be a matter of different permeation rates, not two different equilibrium states.[43]

The Schroeder's paradox is observed in proton-exchange membranes as well, *i.e.*, in perfluorosulfonic acid (Nafion®), and the phenomenon is of great current interest in the fuel cell area.[45-48] There is, thus, a discrepancy in the amount of water absorbed in Nafion® from pure liquid versus from saturated water vapor. The number of water molecules absorbed per acid site in Nafion® is 22 in the liquid phase sorption, whereas 14 in the vapor phase sorption.[45] One possible explanation advanced is that the hydrophobic nature of the polymer makes water uptake difficult when it contacts with vapor. Since the conductivity of proton in the membrane depends strongly on the amount of water in Nafion®, the sorption characteristics of water is important in determining fuel cell performance. Recently, Freger et al.[49] reported a difference in sorption amounts when

sulfonated polyethylene polymer is contacted with different phases. Although a definite explanation for the reason is still not available, they suggested that the effect was probably because of the changes in interfacial energies between the solvent and matrix phase as previously proposed.[45] More recently, McLean et al.[50] also described it as a pervasive and unexplained phenomenon.

It is necessary to understand this intriguing phenomenon in proton-exchange membranes for designing high proton-conducting membranes and for optimizing the operation conditions for fuel cell. This is addressed in this thesis.

2-3. Transport of Protons

In addition to sorption behavior, it is essential to understand the mechanism of proton transfer in solution and in proton-exchange membrane in order to develop better or less expensive fuel cell membranes and membrane-electrode assemblies (MEAs). In fact, the proton, as much as the electron, is ubiquitous and central to the electrochemistry of solutions:[51] it is the basis of the concepts of pH, acids and bases. The proton, which has no electrons and therefore no electron shell, interacts strongly with neighboring molecules, ions or atoms without steric restrictions. The proton is not likely to exist as a free proton in solution because of the attraction to the surrounding ions or molecules.

2-3-1. Proton Transport in Aqueous Solutions

In an aqueous solution of acids, the proton is associated with water molecules and regarded classically as existing in the form of H_3O^+, or hydronium ion. One of the interesting properties in protons is that the mobility of protons is abnormally high as compared with other ions. For example, the mobility of sodium ion, which is approximately the same size of hydronium ion, is 5.19 x 10^{-4} $cm^2s^{-1}V^{-1}$, whereas that of hydronium ion is 36.23 x 10^{-4} $cm^2s^{-1}V^{-1}$ in water solution at 298 K.[24,51] In other words, the

proton moves seven times faster than the sodium ion in water under the same conditions. The abnormal mobility of proton suggests that the proton should transfer by a mechanism fundamentally different from that used by other ions.[52-55]

i). Grotthuss Mechanism[56,57]

In 1806, a time when the existence of the proton was not known, the chemical formula of water was not settled, the notion of molecules was new, and little was known about stationary electricity, Grotthuss ingenuously introduced "chain mechanism" for the transfer of protons in water. Thus, the protons in aqueous solution move through water largely by hopping along the hydrogen bond network rather than "*en masse*" movement of individual H_3O^+ ions through water as normally envisioned by the ordinary diffusive random walk process. This process is called "structural diffusion" or "Grotthuss mechanism". Figure 2-14 shows this proton transfer mechanism schematically. An analogy is that in a row of small balls in contact, the collision of ball at one end of the row with a new ball caused a ball to the far end to detach itself and go off alone.[52] This movement may explain the rapid transport of protons without a need for motion of H_3O^+ through the solution.

ii). Huckel's Mechanism[58]

In 1928, Huckel made the first attempt in terms of more modern views to the proton transfer problem based on the Grotthuss' mechanism. He proposed that the proton jumps from an H_3O^+ to another water molecule followed by a rotation of the resulting new H_3O^+ ion. Figure 2-15 schematically shows this mechanism. This forms the basis of "structural diffusion" theories following thereafter.

iii). Bernal et al.'s Mechanism[59]

In 1933, Bernal et al. proposed a combined mechanism that the proton is transferred by

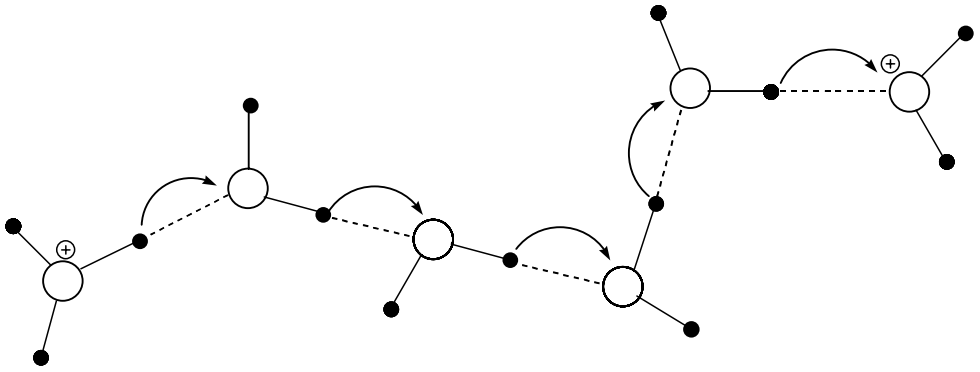

Figure 2-14. The Grotthuss mechanism of proton transfer in aqueous solution.

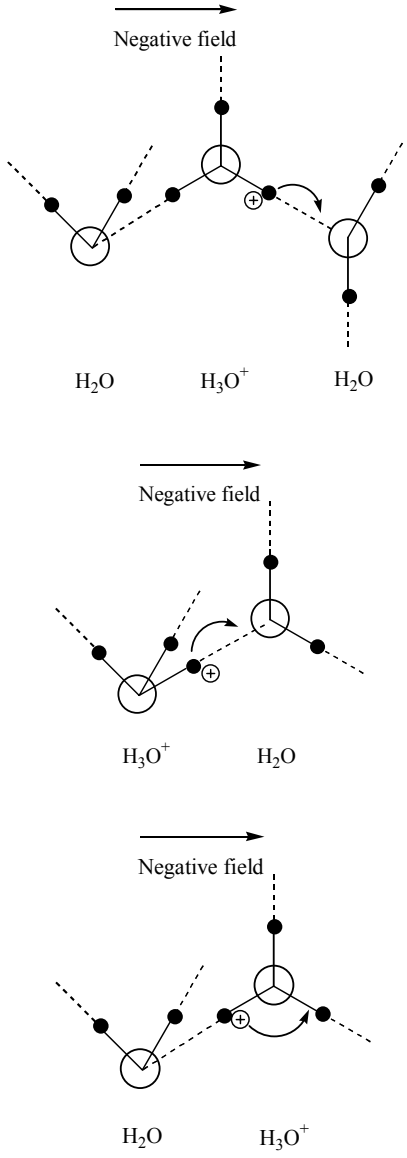

Figure 2-15. Schematic representation of successive steps in an H_3O^+ rotation (Huckel's mechanism).

a tunneling process coupled with water molecule rotation step. Figure 2-16 shows the mechanism. In the tunneling process, the proton can jump from an H_3O^+ ion to a H_2O molecule when the configuration of these molecules is favorable to the transfer (Figure II-16 (a), (b), and (c)). In this favorable orientation, the proton transfers to the adjacent water molecule. But, when it is not in a favorable configuration, the proton cannot jump from H_3O^+ to H_2O and the acceptor H_2O molecule needs to be rotated to the favorable configuration to accept the proton from H_3O^+ (Figure II-3-3, (d) and (e)). Figure 2-17 shows the schematic diagram of the favorable and unfavorable configurations between H_3O^+ and H_2O molecules. The proton transfer can be completed by the tunneling process after the water orientation step. The slower process of the two will determine the rate of proton transfer.

iv). Conway, Bockris and Linton's Mechanism[51,60]

In 1956, Conway, Bockris and Linton gave a detailed calculation of the rates of proton tunneling and the rotation of H_2O molecule for the proton transfer. Figure 2-18 shows the mechanism as described below: I. The proton d is transferred to neighboring water molecule. II. Proton X of H_3O^+ ion approaches H_2O molecule that is not in favorable configuration for the transfer. III. H_2O molecule reorients to a favorable configuration for the transfer of proton X. IV. The proton X jumps to the H_2O molecule, which now becomes H_3O^+. V. The central H_2O molecule reorients for the transfer of proton b. VI. The proton b jumps to the central H_2O molecule and makes it H_3O^+ again. The proton tunnels from H_3O^+ ion to H_2O molecule but the tunneling rate is rapid. This the process is limited by the rate at which the acceptor H_2O molecules reorient so that their free orbitals face the tunneling proton. According to their theory, the time taken in the tunneling process is about 10^{-14} second while the time H_3O^+ ion has to wait to receive a favorably

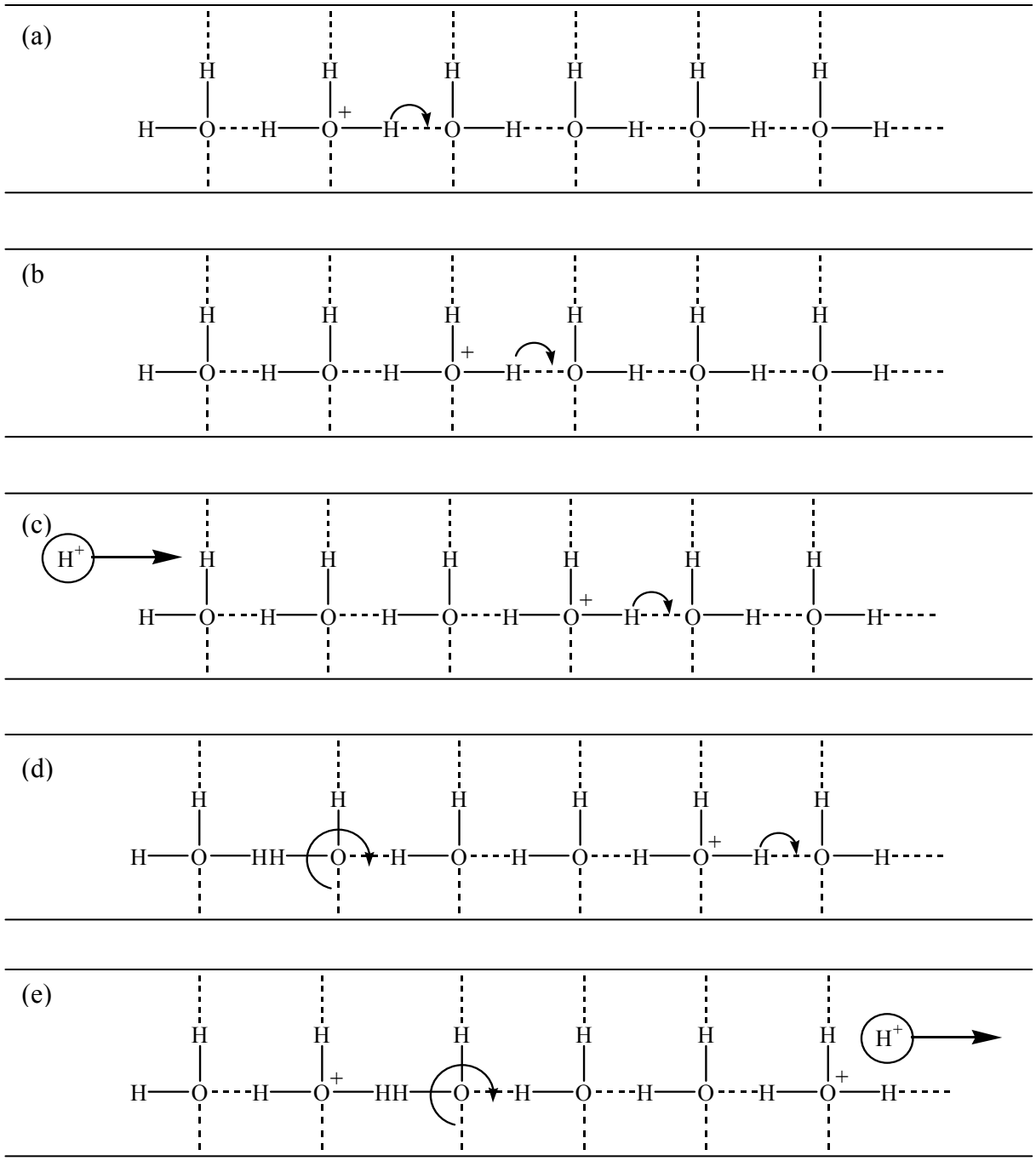

Figure 2-16. Schematic representation of tunneling and water rotation steps (Bernal and Fowler)

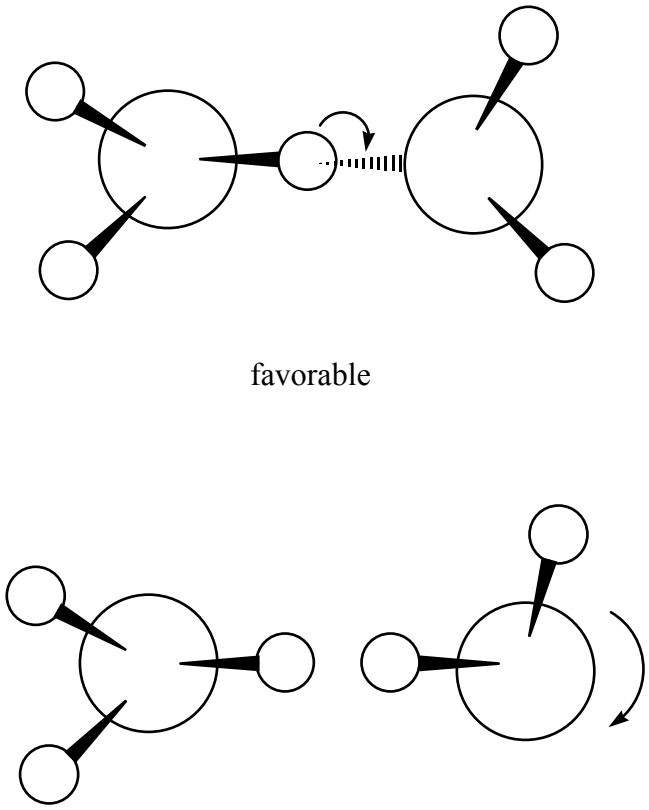

Figure 2-17. Schematic representation of the favorable and unfavorable configurations between H_3O^+ ion and proton accepting H_2O molecule.

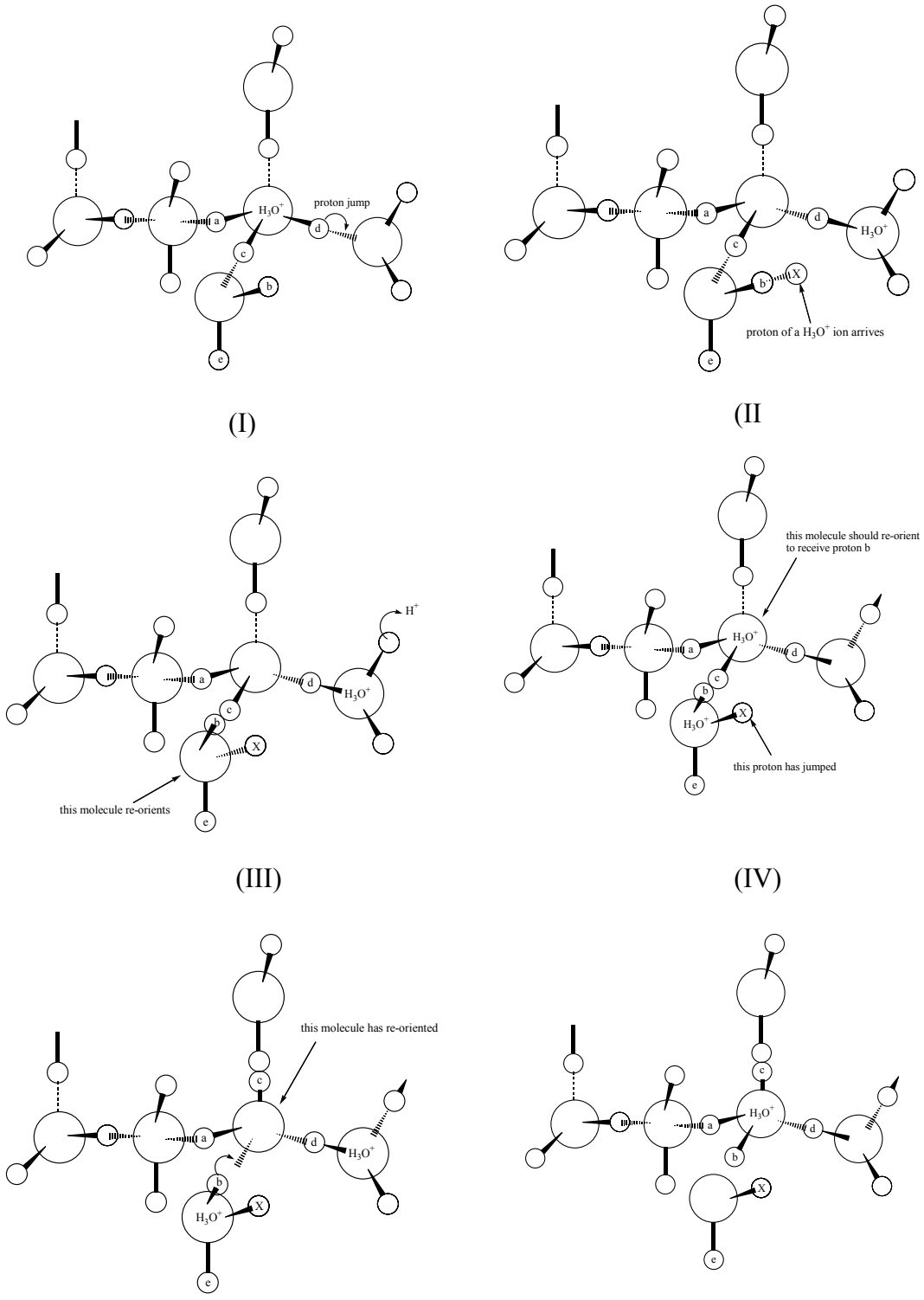

Figure 2-18. Schematic diagram of the proton transfer with tunneling and field induced reorientation.

oriented H_2O molecule is about $2.4x10^{-13}$. Therefore, the proton exists as H_3O^+ for most of its life and the rate determining orientation step of H_2O molecules determines the whole proton transfer process. The analogy has been made to a swing bridge that has to be in a position to receive the proton tunneling through the barrier.

v). Recent Molecular Dynamic Simulations

The chemical state of protons in aqueous solution has been studied and three states are usually discussed in the literature: i) H_3O^+, ii) $H_5O_2^+$ complex[61] with a proton between two water molecules, and iii) $H_9O_4^+$ complex[62] in which an H_3O^+ core is strongly hydrogen-bonded to three water molecules. One may imagine other intermediate structures among the three states. One[63] of the high-level MD simulations shows that the excess proton in water solution can be visualized as a 'fluxional complex' where $H_5O_2^+$, called the "Zundel" ion, and $H_9O_4^+$, called "Eigen" ion, are only important as limiting structures. Figure 2-19 shows the quantum mechanical probability distribution for three hydrogen bonds of H_3O^+ complex in water in terms of probability function P (R_{oo}, δ). The coordinate δ is the difference in distance between the proton and each of two oxygens, i.e., proportional to asymmetric stretch, and R_{oo} is the oxygen-oxygen separation. Figure 2-19a considers the three hydrogen bonds of H_3O^+ with the surrounding three oxygens of bulk water. The high probability of R_{oo}=2.6 Å corresponds to the $H_9O_4^+$ structure due to large asymmetric stretch. The coordinate δ = 0 means an equal sharing of proton and can be represented by $H_5O_2^+$ where R_{oo}=2.5 Å. For neutral bulk water molecule R_{oo} = 2.8 A. A better insight is given by simulating a hydrogen bond through which the proton transfer is most like to occur. Figure 2-19b shows the distribution of hydrogen bond that has smallest δ. It shows the broad and unstructured character indicating many structures between the forms of $H_5O_2^+$ and $H_9O_4^+$. For small value of $|\delta| < 0.1$, the complex shares the proton equally, in

accordance with Zundel's view, and for large values of $|\delta| > 0.3$, the complex possesses the features associated with Eigen's $H_9O_4^+$ complex picture. From the flatness of the

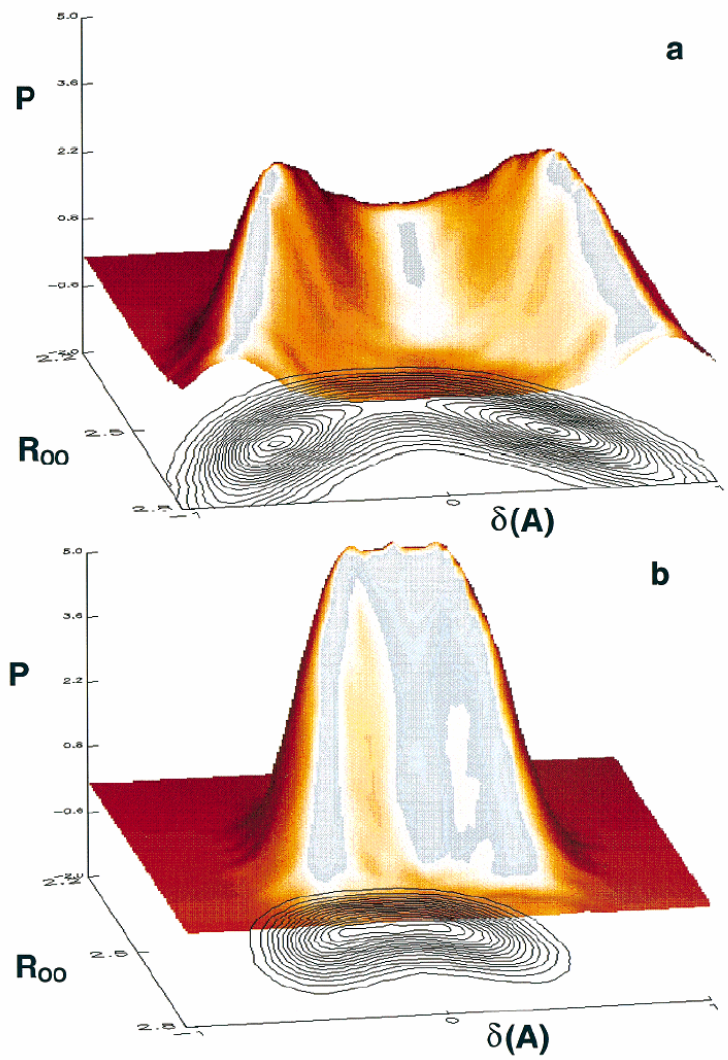

Figure 2-19. The quantum-mechanical probability distribution function P(*Roo*, δ) for (a) three hydrogen bonds of the H_3O^+ complex in water (b) 'most active' of three hydrogen bonds characterized by the smallest value of δ.

probability function, it can be viewed as continuum of other unclassified structures between the two limiting forms.

Recent molecular dynamic simulations have been utilized to understand the proton transport mechanism at the molecular level.[63-70] Figure 2-20 shows the schematics of proton transfer (I. $H_9O_4^+$ structure possessing H_3O^+ core donates three hydrogen bonds to neighboring water molecules that have four hydrogen bonds.[63,70] The formation of hydrogen bonds weakens the surrounding hydrogen bond of the H_2O molecule. One of the H_2O molecule hydrogen bonded to the H_3O^+ core undergoes hydrogen bond breaking with one of its neighbors (except the H_3O^+). II. The acceptor H_2O molecule is left with three hydrogen bonds and it is in 'under-coordinated' state. The cleavage of a hydrogen bond strengthens the neighboring bonds. III. The H_2O molecule takes one of the protons from H_3O^+ to which it is currently hydrogen bonded and become H_3O^+ ion). Thus, the proton diffuses through the $H_9O_4^+$ and $H_5O_2^+$ as limiting structures. There exist many unclassifiable situations in between and the proton defect can be described as being of a 'fluxional complex'. This analysis, based on the first-principles quantum simulation, brings out features of both Eigen's and Zundel's view but shows the complex as a continuum of numerous structures. It is consistent with known experimental results.

2-3-2. Transport of Protons in PEMs

The nature of water within the nanometer dimensions of hydrated PEM has been reported to be different from that of water in the bulk.[71-74] Some of the water molecules in Nafion® are tightly bound to the SO_3^- and thus less hydrogen bonded near the pore surface than in bulk water because of the less water-water molecular contact than in bulk water and the hydrophobic nature of the PTFE backbone. The water molecules in the central region of water-filled pore are expected to behave more like bulk water. The transport properties of PEM are determined by the water content within the hydrophilic domain and the

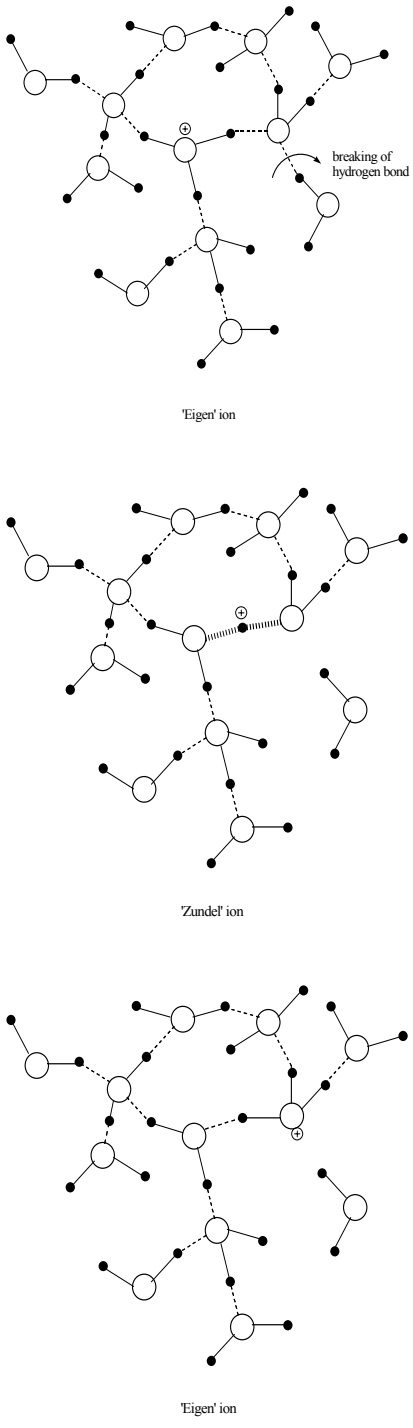

Figure 2-20. Schematics of proton transfer by *ab-initio* MD simulation.

interaction with the acidic functional groups, which becomes more significant as the PEM is less hydrated. Recent molecular mechanics and molecular dynamic simulation studies are also contributing to an understanding of solvation of solvent molecules inside of proton exchange membranes. The molecular fragments of Nafion®, for example trifluorosulfonic acid (CF_3SO_3H), difluoromethane ether (CF_3OCF_3), para-toluene sulfonic acid ($CH_3C_6H_4SO_3H$), perfluorosulfate oligomers and side chain (CF_3-$OCF_2CF(CF_3)OCF_2CF_2SO_3H$), have been employed to simulate the electo-chemical states of solvent molecules in the membrane.[75] *Ab initio* electronic structure calculations have been used to obtain the conformations for the model compounds, and the dissociation and hydration of the acid depend on the structure and the strength of SO_3^-.

Figure 2-21 shows the changes in conformations by adding water molecules to the CF_3SO_3H. The $CF_3SO_3H + H_2O$ conformation shows that the water molecule forms a somewhat shorter hydrogen bond than typical (~2.8 Å) with the acidic proton. Table 2-4 shows the distances SO_3-H, and SO_2O-H-OH_2 for the different number of water molecules added into the system. The SO_3-H distance has increased by 0.086 Å after second water molecule has been added compared with CF_3SO_3H. However, the dissociation of proton from SO_3^- was not observed even after a second water molecule was added. After a third water molecule was added, however, a spontaneous dissociation of acidic proton is observed. When the fourth and fifth water molecules are added, the hydronium ion formed in the third water molecule was still observed. The hydronium ion forms a contact ion pair with SO_3^- anion. Finally, when the sixth water molecule is added, a complete separation of proton from the SO_3^- were observed. In the study of Nafion® oligomer, similar results are reported in that the SO_3^- group forms five hydrogen bonds to the solvent water molecules and they are in the first solvation shell.[74] At low water content, the water-water contact is significantly reduced. In this situation, the hydrogen bonds are expected to be tightened, which decreases the dielectric constant and reduces the bond breaking/forming

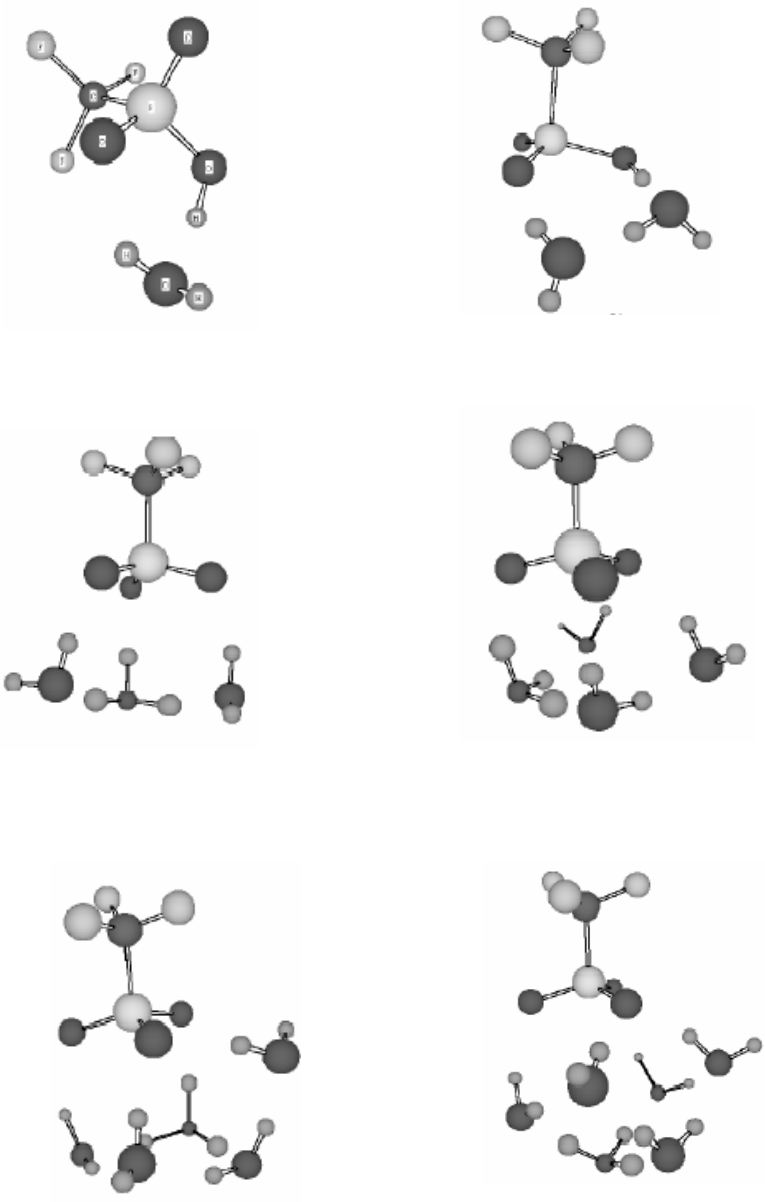

Figure 2-21. Optimized conformation of $CF_3SO_3H + nH_2O$.

Table 2-4. Structural distances of SO_2O-H and SO_2OH-OH_2 of CF_3SO_3H + nH_2Os.

Number of water molecules	d(-SO_2O-H$\cdots$$OH_2$), Å	d(-$SO_2O\cdots$H-OH_2) Å
0	0.973	-
1	1.020	2.595
2	1.059	2.496
3	1.562	2.556
4	1.721	2.658
5	1.739	2.693
6	3.679	4.243

process for proton transfer. The interaction of H_2O with acidic functional group polarizes the protons in the hydrogen bonds and is expected to increase the energy of proton containing complex, which leads to an increased activation enthalpy and therefore to a reduced rate of proton transfer. The distribution of protonic charges and the corresponding electrostatic potential in the vicinity of the functional groups would be influenced by chemical interaction of the proton with the acid anion, and the local dielectric constant of the solvating water which is assumed 6 in the vicinity of the acid groups, and the spatial separation of immobile acid anions, which is usually 6-12 Å.

Although the precise picture of protonated water in Nafion® is not known, all the water molecules within the Nafion® are assumed not to be in the same state. The transfer of proton near pore surface, i.e., within 3-4 Å, which is roughly the size of water molecule, would take place through the tightly bound water molecules along the array of SO_3^- groups. On the other hand, the transfer of proton in the center of the pore would be similar to the transfer in bulk water. Figure 2-22 shows schematically the two kinds of water molecules inside of Nafion®.[76] The transfer of water through surface water can be characterized by higher activation energy and lower proton transfer rate. The surface density of SO_3^- group and the pore structure/size would determine the contributions of proton transfer from the surface and bulk water. As the membrane becomes saturated, the size of pore increases and this will increase the bulk-like portion of water, leading to more bulk-like transfer that gives higher rate of proton transfer in the middle of the pores. Thus, the overall rate of proton transfer increases with pore radius until it reaches saturation, where the average diameter of pores is 4-6 nm.

Paddison et al. developed a statistical mechanical model[77,79] where the transport of protons close to the pore wall (~1.2 nm of the pore wall) was relatively slow and thus was

identified as vehicular transport mechanism, while transport of protons was fast in the central regions of the pore and thus identified as Grotthuss mechanism. Eikering[79]

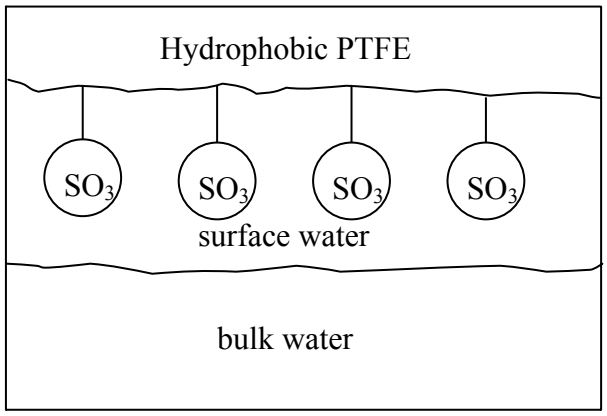

Figure 2-22. The structure of proton exchange membrane in its hydrated state (two types of waters are distinguished).

reported a phenomenological model where the total proton conductivity is obtained from two contributions: one contribution dominates in the middle of the pore and proceeds in a manner similar to that of bulk, and the other contribution dominates near the pore surface along the array of SO_3^- groups. The surface conductivity is considerably smaller and has a higher activation free energy than bulk conductivity. A higher density of SO_3^- group gives rise to high surface conductivity and large pore radii increases the possibility of residing protons in the bulk, where they have higher conductivity. Mafe et al.[80] developed a two-region model to describe proton conductivity of porous fixed charged membranes. The activation energies and diffusion coefficients for the surface conductivities were estimated using a simple microscopic model that considers the counterion displacement from a fixed charged group as the rate limiting process. The bulk conductivity was taken from experimental data and qualitative trends of the two contributions to the total conductivity were provided for ion-exchange membranes rather than for any specific membrane.

Some recent MD simulations have been reported for the transport of protons in Nafion®.[81-86] The macromolecular nature of PEMs makes virtually impossible to handle an entire molecules in an *ab initio* manner and thus, only the polymeric subunits involved in strong interaction with water have been treated. Although such attempts are still in their infancy, they provide insights into the proton transport mechanisms in PEM.

References

1. W. T. Grubb, *J. Electrochem. Soc.*, **106**, 275 (1959).
2. U. S. Pat. 2,913,511 (1959).
3. W. T. Grubb and L. W. Niedrach, *J. Electrochem. Soc.*, **107**, 131 (1960).
4. E. J. Cairns, D. L. Douglas, and L. W. Niedrach, *AIChE J.*, **7**, 551 (1961).
5. C. H. Wirguin, *J. Membr. Sci.*, **120**, 1 (1996).
6. Fuel Cell Handbook (Sixth Edition), U. S. Department Of Energy, 2002.
7. M. Kondoh, N. Yokoyama, C. Inazumi, S. Maezawa, N. Fujiwara, Y. Nishimura, K. Oguro, and H. Takenaka, *J. New Mater. Electrochem. Syst.*, **3**, 61 (2000).
8. M. Kato, S. Maezawa and K. Sato, *Applied Energy*, **59**, 261 (1998).
9. Product Information (http://www.dupont.com/fuelcells/pdf/nae101.pdf).
10. A. Eisenberg, *Macromolecules*, **3**, 147 (1970).
11. T. D. Gierke, *152nd Meeting of the Electrochemical Society Extended Abstracts*, Atlanta, Ga., Abstract No. 438. 1977.
12. W. Y. Hsu and T. D. Gierke, *Macromolecules*, **15**, 101 (1982).
13. K. A. Mauritz, C. J. Hora, and A. J. Hopfinger, *Polym .Prep. Am. Chem. Soc. Div. Polym. Chem.*, **19**, 324 (1978).
14. H. L. Yeager and A. Steck, *J. Electrochem. Soc.*, **128**, 1880 (1981).
15. M. Eikerling, A. A. Kornyshev, and U. Stimming, *J. Phys. Chem.*, **101** (1997) 10807.
16. G. Gebel and J. Lambard, *Macromolecules*, **30**, 7914 (1997).
17. G. Gebel. *Polymer*, **41**, 5829 (2000).
18. S. M. Young, S. F. Trevino, and N. C. Becktan, *J. Polym. Sci.*, **40**, 387 (2002).
19. H. G. Haubold, Th. Vad, H. Jungbluth, and P. Hiller, *Electrochim. Acta*, **46**, 1559 (2001).
20. K. D. Kreuer, *J. Membr. Sci.*, **185**, 29 (2001).
21. P. Zammaretti, A. Fakler, F. Zaugg, K. Spichiger, and E. Ursula, *Anal. Chem.*, **72**,

3689 (2000).

22. J. James, M. Antognozzi, J. Tamayo, T. J. McMaster, J. M. Newton, and M. J. Miles, *Langmuir*, **17**, 349 (2001).
23. H. Helfferich, *Ion Exchange*, McGraw-Hill, NY (1962).
24. P. W. Atkins, *Physical Chemistry*, 3rd ed, W.H. Freeman and Company, NY (1986).
25. H. P. Gregor, *J. Am. Chem. Soc.*, **70**, 1293 (1948).
26. H. P. Gregor, *J. Am. Chem. Soc.*, **73**, 642 (1951).
27. H. P. Gregor and J. I. Bregman, *J. Colloid Sci.*, **6**, 323 (1951).
28. G. E. Boyd and B. A. Soldano, *Z. Elektrochem.*, **57**, 162 (1953).
29. K. A. Mauritz and C. E. Rogers, *Macromolecules*, **18**, 483 (1985).
30. D. Rivin, C. E. Kendrick, P. W.Goibson, and N. S. Schneider, *Polymer*, **42**, 623 (2001).
31. C. Tsonos, L. Apekis, and P. Pissis, *J. Mat. Sci.*, **35**, 5957 (2000).
32. T. Thampan, S. Malhotra, H. Tang, and R. Datta, *J. Electrochem. Soc.,* **147**, 3242 (2000).
33. C. M. Gates and J. Newman, *AIChE J.*, **46**, 2076 (2000).
34. A. B. Geiger, J. Newman, and J. M. Prausnitz, *AIChE J.*, **47**, 445 (2001).
35. P. Futerko and I-M. Hsing, *J. Electrochem. Soc.,* **146**, 2049 (1999).
36. P. V. Schroeder, *Z. Phys. Chem.*, **45**, 75 (1903).
37. W. D. Bancroft, *J. Phys. Chem. Ithaca*, **16**, 395 (1912).
38. P. Stamberger, *The Colloid Chemistry of Rubber*, p. 40, Oxford University Press, London (1929).
39. J. Reilly and W. N. Rae, *Physico-Chemical Methods* Vol. III, p. 364, D. Van Nostrand Company Inc., NY (1948).
40. L. K. Wolff and E. H. Buchner, *Z. Phys. Chem*., **89**, 271 (1915).
41. J. W. G. Musty, R. E. Pattle, and P. J. A. Smith, *J. Appl. Chem.,* **16**, 221

(1966).

42. H. Freundlich, *Colloid and Capillary Chemistry* 3rd ed., p. 672, Oxford University Press, London (1926).
43. R. C. Benning, R. J. Lee, J. F. Jennings, and E. C. Martin, *Ind. Eng. Chem.,* **53**, 45 (1961).
44. A. A. Tager, M. V. Tsilipotkina, L. V. Adamova, and L. K. Kolmakova, *Vysokomol. Soed*., **16B**, 911 (1974).
45. T. A. Zawodzinski, T. E. Springer, J. Davey, R. Jestel, C. Lopez, J. Valerio, and S. Gottesfeld, *J. Electrochem. Soc.,* **140**, 1981 (1993).
46. T. A. Zawodzinski, C. Derouin, S. Radzinski, R. J. Sherman, V. T. Smith, T. E. Springer, and S. Gottesfeld, *J. Electrochem. Soc.,* **140**, 1041 (1993).
47. A. Z. Weber and J. Newman, *J. Electrochem. Soc.*, **150**, A1008 (2003).
48. A. Z. Weber and J. Newman, *J. Electrochem. Soc.*, **151**, A311 (2004).
49. V. Freger, E. Korin, J. Winiak, and E. Korngold, *J. Membr. Sci.,* **164**, 251 (2000).
50. R. S. Mclean, M. Doyle, and B. B. Sauer, *Macromolecules,* **33**, 6541 (2000).
51. J. O'M. Bockris and A. K. N. Reddy, *Modern Electrochemistry*, Plenum Press, NY (1970).
52. J. O'M. Bockris and A. K. N. Reddy, *Modern Electrochemistry 1 Ionics*, Plenum Press, NY (1998).
53. B. E. Conway, "Proton Solvation and Proton Transfer Processes in Solutions", in *Modern Aspect of Electrochemistry*, Vol. 3, p. 43 (1964).
54. T. Erdey-Gruz and S. Lengyel, "Proton Transfer in Solution in Solutions", in *Modern Aspect of Electrochemistry*, Vol. 12, p. 1 (1978).
55. K. D. Krener, *Chem. Mat.*, **8**, 610 (1996).
56. C. J. D. von Grotthuss, *Ann. Chim.*, **LVIII,** 54 (1806).
57. N. Agmon, *Chem. Phys. Lett.*, **244**, 456 (1995).

58. E. Huckel, *Z. Electrochem.*, **34**, 546 (1928).

59. J. D. Bernal and R. H. Fowler, *J. Chem. Phys.*, **1,** 515 (1933).

60. B. E. Conway, J.O'M. Bockris, and H. Linton, *J. Chem. Phys.*, **24**, 834 (1956).

61. G. Zundal and H. Metzger, *Z. Phys. Chem.*, **58**, 225 (1968).

62. E. Wicke, M. Eigen, and T. Ackermann, *Z. Phys. Chem.*, **1**, 340 (1954).

63. D. Marx, M. E. Tuckerman, J. Hutter, and M. Parrinello, *Nature*, **397**, 601 (1999).

64. M. E. Tuckerman, D. Marx, and M. Parrinello, *Nature*, **417**, 925 (2002).

65. M. E. Tuckerman, *J. Phys. Condens. Matter*, **14**, R1297 (2002).

66. U. W. Schmitt and G. A. Voth, *J. Chem. Phys.*, **111**, 9361 (1999).

67. R. Vuilleumier and D. Borgis, *J. Chem. Phys.*, **111**, 4251 (1999).

68. A. A. Kornshev, A. M. Kuznetsov, E. Spohr, and J. Ulstrup, *J. Phys. Chem.*, **107**, 3351 (2003).

69. S. Walbran and A. A. Kornshev, *J. Chem. Phys.*, **114**, 10039 (2001).

70. K. D. Kreuer, *Solid State Ionics*, **136**, 149 (2000).

71. J. B. Hasted, D. M. Ritson, and C. H. Collie, *J. Chem. Phys.*, **16**, 1 (1948).

72. S. Paddison, D. W. Reagor, and T. A. Zawodzinski, *J. Electroanal. Chem.*, **459**, 91 (1998).

73. K. Lebedev, S. Mafe, A. Alcaraz, and P. Ramirez, *Chem. Phys. Lett.*, **326**, 87 (2000).

74. A. Vishnyakov and A. V. Neimark, *J. Phys. Chem. B*, **104**, 4471 (2000).

75. S. J. Paddison, *J. New Mat. Electrochem. Sys.*, **4**, 197 (2001).

76. S. J. Paddison and R. Paul, *Phys. Chem. Chem. Phys.*, **4**, 1158 (2002).

77. S. J. Paddison, *Annu. Rev. Mater. Res.*, **33**, 289 (2003).

78. M. Eikerling, A. A. Kornyshev, A. M. Kuznetsov, J. Ulstrup, and S. Walbran, *J. Phys. Chem. B*, **105**, 3646 (2001).

79. S. Mafe, J. A. Manzanares, and P. Ramirez, *Phys. Chem. Chem. Phys.*, **5**, 376 (2003).

80. X. D. Din and E. E. Michaelides, *AIChE J.*, **44**, 35 (1998).

81. T. Li, A. Alaschin, and P. B. Balbuena, *Ind. Eng. Chem. Res.*, **40**, 4789 (2001).

82. E. Spohr, P. Commer, and A. A. Kornshev, *J. Phys. Chem. B*, **106**, 10560 (2002).

83. J. Ennari, I. Neelov, and F. Sundholm, *Polymer*, **42**, 8043 (2001).

84. R. Jinnouchi and K. Okazaki, *J. Electrochem. Soc.*, **150**, E66 (2003).

85. P. Commer, A. G. Cherstvy, E. Spohr, and A. A. Kornshev, *Fuel Cells*, **2**, 127 (2002).

86. M. Eikerling, A. A. Kornshev, U. Stimming, *J. Phys. Chem. B.*, **101**, 10807 (1997).

PART II.

Thermodynamics and Transport in Nafion®

Chapter 3. Sorption in Proton-Exchange Membranes:

An Explanation of Schroeder's Paradox

Chapter 4. Membrane Swelling, Sorption, and Ion-Exchange Equilibrium

Chapter 5. Proton Diffusion Mechanisms and Conductivity in Nafion®

Chapter 6. Proton Transport in Nafion®/Sulfated ZrO_2 Nanocomposite Membranes

"Man's mind, once stretched to a new idea, never goes back to its original dimensions."

- Oliver Wendell Holmes -

Chapter 3. Sorption in Proton-Exchange Membranes: An Explanation of Schroeder's Paradox

Abstract

A physicochemical model is proposed to describe sorption in proton-exchange membranes (PEMs), which can predict the complete isotherm as well as provide a plausible explanation for the long unresolved phenomenon termed Schroeder's paradox, namely the difference between the amounts sorbed from a liquid solvent versus from its saturated vapor. The solvent uptake is governed by the swelling pressure caused within the membrane as a result of stretching of the polymer chains upon solvent uptake, Π_M, as well as a surface pressure, Π_σ, due to the curved vapor-liquid interface of pore liquid. Further, the solvent molecules in the membrane are divided into those that are chemically, or strongly, bound to the acid sites, λ_i^C, and others that are free to physically equilibrate between the fluid and the membrane phases, λ_i^F. The model predicts the isotherm over whole range of humidities satisfactorily and also provides a rational explanation for the Schroeder's paradox.

3-1. Introduction

Fuel cells based on the proton-exchange membranes (PEMs) are of great potential as efficient and largely pollution-free power generators for mobile and stationary applications.[1-3] The PEM fuel cell comprises a membrane-electrode-assembly (MEA) involving two carbon cloth (or paper) gas-diffusion layers that allow simultaneous transport of gases and water while collecting current, and two carbon supported Pt or Pt alloy catalyst layers where the electrochemical reactions take place, sandwiching a proton-

exchange membrane that allows protons to transfer from the anode to the cathode. The membranes, typically a perfluorosulfonic acid (PFSA) polymer such as Nafion®, consist of a polytetrafluoroethylene (PTFE) backbone with side-chains terminating in $SO_3^-H^+$ groups. They possess little porosity in the dry state. However, in the presence of water or other polar solvents, the membrane swells and the sulfonic acid groups ionize protonating the sorbed solvent molecules that are responsible for conducting the protons.[4,5] The conductivity of Nafion® is highly dependent upon hydration level[6,7] being essentially an insulator below a threshold and rising through several orders of magnitude to about 0.07 ~ 0.1 Siemens/cm at 80 ºC when fully hydrated.[4-7] The extent of the solvent uptake and membrane swelling is controlled by a balance between the internal osmotic pressure of solvent within the pores and the elastic forces of the polymer matrix which, in turn, depend upon the temperature and membrane pretreatment.[8] The membrane pretreatment involves raising the temperature to around the glass transition temperature of Nafion® (111 ºC) to allow the polymer chains to reorient themselves in the presence of water.[9] The membrane is first cleaned in a boiling 3 % H_2O_2 solution, followed by boiling in 0.5 M H_2SO_4 to ensure full protonation, and finally in deionized water. This results in the so-called E (expanded) form. Other pretreatment procedures that have been described in the literature include drying at 80 ºC that produces the N (normal) form, while drying at 105 ºC produces the S (shrunk) form.[10]

The results of water uptake in Nafion® expressed in terms of λ, the number of water molecules per acid site, upon contact with liquid or its saturated vapor are summarized in Table 3-1. There is an unexplained discrepancy in the water uptake in Nafion® from pure liquid ($\lambda_{i,L}^{sat} \approx 22\sim23$) versus that from its saturated vapor ($\lambda_{i,V}^{sat} \approx 13.5\sim14.0$), even though both possess unit activity.[11-18] In fact, when a liquid water-equilibrated membrane was removed and exposed to a saturated water vapor, λ dropped from 22 to 14, indicating that

Table 3-1. The amount of water sorption in Nafion® by liquid water and its saturated vapor about room temperature.

Number of water molecules per sulfonic acid	
Liquid	Vapor
22 (25°C)[11,12]	13.5 (25°C)[14]
22.6 (25°C)[13]	13.5 (25°C)[18]
23 (25°C)[15]	13.6 (25°C)[16]
22.3 (25°C)[17,*]	14 (30°C)[11,12]

The data reported are for proton exchanged *E* form of Nafion membrane.
All data are for Nafion 117 except *.
* Nafion 120 (ion exchange capacity is 0.83 mequiv/g dry proton exchanged form and thickness is 250 μm).
Temperatures of the experiments are given in parenthesis and references are in superscript.

the two states are thermodynamically stable.[11] The phenomenon, known as Schroeder's paradox,[19] is apparently not uncommon in polymer systems but has not so far been satisfactorily explained, although many different explanations have been advanced.[20-29] For instance, it has been attributed to the failure of achieving the same temperature in the saturated vapor as in the liquid phase,[20-22] the low permeation rate of vapor phase adsorption,[23,24] the existence of the meta-stable state only that is sensitive to slight changes in experimental conditions,[25] the structure and rigidity effects of solid substances,[26] the insufficient time of vapor adsorption[21,26] and the poor wetting of the condensates on solid substances.[11] However, these disparate explanations do not provide a satisfactory and general understanding of the phenomenon.

It is important to understand the solvent uptake by proton exchange membranes, so that the fuel cell design and operation can be optimized, which is the objective of this paper. The sorption of water in Nafion® has been modeled based on a finite-layer BET,[5] modified BET,[30] Flory-Huggins,[30,31] or simply fitted using polynomials in activity.[18,32] A sorption model of water in Nation® is proposed here based on the premise that the sorption isotherm is controlled by the swelling pressure determined by the matrix and surface forces of the polymer membrane and sorbed solvent, which in turn affects its chemical potential, and hence the amount sorbed.

3-2. Model Description

When an ion-exchange membrane, *e.g.,* Nafion®, is in equilibrium with a solvent, *e.g.,* water, some of the sorbed solvent molecules are in a physicochemical state that is different from the bulk solvent molecules depending upon their interaction with the membrane. Thus, the sorbed molecules may be associated with: *i)* the ion-exchange site, *e.g.,* sulfonic acid group; or *ii)* the polymer matrix, *e.g.,* fluorocarbon backbone in Nafion®; or *iii)* the

other solvent molecules. In the model developed here, we simply assume that the sorbed solvent molecules are of two types: *i*) those that are strongly, or chemically, bound to the acid sites in the primary salvation layer, akin to chemisorption; and *ii*) others that are physically equilibrated between the fluid and the membrane phases, akin to physisorption. In other words, we do not explicitly account for the solvent interactions with the polymer backbone in this treatise, which is included in the effective spring constant κ of the polymer matrix. It is further assumed that as the membrane swells due to solvent uptake, the solvent molecules meet increasing resistance from the stretched polymer chains resulting in a swelling pressure on the pore liquid. The pressure, of course, alters the solvent chemical potential within the membrane, and hence the sorption equilibrium. When the sorption occurs from the vapor phase, an additional pressure is exerted on the pore liquid by the curved vapor-liquid interface within the pore. This latter effect is invoked here to explain the Schroeder's paradox.

The model, thus, involves a balance of forces.[33,34] Equilibrium is achieved when the elastic pressure of the polymer matrix counterbalances the increased pressure within the pore liquid in an effort of solvent molecules to equalize the chemical potential of the fluid inside and outside of the pore. Figure 3-1 shows a schematic of the polymer matrix in its dry (unswollen) and stretched (swollen) states. The effective spring constant κ of the polymer matrix, much like its Young's modulus, is assumed to depend upon the temperature (*e.g.,* proximity to the glass-transition temperature, T_g), solvent-polymer interaction, and pretreatment procedures. Above the T_g, of course, the membrane would lose integrity eventually forming a dispersion of the polymer in the solvent, *e.g.,* Nafion® gel.[4] It can, thus, be envisioned that the other key variables that affect swelling are; *i*) the polarity of the solvent, *ii*) the nature, *e.g.,* hydrophobicity, of the polymer backbone, *iii*) the concentration of the acid sites, and *iv*) the strength of the acid sites.[35]

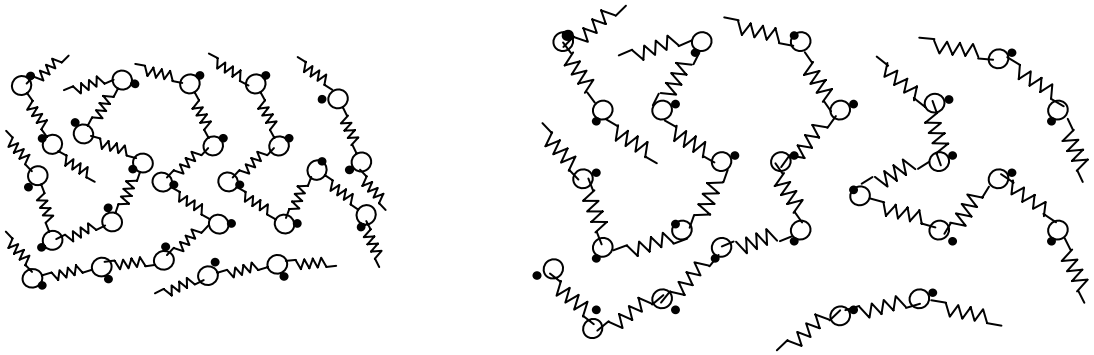

(a) (b)

Figure 3-1. Schematic representation of an ion-exchange membrane in its (a) unswollen and (b) swollen state. The fixed and counter-ions in the membrane are represented by open (○) and filled (●) circles, respectively

3-3. Theoretical Model

The sorbed molecules are, thus, assumed to be of two types: *i*) those that are chemically, or strongly, bound (akin to chemisorption), represented by λ_i^C; and *ii*) those that are 'free' to physically equilibrate (akin to physisorption) between the membrane and the fluid phase, λ_i^F. A Schematic of these two different types of water molecules in Nafion® is shown in Figure 3-2. Thus, the total uptake of solvent by the membrane (number of solvent molecules sorbed/ion exchange site) is written as

$$\lambda_i = \lambda_i^C + \lambda_i^F \qquad [1]$$

The thermodynamic condition for the 'chemical' equilibrium that determines λ_i^C, of course, is

$$\sum_{i=1}^{n} \nu_{\rho i}\mu_i = 0 \quad (\rho = 1, 2, \ldots, q) \qquad [2]$$

where $\nu_{\rho i}$ and μ_i designate the stoichiometric number of species *i* in reaction ρ and the chemical potential of species *i* in solution, respectively. On the other hand, the thermodynamic conditions for describing phase equilibrium between the membrane and external fluid phases are

$$\mu_{i,M} = \mu_{i,F} \ (i = 1, 2, \ldots, n) \qquad [3]$$

which determines λ_i^F.

The general chemical potential for species *i (i = 1,2,. . . , n)* in phase α can be written as a function of temperature, pressure, composition, and other potentials, $\mu_{i,\alpha} = (T, P, a_{i,\alpha}, \Psi_i)$, *e.g.*,

$$\mu_{i,\alpha} = \mu_i^{\circ}\left(T, P^{\circ}\right) + \int_{P^{\circ}}^{p}\left(\overline{V}_{i,\alpha}\right)dP + RT\ln a_{i,\alpha} + \Psi_{i,\alpha} \qquad [4]$$

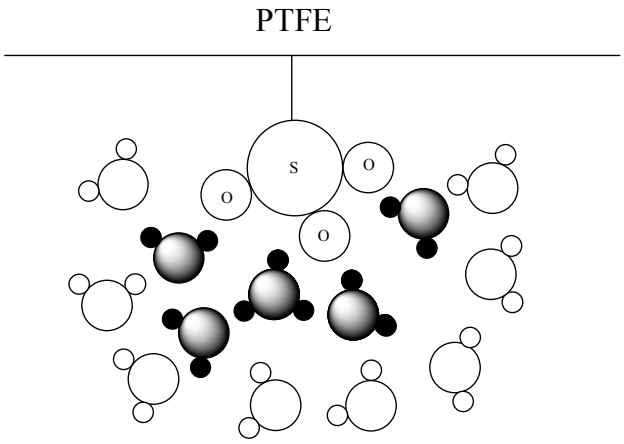

Figure 3-2. The two types of sorbed water molecules in the proton exchange membrane: five strongly bound water molecules in the primary hydration shell, akin to chemisorption and eight free water molecules, akin to physisorption.

where $\mu_i^{\circ}\left(T, P^{\circ}\right)$ is the standard chemical potential of species *i* (*e.g.*, for unit activity), *T* is the temperature, P° is the standard pressure, $\overline{V}_{i,\alpha}$ is the partial molar volume of *i*, $a_{i,\alpha}$ is the activity of *i*, and $\Psi_{i,\alpha}$ represents other potentials in the phase α. For example, for the case where an electrostatic potential ϕ exists in a given phase, for a charged species *i*

$$\Psi_i = z_i F \phi \qquad [5]$$

where z_i is the charge number of species *i* and *F* is the Faraday's constant.[35,36] Of course, the solvents of interest here do not contain any ionic species.

Liquid-Membrane Phase Equilibria

For equilibration between a liquid and membrane phase for an uncharged species *i*, the use of Eqs. 3 and 4 provides for an incompressible solvent leads to

$$\ln \frac{a_{i,M}^{F}}{a_{i,L}} = -\left(\frac{\overline{V}_i}{RT}\right) \Pi_{\mathrm{M}} \qquad [6]$$

where the membrane swelling, or osmotic pressure, $\Pi_{\mathrm{M}} = P_M - P_L$, is the pressure rise within the membrane exerted by the polymer matrix due to stretching to accommodate the imbibed pore liquid.[35,37] Many theoretical models have been proposed for the osmotic pressure,[38-40] which is known to vary as a function of the ionic concentration of solution and elastic network of solid substance.[41] The activity of species *i* within the membrane $a_{i,M}^{F}$ corresponds to the 'free', or non-chemically bound, molecules of *i*, as denoted by the superscript *'F'*.

Vapor-Membrane Phase Equilibria

When the membrane equilibrates with a vapor phase, assuming that the pressure changes within the condensed phase in the pore is caused both due to the stretching of the

polymer network upon solvent uptake, Π_M, as well as that exerted by the curved vapor-liquid interface within the pores, Π_σ, use of Eqs. 3 and 4 results in

$$\ln \frac{a_{i,M}^F}{a_{i,V}} = -\left(\frac{\overline{V}_i}{RT}\right)\left(\Pi_M + \Pi_\sigma\right) \quad [7]$$

where the vapor phase activity $a_{i,V} = P_i / P_i^{sat}$, where P_i is the partial pressure and P_i^{sat} is the vapor pressure of solvent. Π_σ is provided by the equation of Young and Laplace[42,43]

$$\Pi_\sigma = -\frac{2\sigma \cos\theta}{r_p} \quad [8]$$

where θ is the liquid-membrane contact angle and r_p is the mean pore radius of liquid-filled pores as shown in Figure 3-3. For the case of saturated vapor, $P_i = P_i^{sat}$, and Eq. 8 gives

$$\ln a_{i,M}^F = -\left(\frac{\overline{V}_i}{RT}\right)\left(\Pi_M + \Pi_\sigma\right) \quad [9]$$

whereas for the case of pure liquid solvent *i*, from Eq. 6

$$\ln a_{i,M}^F = -\left(\frac{\overline{V}_i}{RT}\right)\Pi_M \quad [10]$$

It is then clear from the Eqs. 9 and 10 that, in general, the amount sorbed from a saturated vapor would be different from that sorbed from a pure liquid, both possessing unit activity. This simple result, thus, provides a plausible explanation for the Schroeder's paradox for the sorption in polymers.

Simplifying Assumptions

The above equations are largely free of assumptions. However, in order to use these results for predictive purposes, it is simply assumed here that the activity coefficients of

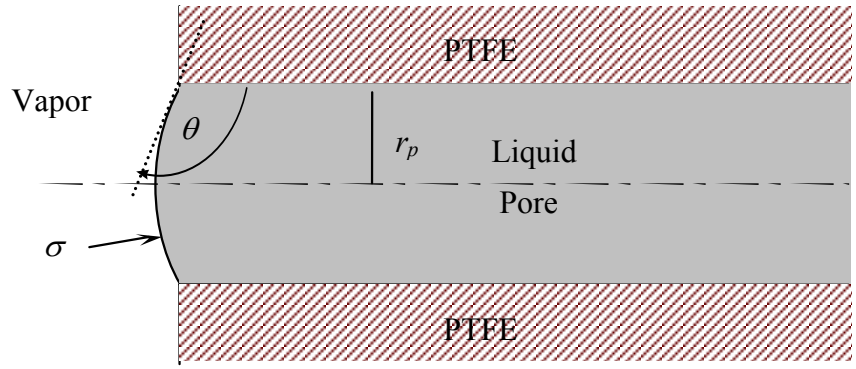

Figure 3-3. Schematic representation of absorbed solvent in the pore when membrane contacts with vapor phase environment.

the physically equilibrated species within the membrane are the same from those as in the liquid phase.[40] Then, for the liquid phase sorption in Eq. 6, $a_{i,M}^{F} / a_{i,L} = \gamma_{i,M}^{F} x_{i,M}^{F} / \gamma_{i,L} x_{i,L} \approx x_{i,M}^{F} / x_{i,L}$,

$$\ln \frac{x_{i,M}^{F}}{x_{i,L}} = - \left(\frac{\overline{V}_i}{RT} \right) \Pi_{\mathrm{M}} \qquad [11]$$

The mole fraction of the 'free' solvent molecules within the membrane is[35,44,45]

$$x_{i,M}^{F} = \frac{\lambda_i^{F}}{\lambda_i^{F} + 1} \qquad [12]$$

It is next assumed that swelling pressure exerted within the pores is linear in solvent uptake,[33-35, 46]

$$\Pi_{\mathrm{M}} = \kappa \, \varepsilon \qquad [13]$$

where the effective spring constant κ is a function of the elasticity of the polymer network, degree of cross-linking, interaction between polymer network and solvent, temperature and membrane pretreatment and history. The pore volume fraction occupied by the liquid, ε, is[5]

$$\varepsilon \approx \frac{\lambda_i}{\frac{\overline{V}_M}{\overline{V}_i} + \lambda_i} \qquad [14]$$

where $\overline{V}_M$ and $\overline{V}_i$ are partial molar volumes of membrane and solvent, respectively. Finally, it is assumed that the pore radius of liquid-filled pores may be estimated using the parallel pore model

$$r_p \approx \frac{2\varepsilon}{S} \qquad [15]$$

The pore specific surface S (m^2/cm^3 membrane) here is assumed not to vary substantially with increasing uptake. These assumptions when utilized in the above expressions provide a predictive model for the phase equilibrium between membrane and liquid (or vapor) phase in terms of common physical properties along with the empirical spring constant, κ.

It has been further reported that the contact angle of water in Nafion 117 membrane varies systematically with the hydration level.[47] Thus, for a completely dry membrane, θ = 116°, which is close to that for PTFE, indicating substantial hydrophobicity. The contact angle decreases gradually at first with θ, and then somewhat more sharply, reaching θ = 98° for vapor saturated membrane with $\lambda_{i,V}^{sat}$ = 14, indicating gradually increasing hydrophilicity.

Chemical Equilibria

Eqs. 2 and 4 when combined yield the usual chemical equilibrium for reaction ρ

$$K_\rho = \exp\left(\frac{-\Delta G_\rho^\circ}{RT}\right) = \prod_{i=1}^{n} a_i^{\nu_{\rho i}} \qquad [16]$$

where K_ρ is the equilibrium constant for reaction ρ and $\Delta G_\rho^\circ \equiv \sum_{i=1}^{n} \nu_{\rho i} G_i^\circ(T,P)$ is the standard Gibbs energy change. Formation of the hydration shell may be described by stepwise equilibrium and the binding of solvent molecules in the shell is assumed to occur by the sequential reactions between the polymer acid groups A^-H^+ and polar solvent molecules BOH (*e.g.,* HOH, CH_3OH) as evidenced by IR spectroscopic analysis.[48]

$$A^-H^+ + BOH \leftrightarrows A^-BOH_2^+ \qquad K_1 \qquad [17]$$

$$A^-BOH_2^+ + BOH \leftrightarrows A^-BOH_2^+(BOH) \qquad K_2 \qquad [18]$$

$$A^-BOH_2^+(BOH) + BOH \leftrightarrows A^-BOH_2^+(BOH)_2 \qquad K_3 \qquad [19]$$

…..

$$A^{-}BOH_2^{+}(BOH)_{\nu-2} + BOH \leftrightarrows A^{-}BOH_2^{+}(BOH)_{\nu-1} \qquad K_\nu \qquad [20]$$

where ν corresponds to the total number of equilibrium steps for the successive equilibrium reaction for the primary solvation shell. The first of these, for instance, represents dissociation of the polymer bound acid group and concomitant protonation of the solvent forming *e.g.*, hydronium ion, whereas the second and subsequent steps represent further solvation. In order to distinguish between chemical and physical equilibrium, the solvent molecules with $K_j \geq 1$ are considered to be strongly bound[49] and the interactions of an acid site with solvent molecules for $K_j \leq 1$ are assumed weak enough to be accounted for by physical equilibration. Using Eq. 16 for these and replacing activities of chemisorbed sites by their fraction of total number of acid sites

$$\theta_1 = K_1\theta_\circ a_i;\ \theta_2 = K_2\theta_1 a_i = K_1K_2\theta_\circ a_i^2;\ \theta_3 = K_1K_2K_3\theta_\circ a_i^3 \ \ldots \text{etc.}, \qquad [21]$$

such that the j^{th} term

$$\theta_j = K_j\theta_{j-1}a_i = \left(\prod_{\rho=1}^{j} K_\rho\right)\theta_\circ a_i^j \qquad [22]$$

where θ_j refers to the fraction of acid sites with j strongly bound solvent molecules. Combining this with total ion-exchange site balance, the isotherm for the strongly bound solvent molecules

$$\lambda_i^C = \frac{\sum_{j=1}^{\nu}\left(\prod_{\rho=1}^{\nu} K_\rho\right) j(a_i)^j}{1+\sum_{j=1}^{\nu}\left(\prod_{\rho=1}^{\nu} K_\rho\right)(a_i)^j} \qquad [23]$$

The use of this expression requires the knowledge of ν equilibrium constants. In order to reduce the number of parameters required for predictions, two simpler cases are considered:

i) If it is assumed that all $K_\rho = K_1$, *i.e.*, all molecules sorb equally strongly, then Eq. 23 simplifies to

$$\lambda_i^C = \frac{K_1 a_i}{1 - K_1 a_i} \left(\frac{1 - (\nu+1)(K_1 a_i)^\nu + \nu (K_1 a_i)^{\nu+1}}{1 - (K_1 a_i)^{\nu+1}} \right) \qquad [24]$$

ii) Clearly, $K_1 >> K_2 >> K_{j-1} >> K_j$, as the energy of interaction decreases quickly with the number of the strongly bound molecules/site. Thus, the proton affinity of each subsequent water molecule drops rapidly. Therefore, if it is assumed that ΔG_ρ° in Eq. 16 is proportional to the inverse ρ^q, *e.g.,* q = 3 corresponding to dispersion interactions,[43] then

$$\prod_{\rho=1}^{\nu} K_\rho = \exp\left[-\frac{\Delta G_1^0}{RT} \left(\sum_{\rho=1}^{j} \frac{1}{\rho^q} \right) \right] \approx K_1 \qquad [25]$$

since the sum of the series is not substantially greater than unity (*e.g.,* for q = 3, and j = 5, it is 1.1856). Using this approximation in Eq. 23, *i.e.*, all K_ρ = 1 except K_1, the simplified isotherm for the strongly sorbed molecules

$$\lambda_i^C = \frac{K_1 a_i}{1 - a_i} \left(\frac{1 - (\nu+1)(a_i)^\nu + \nu (a_i)^{\nu+1}}{1 + (K_1 - 1) a_i - K_1 (a_i)^{\nu+1}} \right) \qquad [26]$$

In reality, the individual equilibrium constants for the successive absorption of solvent molecules drop less quickly. For instance, the first and second ones, and sometimes even third and fourth depending on the type of ions, are significant compared with the rest of the equilibrium constants.[49,50]

Both Eqs. 24 and 26 have the virtue of involving only two parameters, namely, K_1 and ν. Since the reality would lie somewhere between the two extremes represented by these expressions, the intermediate case is represented by a slight modification of Eq. 26, *i.e.*,

$$\lambda_i^C = \lambda_{i,m} \frac{K_1 a_i}{1-a_i} \left(\frac{1-(\nu+1)(a_i)^\nu + \nu(a_i)^{\nu+1}}{1+(K_1-1)a_i - K_1(a_i)^{\nu+1}} \right) \quad [27]$$

where $\lambda_{i,m}$ is an empirical solvation parameter to better account for the sorption between the two limiting cases. For a pure component sorption of saturated vapor or liquid, a_i = 1, the strongly bound molecules, thus, are

$$\lambda_{i,V(L)}^{C,sat} = \lambda_{i,m} \frac{1+\nu}{2\left(1+\frac{1}{K_1\nu}\right)} \approx \lambda_{i,m} \frac{1+\nu}{2} \quad [28]$$

which provides an interrelation between $\lambda_{i,m}$ and ν.

An implicit expression is obtained for the sorption of liquid in terms of activity $a_{i,L}$ by first combining Eq. 27 with Eq. 1, and then substituting to Eqs. 12 and 13 with 14, and finally substituting the activity and pressure expressions to Eq. 6

$$\left\{ \lambda_{i,L} - \frac{\lambda_{i,m} K_1 a_{i,L}}{(1-a_{i,L})} \left[\frac{1-(\nu+1)(a_{i,L})^\nu + \nu(a_{i,L})^{\nu+1}}{1+(K_1-1)a_{i,L} - K_1(a_{i,L})^{\nu+1}} \right] \right\}^{-1} = a_{i,L}^{-1} \exp\left\{ \frac{\overline{V}_i}{RT} \left(\frac{\kappa\lambda_{i,L}}{\lambda_{i,L} + \overline{V}_M / \overline{V}_i} \right) \right\} - 1 \quad [29]$$

while for the case of the vapor phase sorption, the final expression is

$$\left\{ \lambda_{i,V} - \frac{\lambda_{i,m} K_1 a_{i,V}}{(1-a_{i,V})} \left[\frac{1-(\nu+1)(a_{i,V})^\nu + \nu(a_{i,V})^{\nu+1}}{1+(K_1-1)a_{i,V} - K_1(a_{i,V})^{\nu+1}} \right] \right\}^{-1} =$$

$$a_{i,V}^{-1} \exp\left\{ \frac{\overline{V}_i}{RT} \left[\frac{\kappa\lambda_{i,V}}{\lambda_{i,V} + \overline{V}_M / \overline{V}_i} - (S\sigma\cos\theta)\left(1 + \frac{\overline{V}_M}{\overline{V}_i} \frac{1}{\lambda_{i,V}}\right) \right] \right\} - 1 \quad [30]$$

For given $\lambda_{i,m}$, K_1, ν, $\overline{V}_i$, κ, S, σ, θ and $\overline{V}_M$, thus, the sorption isotherm can be determined for vapor or liquid phase sorption. Further, it is then clear from the Eq. 29 and 30 that the solvent loading in liquid sorption, $\lambda_{i,L}$, would in general be different from the solvent loading from the vapor sorption $\lambda_{i,V}$.

3-4. Results and Discussions

In order to apply this model to water sorption in Nafion®, the parameters K_1, $\lambda_{i,m}$, and ν, are determined based on the following considerations. The equilibrium constant K_1 between water and the side chain of SO_3H is approximated by that of sulfuric acid in water for the first ionization. Although different values of the ionization constants have been proposed,[45,51,52] the number of strongly bound solvent molecules, which can be determined separately by several techniques, is not substantially affected by the choice of the equilibrium constant, which is taken as 100. The solvent loading parameter, $\lambda_{i,m}$, is taken as simply as the number of water molecules per acid site for monolayer coverage, since it provides for the correct value of chemically bound solvent molecules.[5,40] The number of equilibrium steps, ν, for hydration of the ions is related to the number of solvent molecules in the hydration shell by Eq. 27. The hydration number of a proton (H^+) is experimentally reported as 3.9 in sulfonated styrene-type ion exchanger,[49] or 4 by comparing the experimental variation of molar volume of water with theoretical variation based on the H_3O^+ ion association.[45] The number of water molecules in the hydration shell around sulfonic acid in Nafion® membrane are also reported to be from 2 to 5, depending on the type of cations coexisting with the sulfonic acid. For example, two water molecules are found to be strongly bound per SO_3^- side chain for K^+ exchanged Nafion® membrane,

whereas for Na^+ and Li^+ membrane the number increases to 3~5 molecules.[53] Thus, the hydration number for Nafion® is expected to be in a range of 4~6 in the fully hydrated state. For sulfonated styrene-type ion exchanger, hydration number of 6 for SO_3H group is reported experimentally,[54] and recent molecular modeling studies also result in 5~6 hydration number for SO_3H.[55,56] The activity of water in Nafion® that is osmotically active is limited to the water molecules that are outside of the first hydration shell. In the dry or low humidity conditions, only a few water molecules are in the hydration shell and are not enough to shield the ions. As the humidity increases, more water molecules become involved in the shielding of sulfonic acid and hydronium ion.

The mean pore radius of liquid-filled pores r_p is obtained in terms of λ_i by combining Eqs. 14 and 15. The average pore radius of Nafion® resulting from this model is 2 nm. The pore size increases with humidity and becomes 4 nm when the membrane is in equilibrium with liquid water. The variation of pore radius with solvent uptake is consistent with what is observed in Nafion® by standard porosimetry method (SPM)[57] (~2 nm), transmission electron microscopy (TEM)[58] (~2.5 nm), small angle scattering with neutron (SANS) and X-rays (SAXS)[59,60] (~2.5 nm) and atomic force microscope (AFM)[61] (~7.5 nm). Although larger pores/cluster aggregates are observed,[57,62] the mean pore radius of up to 4 nm used in this model is in a good agreement with the reported data.

The surface of Nafion® shows a topographic feature of nano-phase separated crystalline fluorocarbon, amorphous fluorocarbon and ionic domains. When the surface is exposed to the increasing humidity, the pore size as well as the surface roughness increases, as observed by SAXS/SANS[60] and AFM.[61] Therefore, the surface in a humid environment may be expected to exhibit larger contact angle as compared with dry condition in light of Wenzel's law[63]

$$\cos\theta_{rough} = \gamma \cos\theta_{flat} \qquad [31]$$

where γ is the roughness factor, defined as the ratio of the actual area of a rough surface to the geometric projected area, θ_{rough} and θ_{flat} are effective contact angles on rough and flat surfaces, respectively. Since γ is always larger than unity and the contact angle for vapor phase sorption is greater than 90°, it is expected the contact angle would be increased by humidification.[43,64] However, the contact angle is actually found to decrease as the humidity increases because of the increased hydrophilicity of the surface.[47,65] The absorbed water in Nafion® interacts with side chain of sulfonic acid groups as well as the fluorocarbon backbone and changes the nanostructure of Nafion® to favor further adherence of water molecule, resulting in increased wettability, or low contact angles. Although the inside wall of pore is also not uniform, the contact angle in pores is assumed to be similar to that of the surface.

The effective spring constant κ is obtained by assuming that five water molecules are strongly bound around an acid site in Nafion® for liquid sorption. Thus, substitution of $x_{i,L}$ = 1.0, λ_i = 22 and λ_i^F = 17 to Eqs. 11-14 provides the effective spring constant κ of 183 atm. The effective spring constant κ varies with the elastic properties of polymer matrix and interaction between the solvent molecules and the polymer structure.

The isotherm of water in Nafion® as predicted by Eq. 30 as a function of humidity using the parameters listed in Table 3-2 is shown in Figure 3-4 along with the experimental data from various groups.[11,14,16,18] In the initial sorption stage, about the first two water molecules per ion are sorbed at the activity (or relative humidity) of water $a_{i,V}$ = 0.1. A high enthalpy change is known to occur for the sorption of the first and second water molecules. However, the hydration energy decreases very quickly as the number of water molecules in the primary shell increases.[66] After the strong sorption of water molecules in the initial stages, thus, the solvent loading increases less steeply with the activity and reaches $\lambda_{i,V}$ = 5~7 at $a_{i,V}$ = 0.7~0.8. In the high activity region above $a_{i,V}$ = 0.8, the

Table 3-2. Parameters employed in the model for the sorption of water in Nafion®.

Parameter	Value	Unit	Comment and references
$\overline{V}_M$	537	cm^3/mol	partial molar volume of Nafion® [5,14]
$\overline{V}_i$	18	cm^3/mol	partial molar volume of water
S	210	m^2/cm^3	specific pore surface area[57]
K_1	100	dimensionless	the first ionization constant of sulfuric acid[5,45,50,51]
ν	4-6	dimensionless	the number of chemical equilibrium steps of reaction[52-55]
$\lambda_{i,m}$	1.8	dimensionless	monolayer coverage being bound[5]
σ	72.1	mN/m	surface tension of water[36,43]
θ	98	dimensionless	contact angle of saturated water vapor in Nafion® [47]
κ	183	atm	calculated assuming five hydration water per acid group

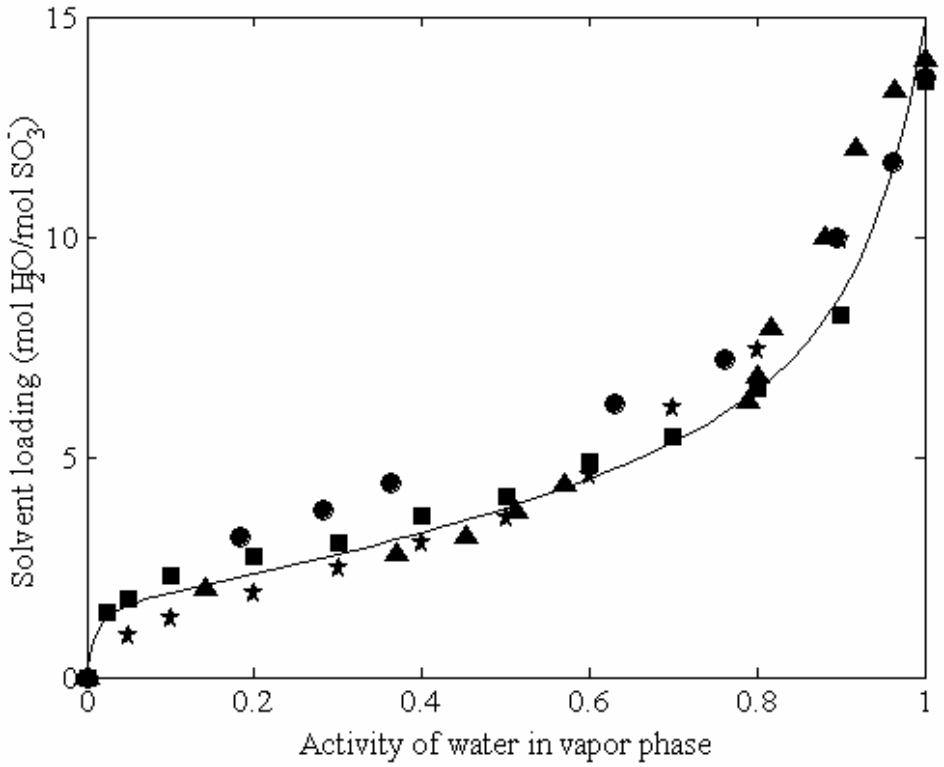

Figure 3-4. Prediction of the water sorption in Nafion®(EW=1100) by the model (Eq. 30) taken ν = 5 together with experimental observations: solid line (model prediction), triangle (ref. 12), square (ref. 14), circle (ref. 16) and star (ref. 18).

sorption of water is very sensitive to the activity of the external water vapor and reaches $\lambda_{i,V}^{sat}$ = 14.9 at saturation. In this high activity region, the water molecules are largely physically sorbed. Generally, the large ions sorb less solvent molecules in the high activity region because they occupy the space which otherwise would be taken up by the free solvent molecules. The model, thus predicts the sorption of water in Nafion® quite precisely throughout the entire range of vapor phase activity including all the characteristic features, namely the high initial slope, gradual increase of the slope after the sorption of the first a few molecules and high slope at activities above $a_{i,V}$ = 0.7~0.8.

In order to explain the Schroeder's paradox for the sorption of water in Nafion®, Eqs. 29 and 30 are reduced, respectively, for the sorption of pure liquid *i*, with $a_{i,L}$ = 1.0 and Eq. 28 to

$$\left[\lambda_{i,L}^{sat} - \frac{\lambda_{i,m}(1+\nu)}{2}\right]^{-1} = \exp\left[\frac{\overline{V}_i}{RT}\left(\frac{\kappa\lambda_{i,L}^{sat}}{\frac{\overline{V}_M}{\overline{V}_i} + \lambda_{i,L}^{sat}}\right)\right] - 1 \qquad [32]$$

and for the sorption of saturated vapor of pure component, with $a_{i,V}$ = 1.0 and Eq. 28 to

$$\left[\lambda_{i,V}^{sat} - \frac{\lambda_{i,m}(1+\nu)}{2}\right]^{-1} = \exp\left\{\frac{\overline{V}_i}{RT}\left[\left(\frac{\kappa\lambda_{i,V}^{sat}}{\frac{\overline{V}_M}{\overline{V}_i} + \lambda_{i,V}^{sat}} - (S\sigma\cos\theta)\left(1 + \frac{\overline{V}_M}{\overline{V}_i}\frac{1}{\lambda_{i,V}^{sat}}\right)\right)\right]\right\} - 1 \qquad [33]$$

It can be inferred from Eqs. 32 and 33 that the solvent loadings from the liquid, $\lambda_{i,L}^{sat}$, and that from saturated vapor, $\lambda_{i,V}^{sat}$, are different in general, which explains the Schroeder's paradox. The reason for this difference is the surface energy of the vapor-liquid interface that affects the chemical potential of the sorbed phase for the case of saturated vapor sorption.

Figure 3-5 shows the solvent loading from the liquid sorption, $\lambda_{i,L}^{sat}$ with changing ν from 4 to 6. The left-hand side (LHS) and right-hand side (RHS) of Eq. 32 are plotted versus $\lambda_{i,L}^{sat}$ and the solvent loading for the liquid sorption can be obtained by the intersection of the plots for different ν. The model predicts the loading of water $\lambda_{i,L}^{sat}$ = 22~23 as ν changes from 4 to 6 as shown in the Figure 3-5. In case of the sorption of water vapor, each side of Eq. 33 is plotted versus $\lambda_{i,V}^{sat}$ in Figure 3-6. At saturated vapor condition, the model predicts the loading of water $\lambda_{i,V}^{sat}$ = 15~16 as shown by the intersection of the plots of LHS and RHS for different values of ν in Eq. 33. There is a clear difference in solvent uptake between liquid and saturated vapor sorption; *that is*, the solvent uptake of vapor phase sorption is less than that of liquid phase. In this case, the difference in λ is about seven, *i.e.*, seven fewer water molecules per acid site on average are sorbed in Nafion® when the molecules are sorbed from the saturated vapor as compared with that from the liquid phase. When the membrane is removed from liquid water and exposed to saturated vapor, some of the water within the membrane evaporates, the vapor-liquid interface is created at pore mouth, and the pore radius is reduced by 1 nm. A new equilibrium is established with fewer water molecules within Nafion®. The size of clusters will be decreased and the number of smaller clusters will hence be increased as inferred from AFM analysis at different humidity conditions.[61,62] The model hence provides a plausible explanation for the Schroeder's paradox.

The model presented here, thus, predicts the entire isotherm, the solvent loadings from the vapor and liquid phase sorption, and explains the Schroeder's paradox for the water sorption in Nafion® satisfactorily. In principle, the model can be applied to Nafion® of different concentration of acid sites, *e.g.*, equivalent weights (EW) from 750 to 1500, different solvents, *e.g.*, methanol, cation-exchanged forms (K^+, Na^+ and Cs^+ etc.), as well as other polymers of different strength of acid sites, nature of chemical units and elasticity,

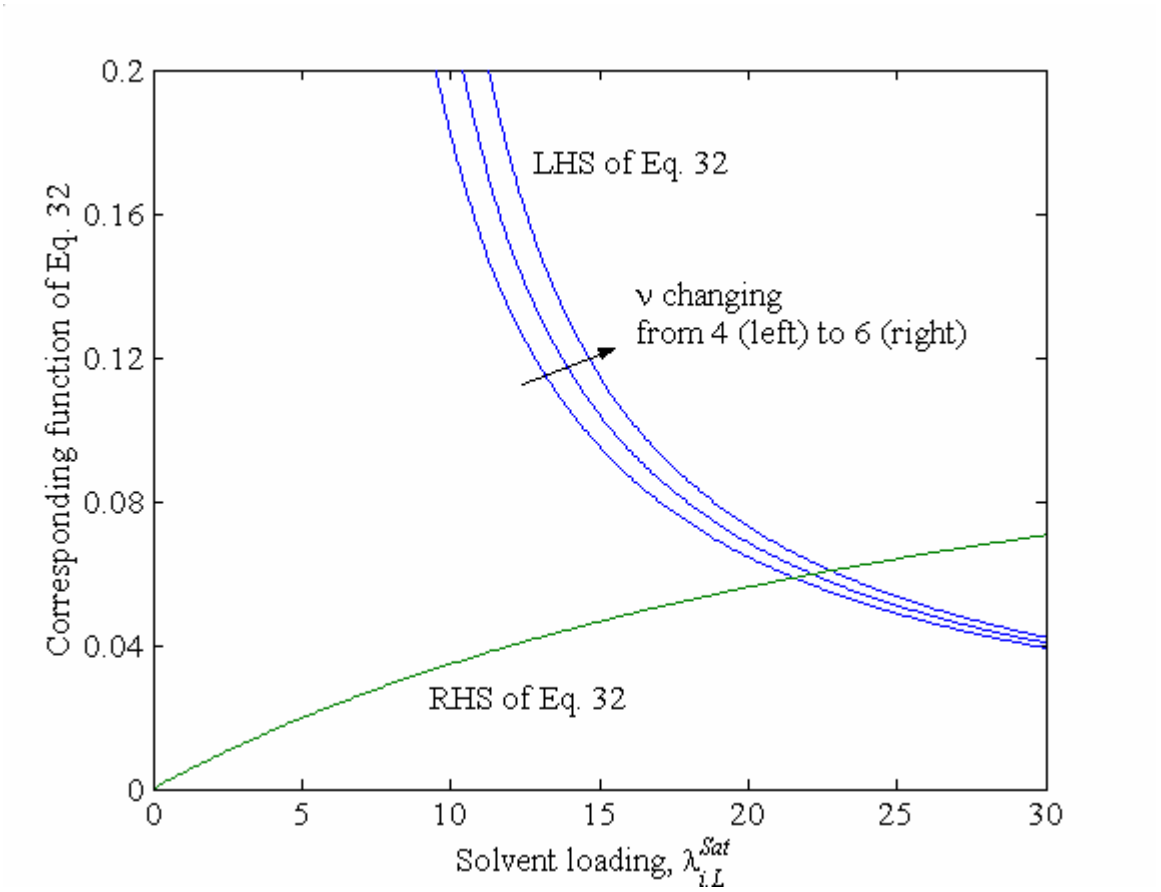

Figure 3-5. Prediction of water loading from the liquid immersion with different equilibrium steps varying from 4 to 6 (Eq. 32).

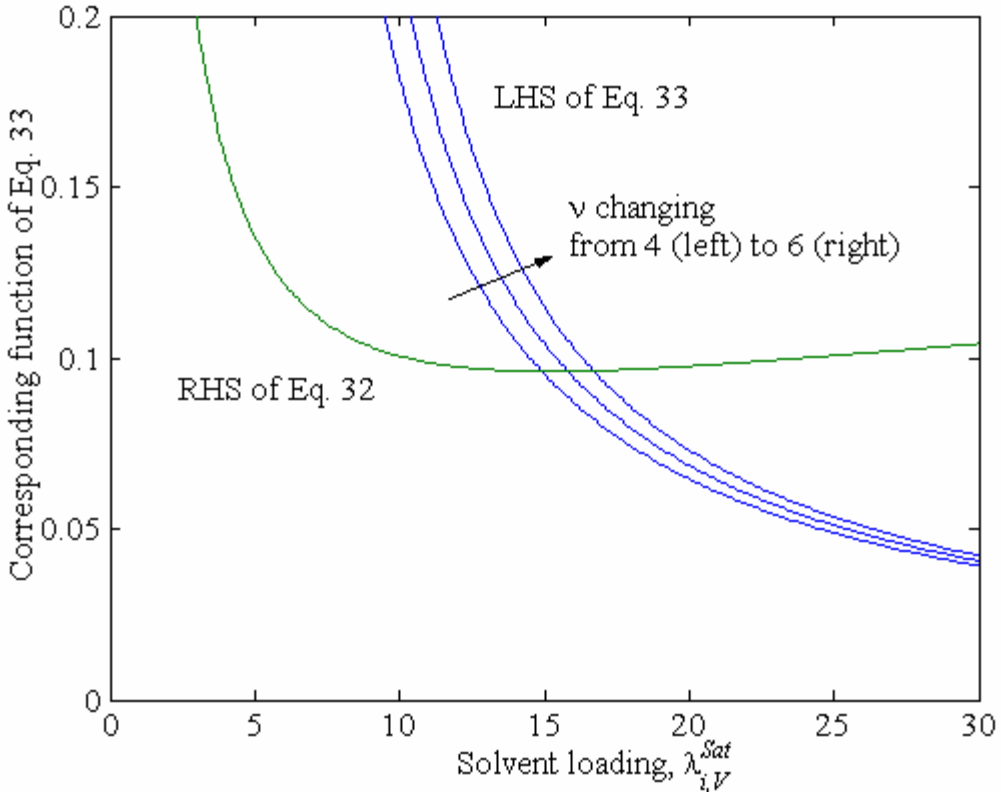

Figure 3-6. Prediction of water loading from the vapor sorption with different equilibrium steps varying from 4 to 6 (Eq. 33).

etc., provided the corresponding model parameters are available. Currently, the model is being further improved to separately account for the effects of polymer elasticity and the interaction between the solvent molecules and polymer, which have been combined to the effective spring constant κ, in terms of the known polymer properties such as shear modulus and the solubility parameters for the interaction of solvent with each chemical unit of the polymer. It is also conceivable that the effect of pretreatment may be accounted for through the visco-elastic behavior of the membrane.

3-5. Conclusions

A physically plausible thermodynamic model is developed here for the sorption of solvent in proton-exchange membrane. The sorption isotherm is a result of equilibrium established in the polymer-solvent system when the swelling pressure due to the uptake of solvent is balanced by the surface and elastic deformation pressures that restrain further stretching of the polymer network. The swelling pressure is obtained from the solvent activity within the polymer membrane and the dissociation characteristics of the ion-exchange site. This model predicts isotherm of water in Nafion® quite precisely and provides insights into the sorption phenomena in the ion-exchange polymers. The derived isotherm equations clearly show the difference in the sorbed amount from the liquid and its saturated vapor based on the surface energy of the vapor-liquid interface, thus providing a reasonable explanation for the Schroeder's paradox.

References

1. P. Costamagna and S. Srinivasan, *J. Power Sources,* **102,** 242 (2001).
2. C. Stone and A. E. Morrison, *Solid State Ionics*, **152-153**, 1 (2002).
3. M. L. Perry and T. F. Fuller, *J. Electrochem. Soc.,* **149**, S59 (2002).
4. W. Grot, *Encyclopedia of Polymer Science and Engineering* Vol. 6, 2nd ed., John Wiley and Sons. Inc., NY (1989).
5. T. Thampan, S. Malhotra, H. Tang, and R. Datta, *J. Electrochem. Soc.,* **147**, 3242 (2000).
6. G. Pourcelly, A. Oikonomen, C. Gavach, and H. D. Hurwitz, *J. Electroanal. Chem.,* **287**, 43 (1990).
7. A. V. Anantaraman and C. L. Gardner, *J. Electroanal. Chem.,* **414**, 115 (1996).
8. W. Y. Hsu and T. D. Gierke, *Macromolecules,* **15**, 101 (1982).
9. R. S. Yeo and A. Eisenberg, *J. Appl. Polm. Sci.,* **21**, 875 (1977).
10. R. S. Yeo and H. L. Yeager, in *Modern Aspects of Electrochemistry,* Vol.16, B. E. Conway, R. E. White, and J. O'M. Bockris, Editors, p. 451, Prenum Press, NY (1985).
11. T. A. Zawodzinski, C. Derouin, S. Radzinski, R. J. Sherman, V. T. Smith, T. E. Springer, and S. Gottesfeld, *J. Electrochem. Soc.,* **140**, 1041 (1993).
12. T. A. Zawodzinski, T. E. Springer, J. Davey, R. Jestel, C. Lopez, J. Valerio, and S. Gottesfeld, *J. Electrochem. Soc.,* **140**, 1981 (1993).
13. J. T. Hinatsu, M. Mizuhata, and H. Takenaka, *J. Electrochem. Soc.,* **141**, 1493 (1994).
14. D. R. Morris and X. Sun, *J. Appl. Polym. Sci.,* **50,** 1445 (1993).
15. E. Skou, P. Kauranen, and J. Hentschel, *Solid State Ionics,* **97**, 333 (1997).
16. K. K. Pushpa, D. Nandan, and R. M. Iyer, *J. Chem. Soc. Faraday Trans. I,* **84**, 2047 (1988).
17. A. Steck and H. L. Yeager, *Anal. Chem.,* **52**, 1215 (1980).

18. D. Rivin, C. E. Kendrick, P. W. Goibson, and N. S. Schneider, *Polymer,* **42**, 623 (2001).
19. P. V. Schroeder, *Z. Phys. Chem.,* **45**, 75 (1903).
20. W. D. Bancroft, *J. Phys. Chem*. *Ithaca,* **16**, 395 (1912).
21. L. K. Wolff and E. H. Buchner, *Z. Phys. Chem*., **89**, 271 (1915).
22. J. W. G. Musty, R. E. Pattle, and P. J. A. Smith, *J. Appl. Chem.,* **16**, 221 (1966).
23. H. Freundlich, *Colloid and Capillary Chemistry* 3rd ed., p. 672, London (1926).
24. R. C. Benning, R. J. Lee, J. F. Jennings, and E. C. Martin, *I. & E. C.,* **53**, 45 (1961).
25. P. Stamberger, *The Colloid Chemistry of Rubber*, p. 40, Oxford University Press, London (1929).
26. A. A. Tager, M. V. Tsilipotkina, L. V. Adamova, and L. K. Kolmakova, *Vysokomol. Soed*., **16B**, 911 (1974).
27. J. Reilly and W. N. Rae, *Physico-Chemical Methods* Vol. III, p. 364, D. Van Nostrand Company Inc., NY (1948).
28. V. Freger, E. Korin, J. Winiak, and E. Korngold, *J. Membr. Sci.,* **164**, 251 (2000).
29. C. M. Gates and J. Newman, *AIChE J.,* **46**, 2076 (2000).
30. C. Tsonos, L. Apekis, and P. Pissis, *J. Mat. Sci.*, **35**, 5957 (2000).
31. P. Futerko and I-M. Hsing, *J. Electrochem. Soc.,* **146**, 2049 (1999).
32. T. E. Springer, T. A. Zawodzinski, and S. Gottesfeld, *J. Electrochem. Soc.,* **138**, 2334 (1991).
33. H. P. Gregor, *J. Am. Chem. Soc.,* **70**, 1293 (1948).
34. H. P. Gregor, *J. Am. Chem. Soc.,* **73**, 642 (1951).
35. H. Helfferich, *Ion Exchange*, McGraw-Hill, NY (1962).
36. P. W. Atkins, *Physical Chemistry* 3rd ed., W. H. Freeman and Company, NY (1986).
37. K. A. Mauritz and C. E. Rogers, *Macromolecules,* **18**, 483 (1985).
38. W. G. McMillan and J. E. Mayer, *J. Chem. Phys.*, **13**, 276 (1945).

39. P. J. Flory, *Principles of Polymer Chemistry*, Cornell University Press, Ithaca, NY (1953).
40. M. A. Yousef, R. Datta, and V. G. J. Rodgers, *AIChE J.,* **48**, 1301 (2002).
41. W. M. Kulicke and H. Nottlemann, *Polymers in Aqueous Media*, Advances in Chemistry Series 223, American Chemical Society, Glass, J. E., Editor, Washington (1989).
42. D. A. Fridrikhsberg, *A Course in Colloid Chemistry*, Mir Publishers, Moscow (1986).
43. A. W. Adamson and A. P. Gast, *Physical Chemistry of Surfaces*, John Wiley & Sons, Inc., NY (1997).
44. J. C. Frazer and R. T. Myrick, *J. Am. Chem. Soc.,* **38**, 1907 (1916).
45. J. O'M. Bockris and A. K. N. Reddy, *Modern Electrochemistry*, Plenum Press, NY (1970).
46. G. E. Boyd and B. A. Soldano, *Z. Elektrochem.,* **57**, 162 (1953).
47. T. A. Zawodzinski, S. Gottesfeld, S. Shoichet, and T. J. McCarthy, *J. Appl. Electrochem.,* **23**, 86 (1993).
48. R. Buzzoni, S. Bordiga, G. Ricchiardi, G. Spoto, and A. Zecchina, *J. Phys. Chem.*, **99**, 11937 (1995).
49. E. Glueckauf and G. P. Kitt, *Proc .Roy. Soc. London A,* **228**, 322 (1955).
50. R. M. Barrer, N. Mackenzie, and D. Macleod, *J. Chem. Soc.,* **2**, 1736 (1952).
51. M. Liler, *Reaction Mechanisms in Sulfuric Acid and Other Strong Acid Solutions*, Academic Press, NY (1971).
52. P. Atkins and L. Jones, *Chemical Principles: The Quest for Insight*, Freeman, NY (1998).
53. S. R. Lowry and K. A. Mauritz, *J. Am. Chem. Soc.,* **102**, 4665 (1980).
54. K. W. Pepper and D. Reichenberg, *Z. Elektrochem.,* **57**, 183 (1953).
55. A. Vishnyakov and A. V. Neimark, *J. Phys. Chem. B,* **104**, 4471 (2000).

56. S. J. Paddison, R. Paul, and T. A. Zawodinski, *J. Electrochem. Soc.,* **147**, 617 (2000).

57. J. Divisek, M. Eikerling, V. Mazin, H. Schmitz, U. Stimming, and Yu. M. Volfkovich, *J. Electrochem. Soc.*, **145**, 2677 (1998).

58. Z. Porat, J. R. Fryer, M. Huxham, and I. Rubinstein, *J. Phys. Chem.*, **99**, 4667 (1995).

59. T. D. Gierke, G. E. Munn, and F. C. Wilson, *J. Polym. Sci.*, **19**, 1687 (1981).

60. G. Gebel, *Polymer*, **41**, 5829 (2000).

61. R. S. Mclean, M. Doyle, and B. B. Sauer, *Macromolecules,* **33**, 6541 (2000).

62. P. J. James, T. J. McMaster, J. M. Newton, and M. J. Miles, *Polymer*, **41**, 4223 (2000).

63. R. N. Wenzel, *I. & E. C.*, **28**, 988 (1936).

64. S. R. Coulson, I. Woodward, J. P. S. Badyal, S. A. Brewer, and C. Willis, *J. Phys. Chem.*, **104**, 98836 (2000).

65. S. H. Anastasiadis, H. Retsos, S. Pispas, N. Hadjichristidis, and S. Neophytides, *Macromolecules*, **36**, 1994 (2003).

66. P. Kebarle, S. K. Searles, A. Zolla, J. Scarborough, and M. Arshadi, *J. Am. Chem. Soc.,* **89**, 6393 (1967).

Chapter 4. Membrane Swelling, Sorption, and Ion-Exchange Equilibrium

Abstract

A thermodynamic model is proposed to describe the sorption of water in Nafion® based on the Flory-Huggins activity model and an appropriate osmotic pressure correction term for the chemical potential of water within the swollen membrane. The key variables for sorption are equivalent weight of ionomer, acid strength of the ionic groups, modulus of polymer elasticity, and interaction between water and polymer. The water uptake per unit mass of dry Nafion® increases with the increasing acid strength of the functional groups, decreasing Young's modulus, and decreasing equivalent weight of Nafion®. The model provides insights on the sorption and swelling behavior of ion-exchange membranes, and this framework can be used to evaluate and design alternate proton-exchange membranes for fuel cell applications.

4-1. Introduction

Fuel cells offer a palpable challenge to the conventional power-generating technologies due to their high efficiency, low environmental impact, and numerous potential applications.[1-3] The proton-exchange membrane (PEM) functions as a solid electrolyte in PEM fuel cells, conducting protons from anode to cathode as well as acting as a separator for the reactant gases, protons and electrons, thus, constitutes the heart of the PEM fuel cells. The most studied PEM is Nafion®, consisting of a hydrophobic polytetrafluoroethylene backbone and a hydrophilic acid group $SO_3^-H^+$ connected to the backbone via side chains of $–O-CF_2-CF-O-CF_2-CF_2-$. Even though it is not cross-linked,

Nafion® is stable in the presence of water due to a balance of the hydrophobicity and hydrophilicity combined with elastic strength, is chemically inert in both oxidative and reductive environments, and is an excellent proton conductor under typical fuel cell operating conditions. For its commercial application in fuel cells, however, it suffers from some drawbacks as well[3], *e.g.*, a limitation on the operating temperature of around 80º C due to drying above 100º C in atmospheric fuel cells and softening over 111º C, as well as a high cost.

These limitations have stimulated a worldwide effort to find alternatives to Nafion®, and a number of new membranes have been proposed, and discarded, based on their conductivity, cost, degradation, thermal and chemical stability, etc. The solid polymer electrolyte membranes are of essentially two types:[4-6] *i*) *proton-exchange membranes (PEMs)* in which the acid site is covalently bound to the polymer, and *ii*) *polymer-acid composites (PACs)* in which basic polymers are simply doped with an acid. The clear advantages of *PEMs* over *PACs* are their relative stability, *i.e.*, acid is not leached out by water, and unit transference number. Host polymers themselves are classified into the following types based on their resistance to chemical degradation: *i)* perfluorinated polymers, *e.g.*, Nafion®, Flemion®, Gore-Select® and Dow membranes; *ii)* partially fluorinated polymers, *e.g.*, poly-α ,β ,β -trifluorostyrene and Ballard Advanced Materials 3rd Generations (BAM3G) polymers; and *iii)* hydrocarbon polymers, *e.g.*, poly(phenylene oxide) PPO, poly(ether ether ketone) PEEK, poly(phosphazine) PP, poly(imides) PI, poly(benzimidazole) PBI. Examples of *PEMs*[4,6] include sulfonated (denoted by preceding S) versions of above polymers (*e.g.*, S-PEEK, S-PBI, etc.), while examples of PACs[5] include phosphoric acid doped PBI (PBI/H_3PO_4), PEO/H_2SO_4 (*or* H_3PO_4), PVA/H_2SO_4 (*or* H_3PO_4), and PEO/H_2SO_4(*or* H_3PO_4). Although some of the host polymers possess attractive thermo-mechanical properties, none of these alternatives have so far proved to be superior to Nafion®.

The proton conductivity of PEMs depends strongly on the host polymer structure and water content in the membrane.[7] A central challenge in the design of new PEMs is thus a fundamental analysis of the structural and water uptake characteristics needed to achieve high proton conductivity. The proposed theoretical structural models of Nafion® include[8]: Gierke's cluster-network model,[9] Mauritz et al.'s elastic model,[10] Yeager and Steck's three-region model,[11] and more other recent models based on the spectroscopic analysis such as SANS,[12] SAXS,[13] and AFM.[14]

The water uptake by polymer membranes at a given relative humidity (RH) is a function of temperature,[15,16] equivalent weight,[17,18] type of counter ions,[19,20] and membrane pretreatment.[15,21] Although several empirical models of water uptake in Nafion® have been proposed, *e.g.*, based on a finite multilayer BET,[22] modified BET,[23] and Flory-Huggins,[23,24] these models provide limited understandings of sorption phenomena in PEMs. Recently, we have proposed[25] a more insightful thermodynamic model that incorporates the effect of swelling pressure within the membrane on the chemical potential of water and hence sorption, based on a "spring constant" of the polymer matrix used as a fitted parameter. Here, we propose a more general thermodynamic model based on the Flory–Huggins theory[26] for activity and Young's modulus of membrane elasticity for osmotic pressure due to polymer stretching. The sorption of water in Nafion® is analyzed and design parameters are deduced from this more fundamental model which contains Flory-Huggins interaction parameter accounting for the interaction of polymer backbone and water.

4-2. Theory

Thermodynamic Equilibrium

A generalized chemical potential $\mu_{i,\alpha}$ of species *i* in phase α can be written as a function of temperature T, pressure P, activity a_i, and other interaction potentials Φ. Assuming these effects to be separable

$$\frac{\Delta\mu_{i,\alpha}}{RT} = \frac{\Delta\mu_{i,\alpha}(T)}{RT} + \frac{\Delta\mu_{i,\alpha}(P)}{RT} + \frac{\Delta\mu_{i,\alpha}(m)}{RT} + \frac{\Delta\mu_{i,\alpha}(\Phi)}{RT} + .. \quad [1]$$

where $\Delta\mu_{i,\alpha}(m)$ contains the configurational (entropic) as well as interaction (enthalpic) terms of mixing. Thus[27]

$$\mu_{i,\alpha} = \mu_i^{\circ}\left(T, P^{\circ}\right) + \int_{P^{\circ}}^{P} \overline{V}_{i,\alpha} dP + RT \ln a_{i,\alpha} + \Psi_{i,\alpha} \quad [2]$$

where $\Psi_{i,\alpha}$ represents potentials generated by other fields. For example, if an electrostatic potential ϕ exists in a given phase,[28,29] $\Psi_{i,\alpha} = z_i F \phi_\alpha$, where z_i is the charge number of species *i* and *F* is the Faraday's constant.

For phase equilibrium between the membrane (*M*) and fluid (*F*) phases, $\mu_{i,M} = \mu_{i,F}$. Use of Eq. 2 in this yields in the absence of external fields

$$\ln \frac{a_{i,M}^{F}}{a_i} = -\left(\frac{\overline{V}_i}{RT}\right) \Pi_S \quad [3]$$

where $a_{i,M}^{F}$ and a_i represent the activity of solvent *i* in the membrane and fluid phases, respectively, $\overline{V}_i$ is the partial molar volume of *i*, and Π_S is the swelling pressure.[29] For the case of sorption from vapor, this includes pressure terms due to stretching of polymer matrix as well as that exerted by the curved vapor-liquid interface in pore of radius r_p[25]

$$\Pi_S = \Pi_M + \Pi_\sigma \quad [4]$$

where Π_σ is given by the equation of Young and Laplace

$$\Pi_\sigma = -\frac{2\sigma\cos\theta}{r_p} \quad [5]$$

where σ is vapor-liquid surface tension, θ is the contact angle, and r_p is pore radius $r_p = 2\varepsilon_i/S$, S is specific surface area (m^2/cm^3), and ε_i is pore volume fraction occupied by the liquid given as

$$\varepsilon_i = \frac{\lambda_i}{\lambda_i + r} \quad [6]$$

where λ_i is the solvent loading (mol H_2O/mol SO_3^-), and r is the ratio of partial molar volume of polymer membrane $\overline{V}_M$ and solvent $\overline{V}_i$, *or* $r = \overline{V}_M / \overline{V}_i$. The total number of water molecules per acid site in the polymer λ_i can be classified as:[25] *i*) those that are strongly, or chemically, bound to the acid site of the polymer, represented by λ_i^C, and *ii*) those that are free to physically equilibrate between the polymer and the fluid phase, λ_i^F

$$\lambda_i = \lambda_i^C + \lambda_i^F \quad [7]$$

Of course, λ_i^C is determined by the reaction equilibrium condition $\sum_{i=1}^{n} \nu_{\rho i}\mu_i = 0$.[25]

Activity

For solvent (*i*)-polymer membrane (*M*) systems, the activity of free solvent in the membrane phase $a_{i,M}^F$ is assumed to be given by the Flory-Huggins model[26] derived on the basis of a quasi-crystalline lattice structure

$$\frac{\Delta\mu_{i,M}(m)}{RT} = \ln a_{i,M}^F = \ln \varepsilon_i^F + \left(1 - \frac{1}{r}\right)\left(1 - \varepsilon_i^F\right) + \chi\left(1 - \varepsilon_i^F\right)^2 \quad [8]$$

where ε_i^F is the volume fraction of free solvent, $\varepsilon_i^F = \lambda_i^F/(\lambda_i + r)$, λ_i^F is solvent loading of free water molecules, and χ is the Flory-Huggins polymer-solvent interaction parameter.

The first two terms on the right hand side of the above represent the configurational (entropic) contributions, while the third represents the interaction (enthalpic) contribution to mixing.

Swelling Pressure and Membrane Elasticity

The swelling pressure may be related to network contractile pressure based on the statistical theory of polymer elasticity. Thus, Flory[26] assumed that the polymer chain length distribution can be represented by a Gaussian distribution, and that the polymer chains deform affinely; *i.e.*, the change in the dimensions of individual chains is the same as that in the takes the form

$$\Pi_M = G\left(\Phi_M{}^{1/3} - \frac{1}{2}\Phi_M \right) \qquad [9]$$

where Φ_M is the volume fraction of polymer given by $\Phi_M = r/(\lambda_i + r)$, and G is the shear modulus of polymer matrix given by the classical theory of polymer elasticity.[26] James and Guth[30] had earlier developed the so-called "Phantom network" theory based on the assumptions that the internal energy is not dependent on the volume, and the entropy may be divided into two parts, one associated with the thermal capacity and the other associated with the number of configurations. Then, the swelling pressure is given by

$$\Pi_M = G\Phi_M{}^{1/3} \qquad [10]$$

For chains of twenty monomers or less, Gusler and Cohen's[31] non-Gaussian model is superior to the Gaussian distribution model, resulting in

$$\Pi_M = G\left(\frac{5}{3}\Phi_M{}^{1/3} - \frac{7}{6}\Phi_M \right) \qquad [11]$$

The above expressions provide finite osmotic pressures at zero swelling, in apparent agreement with experimental results for some polymers.[32] However, in the case of ion-exchange resins, the swelling pressure is experimentally found to be zero in their dry state

and is generally proportional to the extent of swelling.[29,33] Thus, Gregor[34] suggested an empirical Hookean model to represent the experimental data for ion-exchange resins

$$\Pi_M = aV_1 + b \qquad [12]$$

where V_1 is the inner volume, *i.e.*, the total external volume of the resin minus the volume of incompressible polymer matrix including the ionic groups, and a and b are fitted constants. Thus, the above models are not suitable for our purposes.

Recently, Freger[35] has developed a model for phase-separated swollen polymer networks by treating the swelling as a non-affine 'inflation' of the hydrophobic matrix by small aggregates of water molecules, which is in keeping with the structural model of polymer swelling, resulting in

$$\Pi_M = \frac{2}{3} G\left(\Phi_M{}^{1/3} - \Phi_M{}^{7/3}\right) \qquad [13]$$

Although the application of Eq. 13 is limited to low and moderate swelling, it provides the correct limiting dependence of swelling pressure on the solvent content in ion-exchanged polymers. Figure 4-1 provides a comparison of the normalized swelling pressure (Π_M / G) calculated by the various models described versus volume fraction of solvent in the polymer phase. Since only Freger's model shows a zero swelling pressure in the limit of dry condition, it is adopted here.

The shear modulus, G, is related to Young's modulus E and Poisson's ratio υ by[36]

$$E = 2(1+\upsilon)G \qquad [14]$$

Assuming $\upsilon = 0.5$ for Nafion®, the shear modulus is, thus, one third of Young's modulus.

Chemical Equilibrium and Hydration Sheath

From a molecular viewpoint, the acid groups of the polymer interact with water molecules *via* the ion-dipole forces and a certain number of water molecules, depending upon the level of hydration, become strongly (or chemically) associated with the ionic

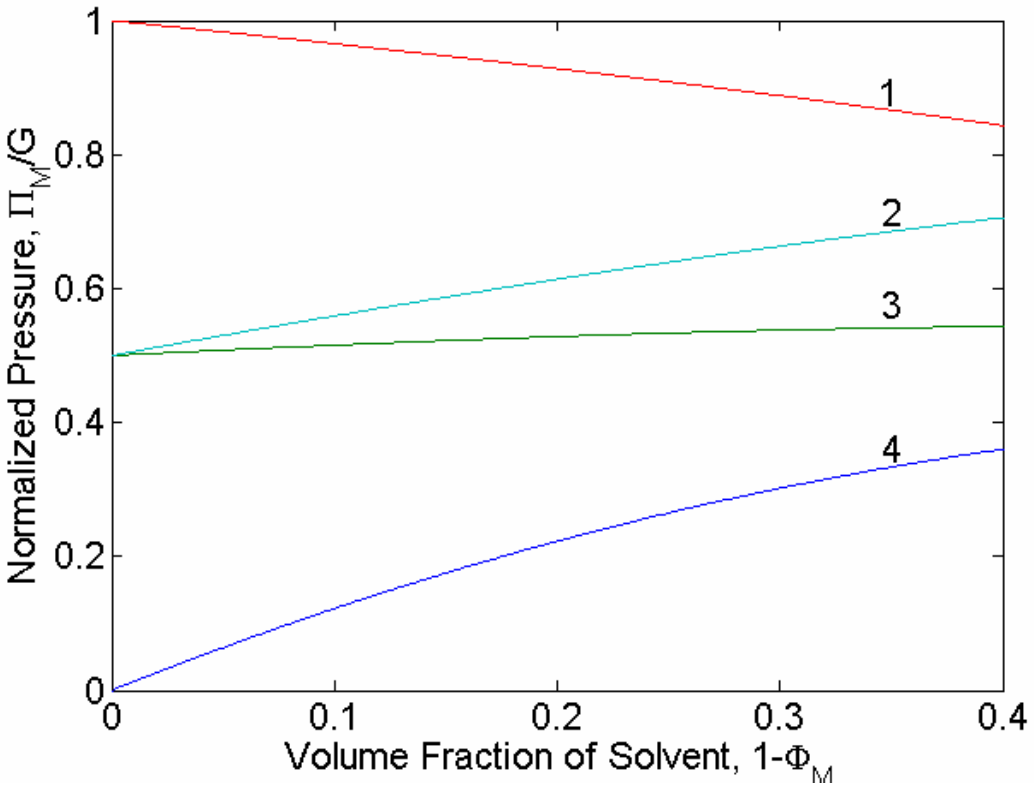

Figure 4-1. The normalized swelling pressure from different models (1: Phantom model, 2: Gusler-Cohen's model, 3: Affine model, and 4: Freger's model).

groups forming the primary hydration sheath.[37] The formation of the hydration sheath may be described by stepwise equilibrium, *i.e.,* the binding of solvent molecules is assumed to occur by sequential reactions between the polymer acid groups $SO_3^-H^+$ and H_2O :[25]

$$SO_3^-H^+ + H_2O \leftrightarrows SO_3^-(H_3O)^+ \qquad K_1 \qquad [15]$$

$$SO_3^-(H_3O)^+ + H_2O \leftrightarrows SO_3^-H_3O^+(H_2O) \qquad K_2 \qquad [16]$$

$$SO_3^-H_3O^+(H_2O) + H_2O \leftrightarrows SO_3^-H_3O^+(H_2O)_2 \qquad K_3 \qquad [17]$$

…..

$$SO_3^-H_3O^+(H_2O)_{\nu-2} + H_2O \leftrightarrows SO_3^-H_3O^+(H_2O)_{\nu-1} \qquad K_\nu \qquad [18]$$

where K_j represents the equilibrium constant of j step and ν corresponds to the total number of such steps. The first of these represents dissociation of the polymer acid group and concomitant protonation of water to form hydronium ion (Figure 4-2), whereas the second and subsequent steps represent formation of solvation sheath of hydronium ion. Due to the very high proton affinity of water, there are no free protons and H_3O^+ itself behaves like an ion, forming a hydration sheath around it.

The chemical equilibria of water molecules described above can be written in terms of solvent activity, equilibrium constants, and fraction of chemisorbed sites of the total number of acid sites as: $\theta_1 = K_1\theta_0 a_i$; $\theta_2 = K_2\theta_1 a_i = K_1K_2\theta_0 a_i^2$; $\theta_3 = K_1K_2K_3\theta_0 a_i^3$ etc., such that the j^{th} term

$$\theta_j = K_j\theta_{j-1}a_i = \left(\prod_{\rho=1}^{j} K_\rho\right)\theta_0 a_i^j \qquad [19]$$

where θ_j refers to the fraction of acid sites with j strongly bound solvent molecules. The effect of pressure on equilibrium constant K_ρ is neglected here on the assumption of no volume change in the hydration reactions. Combining this with total ion-exchange site balance, the isotherm for the strongly bound molecules is

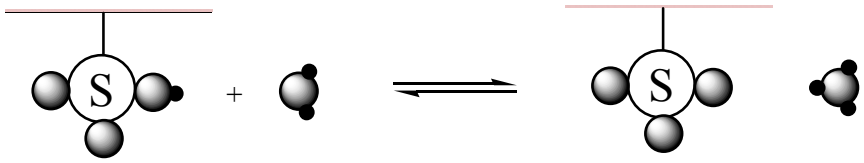

Figure 4-2. A schematic of equilibrium steps forming hydration sheath around sulfonic acid in Nafion®.

$$\lambda_i^C = \frac{\sum_{j=1}^{v}\left(\prod_{\rho=1}^{v} K_\rho\right) j(a_i)^j}{1+\sum_{j=1}^{v}\left(\prod_{\rho=1}^{v} K_\rho\right)(a_i)^j} \qquad [20]$$

The use of this expression requires the knowledge of v equilibrium constants. A simpler expression can be obtained in terms of the ionization constant of the first step K_1 and a parameter $\lambda_{i,m}$ accounting for the balance. This is based on the assumption that K_1 is much larger than the equilibrium constants of the subsequent hydration steps, which is certainly borne out by the proton affinity data available.[38] It was thus shown that an adequate expression for λ_i^C is[25]

$$\lambda_i^C = \lambda_{i,m}\frac{K_1 a_i}{1-a_i}\left(\frac{1-(v+1)(a_i)^v+v(a_i)^{v+1}}{1+(K_1-1)a_i-K_1(a_i)^{v+1}}\right) \qquad [21]$$

The additional parameter $\lambda_{i,m}$ can be estimated from a knowledge of the total number of water molecules in the primary hydration sheath at saturation (a_i = 1.0), when from Eq. 21

$$\lambda_i^{C,sat} = \lambda_{i,m}\frac{(1+v)}{2(1+1/(K_1 v))} \approx \lambda_{i,m}\frac{(1+v)}{2} \qquad [22]$$

The sorption of water in Nafion® can thus be calculated by the substitution of Eqs. 4-8 and Eq. 13 into Eq. 3. This results in an implicit expression for λ_i versus a_i

$$\begin{aligned}&\ln\left(\frac{\lambda_i-\lambda_i^C}{\lambda_i+r}\right)+\left(1-\frac{1}{r}\right)\left(\frac{\lambda_i^C+r}{\lambda_i+r}\right)+\chi\left(\frac{\lambda_i^C+r}{\lambda_i+r}\right)^2-\ln a_i = \\ &-\frac{\overline{V}_i}{RT}\left\{\left[\frac{2}{3}G\left[\left(\frac{r}{\lambda_i+r}\right)^{1/3}-\left(\frac{r}{\lambda_i+r}\right)^{7/3}\right]-S\sigma\cos\theta\left(1+\frac{r}{\lambda_i}\right)\right]\right\}\end{aligned} \qquad [23]$$

where λ_i^C is provided in Eq. 21. The isotherm, *i.e.*, the solvent loading λ_i as a function of activity of fluid phase a_i, can thus be calculated in terms of the parameters obtained *a*

priori except for the Flory-Huggins parameter χ, which is hence the only fitted parameter in this model.

4-3. Experiments

Membrane preparation – Nafion® membrane of EW of 960, 1100 and 1200 are prepared by casting the Nafion® solution based on the procedure described by Moore and Martin.[39] After stirring for 8 hours at room temperature, the solution was cast on a glass dish utilizing a doctor blade. The cast membrane was heat treated in a convection oven at 100º C for 15 minutes, which was sufficient to produce a solid membrane. The fabricated membrane was removed from the glass dish, dried and then placed in a Teflon sleeve and annealed at 170º C at 10 tons for 15 minutes in a mechanical press. This processing step is necessary to produce pliant and insoluble PEMs with mechanical properties similar to those of the commercially available Nafion® films.

Water sorption measurement. – The water uptake of Nafion® was measured via Tapered Element Oscillating Microbalance (TEOM)[40] under different relative humidity (RH) conditions. The changes in sample mass are measured in TEOM via the frequency changes of the oscillating tapered element. The membranes were cut into thin strips (1.5 mm by 1.5 mm) and packed with quartz wool into the oscillating chamber of the TEOM. The water uptake was measured at 25º C from 0 % to 99 % RH. The lines to the TEOM were heat traced to avoid condensation. The changes in real time mass were recorded to determine the sorption amount of water at equilibrium.

Young's modulus measurement. – The Young's modulus of Nafion® was measured under different humidity conditions using the Optoelectronic Holography (OEH) technique. The Young's modulus E can be obtained by the relation

$$E = \frac{4\pi^2 f_n^{\,2} L^4 \rho A}{\beta_n^{\,4} I} \qquad [24]$$

where f_n is the frequency of the nth mode, β_n is a characteristic coefficient, L is the effective length of the sample, ρ is the density, A is the cross-section area of the sample, and I is the moment of inertia of the cross-section of the sample. The experimental details are described elsewhere.[41]

4-4. Results and discussions

The isotherm for water vapor in Nafion® is calculated by Eq. 23. The model parameters, *i.e.*, K_1, $\lambda_{i,m}$, ν, G and χ, were determined based on the following considerations. The first ionization constant K_1 between water and the side chain of SO_3H is approximated as 10^3 based on the report that *pK* of a Nafion® is in the range of -1.0 to -5.1.[42] The parameter, $\lambda_{i,m}$, was obtained from Eq. 22 by assuming $\lambda_i^{C,sat} \approx \nu$ with taking ν = 5-6. This provides $\lambda_{i,m}$ = 1.8, which is also approximately the number of water molecules per acid site for monolayer coverage.[25] Since the number of water molecules in the first hydration shell around sulfonic acid in Nafion® vary from 4 to 6 depending on the type of cations coexisting with the sulfonic acid,[43,44] the number of the equilibrium steps is in the range of 4 to 6 for water sorption in Nafion®. Young's modulus of H^+-Nafion® (EW=1100) at room temperature was measured utilizing the OEH technique described above and fitted using the empirical formula

$$E = E_0 \exp(-2.1753\varepsilon_i) \qquad [25]$$

where E_0 = 316 MPa and ε_i is the volume fraction of water in Nafion®. As the volume fraction of water in the membrane phase increases, the Young's modulus decreases. The Flory-Huggins interaction parameter, χ, is usually a concentration dependent term and is fitted to experimental data on sorption.

Figure 4-3 shows the isotherm of water in Nafion® (EW=1100) in terms of λ_i as a function of the activity of water in vapor phase based on parameters[45-50] listed in Table 4-1 and the concentration dependent Flory-Huggins interaction parameter in Figure 4-4 along with the experimental data from literature.[51-54] In the low activity region, $a_i < 0.75$, water uptake increases with activity by a small amount. After the sorption of strongly bound water molecules in this activity region, the water uptake increases with the activity and reaches $\lambda_{i,V} \approx 6$ at $a_{i,V} = 0.75$. For $a_{i,V} > 0.75$, the water uptake is very sensitive to the activity of the water vapor and reaches $\lambda_{i,V}^{sat} = 14.0$ at saturation. The model reflects the sorption of water in Nafion® very well with the concentration dependent interaction parameter χ.

Figure 4-4 shows the dependence of χ on the volume fraction of free water in Nafion®. The interaction parameter decreases linearly with the volume fraction of free water in Nafion®. This may be explained by the fact that the free water molecules face different environments within the polymer matrix with increasing water imbibitions and thus interaction parameter varies with the water content in Nafion®. In fact, the fitted interaction parameter between water and Nafion® depends on the type of sorption model and parameter employed. Tsonos et al.[23] considered the volume fraction of water in Nafion® based on the total amount of water in Flory-Huggins activity expression and obtained χ increases with water uptake to an activity of water $a_i = 0.79$ and thereafter decreases, while Futerko et al.[24] treated the strongly bound water molecules as part of the Nafion® and found that χ increases linearly with the free water concentration.

In order to use this model for design purposes, the effect of the polymer variables K_1 and E on the amounts of water uptake is analyzed. The pK for Nafion® has been suggested to be in the range between that for methane sulfonic acid ($pK = -1.0$)[46] and tri-

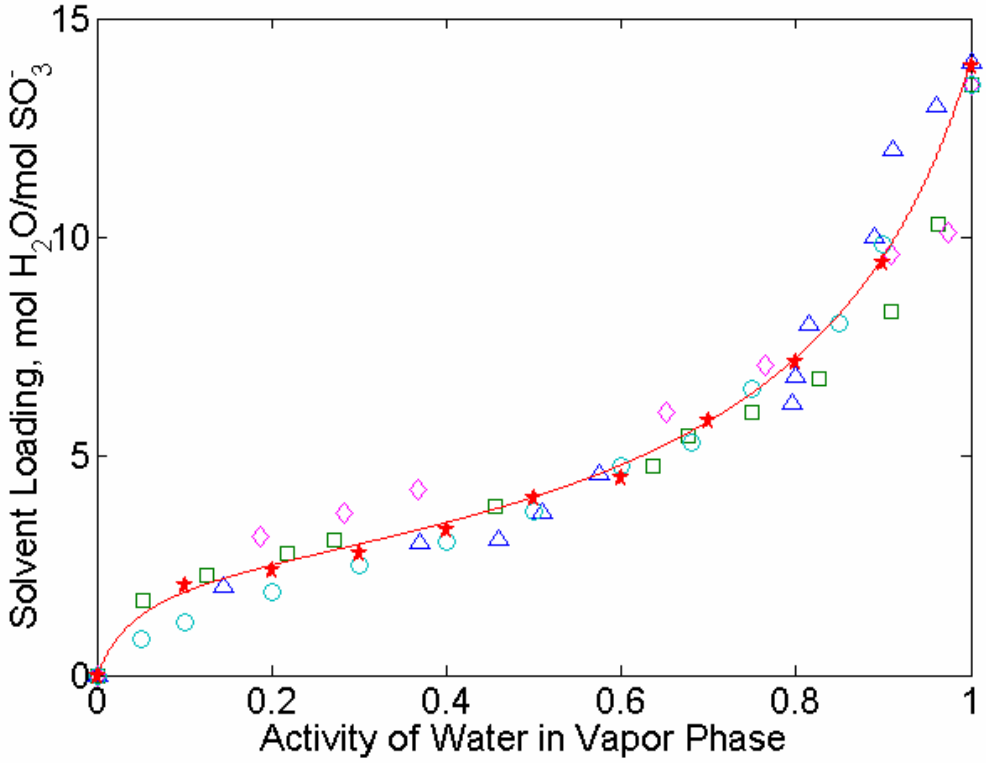

Figure 4-3. The solvent loading vs. activity of water vapor for Nafion® (EW=1100) membrane (triangle: ref. 51, square: ref. 52, diamond: ref. 53, circle: ref. 54, and star: this work).

Table 4-1. Parameter values employed in the model for the sorption of water in Nafion®.

Parameter	Value	Unit	Comments and references
$\overline{V}_M$	537	cm^3/mol	partial molar volume of Nafion® [22]
$\overline{V}_i$	18	cm^3/mol	partial molar volume of water
S	210	m^2/cm^3	specific pore surface area[45]
K_1	1000	dimensionless	the first ionization constant of sulfuric acid[46-49]
ν	5	dimensionless	the number of chemical equilibrium steps of reaction
$\lambda_{i,m}$	1.8	dimensionless	monolayer coverage being bound[22,25]
σ	72.1	mN/m	surface tension of water
θ	98	dimensionless	contact angle of saturated water vapor in Nafion® [50]
χ	0.9-2.4	dimensionless	fitted polymer-solvent interaction parameter

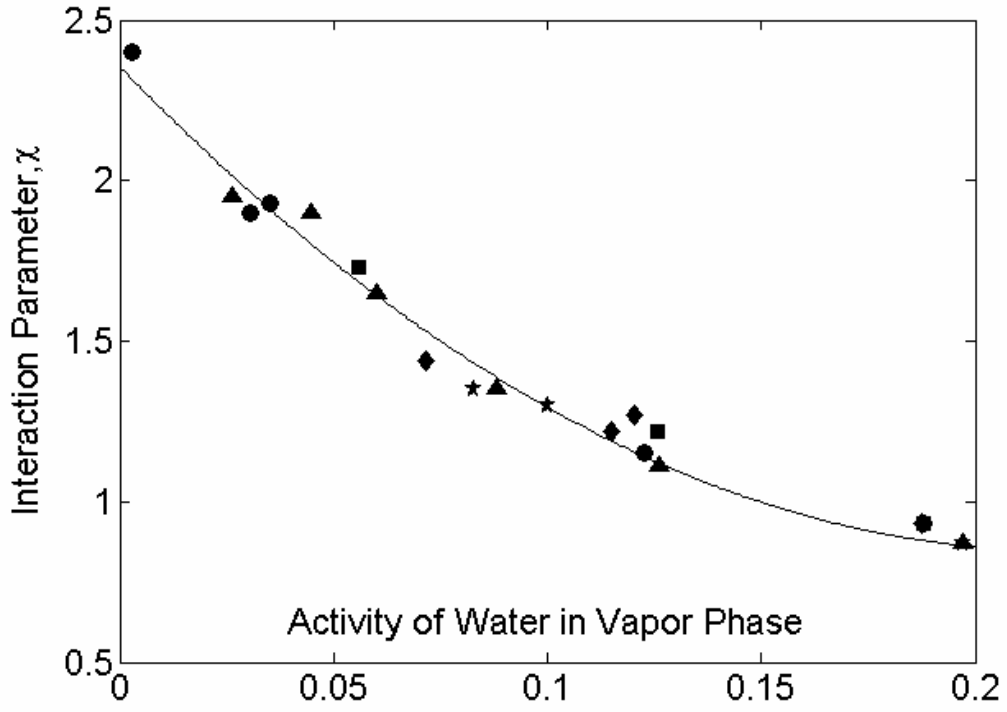

Figure 4-4. The interaction parameter χ as a function of activity of water vapor (triangle: ref. 51, square: ref. 52, diamond: ref. 53, circle: ref. 54, and star: this work).

fluoro methane sulfonic acid (pK = -5.1)[47], and recently been reported to be -3.09[48] and -6[49]. Figure 4-5 shows the effect of the dissociation constant K_1 on the water sorption. As the dissociation constant increases, *i.e.*, pK decreases, the water uptake increases initially and reaches λ_i = 13.9 at $K_1 = 10^2$ and then no further increase in water uptake is predicted. Figure 4-6 shows the effect of Young' s modulus of the polymer in the dry state E_0 on the water uptake. E_0, of course, varies with the polymer type and the temperature. The water uptake increases as expected for polymers having low E_0.

The number density of the acid groups also strongly affects the sorption capacity of the polymer on a weight or volume basis, even though λ_i may remain unchanged. A high number density of acid groups is characterized by lower EW, defined as the average molecular mass associated with one mole of acid group. The EW changes not only the number density but also strongly affects the crystallinity, elasticity, swelling, and the transport properties of the polymer. Therefore, for a given polymer system, EW is one of the most critical design parameters to be optimized. Figure 4-7 compares the model predictions versus experimental results of the water vapor sorption in Nafion® with EW 960, 1100 and 1200 g/equiv. As expected, the water uptake in terms of wt. % of dry membrane increases with decreasing EW. The total number of water per acid site, however, remains the same for EW in the range of 960-1200 in the case of vapor sorption, which is as predicted by the model.

The water uptake from liquid phase has been reported for different EWs of Nafion®. For example, for H^+-Nafion®, water sorption increases with decreasing EW from 1500 to 785 on a dry weight basis.[18] For EW less than 900, the water uptake of Nafion® increases dramatically, *e.g.,* the water uptake reaches 80 wt. % on a dry Nafion® basis at EW of 785. This high water uptake at very low EW can be explained by a substantial decrease of Young's modulus with EW. However, Freger's model adopted here is limited to low

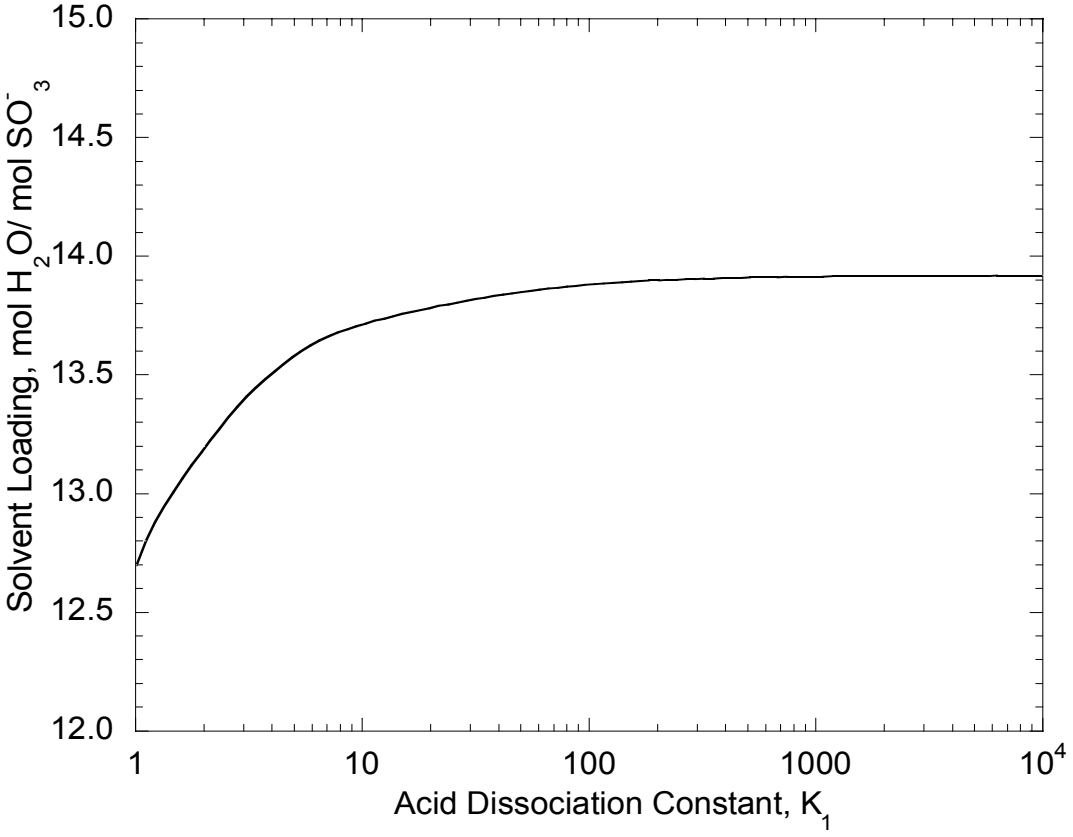

Figure 4-5. The predicted solvent loading with the changes of the dissociation constant.

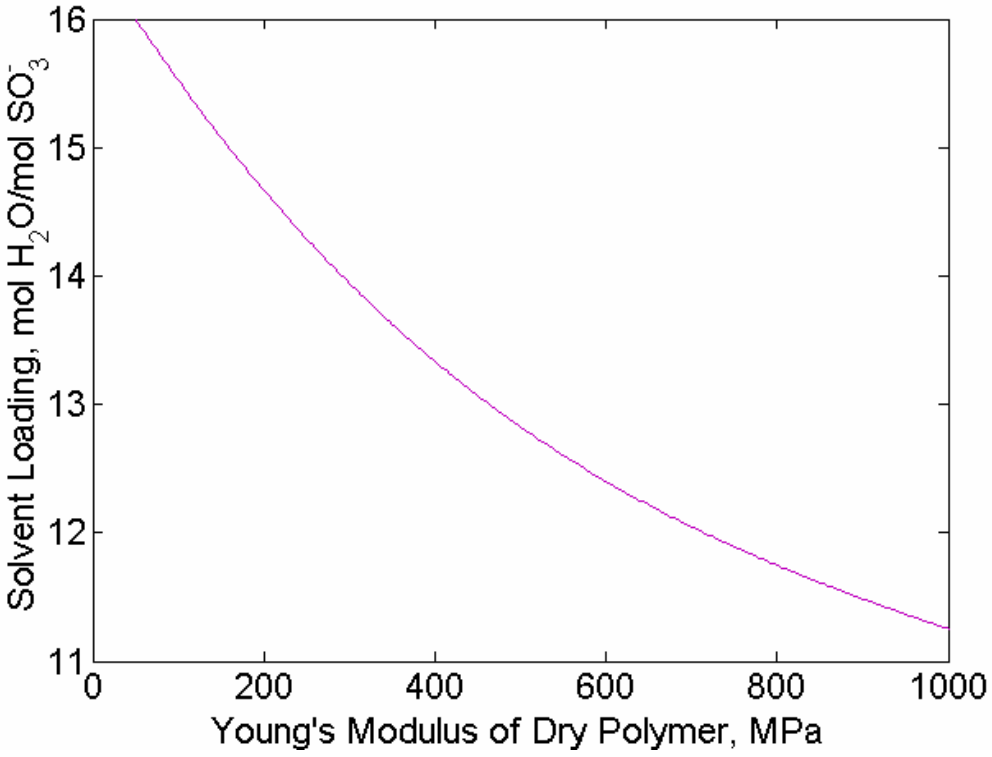

Figure 4-6. The predicted solvent loading with the changes of Young's modulus.

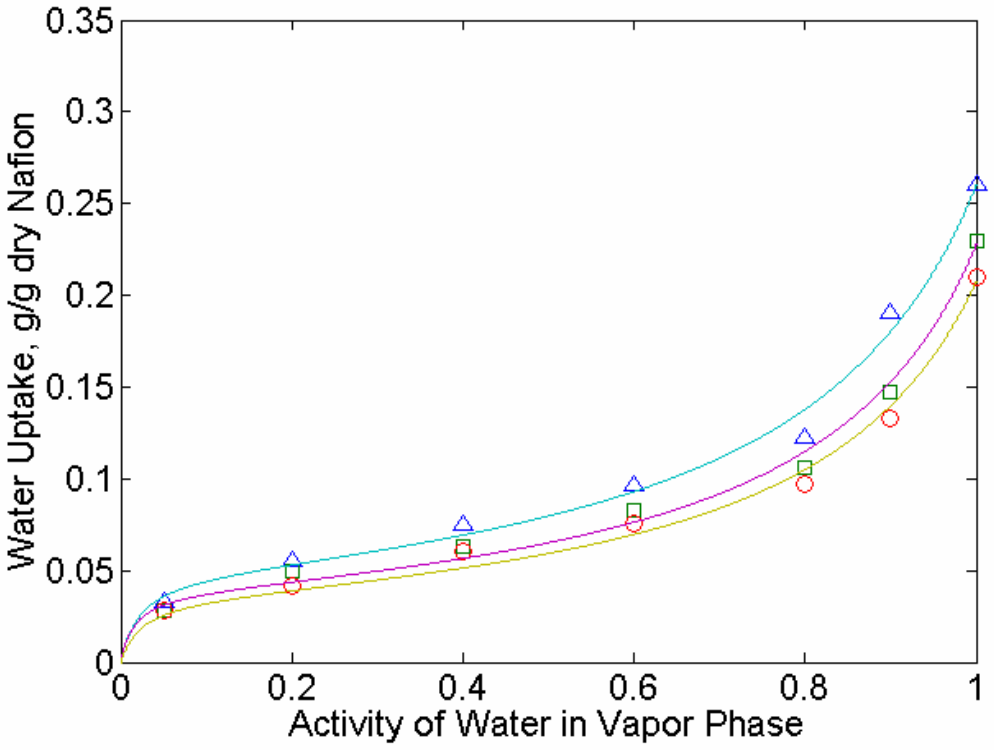

Figure 4-7. Effect of EW on water vapor sorption for different relative humidity conditions at room temperature (triangle: EW=960, square: EW=1100, and circle: EW=1200).

sorption amounts. The membrane becomes very soft at this low EW condition and may lose its integrity forming a gel solution.

In summary, the water uptake of PEMs increases with the activity of the functional group (K_1) up to certain extent, low Young's modulus of polymer elasticity (E), and low equivalent weight (*EW*) of polymer. Although high water uptake is desirable for high proton conductivity in general, too high a water uptake could lead to an overly swollen state and eventual destruction of the membrane. Therefore, an optimal level of water uptake is needed to maintain the stability of the membrane. This can be realized by the appropriate balance of the above properties.

4-5. Conclusions

An insightful sorption model has been proposed based on the thermodynamic analysis using the Flory-Huggins activity and Freger's elastic models. The model reflects the sorption equilibrium in PEMs satisfactorily and contains all the important design variables such as dissociation constant of acid groups, elasticity of polymer matrix, hydrophobicity of polymer surface, spatial distribution of acid groups, and polymer-solvent interaction parameter. For a given polymer system, the sorption amount per unit mass of dry polymer increases with high acid strength, low Young's modulus, and low EW. The thermodynamic sorption model developed here provides a theoretical framework of understanding swelling, sorption, and ion-exchange equilibrium in PEMs. The model also provides helpful design rationale for developing and comparing alternative PEMs for fuel cell applications.

References

1. P. Costamagna and S. Srinivasan, *J. Power Sources,* **102**, 242 (2001).
2. M. L. Perry and T. F. Fuller, *J. Electrochem. Soc.,* **149**, S59 (2002).
3. V. Mehta and J. S. Cooper, *J. Power Sources,* **114**, 32 (2003).
4. J. Roziere and D. J. Jones, *Annu. Rev. Mater. Res.*, **33**, 503 (2003).
5. G. Alberti and M. Casciola, *Annu. Rev. Mater. Res.*, **33**, 129 (2003).
6. M. Rikukawa and K. Sanui, *Prog. Polym. Sci.*, **25**, 1463 (2000).
7. Y. Sone, P. Ekdunge, and D. Simonsson, *J. Electroanal. Chem.,* **143**, 1254 (1996).
8. C. H. Wirguin, *J. Membr. Sci.*, **120**, 1 (1996).
9. T. D. Gierke, *152nd Meeting of the Electrochemical Society Extended Abstracts*, Atlanta, Ga., Abstract No. 438. (1977).
10. K. A. Mauritz, C. J. Hora, and A. J. Hopfinger, *Polym. Prep. Am. Chem. Soc. Div. Polym. Chem.*, **19**, 324 (1978).
11. H. L. Yeager and A. Steck, *J. Electrochem. Soc.*, **128**, 1880 (1981).
12. G. Gebel, *Polymer*, **41**, 5829 (2000).
13. H. G. Haubold, T. Vad, H. Jungbluth, and P. Hiller, *Electrochim. Acta,* **46**, 1559 (2001).
14. R. S. Mclean, M. Doyle, and B. B. Sauer, *Macromolecules,* **33**, 6541 (2000).
15. J. T. Hinatsu, M. Mizuhata, and H. Takenaka, *J. Electrochem. Soc.,* **141**, 1493 (1994).
16. C. M. Gates and J. Newman, *AIChE J*, **46**, 2076 (2000).
17. P. D. Beattie, F. P. Orfino, V. I. Basura, K. Zychowska, J. Ding, C. Chuy, J. Schmeisser, and S. Holdcroft, *J. Electroanal. Chem.*, **503**, 45 (2001).
18. M. Doyle, L. Wang, Z. Yang, and S. K. Choi, *J. Electrochem. Soc.,* **150**, D185 (2003).
19. A. Steck and H. L. Yeager, *Anal. Chem.,* **52**, 1215 (1980).
20. D. Nandan, H. Mohan, and R. M. Lyer, *J. Membr. Sci.*, **71**, 69 (1992).
21. T. A. Zawodzinski, T. E. Springer, J. Davey, R. Jestel, C. Lopez, J. Valerio, and S.

Gottesfeld, *J. Electrochem. Soc.,* **140**, 1981 (1993).

22. T. Thampan, S. Malhotra, H. Tang, and R. Datta, *J. Electrochem. Soc.,* **147**, 3242 (2000).
23. C. Tsonos, L. Apekis, and P. Pissis, *J. Mat. Sci.*, **35**, 5957 (2000).
24. P. Futerko and I. M. Hsing, *J. Electrochem. Soc.,* **146**, 2049 (1999).
25. P. Choi and R. Datta, *J. Electrochem. Soc.,* **150**, E601 (2003).
26. P. J. Flory, *Principles of Polymer Chemistry*, Cornell University Press, Ithaca, NY (1953).
27. J. W. Tester and M. Modell, *Thermodynamics and Its Applications* 3rd ed., Prentice-Hall Inc., Upper Saddle River, NJ (1997).
28. P. W. Atkins, *Physical Chemistry*, 3rd ed., W.H. Freeman and Company, NY (1986).
29. H. Helfferich, *Ion Exchange*, McGraw-Hill, NY (1962).
30. H. M. James and E. Guth, *J. Chem. Phys.*, **11**, 455 (1943).
31. G. M. Gusler and Y. Cohen, *Ind. Eng. Chem. Res.*, **33**, 2345 (1994).
32. M. Gottlieb and R. J. Gaylord, *Macromolecules*, **17**, 2024 (1984).
33. G. E. Boyd and B. A. Soldano, *Z. Elektrochem.,* **57**, 162 (1953).
34. H. P. Gregor, *J. Am. Chem. Soc.,* **73**, 642 (1951).
35. V. Freger, *Polymer*, **43**, 71 (2002).
36. E. A. Grulke, *Polymer Process Engineering*, Prentice-Hall, Inc., Englewood Cliff, NJ (1994).
37. J. O'M. Bockris and A. K. N. Reddy, *Modern Electrochemistry*, Plenum Press, NY (1970).
38. E. Glueckauf and G. P. Kitt, *Proc. Roy. Soc. London A,* **228**, 322 (1955).
39. R. B. Moore and C. R. Martin, *Anal. Chem.*, **58**, 2570 (1986).
40. J. E. Resoke and M. A. Barteu, *J. Phys. Chem. B*, **101,** 1113 (1997).
41. S. P. Mizar and R. J. Pryputniewicz, *Proc. IX Internat. Congress on Exp. Mech.,* The

Society for Experimental Mechanics, Bethel, CT, p. 1013 (2003).

42. R. W. Kopitzke, C. A. Linkous, H. R. Anderson, and G. L. Nelson, *J. Electrochem. Soc.,* **147**, 1677 (2000).
43. S. R. Lowry and K. A. Mauritz, *J. Am. Chem. Soc.,* **102**, 4665 (1980).
44. A. Vishnyakov and A. V. Neimark, *J. Phys. Chem. B,* **104**, 4471 (2000).
45. J. Divisek, M. Eikerling, V. Mazin, H. Schmitz, U. Stimming, and Yu. M. Volfkovich, *J. Electrochem. Soc.*, **145**, 2677 (1998).
46. V. Z. P. Stang and V. Zhdankin, in *Chemistry of Organic Fluorine Compounds II*, M. Hudlicky and A. E. Pavlath, Editors, p. 956, American Chemical Society, Washington, DC (1995).
47. B. E. Smart, in *Chemistry of Organic Fluorine Compounds II*, M. Hudlicky and A. E. Pavlath, Editors, p. 988, American Chemical Society, Washington, DC (1995).
48. C. Ma, L. Zhang, S. Mukerjee, D. Ofer, and B. Nair, *J. Membr. Sci.*, **219**, 123 (2003).
49. K. D. Kreuer, *J. Membr. Sci.*, **185**, 29 (2001).
50. T. A. Zawodzinski, S. Gottesfeld, S. Shoichet, and T. J. McCarthy, *J. Appl. Electrochem.,* **23**, 86 (1993).
51 T. A. Zawodzinski, M. Neeman, L. O. Shillerud, and S. Gottesfeld, *J. Phys. Chem.,* **95**, 6040 (1991).
52. D. R. Morris and X. Sun, *J. Appl. Polym. Sci.,* **50**, 1445 (1993).
53. K. K. Pushpa, D. Nandan, and R. M. Iyer, *J. Chem. Soc. Faraday Trans. I,* **84**, 2047 (1988).
54. D. Rivin, C. E. Kendrick, P. W. Goibson, and N. S. Schneider, *Polymer,* **42**, 623 (2001).

Chapter 5. Proton Diffusion Mechanisms and Conductivity in Nafion®

Abstract

A pore transport model is proposed to describe proton diffusion at various hydration levels within Nafion® by incorporating structural effect upon water uptake and various proton transport mechanisms, namely proton hopping on pore surface, Grotthuss diffusion in pore bulk, as well as ordinary mass diffusion of hydronium ions. The diffusion coefficients are obtained *a priori* based on a comprehensive random walk framework that connects the molecular details of proton transfer to the continuum diffusion coefficients. The proton conductivity in contact with water vapor is accurately predicted as a function of relative humidity without any fitted parameters. A maximum conductivity in contact with liquid water is predicted by the model for EW between 900 and 1000, in good agreement with the experimental measurements. The model is insightful and can be extended to other polymer electrolytes for fuel cell applications.

5-1. Introduction

The proton exchange membrane (PEM) plays a central role as the polymer electrolyte medium for the conduction of protons in PEM fuel cells. Due to the importance of facile proton transport on fuel cell performance, studies on the proton transport have been carried out not only for understanding the transport mechanism but also for designing new PEMs based on a fundamental appreciation. Nafion®, the most attractive polymer electrolyte developed so far, shows excellent proton conductivity but only soaked in water which is the medium for proton transport.[1,2] In chapters 3 and 4,[3] a thermodynamic model has been

provided a for sorption of water in PEM. Here, a related problem of proton diffusion in hydrated PEMs is considered.

The study of proton transport in aqueous solution has received considerable attention for over a century because of its paramount importance in chemical, biological, and electrochemical systems. In aqueous solutions of acids, the proton exists as hydronium ion, which is itself hydrated, *e.g.*, as $H_5O_2^+$, or $H_9O_4^+$.[4,5] The mobility of the proton is abnormally high as compared with other ions of a size similar to hydronium ion, and is explained in terms of contribution by the structural diffusion of protons, or the so-called Grotthuss mechanism, alternatively called the "relay" mechanism, in which the transport of protons is determined by the rate at which hydrogen bond between a hydronium ion and a water molecule forms rather than by the slower rate at which hydronium ions may migrate *en masse*, also called vehicular mechanism. The Grotthuss mechanism was proposed about two hundred years ago,[6] and later further developed by Huckel,[7] Bernal and Fowler,[8] Conway et al.,[9] and Agmon.[10] More recently, a number of molecular dynamic (MD) simulations have been proposed to model the transport properties of an excess proton in bulk phase water.[11-16]

The transport property of protons in PEMs is strongly dependent upon the structure and physicochemical nature of the materials, which in turn varies with the level of hydration. In spite of substantial effort to understand proton transport phenomena in PEMs based on a statistical mechanics,[17] phenomenological approaches,[18,19] and MD simulations[20-24], an accepted transport mechanism in PEMs has not been advanced yet due to their complex nanostructure and inhomogeneous nature when hydrated.

In this chapter, we present a theoretical conductivity model that provides a complete phenomenological picture of proton transfer in Nafion®. The model is based on the parallel pore model incorporating various proton transport mechanisms such as surface proton hopping, Grotthuss diffusion, and the traditional *en masse* diffusion. The analysis

here provides a theoretical framework for the general understanding of the proton transport in PEMs as well as helpful principles for designing new PEMs for fuel cell applications.

5-2. Experiments

Membrane preparation – Nafion® of equivalent weights (EWs) of 960 and 1100 were prepared by casting the Nafion® solution. After stirring for 8 hours at room temperature, the solution was cast on a glass dish utilizing a doctor blade. The cast membrane was heat treated in a convection oven at 100º C for 15 minutes, which was sufficient to produce a solid membrane. The fabricated membrane was removed from the glass dish, dried and then placed in a Teflon sleeve and annealed at 170º C at 10 tons for 15 minutes in a mechanical press. This processing step is necessary to produce pliant and insoluble PEMs with mechanical properties similar to those of the commercially available Nafion® films.

Proton conductivity measurements – A Nafion® sample was sandwiched between two Pt electrodes each on either side of the membrane to measure the conductivity and placed in a humidity controlled chamber. The humidity of the chamber was monitored utilizing a dewpoint/temperature probe (HMP 238, Vaisala, Woburn, MA). A dry nitrogen stream was saturated with water by passing it through a humidifier, which was then combined with a dry stream of nitrogen to control RH. The conductivity of the PEM was measured at 25º C from 0 % to 99 % RH. The conductivity measurements were made with a perturbation voltage of 10 mV in the frequency range 0.01 Hz to 10^6 Hz using a Solartron SI 1260 FRA (Solartron, Hampshire, U.K.). Both real and imaginary components of the impedance were measured and the real z axis intercept was closely approximated to provide an estimate of the membrane resistance, and hence, conductivity.

5-3. Theory

The proton conductivity in Nafion® is largely determined by the water content within the hydrophilic domains. At low water contents, not all acid sites are dissociated[25] and the contact between water molecules via hydrogen bonding is low, resulting in a low dielectric constant and thus low rate of proton transfer, which is limited to the surface region. At high water contents, however, the properties of water in Nafion® approach those of bulk water. Thus, two different water environments in Nafion® have usually been distinguished.[20,26,27] For example, the water in the middle of the pore is referred to as "bulk water" and the mobility of protons through this bulk water is fast. However, water near the pore surface along the array of SO_3^- groups is referred to as "surface water" and the proton mobility through this surface water is considerably smaller than that in the bulk due to the strong electrostatic attraction of SO_3^- groups. Thus, the measured effective proton conductivity of Nafion® is the result of weighted average of the surface and bulk conductivities depending upon the radial distribution of protons and water content in Nafion®.[26]

We assume that the transport of protons in Nafion® is carried out via *i*) surface diffusion mechanism occurring close to the pore wall or under low water activity, *i.e.*, in a layer of around 1 nm from the pore wall,[23,26] and *ii*) bulk diffusion mechanism prevailing in the central region of the pore or under high water activity condition.[20,27,28] In the bulk, proton diffusion is predominantly via the Grotthuss mechanism but the H_3O^+ ion also undergoes traditional mass diffusion,[16,20,28] *i.e.*, the so-called *en masse* diffusion. Figure 5-1 shows the various mechanisms along with an electrical analog. Thus, the proton conductivity in a pore σ_p can be written as

$$\sigma_p = \sigma_{H^+}^{\Sigma} + \sigma_{H^+}^{G} + \sigma_{H^+}^{E} \qquad [1]$$

where $\sigma_{H^+}^{\Sigma}$, $\sigma_{H^+}^{G}$, and $\sigma_{H^+}^{E}$ represent the contributions of proton conductivity from the surface, Grotthuss, and *en masse* diffusion mechanisms, respectively.

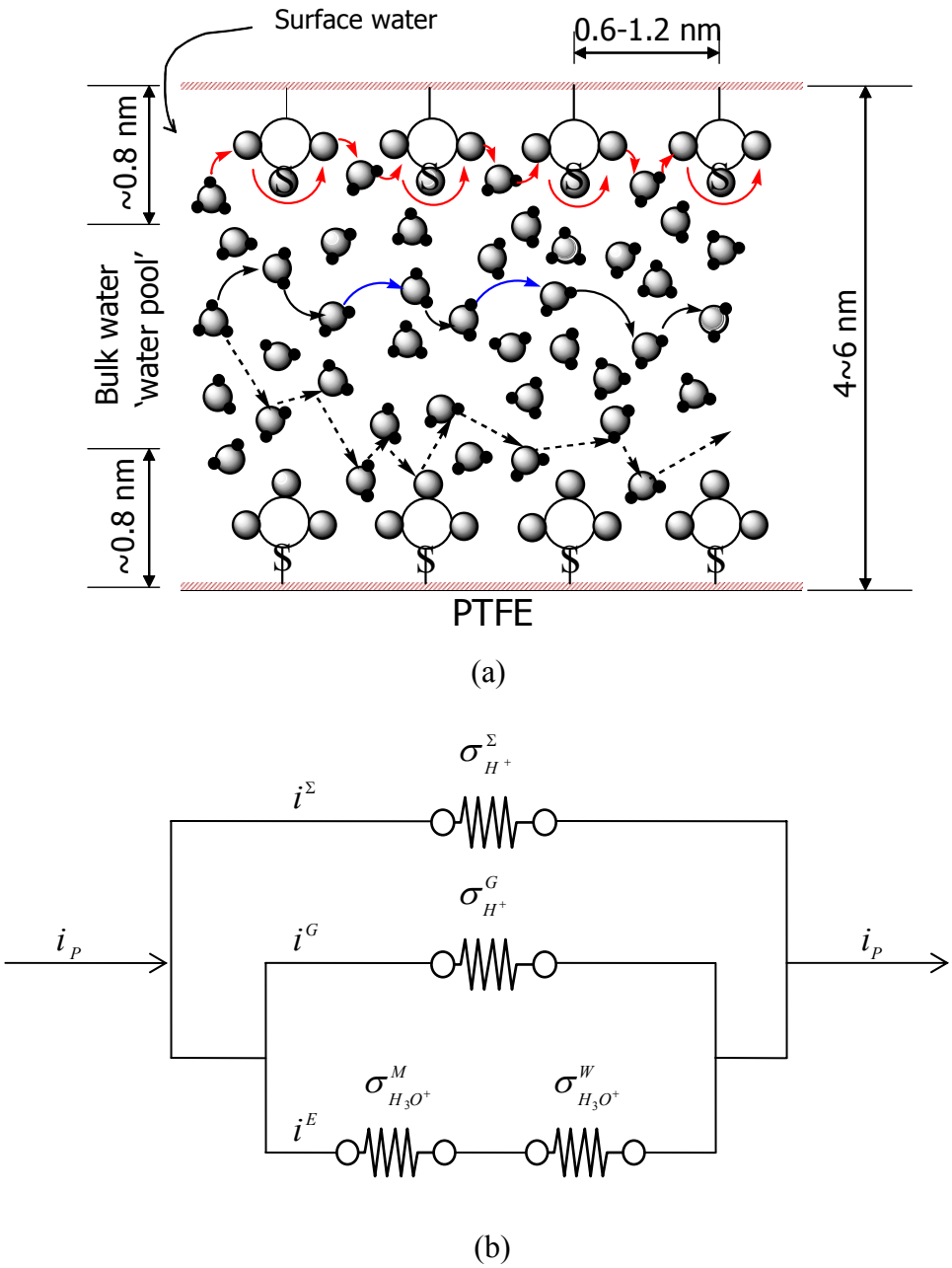

Figure 5-1. A simplified picture of structure and proton transfer in Nafion® in fully hydrated state (a), and electrical analog of the proton transport in Nafion® (b).

In turn, the conductivity of proton can be written using the Nernst-Einstein relation[29,30]

$$\sigma_{H^+}^{\alpha} = \frac{F^2}{RT} D_{H^+}^{\alpha} C_{H^+}^{\alpha} \quad [2]$$

where F is Faraday's constant, R is gas constant, T is temperature, $D_{H^+}^{\alpha}$ and $C_{H^+}^{\alpha}$ are the diffusion coefficient and the concentration of hydronium ions participating in the diffusion mechanism α, respectively.

For *en masse* diffusion, the diffusion coefficient can be written as[31]

$$\frac{1}{D_{H^+}^{E}} = \frac{x_w}{D_{H^+}^{W}} \left(1 + \frac{1 - x_w}{x_w} \frac{D_{H^+}^{W}}{D_{H^+}^{M}} \right) \quad [3]$$

where x_w is the mole fraction of water in the membrane phase, $D_{H^+}^{W}$ and $D_{H^+}^{M}$ are the Stefan-Maxwell diffusion coefficient of hydronium ion and bulk water in the pore, and hydronium ion and the polymer matrix M, respectively.[32] Since the water concentration in PEMs is high even at low activity, *e.g.*, $x_w = 0.67$ at $a_i = 0.1$, and quickly approaches to 1, Eq. 3 may be simplified to

$$\frac{1}{D_{H^+}^{E}} \approx \frac{1 + \delta}{D_{H^+}^{W}} \quad [4]$$

where $\delta \equiv (D_{H^+}^{W} / D_{H^+}^{M})[(1 - x_w) / x_w]$. Thus, the total proton conductivity in a pore within Nafion® can be written in terms of diffusion coefficients, concentrations, and the ratio δ

$$\sigma_p = \frac{F^2}{RT} \left[D_{H^+}^{\Sigma} C_{H^+}^{\Sigma} + D_{H^+}^{G} C_{H^+} + \frac{D_{H^+}^{W}}{1 + \delta} C_{H^+} \right] \quad [5]$$

where σ_P denotes proton conductivity within a pore in PEM.

Next, considering the tortuous nature of the pore and the reduced cross-sectional area available for proton transport, a parallel pore model[33,34] is utilized. The effective diffusion coefficient for the membrane is thus obtained by multiplying the diffusion coefficient for

single pore by ε_i / τ, where $\varepsilon_i = \lambda_i /(\lambda_i + r)$, λ_i is the moles of water sorbed per acid site, r is the ratio of partial molar volume of membrane to that of water,[3] and τ is the tortuosity factor[35] Then, the overall membrane conductivity σ_{H^+} is

$$\sigma_{H^+} = \frac{\varepsilon_i}{\tau}\left[\frac{F^2}{RT}\left(D^{\Sigma}_{H^+}C^{\Sigma}_{H^+} + D^{G}_{H^+}C_{H^+} + \frac{D^{W}_{H^+}}{1+\delta}C_{H^+}\right)\right] \quad [6]$$

The tortuosity factor τ varies with the water content ε_i in Nafion®. The total conductivity thus, depends directly upon the structural characteristics represented by δ and τ, as well as the distribution of proton concentration between the surface and the bulk regions within the membrane, *i.e.*, $C^{\Sigma}_{H^+}$ and C_{H^+}, respectively, which in turn are determined by the acid strength of the functional groups and the water content. The sorption of water and the resulting dissociation of acid groups are considered in chapter 3 and 4.[3]

Parameter Identification

As per the random-walk view of diffusion, the diffusion coefficient of proton is given by Einstein-Smoluchowski equation[36,37]

$$D_{H^+} = \frac{l^2}{\kappa\tau_D} \quad [7]$$

where κ is a constant dependent upon the dimensionality of random-walk (κ = 2, 4 or 6 for a one-, two-, or three-dimensional walk, respectively), l is the mean step distance, and τ_D is the mean time between successive steps. The use of Eq. 7 does not necessarily mean protons transfer via "hopping" mechanism.[36] In fact, we will apply this viewpoint to obtain diffusion coefficient for all three mechanisms of proton conduction in Nafion®, namely, surface, Grotthuss, and *en masse* diffusions.

Surface Diffusion Coefficient

Figure 5-2 shows a schematic representation of the "surface" hopping of a proton by means of a series of hops between adjacent sulfonic acid sites. Since the distance between the ionic groups is too large (0.6-1.2 nm) for the proton to step directly from one SO_3^- to the next, it must hop via intermediate water molecules,[19,23] representing the distance l_Σ. In order for this to occur, the proton should possess adequate energy to surmount the energy of activation resulting from the electrostatic attraction between the sulfonic ion SO_3^- and the hydronium ion H_3O^+. It is assumed that this is the rate-determining step due to strong interaction of ionic groups.[28] Any additional hops to other water molecules before reaching the next sulfonic acid group are rapid.

For the two dimensional surface diffusion, $\kappa_\Sigma = 4$, and the τ_D^Σ can be written as

$$\tau_D^\Sigma = \nu_0^{-1} \exp\left(\frac{\Delta G_\Sigma^{e,0}}{k_B T}\right) \qquad [8]$$

where ν_0 is the thermal frequency, $\nu_0 = k_B T / h$, k_B is the Boltzmann constant, h is the Planck constant, and $\Delta G_\Sigma^{e,0}$ is the effective Gibbs free energy of activation for surface diffusion. The activation energy may include conformational fluctuation of potential barrier and the control of optimum conformation of the molecules participating in the proton transport near the surface of Nafion®.[2] We assume here that the Coulombic interaction energy between the negatively charged fixed sulfonic ion and the positively charged hydronium ion represents the mean energy barrier for the proton step from a hydronium ion to the next water molecule. Thus, the activation barrier for the first step of a proton from the hydronium ion, which is closest to fixed sulfonic acid, to a next water molecule is the Coulombic energy between the fixed sulfonic ion and the positively charged hydronium ion minus the Coulombic energy between the sulfonic ion and the hydronium ion just formed after receiving a proton from the hydronium ion closest to the

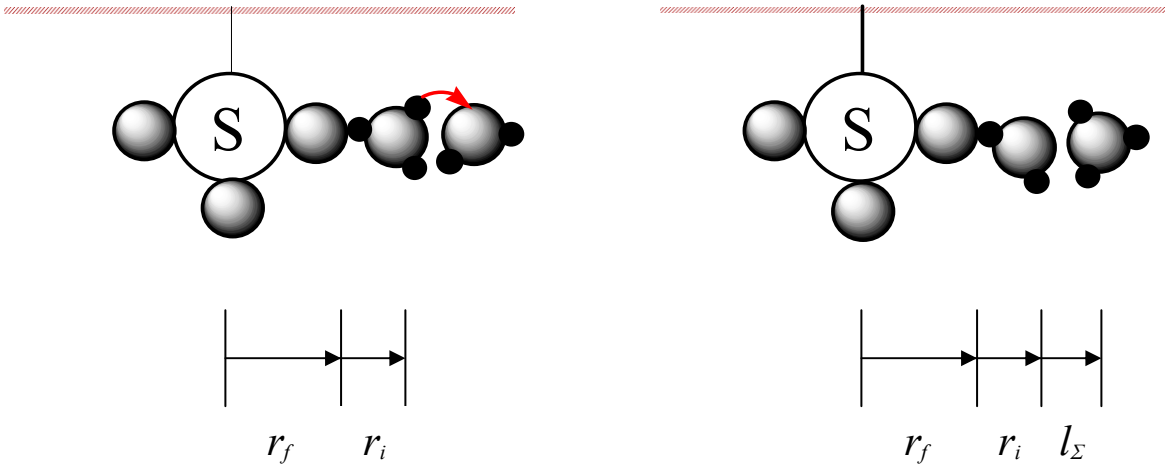

Figure 5-2. A schematic representation of the first proton hopping at the surface of Nafion® (a: before and b: after the first jump).

sulfonic acid groups. Thus, the surface activation energy for the p^{th} hop in a series of p = *1,2,3,..n* proton steps starting from the hydronium ion adjacent to the fixed anion can be written as[27]

$$\Delta G_{e,0}^{\Sigma} = -\frac{(q_{e^-})^2}{4\pi\varepsilon_0\varepsilon_r}\left[\frac{1}{R_f + R_i + pl_{\Sigma}} - \frac{1}{R_f + R_i + (p-1)l_{\Sigma}}\right] \quad [9]$$

where ε_0 is the permittivity of free space, ε_r is the relative permittivity of the medium, q_{e^-} is the electrostatic charge, R_f is the effective radius of fixed anion groups, and R_i is the radius of the hydronium ion. Since the Coulombic interaction energy decreases quickly with the distance from the fixed anion site, and the dielectric constant of water is quite low in the surface layer, the first step is considered to be rate-determining for the overall surface proton hopping. Thus, $\Delta G_{\Sigma}^{e,0}$ represents the effective energy barrier for surface diffusion

$$\Delta G_{e,0}^{\Sigma} \approx \frac{(q_{e^-})^2}{4\pi\varepsilon_0\varepsilon_r}\left[\frac{l_{\Sigma}}{(R_f + R_i + l_{\Sigma})(R_f + R_i)}\right] \quad [10]$$

It must be mentioned that this analysis is simplified, since in reality, the Coulombic interaction of adjacent sulfonic acid groups must also be taken into account. In fact, that makes the Coulombic barrier sinusoidal.[2] Since beyond the midway point between two adjacent sites, there would be an attraction to the next site. Nonetheless, this does not invalidate the assumption that the first hop is the rate-determining step and successive hops between two neighboring sites become easier.

The radius of a hydronium ion R_i is taken as 0.143 nm based on the radius of water molecule R_{H_2O} = 0.143-0.144 nm[38,39] while the O-O distance between water molecules d_{OO} = 0.275-0.294 nm.[40-42] The radius of the fixed sulfonic acid R_f is 0.244-0.266 nm[24] accounting for the bond length of S-O in sulfonic acid R_{SO} = 0.144-0.146 nm[30,36,43] and the

radius of negatively charged oxygen being about 0.10-0.12 nm.[31,44,45] The distance between two oxygen atoms in both the Zundal ($H_5O_2^+$) and Eigen form ($H_9O_3^+$) is shorter, *i.e.*, 0.24-0.28 nm, than the O-O distance between water molecules as reported by molecular dynamic simulations.[46-50] The hopping length l_Σ corresponds to the O-O distance in the proton hydrated forms and thus, l_Σ is taken as 0.255 nm.[51] The dielectric constant of water in ionic solutions varies with the distance from the ions present in the solution[52-54] and ε_r = 6 has been used[28] for water in contact with an ion (or for water in the primary hydration sheath of an ion). Combining Eq. 8 and 10 with Eq. 7 provides the surface diffusion coefficient for proton hopping in Nafion®. Taking R_f = 0.254 nm, R_i = 0.143 nm, ε_r = 6, and l_Σ = 0.255 nm gives the surface diffusion coefficient $D_{H^+}^{\Sigma}$ = 1.01 x 10^{-7} cm^2/s at room temperature. This is in agreement well with a previous result[20] for high activation energy of the surface diffusion process.

Grotthuss Diffusion Coefficient

In order to obtain diffusion coefficient for Grotthuss mechanism, it is assumed that the reorientation of proton accepting water molecule is the rate-determining step in agreement with the literature.[9-13] This includes hydrogen-bond cleavage between the proton accepting water molecule and a nearby water molecule, and reorientation of the proton accepting molecule towards the hydronium ion to be in a receptive position. The proton transport itself following this rearrangement step is rapid. Agmon[10] and recent MD simulations[11-13] also supports this as the rate-determining for the structural proton transport mechanism in water.

Figure 5-3 shows a schematic of the reorientation process due to the interaction between a charged ion (hydronium ion) and water as a dipole. Assuming that the excess charge is

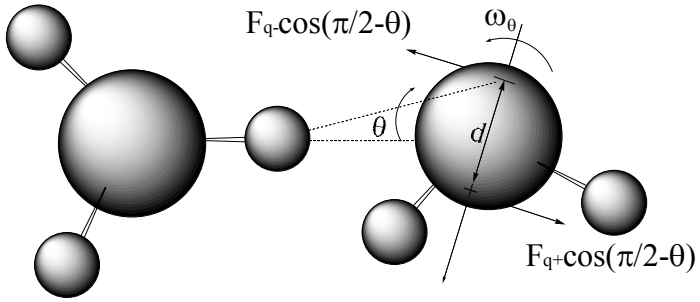

Figure 5-3. The hydrodynamic model of Grotthuss diffusion mechanism of protons in the pore bulk.

centered on the proton just prior to its transfer, the torque on the dipole at an orientation angle θ that tends to rotate the water molecule towards the hydronium ion is

$$T_\theta \approx -\frac{1}{4\pi\varepsilon_r\varepsilon_0}\frac{\mu_w(z_{H^+}q_{e^-})}{\delta^2}\sin\theta \qquad [11]$$

where z_{H^+} is the charge number of ion, q_{e^-} the electronic charge, μ_w is the dipole moment of water, and δ is the distance between the proton in hydronium ion and proton accepting water molecule. This, of course, varies with θ and a maximum torque is obtained for $\theta = \pi/2$

$$T_{\max} = \frac{1}{4\pi\varepsilon_r\varepsilon_0}\frac{\mu_w(z_{H^+}q_{e^-})}{\delta^2} \qquad [12]$$

From the hydrodynamics on the other hand, for a sphere of radius R_w rotating at an angular velocity ω_θ in a continuum fluid of viscosity η, the torque needed to maintain the rotation[35,55]

$$T_\theta = \zeta_{rot}\omega_\theta \qquad [13]$$

where $\zeta_{rot} = 8\pi\eta R_w^3$ represents the rotational friction. The application of this to the rotation of a water molecule tacitly assumes that the viscosity of a fluid includes the effect of intermolecular forces such as hydrogen bonding among water molecules. Equating Eq. 11 with 13 and using Eq. 12 gives

$$\omega_\theta = -\frac{T_{\max}}{\zeta_{rot}}\sin\theta \qquad [14]$$

Thus, the angular velocity ω_θ is a function of angle between the dipole moment vector and the ion. In order to calculate the time for the arrangement τ_D^G from an initial θ, θ_I, to a final θ, θ_F, where proton transfer can occur, we assume pseudo-steady state

$$\tau_D^G = \int_{\theta_I}^{\theta_F} \frac{d\theta}{\omega_\theta} \quad [15]$$

Substituting Eq. 14 into 15 for ω_θ

$$\tau_D^G = \tau_c \int_{\theta_F}^{\theta_I} \frac{d\theta}{\sin\theta} \quad [16]$$

where the characteristic time constant $\tau_c \equiv \zeta_{rot} / T_{\max}$, *i.e.*,

$$\tau_c = \frac{32\pi^2 \eta \varepsilon_0 \varepsilon_r R_w^3 \delta^2}{\mu_W (z_{H^+} q_{e^-})} \quad [17]$$

Integration of Eq. 16 provides the time for rotation as

$$\tau_D^G = \tau_c \ln\left[\frac{\tan(\theta_I / 2)}{\tan(\theta_F / 2)}\right] \quad [18]$$

Thus, the proton hopping time for Grotthuss diffusion may be calculated *a priori* from Eq. 18 with parameters η, ε_r, R_w, δ, μ_w, θ_I and θ_F. The hydrodynamic radius of the water molecule is taken as R_w = 0.141 nm, and the distance of the proton of the hydronium ion and the water molecule is taken as δ = 0.143 nm. The dipole moment of liquid water μ_W is typically[56-58] 2.4 - 3.0 D (1 D = 3.336 x 10^{-39} C m) and is taken as μ_W = 2.95 D based on the recent calculations.[59,60] According to CBL (Conway, Bockris, and Linton) theory,[9,61,62] the average angle of rotation required for the proton accepting water molecule to rotate through for the favorable position is 105-111º. As shown in Figure 5-3, the average initial angle of one of the sp^3 orbitals on oxygen is taken as 120º, or $\theta_I = 2\pi/3$.[9] Then, the final angle required for the proton transfer is θ_F = 9-15º, *i.e.*, $\theta_F = \pi/20$-$\pi/12$.[9] Assuming this rearrangement of the proton accepting water molecule as the rate-determining step, the mean time for arrangement τ_D^G corresponds to the mean hopping time for Grotthuss

diffusion. This hopping time is not the same[63,64] as the dielectric relaxation time, which is related to molecular rotation characteristic time.

Thus, $\kappa_G = 6$ in Eq. 7 for the three-dimensional Grotthuss diffusion, and τ_D^G given by Eq. 18, the diffusion coefficient for Grotthuss mechanism $D_{H^+}^G$ can be calculated with the parameters described above. Figure 5-4 shows the Grotthuss hopping time τ_D^G for the variation of the angles suggested by Conway et al.[9,61] The calculated hopping time τ_D^G at room temperature is in the range of 1.40-1.68 ps, which agrees very well with around 1.5 ps obtained from NMR line narrowing measurement.[65,66] Thus, the Grotthuss diffusion coefficient of $D_{H^+}^G \approx 7 \times 10^{-5}$cm^2/s is obtained for 107-108º rotation angle of the proton accepting water molecule for $l_G = 0.255$ nm, which is the distance between O-O of proton hydrated molecule. Although this model is rather simple, it captures the essence of the phenomenon and provides insights into the Grotthuss diffusion mechanism, and predicts a very reasonable value for the Grotthuss diffusion coefficient of proton transport in the bulk water. This theoretical framework may be further improved by accounting other interaction forces such as attractive and repulsive interaction by Lennard-Jones model,[31,36] electrostatic charge distributions among hydrogen atoms in the hydronium ion, and the quadruple nature of water molecule, etc.

En Masse Diffusion

The *en masse* diffusion coefficient of hydronium ion may be calculated by Stokes-Einstein equation considering hydronium ion as a diffusing entity in the medium of water

$$D_{H^+}^W = \frac{k_B T}{6\pi\eta R_i} \qquad [19]$$

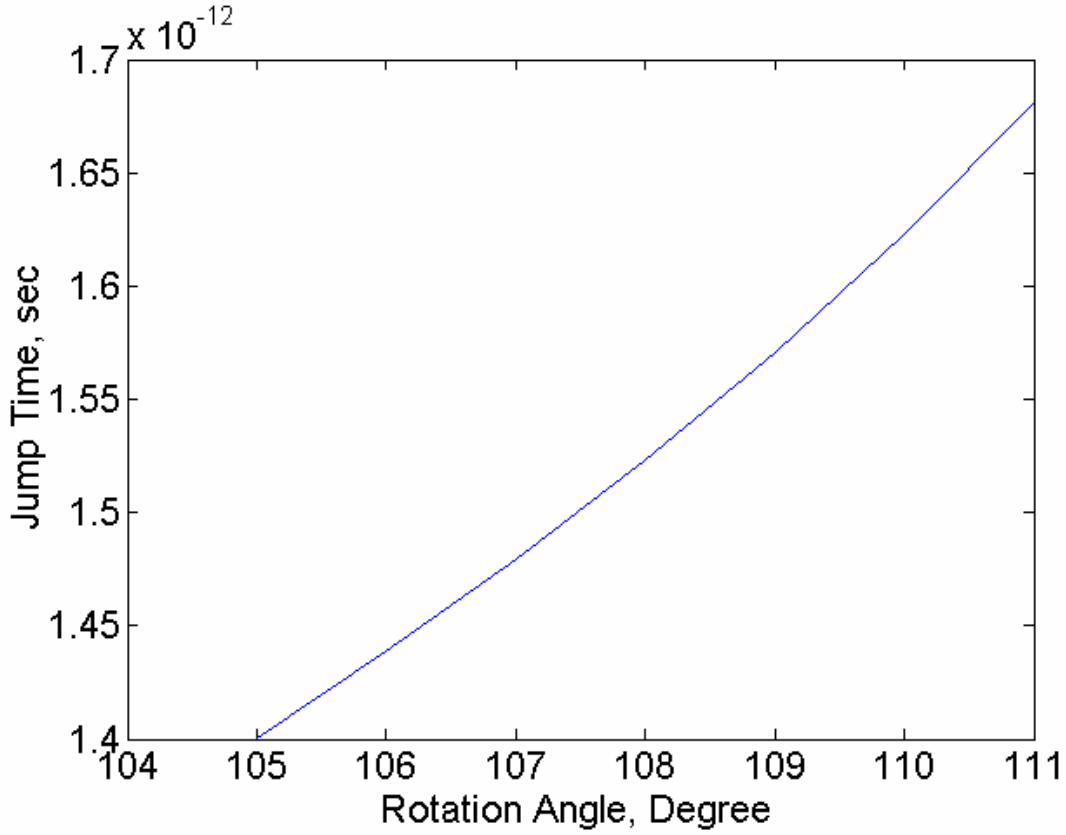

Figure 5-4. The Grotthuss hopping time for the variations of rotation angle of the proton accepting water molecule.

where η is the viscosity of the medium and R_i is the radius of hydronium ion. In the light of Einstein-Smoluchowski equation, the mean step time τ_D^E for three-dimensional *en masse* diffusion can be written as[38,68]

$$\tau_D^E = \frac{\pi \eta R_i l_E^2}{k_B T} \qquad [20]$$

where l_E is the mean step length for the *en masse* diffusion. Since the hydronium ion moves as a whole the mean step length is taken as l_E = 0.28 nm, the O-O distance between two water molecules. Thus, the mean step time τ_D^E = 7.63 ps is obtained for the *en masse* diffusion of hydronium ion from the Eq. 20. This means that the hydronium ion as a diffusing entity moves 0.28 nm in three-dimension from the previous position in 7.63 ps.[68] Substitution of κ_E = 6, τ_D^E = 7.63 ps, and l_E = 0.28 nm in Eq. 7 gives the diffusion coefficient for *en masse* diffusion $D_{H^+}^W$ = 1.71 x 10^{-5} cm^2/s, certainly a reasonable value. However, there are two uncertainties here. First, the radius R_i of the diffusing entity, since it is unlikely to be simply a hydronium ion without any associated water. Secondly, Stokes-Einstein equation is known to give only an approximation of the diffusion coefficient for molecular species. Thus, the diffusion coefficient for *en masse* diffusion may be approximated here by simply the self-diffusion coefficient of water which has been reported as 2.26-2.3 x 10^{-5} cm^2/s.[36,67]

When the Grotthuss diffusion of the proton is added to the *en masse* diffusion of hydronium ion, the absolute value of the proton diffusion coefficient in aqueous solution can be obtained. In fact, the diffusion coefficient of protons at the room temperature in water is known to be 9.31 x 10^{-5} cm^2/s.[36] Hence, we take the diffusion coefficient for *en masse* diffusion $D_{H^+}^W$ = 2.26 x 10^{-5} cm^2/s, which provides the mean step time of 5.78 ps for the mean step length l_E = 0.28 nm for hydronium ions.

Table 5-1 summarizes the mean step time and mean step distance for the surface, Grotthuss, and *en masse* diffusion mechanisms within the framework of the Einstein-Smoluchowski relation. The mean step time, defined here as the time for movement through roughly one molecular distance for the corresponding mechanisms, is smallest for the Grotthuss mechanism, indicating the Grotthuss diffusion is the fastest proton transport mechanism within Nafion®. The *en masse* diffusion is slower than the Grotthuss mechanism as shown by the higher mean step time. The mean step time for the surface diffusion is much higher than that of the other two mechanisms and thus, the surface diffusion does not contribute much to the overall conductivity of protons except at low water levels. This also indicates the proton conductivity is quite low at low water content in which protons transfer mostly via the surface diffusion mechanism.

The Diffusion Coefficient Ratio, δ

An alternative interpretation of the Einstein-Smoluchowski relation is to define l/τ_D as a mean velocity of hydronium ion between successive collisions. Then from Eq. 7

$$D_{H^+}^W = \frac{1}{\kappa} l_E \bar{v}_i \qquad [21]$$

where $\bar{v}_i$ is the mean speed of hydronium ions and l_E may be viewed as the mean free path between successive collisions. This is the same vein as the expression derived from the kinetic theory.[36,71]

Based on the analogy, the parameter δ may be estimated as follows. Using $x_w \approx \lambda_i/(\lambda_i + 1)$ in Eq. 4, δ may be rewritten as

$$\delta = \frac{1}{\lambda_i} \frac{D_{H^+}^W}{D_{H^+}^M} \qquad [22]$$

Table 5-1. The mean step time and distance of the three diffusion mechanisms in Einstein-Smoluchowski equation.

	Surface Diffusion	Grotthuss Diffusion	*En masse* Diffusion
Step Time, τ_D	1.61×10^{-9} sec	1.5×10^{-12} sec	5.78×10^{-12} sec
Step Distance, l	0.255 nm	0.255 nm	0.28 nm

Thus, the parameter δ can be interpreted as the ratio of Stefan-Maxwell diffusion coefficients, $D_{H^+}^W$ and $D_{H^+}^M$. Applying the expressions from elementary kinetic theory,[36,71] for the parameter l_E and $\bar{v}_i$ to Eq. 21 and substituting the results into Eq. 22

$$\delta = \frac{1}{\lambda_i}\left(\frac{d_{H^+M}}{d_{H^+W}}\right)^2\left(\frac{m^*_{H^+M}}{m^*_{H^+W}}\right)^{1/2} \qquad [23]$$

where d_{ij} is the distance between the centers of the spheres i and j when the collision occurs, and m^*_{ij} represents the reduced molecular mass of i and j, $1/m^*_{ij} = 1/m_i + 1/m_j$.[36,71] Since $m_{H_3O^+} \approx m_W$ and $m_M >> m_W$, the reduced molecular mass is $1/m^*_{H^+W} = 1/m_{H_3O^+} + 1/m_W \approx 2/m_W$ and $1/m^*_{H^+M} = 1/m_{H_3O^+} + 1/m_M \approx 1/m_W$. Substitution of this into Eq. 23 and use of $d_{H^+M}/d_{H^+W} \approx (\overline{V}_M/\overline{V}_{H_3O^+})^{1/3} \approx (\overline{V}_M/\overline{V}_{H_2O})^{1/3}$ gives

$$\delta = \frac{\sqrt{2}}{\lambda_i}(r)^{2/3} \qquad [24]$$

where r is the ratio of partial molar volume of Nafion® to that of water. Thus, the ratio δ depends upon the EW and water content in Nafion®.

Distribution of Protons between the Surface and Bulk Regions

Some of the dissociated protons remain close to the anion surface sites and participate in surface diffusion, whereas others with a higher degree of hydration breakaway into the pore bulk and participate in bulk diffusion comprising of Grotthuss and *en masse* mechanisms. The hydronium layer near the sulfonic ion SO_3^- is much like the inner Helmholtz layer, in which the water and hydronium ions are bound tightly to the fixed anion groups. The concentration of protons in this layer may thus be obtained by the

electrical diffuse double layer approach,[72] in which, for instance, the hydronium ions within 1 nm from the surface may be regarded as surface protons.

Here, we follow an alternative approach in which dissociated acid sites with up to two water molecules are assumed to remain close to the surface and designated as surface water, while those with more than two water molecules move away from the surface to the pore bulk. This is based on the hypothesis that sulfonic acid groups are sufficiently strong acids so that ion pairs $SO_3^-H_3O^+$ or $SO_3^-H_5O_2^+$ are formed rather than undissociated sulfonic acid groups.[2] The balance of acid site gives

$$\theta_0 + \theta_1 + \theta_2 + \theta_3 .... = \theta_0 + \theta_1 + \theta_2 + \theta_{>2} = 1 \qquad [25]$$

where θ_j denotes the fraction of acid sites with *j* bound water molecules. Using $\theta_j = K_j \theta_{j-1} a_i = \prod_{\rho=1}^{j} K_\rho \, \theta_0 a_i^j$ in Eq. 25 provides

$$\theta_0 = \frac{1}{1 + \sum_{j=1}^{\nu} \left(\prod_{\rho=1}^{j} K_\rho \right) (a_i)^j} \qquad [26]$$

Since $K_1 > K_2$ and taking $K_j = 1$ for $j > 2$, Eq. 26 reduces to

$$\theta_0 \approx \frac{1 - a_i}{(1 - a_i)(1 + K_1 a_i) + K_1 K_2 a_i^2 \left(1 - a_i^{\nu-1}\right)} \qquad [27]$$

Applying $\theta_1 = K_1 a_i \theta_0$, $\theta_2 = K_1 K_2 a_i^2 \theta_0$, $\theta_{>2} = 1 - \theta_0 - \theta_1 - \theta_2$, and $C_{H^+,0} = 1/(\lambda_i \overline{V}_i)$, the concentration of surface protons $C_{H^+}^{\Sigma} \approx C_{H^+,0}(\theta_1 + \theta_2)$ is, thus

$$C_{H^+}^{\Sigma} = \frac{1}{\lambda_i \overline{V}_i} \frac{K_1 a_i (1 - a_i)(1 + K_2 a_i)}{(1 - a_i)(1 + K_1 a_i) + K_1 K_2 a_i^2 \left(1 - a_i^{\nu-1}\right)} \qquad [28]$$

while that of bulk protons $C_{H^+} \approx C_{H^+,0} \theta_{>2}$ is

$$C_{H^+} = \frac{1}{\lambda_i \overline{V}_i} \frac{K_1 K_2 a_i^3 \left(1 - a_i^{\nu-2}\right)}{(1 - a_i)(1 + K_1 a_i) + K_1 K_2 a_i^2 \left(1 - a_i^{\nu-1}\right)} \qquad [29]$$

The equilibrium constants K_1 and K_2 are taken as 1000 and 200, respectively based on the dissociation constant of sulfonic acid[73,74] and the proton affinity data.[75] It is evident that the surface proton concentration is high at low water content and then decreases as the water content increases for a given EW, while the bulk concentration increases monotonically with water content.

Tortuosity Factor

The tortuosity of Nafion® depends upon the porosity ε_i or volume fraction of water. Several expressions for tortuosity have been proposed for porous media and membranes. Thus, tortuosity models have been developed based on the statistical analysis of diffusion coefficients,[76] free volume theory,[77] and power series expansion[78] etc. These models provide similar values of tortuosity factor for Nafion® for the sorption range of interest. Here, we adopt Preger's model,[76] which has been previously used[78] for Nafion®

$$\tau = \frac{2(1-\varepsilon_i) + 2\varepsilon_i \ln \varepsilon_i - 0.5\varepsilon_i (\ln \varepsilon_i)^2}{\varepsilon_i (1-\varepsilon_i) + \varepsilon_i^2 \ln \varepsilon_i} \qquad [30]$$

Thus, the tortuosity τ depends on the water content ε_i, which in turn varies with activity and EW.

5-4. Simulations

Figure 5-5 shows the conductivity data[79, 80] of Nafion® (EW=1100) at room temperature as a function of activity of water vapor along with the model predictions from Eq. 6 with the parameters shown in Table 5-2. Thus, the total proton conductivity in Nafion® is the result of three contributions: *i*) $\sigma_{H^+}^{\Sigma}$, surface conductivity via proton hopping, *ii*) $\sigma_{H^+}^{G}$, bulk conductivity via Grotthuss diffusion, and *iii*) $\sigma_{H^+}^{E}$, bulk conductivity via *en masse* diffusion. Except for very low activity of water vapor, the

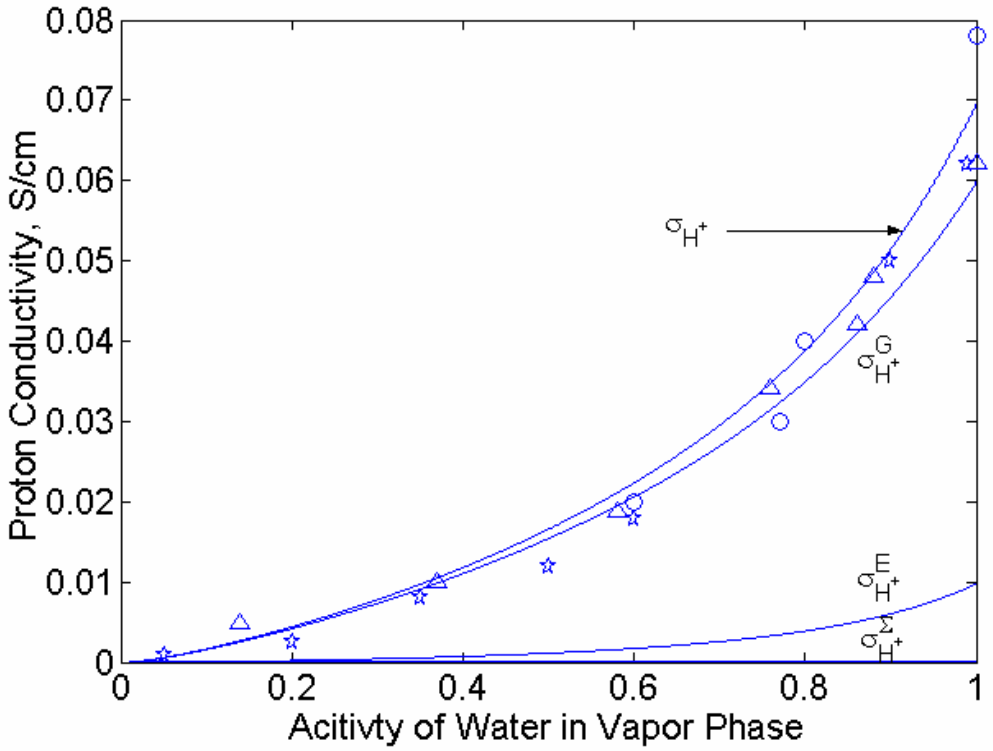

Figure 5-5. Proton conductivity of Nafion® of EW = 1100 (circle: ref. 79, triangle: ref. 80, star: this work, and solid line: model predictions).

Table 5-2. Parameter values employed in the model for proton conductivity in Nafion® at room temperature.

Parameter	Value or Eq.	Unit	Comment
$C_{H^+}^{\Sigma}$	Eq. 28	mol/cm^3	surface concentration of protons
C_{H^+}	Eq. 29	mol/cm^3	concentration of protons in the pore bulk
τ	Eq. 30	dimensionless	tortuosity of Nafion®
$D_{H^+}^{\Sigma}$	1.01 x 10^{-7}	cm^2/s	surface diffusion coefficient of proton
$D_{H^+}^{G}$	7.05 x 10^{-5}	cm^2/s	Grotthuss diffusion coefficient of proton
$D_{H^+}^{W}$	2.26 x 10^{-5}	cm^2/s	*en masse* diffusion coefficient of proton

Grotthuss diffusion in the bulk is the dominant contributor to the total conductivity. At very low activity the surface fraction of the water is dominant, *i.e.*, more than 90 % of water is surface water at a_i = 0.1 and thus, the total proton conductivity is quite low but not zero as assumed in percolation models, due to the high activation barrier for hopping of surface protons. It is noteworthy that the predictions in Figure 5-5 involve no fitted parameters.

Figure 5-6 compares the conductivity data of EW = 960 with the model. For EW = 960, the proton conductivity is increased compared with EW = 1100 at the same activity conditions because volume fraction of water is increased while the tortuosity decreases accordingly, which facilitate the proton transfer through the pore. Similar to EW = 1100, the Grotthuss diffusion controls the total conductivity of protons in Nafion®. The effect of EW of PEMs is explored by comparing the proton conductivity predicted by the model with the experiment for liquid water for Nafion® of EW in the range of 800-1200. Table 5-3 shows the proton conductivity of Nafion® swollen in liquid water at room temperature predicted by the model along with the experimental results by Doyle et al.[81,82] It is remarkable that the model estimates the proton conductivity very well over the range of EW. The maximum conductivity of Nafion® predicted by the model is for EW in between 900 and 1000, which is exactly the range obtained in experimental measurements. For EW less than 900, the proton conductivity decreases because the dilution effect of protons at very low EW overwhelms the increase due to increase of water volume fraction and decrease in tortuosity.

In summary, the proton conductivity depends on the porosity ε_i, tortuosity τ, proton concentrations in the surface $C_{H^+}^{\Sigma}$ and bulk C_{H^+}, diffusion coefficients for the surface $D_{H^+}^{\Sigma}$, Grotthuss $D_{H^+}^{G}$, and the *en masse* mechanisms $D_{H^+}^{W}$, and the ratio δ. These are the basic design variables that need to be optimized for developing alternative high proton-

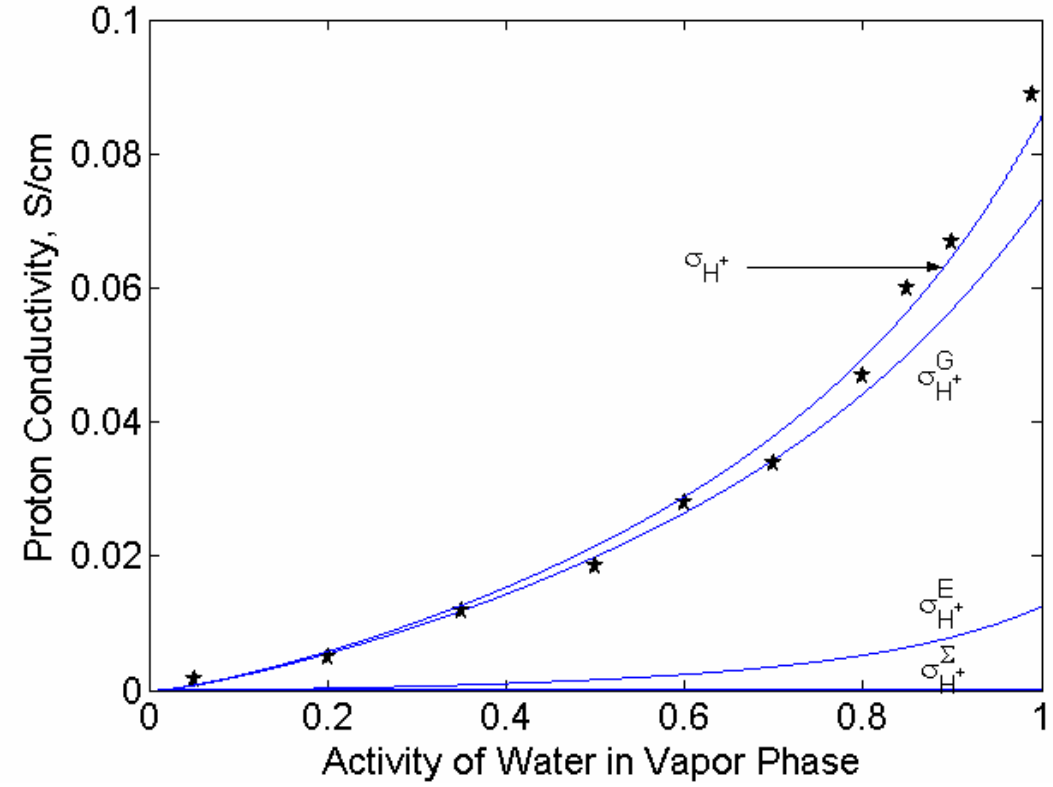

Figure 5-6. Comparison of proton conductivity data of Nafion® of EW = 960 with the model.

Table 5-3. Comparison of the theoretical and experimental values of proton conductivity for various EWs of Nafion®.

Equivalent Weight (EW)	Conductivity (S/cm) Theory	Experiment	Deviation from Theory (S/cm)	Tortuosity
800	0.091	0.093	2.0×10^{-3}	1.30
900	0.115	0.116	1.0×10^{-3}	2.29
1000	0.100	0.114	1.4×10^{-2}	2.63
1100	0.086	0.090	4.0×10^{-3}	2.98
1200	0.068	0.065	3.0×10^{-3}	3.85

conducting polymers for fuel cell applications. In general, it is desirable to have PEMs that can sorb more water at a given activity due to the water-assisted transport mechanisms, but only up to a certain point until dilution effect on the proton concentration becomes significant. For a given PEM system, the membrane becomes more porous and less tortuous when it sorbs large amounts of water, which in turn increase the conductivity of protons in the membranes. The distribution of protons between the surface $C_{H^+}^{\Sigma}$ and the pore bulk C_{H^+} depends upon the acid strength of the functional groups. Since the Grotthuss diffusion in the pore bulk is the major contributor to the total conductivity, the formation of high fraction of bulk hydronium ions is needed for the fast transfer of protons through the membrane. The high water uptake or enhanced swelling can increase the bulk water but, as mentioned above, too high a water uptake leads to a dilution of proton concentration and even a membrane failure in an operating fuel cell. Especially for methanol fuel cell application, high water uptake and swelling is not desirable due to the well known methanol crossover problem.

5-5. Conclusions

A comprehensive proton transport model has been proposed based on the understanding of various transport mechanisms in PEMs, such as surface hopping, Grotthuss diffusion, and *en masse* diffusion mechanisms. The proton conductivity of PEMs depends on the water content and structural variables such as porosity, tortuosity, the ratio of diffusion coefficients δ, distributions of protons, and diffusion coefficients for the proton conduction processes. The formation of high fraction of pore bulk water in PEMs is desirable for high conductivity because of the faster transfer mechanism in the middle of the pores rather than at the surface. This is perhaps a key reason for the success of Nafion®, where surface hydrophobicity helps water cluster formation away from

surface. Most of the design variables of the proton conductivity model are related directly or indirectly to the amount of water uptake in PEMs, and thus, the sorption and the water-assisted proton conduction should be addressed together in designing new PEMs. The transport model developed here provides a theoretical framework for understanding the proton transfer in PEMs and should also be helpful in systematically developing alternate high proton-conducting PEMs for fuel cell applications.

References

1. S. J. Paddison, *Annu. Rev. Mater. Res.*, **33**, 289 (2003).
2. P. Commer, A. G. Cherstvy, E. Spohr, and A. A. Kornshev, *Fuel Cells*, **2**, 127 (2002).
3. P. Choi, N. H. Jalani, and R. Datta, *J. Electrochem. Soc.*, submitted (2004).
4. E. Wicke, M. Eigen, and T. Ackermann, *Z. Phys. Chem.*, **1**, 340 (1954).
5. G. Zundal and H. Metzger, *Z. Phys. Chem.*, **58**, 225 (1968).
6. C. J. D. von Grotthuss, *Ann. Chim.*, **LVIII**, 54 (1806).
7. E. Huckel, *Z. Electrochem.*, **34**, 546 (1928).
8. J. D. Bernal and R. H. Fowler, *J. Chem. Phys.*, **1**, 515 (1933).
9. B. E. Conway, J. O'M. Bockris, and H. Linton, *J. Chem. Phys.,* **24**, 834 (1956).
10. N. Agmon, *Chem. Phys. Lett.*, **244**, 456 (1995).
11. D. Marx, M. E. Tuckerman, J. Hutter, and M. Parrinello, *Nature*, **601**, 397 (1999).
12. M. E. Tuckerman, *J. Phys. Condens. Matter*, **14**, R1297 (2002).
13. M. E. Tuckerman, D. Marx, and M. Parrinello, *Nature*, **417**, 925 (2002).
14. U. W. Schmitt and G. A. Voth, *J. Chem. Phys.*, **111**, 9361 (1999).
15. R. Vuilleumier and D. Borgis, *J. Chem. Phys.*, **111**, 4251 (1999).
16. A. A. Kornshev, A. M. Kuznetsov, E. Spohr, and J. Ulstrup, *J. Phys. Chem.*, **107**, 3351 (2003).
17. S. J. Paddison, R. Paul, and T. A. Zawodzinski, *J. Electrochem. Soc.*, **147**, 617 (2000).
18. M. Eikerling, A. A. Kornyshev, and U. Stimming, *J. Phys. Chem. B*, **101**, 10807 (1997).
19. M. Eikerling and A. A. Kornyshev, *J. Electroanal. Chem.*, **502**, 1 (2000).
20. M. Eikerling, A. A. Kornyshev, A. M. Kuznetsov, J. Ulstrup, and S. Walbran, *J. Phys. Chem. B*, **105**, 3646 (2001).
21. X. D. Din and E. E. Michaelides, *AIChE J.*, **44**, 35 (1998).
22. T. Li, A. Alaschin, and P. B. Balbuena, *Ind. Eng. Chem. Res.*, **40**, 4789 (2001).

23. E. Spohr, P. Commer, and A. A. Kornshev, *J. Phys. Chem. B*, **106**, 10560 (2002).
24. R. Jinnouchi and K. Okazaki, *J. Electrochem. Soc.*, **150**, E66 (2003).
25. R. Paul and S. J. Paddison, *J. Chem. Phys.*, **115**, 7762 (2001).
26. S. J. Paddison and R. Paul, *Phys. Chem. Chem. Phys.*, **4**, 1158 (2002).
27. S. Mafe, J. A. Manzanares, and P. Ramirez, *Phys. Chem. Chem. Phys.*, **5**, 376 (2003).
28. J. Ennari, M. Elomaa, and F. Sundholm, *Polymer*, **40**, 5035 (1999).
29. G. Prentice, *Electrochemical Engineering Principles*, Prentice-Hall, Inc., Englewood Cliffs, NJ (1991).
30. J. O'M. Bockris and A. K. N. Reddy, *Modern Electrochemistry 1 Ionics*, Plenum Press, NY (1998).
31. T. Thampan, S. Malhotra, H. Tang, and R. Datta, *J. Electrochem. Soc.*, **147**, 3242 (2000).
32. K. S. Spiegler, *Trans*. *Faraday Soc.*, **54**, 1408 (1958).
33. A. G. Guzman-Garcia, P. N. Pintauro, M. W. Verbrugge, and R. F. Hill, *AIChE J.*, **36**, 1061 (1990).
34. E. H. Cwirko and R. G. Carbonell, *J. Membr. Sci.*, **67**, 227 (1992).
35. R. B. Bird, W. E. Stewart, and E. N. Lightfoot, *Transport Phenomena*, 2nd ed., John Wiley & Sons, Inc., NY (2002).
36. P. W. Atkins, *Physical Chemistry*, 3rd ed., W.H. Freeman and Company, NY (1986).
37. J. Philibert, *Atom Movements Diffusion and Mass Transport in Solids*, Les Editions de Physique, Les Ulis (1991).
38. N. Agmon, *J. Phys. Chem.*, **100**, 1072 (1996).
39. A. Narten and H. Levy, *J. Chem. Phys.*, **55**, 2263 (1971).
40. P. L. Silvestrelli and M. Parrinello, *J. Chem. Phys.*, **111**, 3572 (1999).
41. D. Eisenberg and W. Kauzmann, *The Structure and Properties of Water*, Oxford University Press, NY (1969).

42. A. K. Soper, F. Bruni, and M. A. Ricci, *J. Chem. Phys.*, **106**, 247 (1997).

43. I. Rozas and D. F. Weaver, *J. Chem. Soc., Perkin Trans 2*, **3**, 461 (1996).

44. T. K. Ghanty and S. W. Ghosh, *J. Phys. Chem.*, **98**, 9197 (1994).

45. P. K. Chattaraj, A. Cedillo, and R. G. Parr, *J. Chem. Phys.*, **103**, 10621 (1995).

46. R. Triolo and A. H. Narten, *J. Chem. Phys.*, **63**, 3624 (1975).

47. Y. Guissani, B. Guillot, and S. Bratos, *J. Chem. Phys.*, **88**, 5850 (1988).

48. J. Lobaugh and G. A. Voth, *J. Chem. Phys.*, **104**, 2056 (1996).

49. M. E. Tuckerman and G. J. Martyna, *J. Phys. Chem. B*, **104**, 159 (2000).

50. S. Walbran and A. A. Kornyshev, *J. Chem. Phys.*, **114**, 10039 (2001).

51. N. Agmon, *J. Phys. Chem.*, **100**, 1072 (1996). Errata: N, Agmon *J. Phys. Chem.*, **101**, 4352 (1997).

52. J. B. Hasted, D. M. Ritson, and C. H. Collie, *J. Chem. Phys.*, **16**, 1 (1948).

53. S. J. Paddison, D. W. Reagor, and T. A. Zawodzinski, *J. Electroanal. Chem.*, **459**, 91 (1998).

54. K. Lebedev, S. Mafe, A. Alcaraz, and P. Ramirez, *Chem. Phys. Lett.*, **326**, 87 (2000).

55. P. Debye, *Polar Molecules*, Dover, NY (1929).

56. C. A. Coulson and D. Eisenberg, *Proc. R. Soc. London Ser. A*, **291**, 445 (1966).

57. L. D. Site, A. Alavi, and R. M. Lunden-Bell, *Mol. Phys.*, **97**, 1683 (1999).

58. Y. S. Badyal, M. L. Saboungi, D. L. Price, S. D. Shastri, D. R. Haeffner, and A. K. Soper, *J. Chem. Phys.*, **112**, 9206 (1948).

59. P. L. Silvestrelli and M. Parrinello, *J. Chem. Phys.*, **111**, 3572 (2002).

60. A. V. Gubskaya and P. G. Kusalik, *J. Chem. Phys.*, **117**, 5290 (2002).

61. B. E. Conway, in *Modern Aspects of Electrochemistry*, No. 3, J. O'M Bockris and B. E. Conway, Editors, p. 43-148, Plenum, NY (1964).

62. T. Erdey-Gruz and S. Langyel, in *Modern Aspects of Electrochemistry*, No. 12, J. O'M Bockris and B. E. Conway, Editors, p. 1-40, Plenum, NY (1977).

63. J. B. Hasted, *Aqueous Dielectrics*, Chapman and Hill, London (1973).

64. B. Cohen and D. Huppert, *J. Phys. Chem. B*, **107**, 3598 (2003).

65. S. Meiboom, *J. Chem. Phys.*, **34**, 375 (1961).

66. B. Halle and G. Karlstrom, *J. Chem. Soc. Faraday Trans. 2*, **79**, 1047 (1983).

67. R. Mills, *J. Phys. Chem.*, **77**, 685 (1973).

68. R. Furth, *Investigations on the Theory of the Brownian Movement by Albert Einstein, Ph. D.*, Dover, NY (1956).

69. M. Marcus, *Ion Properties*, Marcel Dekker, NY (1997).

70. B. E. Conway, *Ionic Hydration in Chemistry and Biophysics*, Elsevier, Amsterdam (1985).

71. J. W. Moore and R. G. Pearson, *Kinetics and Mechanism*, 3rd ed., Wiley, NY (1981).

72. N. Lakshminarayanaih, *Equations of Membrane Physics*, Academic Press, NY (1984).

73. C. Ma, L. Zhang, S. Mukerjee, D. Ofer, and B. Nair, *J. Membr. Sci.*, **219**, 123 (2003).

74. K. D. Kreuer, *J. Membr. Sci.*, **185**, 29 (2001).

75. E. Glueckauf and G. P. Kitt, *Proc. Roy. Soc. London A,* **228**, 322 (1955).

76. S. Prager, *J. Chem. Phys.*, **33**, 122 (1960).

77. H. Yasuda, E. Lamaze, and L. D. Ikenberry, *Makromol. Chem.*, **118**, 19 (1968).

78. S. Koter, *J. Membr. Sci.*, **206**, 201 (2002).

79. Y. Sone, P. Ekdunge, and D. Simonsson, *J. Electroanal. Chem.,* **143**, 1254 (1996).

80. T. A. Zawodzinski, C. Derouin, S. Radzinski, R. J. Sherman, V. T. Smith, T. E. Springer, and S. Gottesfeld, *J. Electrochem. Soc.,* **140**, 1041 (1993).

81. M. Doyle, L. Wang, Z. Yang, and S. K. Choi, *J. Electrochem. Soc.,* **150**, D185 (2003).

82. M. Doyle, M. E. Lewittes, M. G. Roelofs, and S. A. Perusich, *J. Phys. Chem. B*, **105**, 9387 (2001).

Chapter 6. Proton Transport in Nafion®/Sulfated ZrO_2 Nanocomposite Membranes

Abstract

A proton transport model is developed to describe proton diffusion in Nafion®/(ZrO_2/SO_4^{2-}) nanocomposite membrane designed for operation at high temperature and low relative humidity conditions. The model accounts for various proton transport mechanisms such as proton hopping at surface, and structural diffusion and *en masse* diffusion of hydronium ions in the pore bulk. The proton conductivity in the composite membrane depends upon i) the water content, which affects structural parameters such as porosity and tortuosity, ii) diffusion coefficients at surface and bulk regions, and iii) proton concentration on the surface on the surface and in the pores. The conductivity of the membrane in contact with water vapor is accurately predicted as a function of relative humidity without any fitted parameters. Nafion®/(ZrO_2/SO_4^{2-}) composite membrane shows higher proton conductivity compared with Nafion at the same temperature and humidity conditions due to the improved water uptake and additional acid sites. The model provides a theoretical framework for understanding proton conduction in Nafion®/(ZrO_2/SO_4^{2-}) membrane and can be used to investigate performance of new composite proton exchange membranes at elevated temperatures for fuel cell applications.

6-1. Introduction

Recently, extensive research efforts have been made worldwide to find new proton conducting materials for proton-exchange membrane (PEM) fuel cell applications that can overcome the limitations of conventional polymer electrolytes such as Nafion®, currently

one of the main obstacles to commercialization of PEM fuel cells.[1-3] They are expensive, mechanically unstable at high temperatures, and conductive only when soaked in water, which limits the fuel cell operating temperature to 80^{o} C, which in turn results in low CO tolerance. The operation of fuel cells at higher temperature provides many advantages[4,5] such as improved kinetics at the surface of electrodes, which is especially important in methanol and CO-containing reformate feeds, faster conduction of protons across PEM, more efficient cooling, and the possibility of integrating fuel cells with methanol reformer, which can result in a compact fuel cell system. Thus, the development of membranes which are mechanically and chemically stable at high temperatures while providing good conductivity under low relative humidity (RH) is an active area of research.

A route to developing "high temperature membranes" is via modification of polymer (host membrane) by the incorporation of hygroscopic oxides such as SiO_2 to increase water uptake, or inorganic solid acids such as heteropoly acids, zirconium phosphate, or ZrO_2/SO_4^{2-} to increase the water uptake as well as the concentration of acid sites to further enhance proton conductivity of the membrane. Recent examples of polymer/inorganic composite membranes are Nafion®/SiO_2,[6,7] Nafion®/Al_2O_3,[8] Nafion®/TiO_2,[9] Nafion®/ZrO_2,[10] Nafion®/ZrP,[11] Nafion®/PTA,[12] Nafion®/Zeolite,[13] SPEK/ZrO_2,[14] SPEEK/ZrP,[15] SPEK/(ZrO_2/TPA),[16] and PBI/(SiWA+SiO_2),[17] etc. These membranes can be prepared by casting a bulk or colloidal mixture of powder with a polymer solution, or alternatively *in-situ* formation within a preformed polymer membrane. The size and dispersion of solid particles are of special importance in either fabrication methods. The *in-situ* method is based on sol-gel reactions in the membrane and the formation of nanometer sized particles within the host membrane. These composite membranes prepared via the sol-gel method include Nafion®/ZrO_2,[18] Nafion®/SiO_2,[19] Nafion®/TiO_2,[20] and PEO®/SiO_2.[21]

The composite membranes show a higher water uptake,[6] reduced methanol crossover,[14] improved mechanical properties at higher temperatures,[17] and improved fuel cell performance,[8,11,22] although the reasons for the performance enhancement are not clearly elucidated and the long-term stability of these membranes is still in question. In spite of their substantial increase in water uptake, the improved proton conductivity has not been yet proven and is an object of current debate. For example, Miyake et al.[6] reported that the conductivity of sol-gel prepared Nafion®/SiO_2 composite membrane was found to be 0.185 S/cm, 0.16 S/cm, and 0.112 S/cm for 4-5%, 10-12 %, and 16-17 % loadings of SiO_2, respectively, while that of Nafion was 0.21 S/cm at the same condition of 120^0C and 78 % RH. On the other hand, Arico et al.[7] reported higher proton conductivity of inorganic acid doped composite membranes such as Nafion®/SiO_2, Nafion®/(PWA+SiO_2), and Nafion®/ZrO_2 over the entire temperature range of their experiments. Therefore, it is of interest to analyze the proton transport mechanisms in polymer and polymer/inorganic membranes, which might provide a better understanding of the strengths and weaknesses of alternate approaches for developing good proton conducting materials suitable at high temperatures.

In the present work, Nafion/(SO_4^{2-}/ZrO_2) membranes were prepared via *in-situ* sol-gel technique and compared with unmodified Nafion® in terms of water uptake and proton conductivity under different relative humidity conditions. The objective of this chapter is to develop an understanding of the proton transport mechanisms in composite membranes, so that a framework for the design of high proton conductivity can be developed. A theoretical proton conductivity model is, thus, developed here based on the parallel pore model incorporating various proton transport mechanisms such as surface proton hopping, Grotthuss diffusion, and traditional *en masse* diffusion. This is an extension of previous chapter on transport of protons in polymer electrolyte membranes.

6-2. Experiments

Membrane preparation – A Nafion®/(ZrO_2/SO_4^{2-}) composite membrane was prepared via *in-situ* sol-gel synthesis developed by Watanabe et al.[9] Nafion® 112 served as the template that directs the morphology and size of the oxide particle in the PEM matrix. As received Nafion® was purified by boiling in pure water at 60^0 C for 30 minutes, treated in 3 wt % H_2O_2 solution at 60^0 C for 30 minutes, and washed with deionized water at 60^0 C for 30 minutes. It was then converted to Na^+ form by heating in 1 M NaOH solution at 60^0 C for 30 minutes and washed with deionized water. The Na^+ form of Nafion® was soaked in $Zr(OCH(CH_3)_2)_4$ ZrP/2-propanol solution at 25^0C for 24 hours. The membrane was then removed, blotted, and placed in 2-propanol/H_2O solution for 2 hours at 80^0C. After the hydrolysis and condensation reactions, the membrane was removed and vacuum dried thoroughly at 25^0C for 24 hours and then at 110^0C for 2 hours. The membrane was next boiled in 1 M H_2SO_4 solution at 60^0C for 1 hour to sulfate the ZrO_2 nanoparticles and finally rinsed in water.

Water uptake measurements – The Tapered Element Oscillating Microbalance (TEOM) was used to measure water uptake in the various membranes. The details of the technique are provided elsewhere.[10] The water uptake was measured for Nafion and Nafion®/(ZrO_2/SO_4^{2-}) composite membranes at 25^0 C and 90^0 C from 0 % to 90 % RH.

Proton conductivity measurements – The membrane conductivity was measured by AC impedance spectroscopy at 25^0 C and 90^0 C from 0 % to 90 % RH as described by us previously.[10] The humidity of the membrane-containing chamber was monitored utilizing a dewpoint/temperature probe. A dry nitrogen stream was saturated with water by passing it through a humidifier, which was then combined with a dry stream of nitrogen to control the RH in the conductivity chamber.

6-3. Theory

Figure 6-1 shows a schematic representation of the composite membrane in which both the polymer and the inorganic particles are viewed as "dust" species, each possessing acid sites. The absorbed water molecules interact with the host membrane as well as solid inorganic particles depending upon their hydrophilicity and acid strength of the ionic sites. The water molecules within the composite membrane may be classified as "bulk water" away from the acid groups and "surface water" in proximity of the acid groups. Thus, it is assumed that the protons in the composite membranes diffuse via *i*) surface diffusion mechanism occurring close to the acid groups, the primary mechanism under low water activity, and *ii*) bulk diffusion mechanism in the region away from the acid groups, the dominant mechanism under high water activity condition. In the bulk, proton diffusion is predominantly via the Grotthuss mechanism but the H_3O^+ ion can also undergoes traditional mass diffusion, *i.e.*, the so-called *en masse* diffusion. The overall proton conductivity of composite membranes σ_{H^+} can, thus, be written as[23]

$$\sigma_{H^+} = \frac{\varepsilon_i}{\tau}\left[\frac{F^2}{RT}\left(D^{\Sigma}_{H^+}C^{\Sigma}_{H^+} + D^{G}_{H^+}C_{H^+} + D^{E}_{H^+}C_{H^+}\right)\right] \quad [1]$$

where ε_i is porosity of membrane, τ is tortuosity factor, F is Faraday's constant, R is gas constant, T is temperature, $D^{\Sigma}_{H^+}$, $D^{G}_{H^+}$, and $D^{E}_{H^+}$ are the diffusion coefficients for surface, Grotthuss, and *en masse* mechanisms, respectively, and C_{H^+} and $C^{\Sigma}_{H^+}$ are the concentrations of protons participating in diffusion in the bulk and surface phases, respectively.

Parameter Identification

Diffusion Coefficients

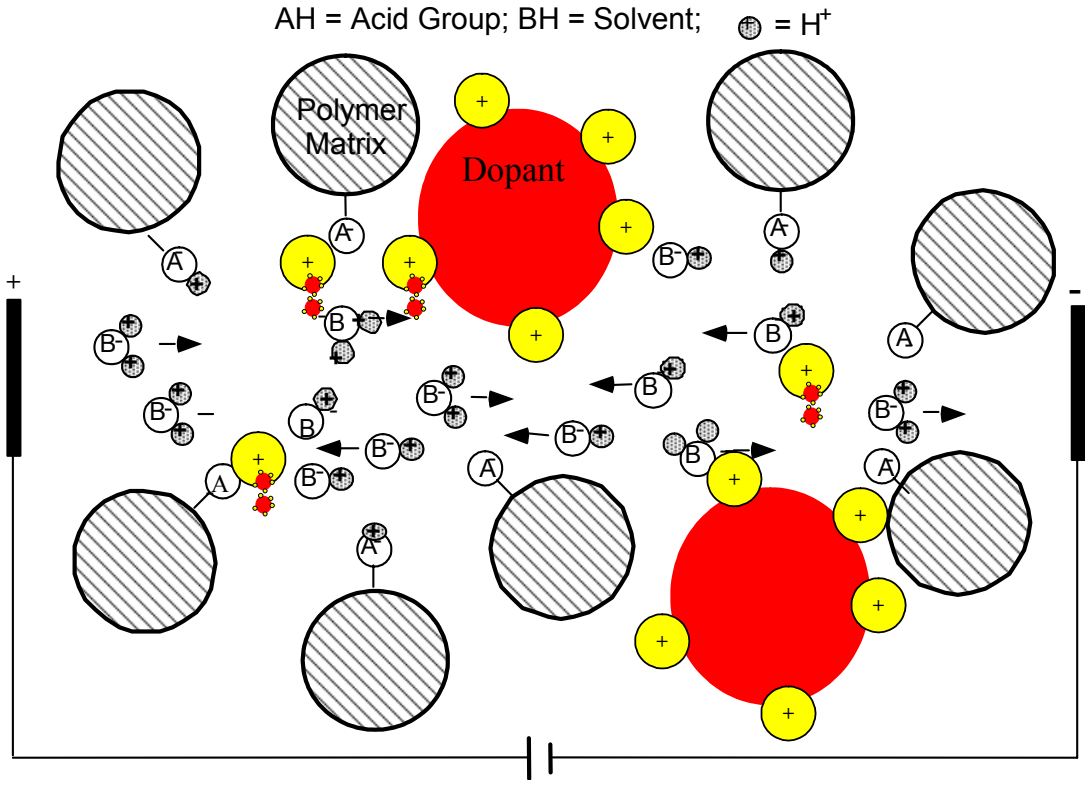

Figure 6-1. A schematic diagram of Nanocomposite membranes.

The acid groups of the composite membrane are composed of those of the host membrane (i.e., Nafion®) and solid acid (i.e., ZrO_2/SO_4^{2-}). The surface diffusion coefficient of protons can be obtained from

$$\frac{1}{D_{H+}^{\Sigma}} = \frac{x_M^{\Sigma}}{D_{H+,M}^{\Sigma}} + \frac{x_{SA}^{\Sigma}}{D_{H+,SA}^{\Sigma}} \quad [2]$$

where $D_{H+,M}^{\Sigma}$ is the surface diffusion coefficient of protons of the host membrane (M), $D_{H+,SA}^{\Sigma}$ is the surface diffusion coefficient of protons of the inorganic solid acid (SA), x_M^{Σ} is the fraction of surface protons attached to the host membrane, and x_{SA}^{Σ} is the fraction of surface proton attached to the acid groups of the inorganic solid acid particles. The fraction of membrane acid groups can be written in terms of the molar ratio of inorganic solid acid and membrane acid group, i.e., $x_M^{\Sigma} = 1/(1+q)$ and $x_{SA}^{\Sigma} = q/(1+q)$, where q = moles of acid sites from (ZrO_2/SO_4^{2-})/moles of SO_3^- on Nafion®. For w grams of solid acid with the average particle size of diameter d_p, the moles of effective surface acid from the solid acids is $(6w/d_p\rho_p)C_{H+,SA}^*$, where ρ_p is the inorganic solid acid particle density and $C_{H+,SA}^*$ [mol/m^2] is the effective surface site density of acid groups on the surface of sulfated zirconia particles. Thus, the molar ratio of acid site for *w* grams of solid acid per gram of host membrane is

$$q = \left(\frac{6w}{d_P \rho_P} EW_M \right) C_{H+,SA}^* \quad [3]$$

where EW_M represents the equivalent weight of the host membrane.

The surface diffusion coefficients, $D_{H+,M}^{\Sigma}$ and $D_{H+,SA}^{\Sigma}$, can be obtained by applying the Einstein-Smoluchowski relation,[24] $D = l_{\Sigma}^2 / \kappa \tau_D^{\Sigma}$, where l_{Σ} is the mean step distance, κ is dimensionality constant (4 for 2-dimensional diffusion), and τ_D^{Σ} is the mean time between

successive steps. The hopping time is given by $\tau_D^{\Sigma} = \nu_0^{-1} \exp\left(\Delta G_{\Sigma}^{e,0} \Big/ k_B T \right)$, where ν_0 is the thermal frequency, k_B is the Boltzmann constant, h is the Planck constant, $\Delta G_{\Sigma}^{e,0}$ is the effective Gibbs free energy of activation for surface diffusion around acid groups. Substitution of the acid fractions (i.e., x_M^{Σ} and x_{SA}^{Σ}) and diffusion coefficients (i.e., $D_{H+,M}^{\Sigma}$ and $D_{H+,SA}^{\Sigma}$) into Eq. 2 provides

$$D_{H+}^{\Sigma} = \frac{1 + \left(\frac{6w}{d_p \rho_p} EW_M \right) C_{H+,SA}^{*}}{4} \left(\frac{k_B T}{h} \right) \left[\frac{l_{\Sigma,M}^2 \exp\left(\frac{-\Delta G_{\Sigma,M}^{e,0}}{k_B T} \right)}{1 + C_{H+,SA}^{*} \left(\frac{6w}{d_p \rho_p} EW_M \right) \left(\frac{l_{\Sigma,M}^2}{l_{\Sigma,SA}^2} \right) \exp\left(\frac{-\Delta G_{\Sigma,M}^{e,0} + \Delta G_{\Sigma,SA}^{e,0}}{k_B T} \right)} \right] \quad [4]$$

where $\Delta G_{\Sigma,M}^{e,0}$ is the effective Gibbs free energy of activation for the surface diffusion around membrane acid groups, and $\Delta G_{\Sigma,SA}^{e,0}$ is the effective Gibbs free energy of activation for the surface diffusion around acid groups of solid acid. The Gibbs free energy $\Delta G_{\Sigma}^{e,0}$ can be calculated by assuming that the first step is rate-determining for the overall surface proton hopping among surface water molecules based on the rapid decrease in Coulombic interaction energy with the distance from the acid sites and low dielectric constant of water in the surface layer[23,25]

$$\Delta G_{\Sigma}^{e,0} \approx \frac{(q_{e^-})^2}{4\pi\varepsilon_0\varepsilon_r} \left[\frac{l_{\Sigma}}{(R_f + R_i + l_{\Sigma})(R_f + R_i)} \right] \quad [5]$$

where ε_0 is the permittivity of free space, ε_r is the relative permittivity of the medium, q_{e^-} is the electrostatic charge, R_f is the effective radius of acid groups, and R_i is the radius of the hydronium ion. Since ε_r and R_f are not, in general, same for the membrane and the solid acid, the activation energies for proton surface diffusion may be different on the acid sites of the host membrane and solid acids. Of course, the mean step distance among acid sites on membrane and solid acid are also different.

The diffusion coefficient for Grotthuss mechanism depends upon the rate at which the hydrogen bond forms and breaks between proton receiving and donating water molecules. The proton in aqueous solution is commonly visualized as hydronium ion, H_3O^+, in which the three hydrogen atoms share the charges equally, or as Zundal ion, $H_5O_2^+$, in which a proton is shared between two water molecules, or as Eigen ion, $H_9O_4^+$, in which the hydronium ion is strongly bound with three water molecules. In fact, there are many and complex states of hydrated protons, $H^+(H_2O)_n$, and the three states mentioned above are considered only as limit or ideal structures. [26-28] The rate-determining step for proton transport via Grotthuss mechanism includes hydrogen-bond cleavage between the proton accepting water molecule and a nearby water molecule, and the reorientation of the proton accepting adjacent water molecule towards the hydronium ion to be in a receptive position. The rotational diffusion coefficient of water molecule can be written as[29]

$$D_R = k_B T / 8\pi\eta R_w^3 \qquad [6]$$

where η is the viscosity of water and R_w is the radius of water molecule. Using the Einstein relation $\tau_D = 1/2D_R$, the relaxation time is given as

$$\tau_D = 4\pi\eta R_w^3 / k_B T \qquad [7]$$

The proton diffusion by Grotthuss mechanism is characterized by the water reorientation time τ_D^G = 1.5 ps at room temperature,[30] which is measured and also calculated by us from the relation between the force of water dipole with the hydronium ion and torque for translational rotation.[23] Thus the Grotthuss diffusion coefficient is calculated as $D_{H+}^G \approx 7$ x 10^{-5} cm^2/sec from $D_{H+}^G = l_G^2 / 6\tau_D^G$, where l_G = 0.255 nm, O-O distance of $H_5O_2^+$ ion, and τ_D^G = 1.5 ps.

The *en masse* diffusion coefficient of hydronium ion in a dusty-fluid medium consisting of water, membrane acid sites, and solid acids, the latter two considered as immobile dust species, can be written as

$$\frac{1}{D_{H+}^{E}} = \frac{x_W}{D_{H+}^{W}}\left(1 + \frac{x_M}{x_W}\frac{D_{H+}^{W}}{D_{H+}^{M}} + \frac{x_{SA}}{x_W}\frac{D_{H+}^{W}}{D_{H+}^{SA}}\right) \quad [8]$$

where x_W, x_M, and x_{SA} denote the fraction of water, membrane, and solid acid, respectively, and D_{H+}^{W}, D_{H+}^{M}, and D_{H+}^{SA} denote the Stefan-Maxwell diffusion coefficients of hydronium ion and bulk water, hydronium ion and polymer matrix, and hydronium ion and solid acids, respectively. The fraction of water in the membrane can be written as $x_W = \lambda_W / (\lambda_W + 1)$, where the solvent loading λ_W is given by

$$\lambda_W = \frac{p(1+w)}{MW_W\left(1/EW_M + \left(6w/d_p\rho_p\right)C_{H+,SA}^{*}\right)} \quad [9]$$

where p is the mass of absorbed water per mass of dry composite membrane, and MW_W is the molecular weight of water. Using the analogy between Einstein-Smoluchowski relation and elementary kinetic theory, the diffusion coefficient ratios can be calculated as[23] $D_{H+}^{W} / D_{H+}^{M} \approx \sqrt{2}(r_{M/W})^{2/3}$ and $D_{H+}^{W} / D_{H+}^{SA} \approx \sqrt{2}(r_{SA/W})^{2/3}$, where $r_{M/W}$ and $r_{SA/W}$ is the ratio of partial molar volume of membrane to that of water, and partial molar volume of solid acid to that of water, respectively. Using these in Eq. 8 and from $x_M / x_W = 1/\lambda_W(1+q)$ and $x_{SA} / x_W = q/\lambda_W(1+q)$, the *en masse* diffusion coefficient of hydronium ion for the medium composed of water, polymer matrix and solid acids can be written as

$$D_{H^+}^{E} = \left\{\frac{(\lambda_W + 1)\left(1 + \frac{6w}{d_P\rho_P}EW_M C_{H+,SA}^{*}\right)}{\lambda_W\left(1 + \frac{6w}{d_P\rho_P}EW_M C_{H+,SA}^{*}\right) + \sqrt{2}(r_{M/W})^{2/3} + \sqrt{2}(r_{SA/W})^{2/3}\frac{6w}{d_P\rho_P}EW_M C_{H+,SA}^{*}}\right\} D_{H+}^{W} \quad [10]$$

Thus, the *en masse* diffusion coefficient depends upon the amount of water uptake (λ_W), particle size of inorganics (d_p), the amount of loading of inorganics (w), the ratios of partial molar volume of host membrane to water ($r_{M/W}$) and that of inorganics to water ($r_{S/W}$), surface acid site density of the inorganics $C^*_{H+,SA}$ and hydronium ion *en masse* diffusion coefficient in aqueous water (D^W_{H+}).

The *en masse* diffusion coefficient of hydronium ion through water D^W_{H+} is obtained from the Stokes-Einstein relation or usually approximated[29] simply as the self-diffusion coefficient of water, which has been reported as 2.1-2.3 x 10^{-5} cm^2/s at room temperature, based on considering the hydronium ion as a diffusing entity in water. The Stokes-Einstein relation[24,31] provides

$$D^W_{H+} = \frac{k_B T}{6\pi\eta R^*_{H_3O^+}} \qquad [11]$$

where η is the viscosity of the medium and $R^*_{H_3O^+}$ is the hydrodynamic radius of hydronium ion. Since the Stokes-Einstein equation provides only an approximation of the diffusion coefficient for molecular species, we simply take D^W_{H+} as the self-diffusion coefficient of water. In fact, this corresponds the effective water radius $R^*_{H_2O}$ = 0.108 nm, smaller than the geometric radius of water molecule R_{H_2O} = 0.143-0.144. Since the overall experimental bulk diffusion coefficient of proton (considering of Grotthuss and en masse mechanism) in water is known as 9.31 x 10^{-5} cm^2/s at room temperature,[24] the Grotthuss diffusion coefficient is sometimes estimated by subtracting the self diffusion coefficient of water molecule from the experimental proton diffusion coefficient.[29]

Distribution of Protons Between the Surface and Bulk Regions

Some of the dissociated protons remain close to the anion surface sites and participate in surface diffusion, while others with a higher degree of hydration break away into the pore bulk and participate in bulk diffusion comprising of Grotthuss and *en masse* mechanisms. To distinguish between the two, we simply assume here that the dissociated acid sites with up to two water molecules remain close to the surface and designate these sites as surface water, while those with more than two water molecules move away from the surface to the pore bulk. The total concentration of acid sites in the composite membranes is calculated[32] from $C_{H^+,0} = 1/\lambda_W \overline{V}_w$, and the concentration of surface protons $C^{\Sigma}_{H^+} \approx C_{H^+,0}(\theta_1 + \theta_2)$, where θ_i denotes the fraction of refers to the fraction of acid sites with i bound water molecule.[23] Since the acid sites are in both the host membrane and solid acids, the total surface concentration is $C^{\Sigma}_{H+} = C^{\Sigma}_{H+,M} + C^{\Sigma}_{H+,SA}$. In terms of surface fraction of total concentration, the surface concentration can be written as $C^{\Sigma}_{H+,M} = f^{\Sigma}_{M} C_{H+,0}$ and $C^{\Sigma}_{H+,SA} = f^{\Sigma}_{SA} C_{H+,0}$, where f^{Σ}_{M} and f^{Σ}_{SA} represent the surface fraction of protons near host membrane and solid acid, respectively[23]

$$f^{\Sigma}_{M} = \frac{d_P \rho_P}{\left(d_P \rho_P + 6wEW_M C^{*}_{H+,SA}\right)}\left[\frac{K_{1,M} a_w \left(1-a_w\right)\left(1+K_{2,M} a_w\right)}{\left(1-a_w\right)\left(1+K_{1,M} a_w\right)+K_{1,M}K_{2,M}a_w^2\left(1-a_w^{\nu-1}\right)}\right] \qquad [12]$$

while the surface fraction of proton near solid acid is

$$f^{\Sigma}_{SA} = \frac{6wEW_M C^{*}_{H+,0}}{\left(d_P \rho_P + 6wEW_M C^{*}_{H+,SA}\right)}\left[\frac{K_{1,SA} a_w \left(1-a_w\right)\left(1+K_{2,SA} a_w\right)}{\left(1-a_w\right)\left(1+K_{1,SA} a_w\right)+K_{1,SA}K_{2,SA}a_w^2\left(1-a_w^{\nu-1}\right)}\right] \qquad [13]$$

where $\overline{V}_w$ is partial molar volume of water, ν is the number of equilibrium steps with acid groups, K_i is equilibrium steps between water and acid groups, a_w is the activity of water in surroundings. The bulk concentration of proton is given by $C_{H+} = C_{H+,0}(1-\theta_0-\theta_1-\theta_2)$ and can be approximated as $C_{H+} \approx C_{H+,0} - C^{\Sigma}_{H+,M} - C^{\Sigma}_{H+,SA}$. Since the two dissociation constants in water K_1 and K_2 for the first and subsequent hydration steps will be different

for the sulfonic acid and the inorganic solid acids, the concentrations of surface proton also vary with the strength of ions. The two equilibrium constants for Nafion® $K_{1,M}$ and $K_{2,M}$ are taken as 1000 and 200, respectively, based on the dissociation constant of sulfonic acid and the proton affinity data.[33-35] The sulfated zirconia is usually regarded as[36] "superacid" ($H_0 < -16$) due to its strong acidity which is greater than that of 100 % sulfuric acid for which $H_0 \approx -12$, where H_0 is Hammett indicator, although some studies[37,38] have indicated that the sulfated zirconia is not highly acidic and the catalytic activity is more related to its ability to stabilize transition state complex of reactants on the surface than its acidity. Here, $K_{1,SA}$ and $K_{2,SA}$ are also, thus, taken simply as 1000 and 200, respectively. The fraction of surface protons is high at low water content and then decreases as the water content of the composite membrane increases, while the bulk concentration increases monotonically with water content.

Porosity and Tortuosity

The total volume of the composite membrane is the sum of the three components, water, host membrane and solid acid. The porosity (volume fraction of water) of the membrane is, then,

$$\varepsilon_i = \frac{\lambda_W \left(1/EW_M + w/MW_{SA}\right)}{\lambda_W \left(1/EW_M + w/MW_{SA}\right) + r_{M/W}/EW_M + w r_{SA/W}/MW_{SA}} \qquad [14]$$

where $r_{M/W}$ is the ratio of partial molar volume of membrane to that of water, $r_{SA/W}$ is the ratio of partial molar volume of solid acids to that of water. The tortuosity factor τ is usually determined experimentally. Here, we adopt the predictive Preger's model which has been previously used[39] for Nafion®

$$\tau = \frac{2(1-\varepsilon_i) + 2\varepsilon_i \ln \varepsilon_i - 0.5\varepsilon_i (\ln \varepsilon_i)^2}{\varepsilon_i (1-\varepsilon_i) + \varepsilon_i^2 \ln \varepsilon_i} \qquad [15]$$

Thus, the tortuosity factor τ depends upon the porosity ε_i, which in turn varies with the amount of water uptake, equivalent weight of host membrane, the amount of inorganics, molecular weight of inorganics, and the ratios of partial molar volumes, as shown in Eq. 14.

6-4. Results and Discussions

Table 6-1 shows the water sorption data of Nafion® and Nafion®/(ZrO_2/SO_4^{2-}) composite membranes determined experimentally at 25^0Cand 90^0C using the TEOM. The incorporation of ZrO_2/SO_4^{2-} increases water uptake as well as provides a new acid site for proton transport. The surface structure of ZrO_2/SO_4^{2-} has been studied extensively and many models have been proposed.[40-42] Figure 6-2 shows the interconversion of Lewis acid site into Bronsted acid sites by the presence of water molecules, based on the observation via IR spectra of pyridine adsorption.[43] The total surface acid site concentration in the composite membrane due to inorganic solid acids is the sum of two acid sites, $C^*_{H+,SA} = C^*_{H+,SA(B)} + C^*_{H+,SA(L)}$, where $C^*_{H+,SA}$, $C^*_{H+,SA(B)}$, and $C^*_{H+,SA(L)}$ denote the total, Bronsted, and Lewis acid sites concentration, respectively. The surface site density is reported[44] in a range of $C^*_{H+,SA(B)} \approx 10^{17} \sim 10^{18}$ molecules/m^2 and $C^*_{H+,SA(L)} = 10^{17} \sim 10^{18}$ molecules/m^2, and thus $C^*_{H+,SA} \approx 10^{18}$ molecules/m^2, corresponding to 1.67 x10^{-6} mol/m^2, based on the assumption that both sites are responsible for the generation of hydronium ions and participate in the transport of protons in the composite membrane. Figure 6-3 shows the overall surface diffusion coefficient of composite membrane as expected by Eq. 4 as a function of acid site density for the parameters given in Table 6-2. The amount of ZrO_2/SO_4^{2-} added to the host membrane was determined as 3 wt. % by ash analysis. As the acid site density increases, the surface diffusion coefficient increases linearly because the acid sites of ZrO_2/SO_4^{2-} participate in the surface diffusion mechanism and contribute to

Table 6-1. Data for water sorption in Nafion and Nafion/(ZrO_2/SO_4^{2-}) nanocomposite.

Activity	Nafion (g water/g dry Nafion)		Nafion/(ZrO_2/SO_4^{2-}) (g water/g dry composite)	
	25^0C	90^0C	25^0C	90^0C
0.1	0.0339	0.0344	0.0351	0.0413
0.2	0.0491	0.0488	0.0498	0.0586
0.3	0.0573	0.0499	0.0510	0.0599
0.4	0.0655	0.0614	0.0626	0.0737
0.5	0.0659	0.0749	0.0764	0.0899
0.6	0.0810	0.0875	0.0893	0.1051
0.7	0.0949	0.1127	0.1150	0.1352
0.8	0.1080	0.1309	0.1343	0.1584
0.9	0.1490	0.1710	0.1743	0.2053
1.0	0.2291	0.2701	0.2754	0.3247

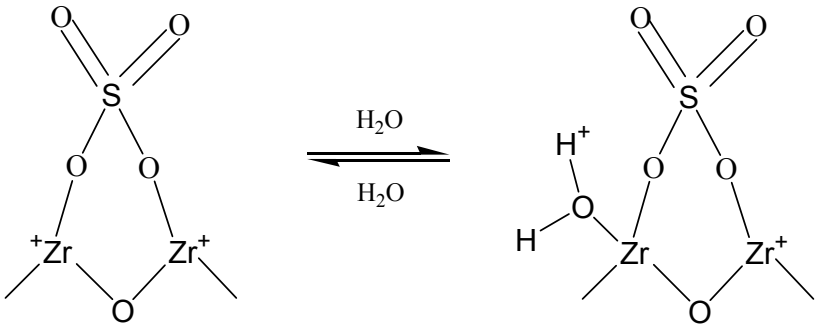

Figure 6-2. Structure of ZrO_2/SO_4^{2-} solid acid.

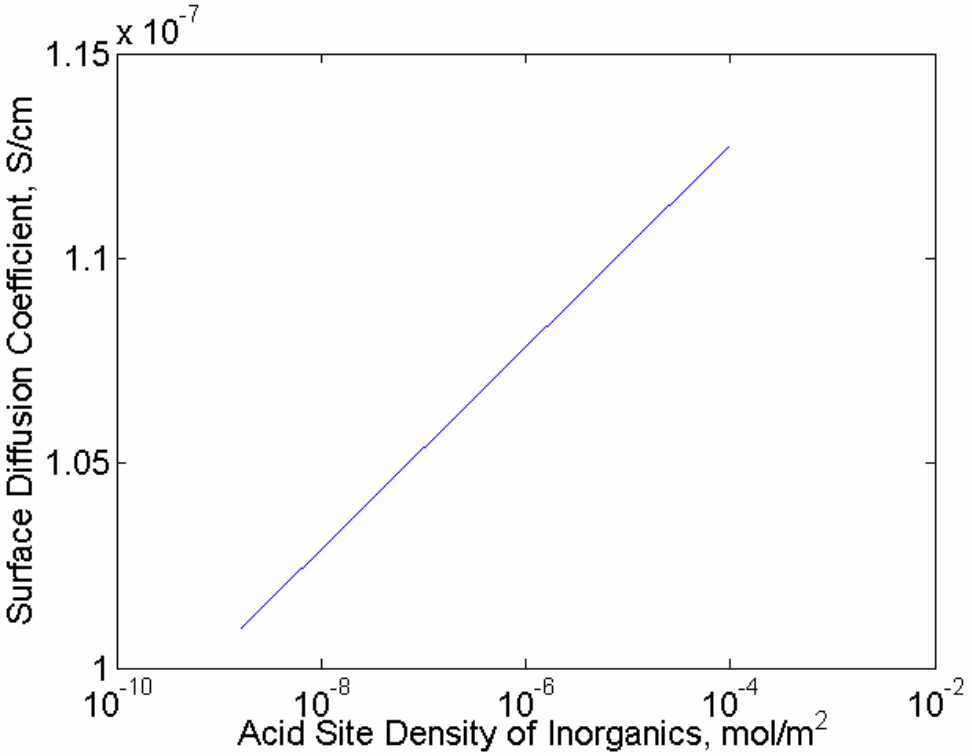

Figure 6-3. The effect of acid site density on the surface diffusion coefficient.

Table 6-2. Parameter values employed in the model at room temperature.

Diff. Coef.	Symbols	Values	Units	Comments
$D_{H^+}^{\Sigma}$	EW_M	1100	g/equiv.	equivalent weight of membrane
	MW_{SA}	219.29	g/mol	molecular weight of solid acid
	$w_{SA/M}$	0.03	dimensionless	weight ratio of solid acid to membrane
	$C_{H+,SA}^{*}$	1.67×10^{-6}	mol/m^2	surface acid site density of sulfated zirconia
	k_B	1.38×10^{-23}	J/K	Boltzmann constant
	h	6.626×10^{-34}	J·sec	Planck constant
	l_{Σ}	0.255	nm	jump length of surface proton
	$R_{F(M)}$	0.254	nm	radius of acid site of membrane
	$R_{F(SA)}$	0.260	nm	radius of acid site of solid acid
	R_{H2O}	0.143	nm	radius of water molecule
	ε_0	8.854×10^{-12}	$C^2/J/m$	permittivity
	$\varepsilon_{r(M)}$	6	dimensionless	relative permittivity of membrane
	$\varepsilon_{r(SA)}$	6	dimensionless	relative permittivity of solid acid
	q_{e^-}	1.602×10^{-19}	C	electronic charge
$D_{H^+}^{G}$	l_G	0.255	nm	proton jump length in Grotthuss mechanism
	τ_D^G	1.5	ps	proton jump time in Grotthuss mechanism
$D_{H^+}^{E}$	λ_W	Eq. 9	dimensionless	mol H_2O/mol composite membrane
	$r_{M/W}$	29.83	dimensionless	partial molar volume ratio of membrane to water
	$r_{SA/W}$	2.068	dimensionless	partial molar volume ratio of solid acid to water

the total surface diffusion coefficient. The acid site density is also directly related to the size of particle, as shown in Eq. 4. That is, the increase in site density $C^*_{H+,SA}$, or increase in surface area via a decrease in the particle size d_p have the same effect Therefore, a small size particle with high surface acid density is favorable for higher acidity and surface diffusion of protons in the composite membrane. The surface diffusion coefficient of Nafion® is 1.01 x 10^{-7} cm^2/sec at 25^0C, which is obtained by substituting w = 0 in Eq. 4. Figure 6-4 shows the *en masse* diffusion coefficients of composite membrane at 25^0 C and 90^0 C. The diffusion coefficient increases with the vapor phase activity due to the increase of water content as shown in Eq. 10. The model predicts a diffusion coefficient of 1.35 x10^{-5} cm^2/s and 4.71 x 10^{-5} cm^2/s at 25^0 C and 90^0 C, respectivel for the composite membrane contacting with saturated water vapor. This is roughly two orders of magnitude higher than the surface diffusion coefficients at the same temperature and activity conditions. Figure 6-5 compares the porosity/tortuosity, ε_i / τ, as a function of the activity of water in vapor phase for Nafion® and Nafion®/(ZrO_2/SO_4^{2-}) composite membranes. Thus, composite membrane provides a higher porosity/tortuosity ratio, that is desirable as it directly affects the conductivity (Eq. 1).

Figures 6-6 and 6-7 show the experimental conductivity data of Nafion® along with the model prediction at 25^0C and 90^0C, respectively, based on the water uptake measurement provided in Table 6-1. The effect of temperature on the Grotthuss and *en masse* diffusion coefficients was obtained from the following considerations. In an aqueous electrolyte solution of acids, $D_{H+} = D^G_{H+} + D^E_{H+}$, where D_{H+}, D^G_{H+}, and D^E_{H+} denote total, Grotthuss and *en masse* diffusion coefficients, respectively. The *en masse* diffusion coefficient is obtained from the self-diffusion coefficient of water molecule available over the temperature range of 0^0C -100^0 C.[45] Then, the Grotthuss diffusion coefficient can be calculated[46-48] by subtracting the *en masse* diffusion coefficient from the total diffusion

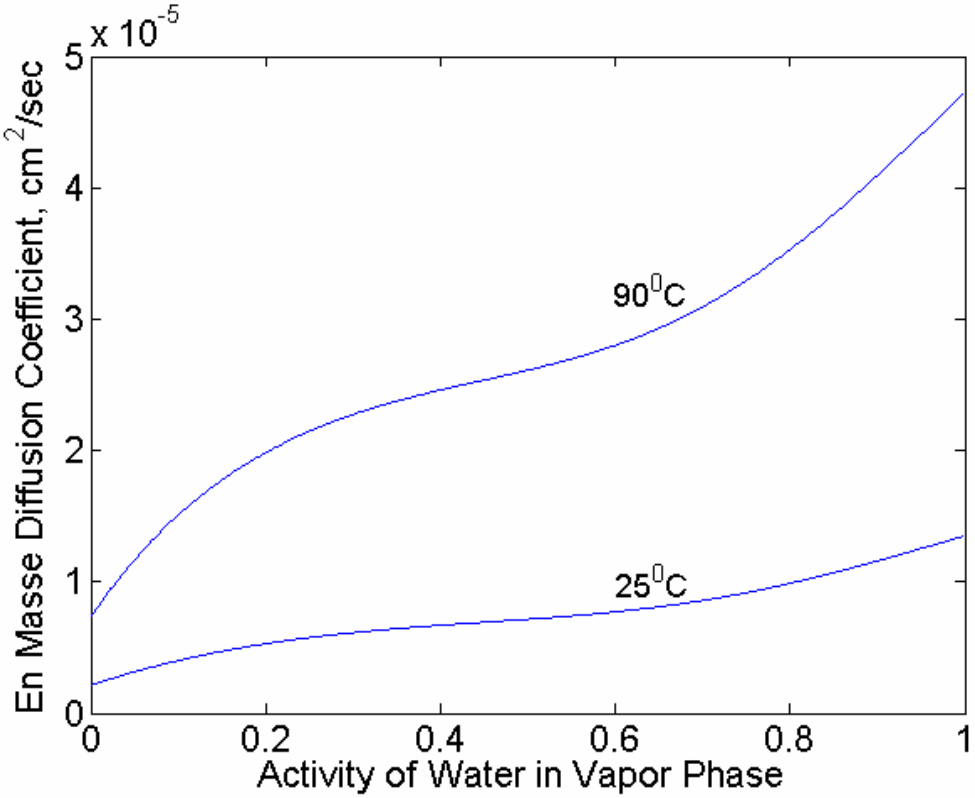

Figure 6-4. The effect of water vapor activity on the en masse diffusion coefficient.

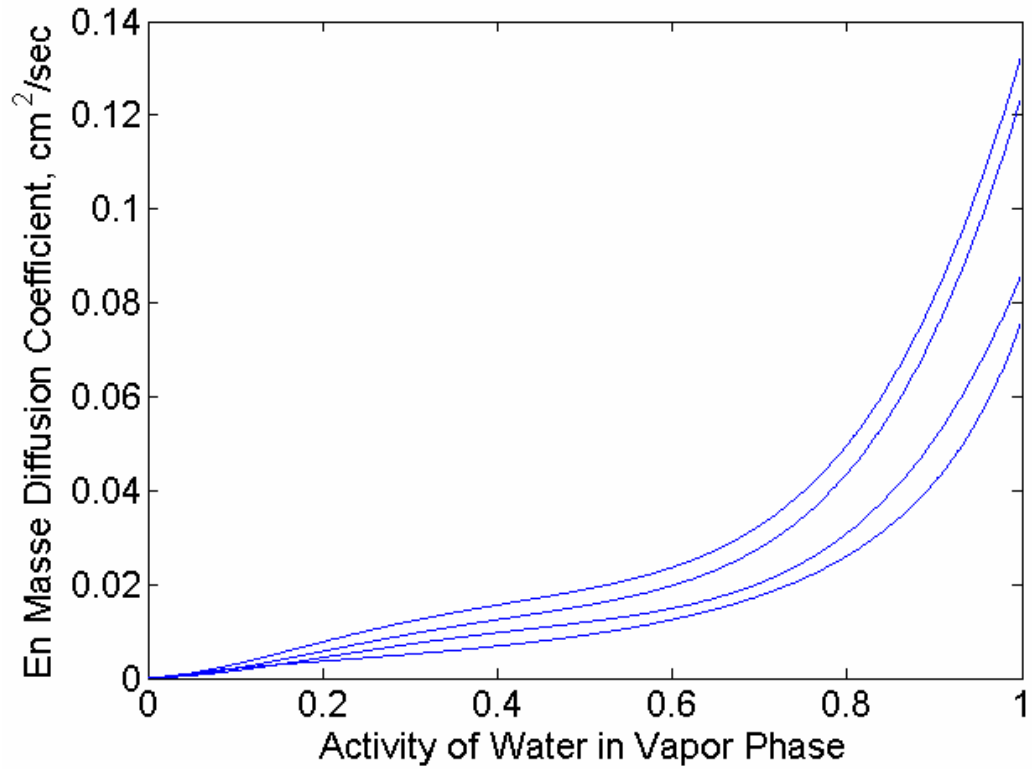

Figure 6-5. The effect of water vapor activity on the porosity/tortuosity ratio (From the top: 90^0C composite, 25^0C composite, 90^0C).

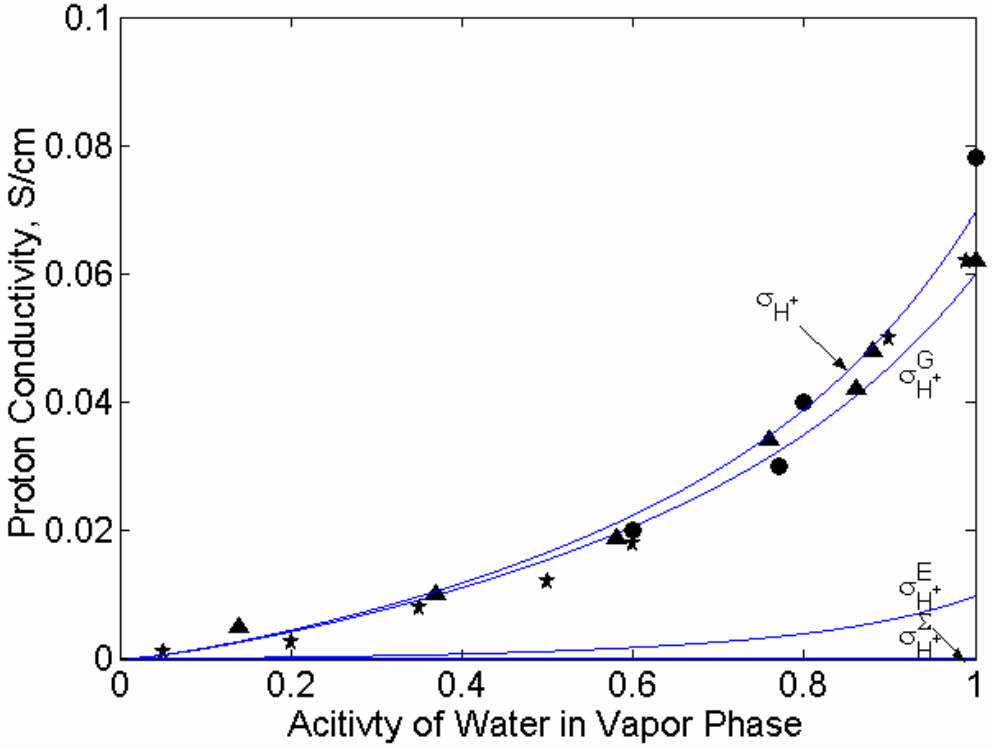

Figure 6-6. Proton conductivity of Nafion at 25^0 C.

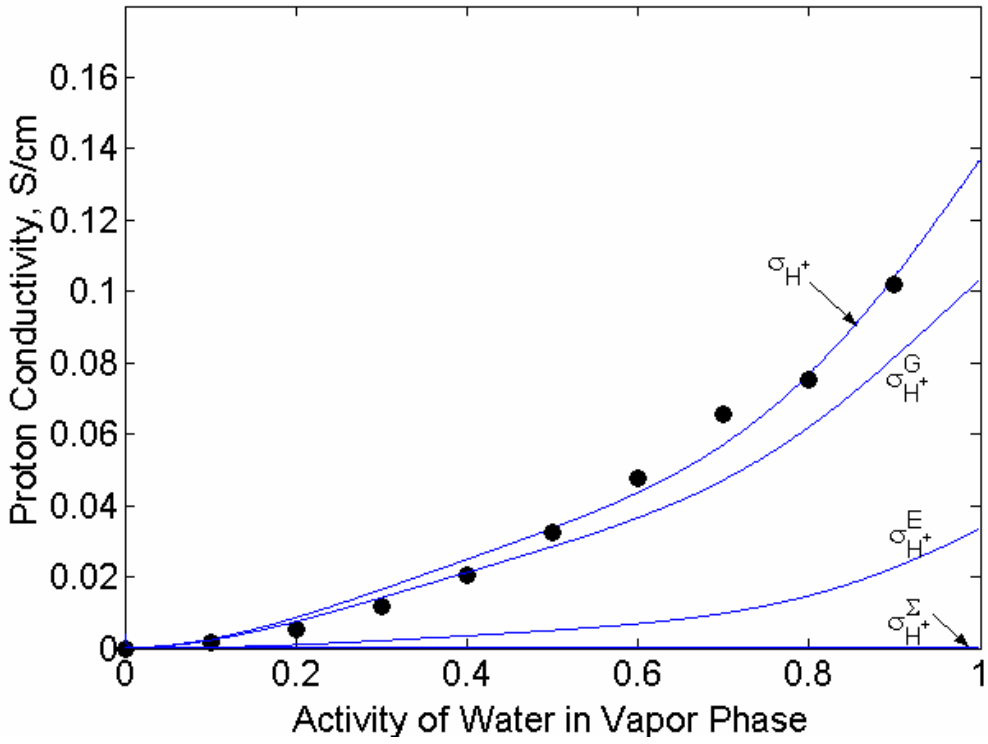

Figure 6-7. Proton conductivity of Nafion at 90^0 C.

coefficient, which is obtained from the limiting ionic molar conductivity data given by[49] $\lambda^0_{H+,T} = \lambda^0_{H+,298K}(1+0.0139(T-298))$, where $\lambda^0_{H+,298K}$ and $\lambda^0_{H+,T}$ are the limiting molar conductivity of proton at 298 K and temperature T (K), respectively. The model, thus, predicts proton conductivity of 0.04 S/cm and 0.06 S/cm at 25^0C and 90^0C for 80 % relative humidity conditions, respectively.

Figures 6-8 and 6-9 show the proton conductivity of Nafion/(ZrO_2/SO_4^{2-}) composite membrane at 25^0 C and 90^0 C, respectively. The proton conductivity of composite membrane is higher than that of Nafion® over the whole activity range of water vapor. For example, at 80 % relative humidity, conductivities of 0.06 S/cm and 0.105 S/cm are predicted for the composite membranes at 25^0C and 90^0C, respectively. This is due to the increased water uptake along with the increase of strong acid sites provided by ZrO_2/SO_4^{2-}. The proton conductivity increases with the activity of water and with temperature.

Figure 6-10 shows the effect of temperature on the proton conductivity at 80 % relative humidity condition. The Nafion®/(ZrO_2/SO_4^{2-}) composite membranes can, thus, provide higher proton conductivity than unmodified Nafion® over the entire range of temperatures. The proton conductivity of Nafion® can be improved by as much as 20 % with the incorporation of ZrO_2/SO_4^2 in the membrane via *in-situ* sol-gel technique if the parameters such as particle size and particle distributions are carefully controlled during the preparation procedure. The total proton conductivity in the membranes depends on i) the sorption equilibrium which affects water content and thus the porosity and tortuosity factor, diffusion coefficients, and acid concentration and distribution between surface and bulk.

The polymer/inorganic composite membranes are, thus, very promising, as it can provide better proton conductivity along with improved mechanical stability at higher temperature along with reduced methanol crossover. The model developed here may be

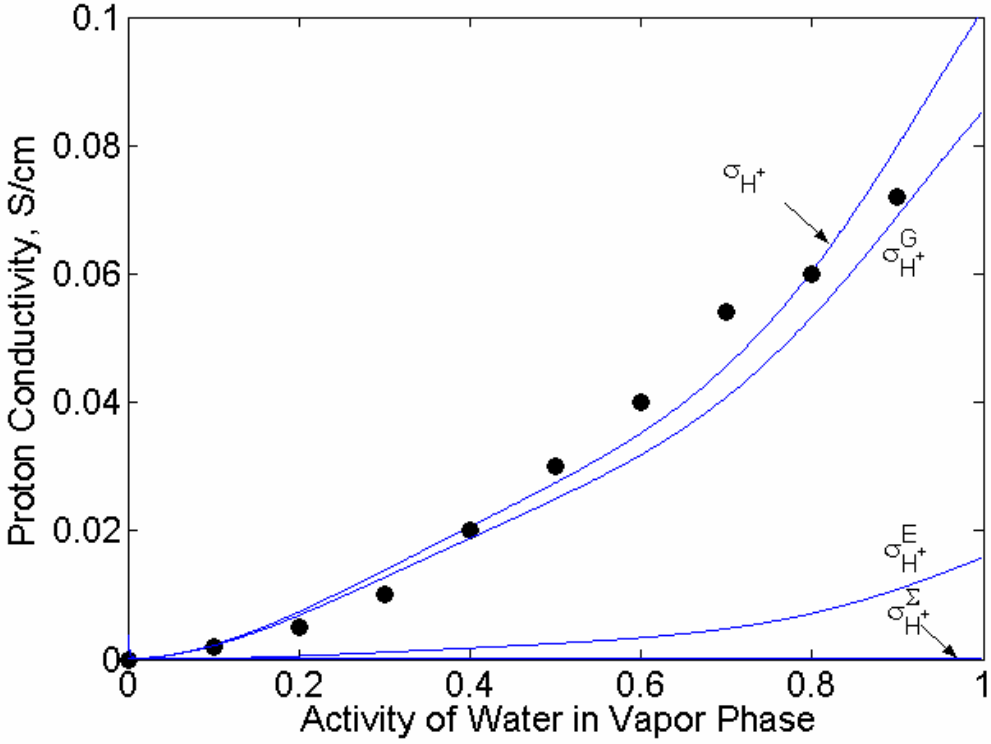

Figure 6-9. Proton conductivity of Nafion/(ZrO_2/SO_4^{2-}) at 25^0 C.

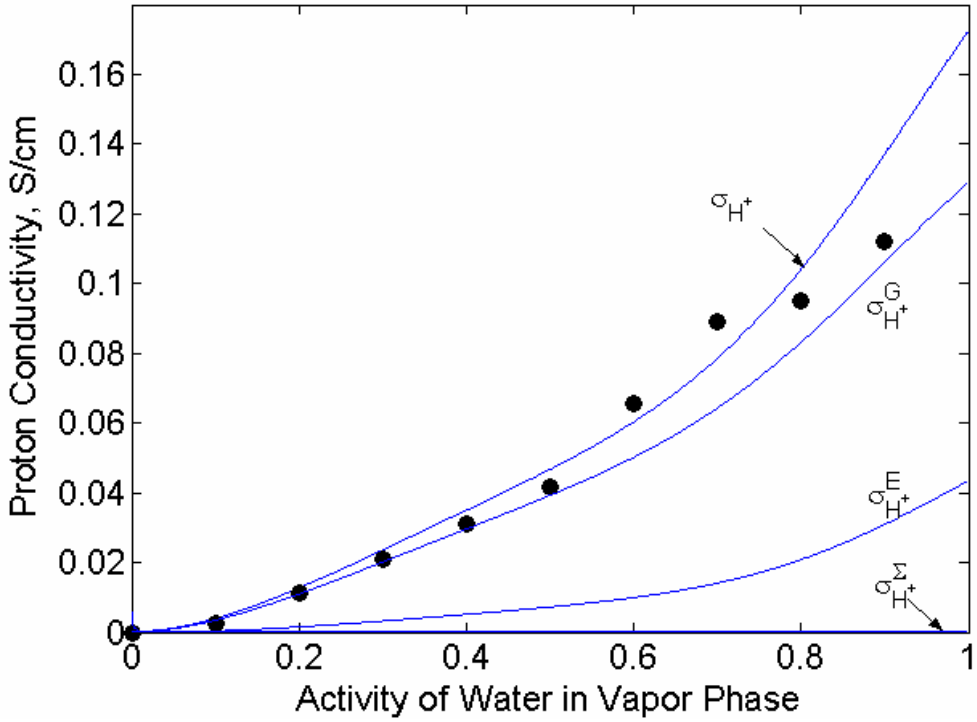

Figure 6-9. Proton conductivity of Nafion/(ZrO_2/SO_4^{2-}) at 90^0 C.

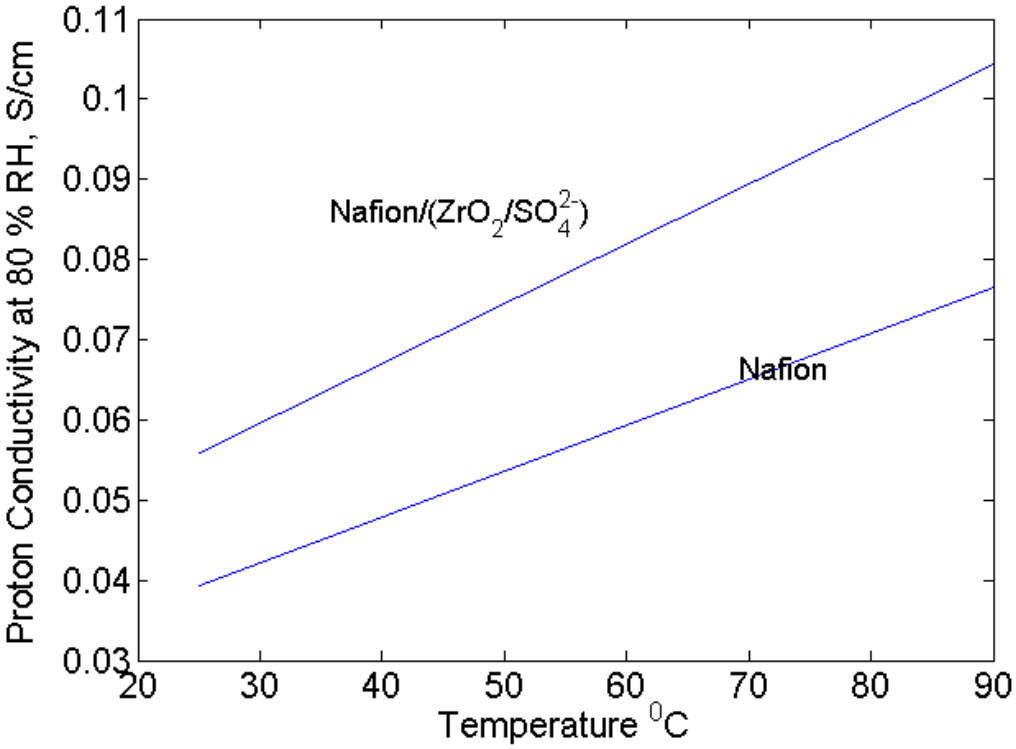

Figure 6-10. The effect of temperature on the proton conductivity.

applicable to other inorganics of different water sorption capacity, solid acidity, and surface acid density, and also extended to proton exchange membranes other than Nafion®.

6-5. Conclusions

A comprehensive proton transport model in Nafion/(ZrO_2/SO_4^{2-}) composite membrane has been proposed based on the understanding of structural and physicochemical properties of Nafion® and ZrO_2/SO_4^{2-}. The proton conductivity in the composite membrane depends on the water content, diffusion coefficients at the surface and bulk regions in the membrane, and concentration and distribution of protons. The model accounts for the acidity, surface acid density, particle size, and the amount of loading of the inorganics. The higher proton conductivity of the composite membrane compared with that of Nafion® is observed experimentally and also adequately predicted by the model without fitted parameters. The results are encouraging and this polymer/inorganic membrane can be classified as a remarkable family of proton exchange membranes which have great potential in fuel cell applications. The transport model developed here provides a theoretical framework for understanding the proton transfer in composite PEMs and should also be helpful in systematically investigating alternate high proton-conducting PEMs for fuel cell applications.

References

1. G. Alberti and M. Casciola, Annu. *Rev. Mater. Res.*, 33, 129 (2003).
2. B. C. H. Steele and A. Heinzel, *Nature*, **414**, 345 (2001).
3. P. Jannasch, *Curr. Opin. Colloid Interf. Sci.*, **8,** 96 (2003).
4. Q. Li, R. He, J. O. Jensen, and N. J. Bjerrum, *Chem. Mater.*, **15**, 4896 (2003).
5. C. Yang, P. Costamagna, S. Srinivasan, J. Benziger, and A. B. Bocarsly, *Journal of Power Sources,* **103**, 1 (2001).
6. N. Miyake, J. S. Wainright, and R. F. Savinell, *J. Electrochem. Soc.*, **149**, A256 (2001).
7. A. S. Arico, V. Baglio, A. D. Blasi, and V. Antonucci, *Electrochem. Comm.*, **5**, 862 (2003).
8. A. S. Arico, V. Baglio, A. D. Blasi, P. L. Antonucci, and V. Antonucci, *Solid State Ionics*, **161**, 251 (2003).
9. H. Uchida, Y. Ueno, H. Hagihara, and M. Watanabe, *J. Electrochem. Soc.*, **150**, A57 (2001).
10. T. Thampan, N. H. Jalani, P. Choi, and R. Datta, *J. Electrochem. Soc.*, 2004, Submitted.
11. P. Costamagna, C. Yang, A. B. Bocarsly, and S. Srinivasan, *Electrochim. Acta*, **47**, 1023 (2002).
12. S. Malhotra and R. Datta, *J. Electrochem. Soc.*, **144**, L23 (1997).
13. D. H. Jung, S. Y. Cho, D. H. Peck, D. R. Shin, and J. S. Kim, *J. Power Sources*, **118**, 205 (2003).
14. S. P. Nunes, B. Ruffmann, E. Rikowski, S. Vetter, and K. Richau, *J. Membr. Sci.*, **203**, 215 (2002).
15. B. Bonnet, D. J. Jones, J. Roziere, L. Tchicaya, G. Alberti, M. Casciola, L. Massinelli, B. Baner, A. Peraio, and E. Ramunni, *J. New. Mater. Electrochem. Syst.*, **3**, 87 (2000).
16. M. L. Ponce, L. Prado, B. Ruffmann, K. Richau, R. Mohr, and S. P. Nunes, *J. Membr.*

Sci., **217**, 5 (2003).

17. P. Staiti, *Materials Letters*, **47**, 241 (2001).
18. W. Apichatachutapan, R. B. Moore, and K. A. Mauritz, *J. Appl. Polym. Sci.*, **62**, 417 (1996).
19. Q. Deng, R. B. Moote, and K. A. Mauritz, *J. Appl. Polym. Sci.*, **68**, 747 (1998).
20. P. Liu, J. Bandara, Y. Lin, D. Elgin, L. F. Allard, and Y. P. Sun., *Langmuir*, **18**, 10389 (2002).
21. I. Honma, O. Nishikawa, T. Sugimoto, S. Nomura, and H. Nakajima, *Fuel Cells*, **2**, 52 (2002).
22. K. T. Adjemian, S. J. Lee, S. Srinivasan, J. Benziger, and A. B. Bocarsly, *J. Electrochem. Soc.*, **149**, A256 (2002).
23. P. Choi, N. H. Jalani, and R. Datta, *J. Electrochem. Soc.*, 2004, Submitted.
24. P. W. Atkins, *Physical Chemistry*, 3rd ed., W.H. Freeman and Company, NY (1986).
25. S. Mafe, J. A. Manzanares, and P. Ramirez, *Phys. Chem. Chem. Phys.*, **5**, 376 (2003).
26. D. Marx, M. E. Tuckerman, J. Hutter, and M. Parrinello, *Nature*, **601**, 397 (1999).
27. M. E. Tuckerman, *J. Phys. Condens. Matter*, **14**, R1297 (2002).
28. M. E. Tuckerman, D. Marx, and M. Parrinello, *Nature*, **417**, 925 (2002).
29. N. Agmon, *J. Phys. Chem.*, **100**, 1072 (1996).
30. S. Meiboom, *J. Chem. Phys.*, **34**, 375 (1961).
31. J. O'M. Bockris and A. K. N. Reddy, *Modern Electrochemistry 1 Ionics*, Plenum Press, NY (1998).
32. T. Thampan, S. Malhotra, H. Tang, and R. Datta, *J. Electrochem. Soc.*, **147**, 3242 (2000).
33. C. Ma, L. Zhang, S. Mukerjee, D. Ofer, and B. Nair, *J. Membr. Sci.*, **219**, 123 (2003).
34. K. D. Kreuer, *J. Membr. Sci.*, **185**, 29 (2001).
35. E. Glueckauf and G. P. Kitt, *Proc. Roy. Soc. London A,* **228**, 322 (1955).

36. G. A. Olah, G. K. S. Prakash, J. Sommer, *Superacid*, John Wiley and Sons, NY (1985).

37. R. Drago and N. Kob, *J. Phys. Chem. B*, 101, 3360 (1997).

38. F. Haase and J. Sauer, *J. Am. Chem. Soc.*, 120, 13503 (1998).

39. S. Koter, *J. Membr. Sci.*, **206**, 201 (2002).

40. B. Li and R. D. Gonzalez, *Ind. Eng. Chem. Res.*, **35**, 3141 (1996).

41. T. Kanougi, T. Atoguchi, and S. Yao, *J. Mol. Catal. A*, **177**, 289 (2002).

42. A. R. Ramadan, N. Yacoub, and J. Ragai, *J. Mater. Sci.*, 39, 1383 (2004).

43. K. Arata, M. Hino, *Mater. Chem. Phys.*, 26, 213 (1990).

44. M. T. Tran, N. S. Gnep, G. Gzabo, and M. Guisnet, *Appl. Catal. A: General*, **171**, 207 (1998).

45. J. H. Simpson, H. Y. Carr, *Phys. Rev*., **111**, 1201 (1958).

46. J. Ennari, M. Elomaa, and F. Sundholm, *Polymer*, **40**, 5035 (1999).

47. B. Cohen and D. Huppert, *J. Phys. Chem. B*, **107**, 3598 (2003).

48. N. Agmon, *Chem. Phys. Lett.*, **244**, 456 (1995).

49. P. Berezanski, in *Handbook of Instrumental Techniques for Analytical Chemistry*, Chap. 39, p. 749-764, F. Settle Ed., Prentice-Hall, Upper Saddle River, NJ (1997).

50. B. D. Cornish and R. J. Speedy, *J. Phys. Chem.*, **88**, 1888 (1984).

51. Y. Sone, P. Ekdunge, and D. Simonsson, *J. Electroanal. Chem.,* **143**, 1254 (1996).

52. T. A. Zawodzinski, C. Derouin, S. Radzinski, R. J. Sherman, V. T. Smith, T. E. Springer, and S. Gottesfeld, *J. Electrochem. Soc.,* **140**, 1041 (1993).

PART III.

Fuel Cell Systems

Chapter 7. Direct Methanol Fuel Cell (DMFC)

Chapter 8. Fuel Cell with Pd Nonporous Anode

Chapter 9. Water Electrolysis in Regenerative Fuel Cells

"Imagination is more important than knowledge."
- Albert Einstein -

Chapter 7. Direct Methanol Fuel Cell (DMFC)

7-1. Introduction

Direct Methanol Fuel Cells (DMFC) was pioneered by Shell Research in England and Exxon-Alsthom in France in the 1960 and 1970s, and is considered as a highly promising power source for future applications.[1-10] The great advantage of DMFC is that it is a relatively simple system that uses methanol directly as a fuel. Methanol is much easier than hydrogen in terms of energy density, handing, storing, and using the infrastructure for its distribution. However, near-term projected applications are expected as power sources for cellular phones, laptop computers and small electronic toys because DMFC system produces relatively low power density compared with hydrogen fuel cell due to the poor kinetics of anode reaction and methanol crossover. Potential applications of DMFC are shown in Table 7-1 as a function of power output of the device.

This chapter deals with these technological issues. First, a basic DMFC performance model and a simple kinetic model of the electrochemical methanol oxidation are developed. Second, experimental observation of oscillatory behavior of the current at constant voltage mode is reported during the DMFC operation. Third, the so-called "methanol crossover" problem is explored to block the transport of methanol through the PEM completely via the formation of thin palladium layer in anode side of DMFC.

7-2. Experiment

Catalyst preparation - Electrodes for MEA are prepared as follows. First, put Pt and PtRu catalyst (Johnson Matthey) in water and add ethanol solution in order. Second, add 10 wt % Nafion® solution, from a solution of 5 wt % Nafion® dissolved in a mixture of water and

Table 7-1. Potential applications of DMFCs (ref. 6).

Potential Applications	Field	Rated Power	Overall Efficiency Requirement, %	Specific Power, W/kg	Operation Temperature, ^{0}C
Transportation	Electromotive	20-50 kW	35-45	350-500	130-150
	APU	3-5 kW	35-45	350-500	130-150
Portable	Laptop	50-100 W	20	50	0-45
	Cellular Phone	1-3 W	20	30	0-45
Stationary	Residential	5-10 kW	35-45	200	90-150
	Remote Power Generation	10-100 kW	35-45	200	90-150

low aliphatic alcohol, to the catalyst solution and mix homogeneously using sonicator for 24 hours. Third, spread the solution on a carbon cloth (E-TEK), a diffusion backing layer.

Membrane pretreatment - Membranes are pretreated by consecutive boiling the Nafion® 117 for 3 hours in 5 vol % H_2O_2, 3 hours in de-ionized water, 3 hours in 1 M H_2SO_4 solution and 3 hours in de-ionized water.

MEA preparation - MEAs are prepared by placing electrodes either side of a pretreated Nafion® 117 and hot pressing at 100 kg/cm^2 for 3 minutes at 135^{0}C.

Fuel cell experiment - Figure 7-1 shows a schematic diagram of direct methanol fuel cell. Methanol solution is fed continuously into the anode, diffused through the diffusion layer and is electrochemically reduced on the anode surface to produce protons and electrons. An oxidant, *e.g.,* oxygen or air, is fed continuously into the cathode and reacts upon dissociation with the electrons traveling through an external wire and protons diffusing through the membrane to produce water. The DMFC experiments were carried out in different temperatures and pressures. The catalyst loadings used were 4 mg PtRu/cm^2 and 4 mg Pt/cm^2 for the anode and cathode, respectively. The concentration of methanol feed solution used was 1 M and the anode flow rate was 0.5 – 2 ml/min. Pure oxygen was used for the cathode feed and its flow rate was 40 ml/min. The flow rate of methanol solution and the oxygen gas was carefully controlled by electronic Pump Controller (ISD Series D) and Mass Flow Controller (Tylan General RO 28), respectively. The current and voltage of the cell was controlled by the Electronic Load (HP 6060B Electronic Load with HP 6651 DC Power Supply). Temperature of the cell was controlled by Temperature Controller.

Open circuit voltage measurement – The open circuit voltage (OCV) of the DMFC was measured after the cell was switched from a load to a no load condition. In other words, during the DMFC experiment, the external load was cut off and the change in the cell

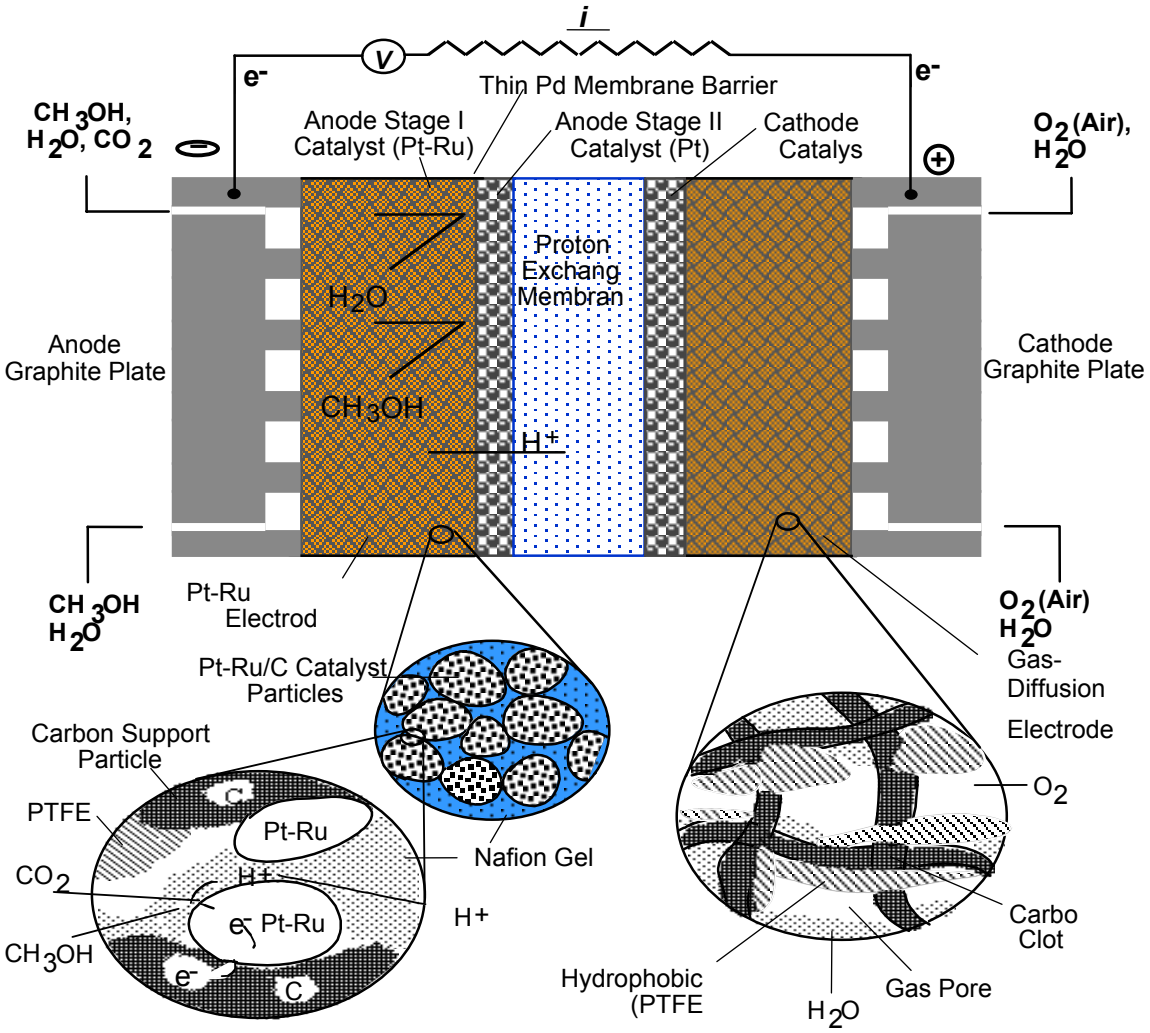

Anode : $CH_3OH\ (l) + H_2O\ (l) \rightarrow CO_2\ (g) + 6H^+ + 6e^-$	$E^0(25^0C) = 0.02$ V
Cathode : $1.5O_2\ (g) + 6H^+ + 6e^- \rightarrow 3H_2O\ (l)$	$E^0(25^0C) = 1.23$ V
Overall : $CH_3OH\ (l) + 1.5O_2\ (g) \rightarrow CO_2\ (g) + 2H_2O\ (l)$	$E^0(25^0C) = 1.21$ V

Figure 7-1. A schematic diagram of cross-section of DMFC.

voltage with time was measured using a Multimeter. The voltage of the cell increased quickly, reached a peak value, and then starts to decline, eventually becoming stabilized. This stabilized value was taken as the OCV of the cell at the reaction condition.

Conductivity measurement - Conductivity of Nafion 117 was obtained using AC impedance (Solatron SI 1287 with SI 1260). The impedance spectra were measured in constant voltage mode by sweeping the frequencies over the 0.01 Hz to 10 KHz range. Two-electrode mode was performed with the cell. Resistance of the Nafion 117 was measured and the conductivity is calculated by the following relation

$$\sigma = \frac{L}{RA} \qquad [1]$$

where R is resistance and L is a length of segment along the field and A is the cross-sectional area perpendicular to the field vector. Standard sample of 0.1 M KCl was used to calibrate the cell.

7.3 Results and Discussions

DMFC Performance – Figures 7-2 through 7-5 shows DMFC performance for the temperature and pressure ranges of 60^0C - 90^0C, 0 - 2 atm, respectively. The flow rates of methanol solution were changed from 0.5 ml/min to 2 ml/min. Several variables affect the cell voltage-current characteristics of DMFC: temperature, pressure, methanol concentration, oxygen partial pressure, flow rates of the feed, etc. In addition to this, types of proton exchange membranes, method of catalyst preparation, and overall electrode structure also affect the performance of DMFC. In general, high temperature and pressure give rise to a better DMFC performance. At high temperature, the reaction rate at the electrodes is increased and ohmic resistance becomes reduced. Therefore, the improvement of performance with temperature can be attributed to the enhanced anode kinetics and a reduction of corresponding polarization. Further, the conductivity of Nafion

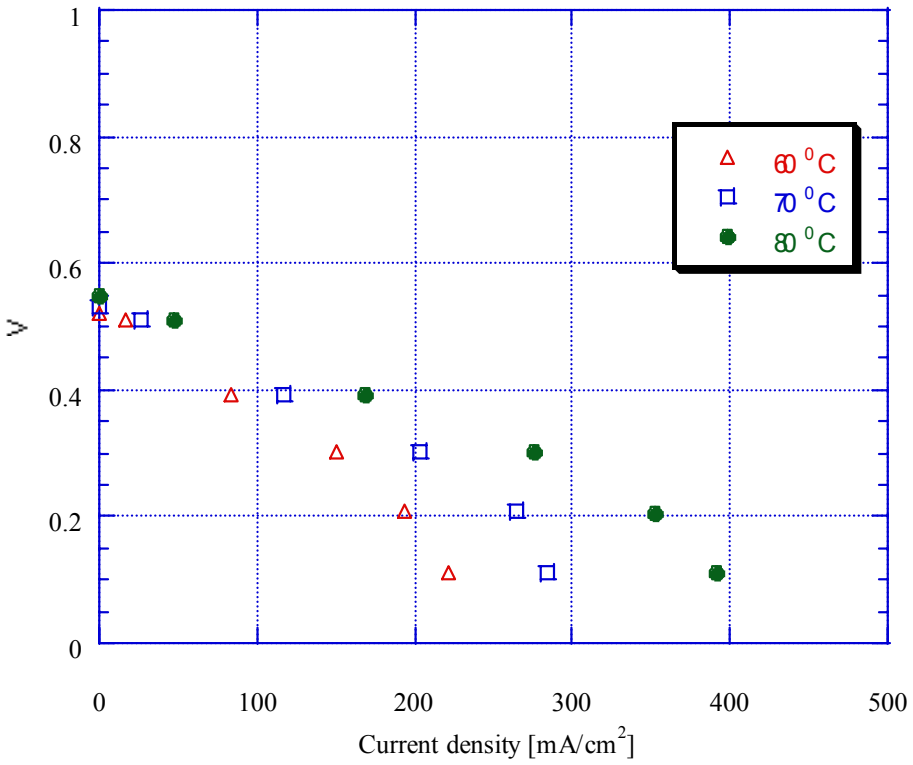

Figure 7-2. DMFC performance at 0 atm (gauge), 1M methanol 1ml/min, and O_2 40 ml/min.

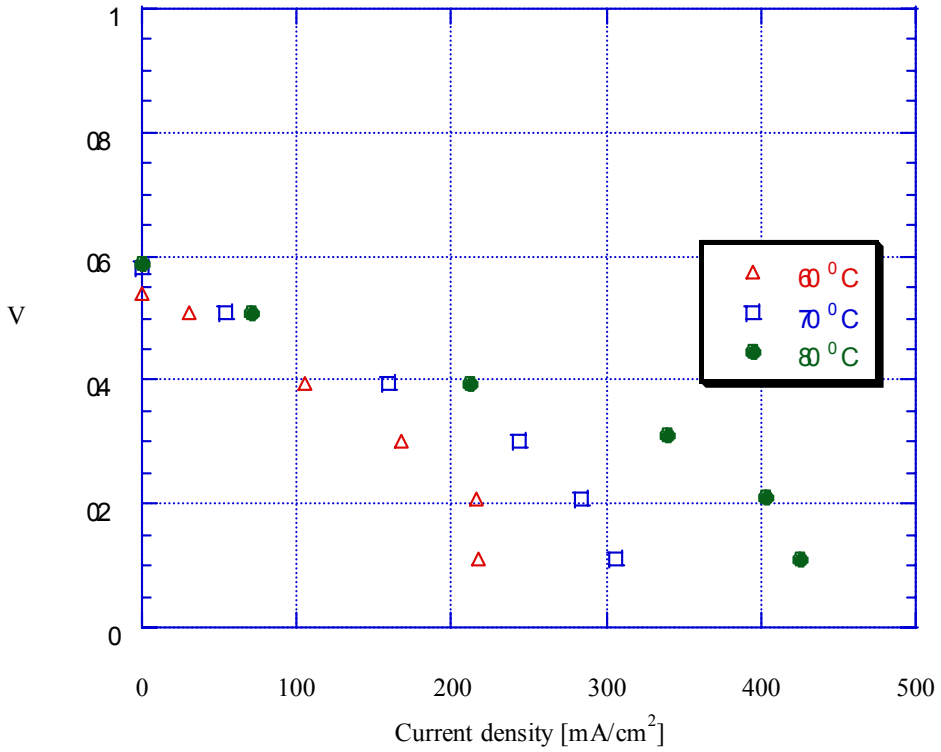

Figure 7-3. DMFC performance at 1 atm (gauge), 1M methanol 1ml/min, and O_2 40 ml/min.

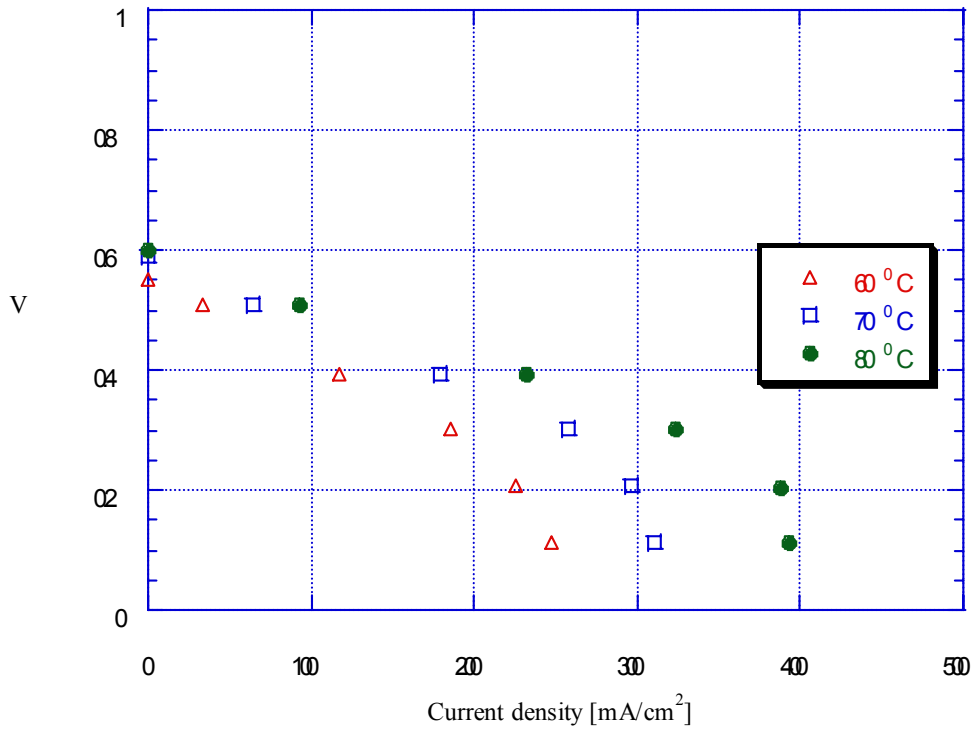

Figure 7-4. DMFC performance at 2 atm (gauge), 1 M methanol 1ml/min, and O_2 40 ml/min.

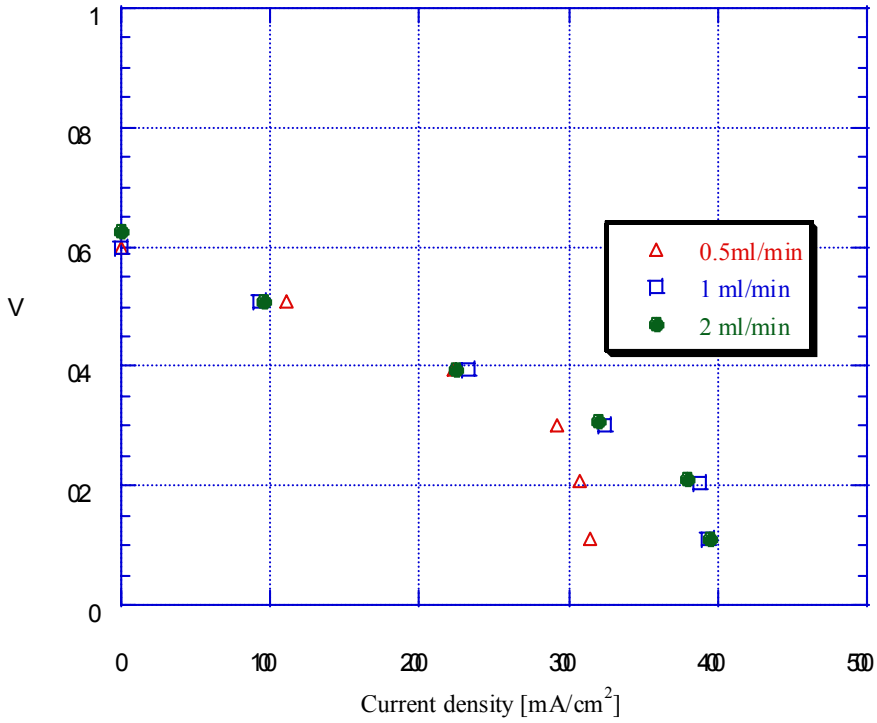

Figure 7-5. Effect of flow rate of methanol solution at 2 atm, 1 M methanol, and O_2 40 ml/min.

increases with the temperature. Figure 7-2 shows cell polarization data for the different temperatures with methanol concentration of 1 M and pure oxygen at atmospheric conditions. At low current densities, the effect of varying temperature is not appreciable and the variation OCV is small for the temperature range investigated. DMFC performance increases with the temperature and pressure (Figure 7-2, 7-3, and 7-4). Pressurizing the cathode side reduces the methanol crossover and enhanced cathode performance, leading to a higher cell voltage. Figure 7-5 shows the effect of flow rate of methanol solution at 2 atm. At low current densities, no difference in DMFC performance was observed. However, at higher current densities, the performance was lower at the low flow rate of 0.5 ml/min. The performance was, however, unchanged at 1 or 2 ml/min.

Open Circuit Potential – The thermodynamic reversible potential for DMFC is 1.21 V. However, the measured open circuit voltage (OCV) of DMFC is in the range of 0.5 V - 0.8 V. The reported OCVs are not coincident because of its unsteady nature when the system is changed from load to unload condition. Figure 7-6 shows the variation of OCV with time. Initially, OCV increases very quickly and decreases slowly and reaches a steady state value after 3 minutes. The reason for this seems related to the methanol crossover. Table 7-2 shows the OCV of DMFC at different temperatures and pressures. In all cases, the OCV shows the transient behavior when the cell switched from load to no load condition. The steady state OCV is obtained after the steady state value is reached in the no load condition. Possible reasons for this are potentials of mixed reactions and poisoning of anode and cathode by CO-like intermediate species. While in principle, OCV should not affected by poisoning, in fact a minute current is drawn when the Multimeter is used, leading to overpotentials at both the anode and especially the cathode. Similar cathode overpotential is responsible for OCV of H_2-O_2 fuel cell to be around 1. 0 V instead of the Nernst potential of 1. 23 V.

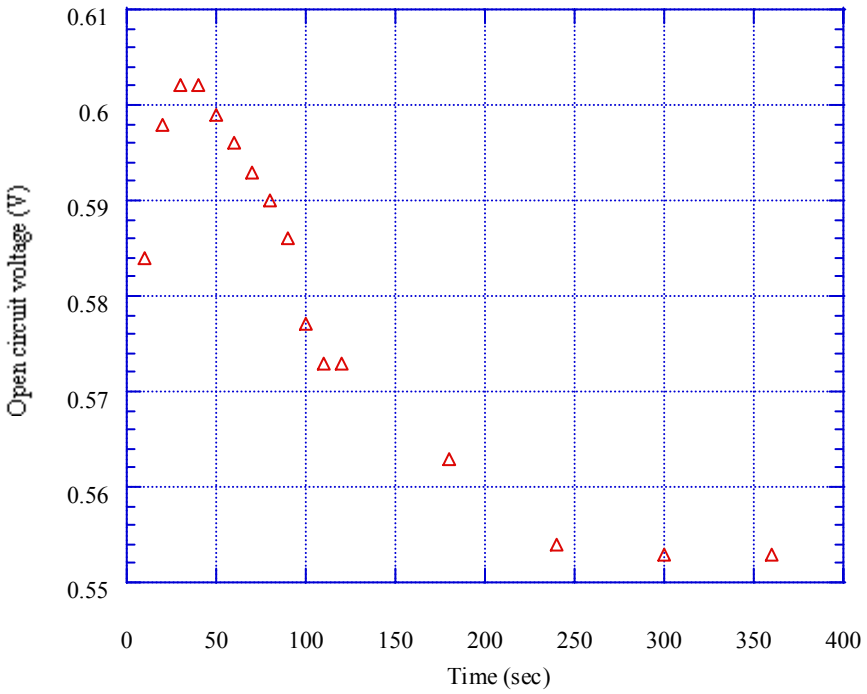

Figure 7-6. The change of OCV after a load is removed from 0.1 V at 25^0C and 0 atm O_2.

Table 7-2 Open circuit voltage of DMFC
(1M methanol 0.5ml/min, pure oxygen 40 ml/min).

Temp (^{0}C)	P (atm)	Open Circuit Voltage (Volt)
25	0	0.553
	1	0.554
	2	0.542
50	0	0.557
	1	0.614
	2	0.606
80	0	0.620
	1	0.643
	2	0.654

Conductivity of protons in Nafion® – Table 7-3 shows the measured conductivity of Nafion® in water and methanol solutions. The conductivity of Nafion® in water is higher than that in methanol. The conductivity corresponds to the H^+ equivalent conductance in water and methanol.

7-4. Modeling of DMFC

a) Steady State Modeling – DMFC using liquid methanol, instead of vaporized methanol, is desirable because of easy start up and maintenance of high humidity that is critical for the proton transfer through the PEM. The physicochemical phenomena taking place inside of DMFC are complex: carbon dioxide is formed within the anode catalyst layer and released as bubbles because of its low solubility in the liquid phase, which also impedes the methanol flux; methanol permeates through the membrane to the cathode generating a mixed potential, the kinetics of six electron generation at the anode involves several steps of reaction including many carbon-containing intermediates that make further reaction difficult because of their strong affinity for the catalyst surface. Because of the complexity of the system, a simple steady state model of DMFC is developed here based on the following assumptions.

1. Anode compartment is considered well-mixed, i.e., as a continuous stirred tank reactor (CSTR).
2. The diffusion of methanol, carbon dioxide and oxygen through the PEM is neglected.
3. The following electrochemical reactions take place: oxidation of methanol at anode and reduction of oxygen at cathode side of the cell.

Figure 7-1 is used for analysis of DMFC. The conservation equations at steady state for each compartment of the cell are given as follows:

Anode Chamber (AC)

Table 7-3. Conductivity of methanol solution.

	Methanol solution						
	H_2O	1M	2M	5M	10M	17M	Methanol
Conductivity (S/cm)	0.073	0.07	0.067	0.061	0.05	0.038	0.025

$$F_A\left(C_{CH3OH,in} - C_{CH3OH,out}\right) = N_{CH3OH,a}A \quad [2]$$

$$F_A\left(C_{H2O,in} - C_{H2O,out}\right) = N_{H2O,a}A \quad [3]$$

Anode Diffusion Layer (ADL)

$$\frac{dN_{i,z}}{dz} = 0 \quad [4]$$

$$N_{CH3OH,ab} = \frac{D^e_{ab}}{L_{ab}}\left(C_{CH3OH,a} - C_{CH3OH,b}\right) \quad [5]$$

Anode Catalyst Layer (ACL)

At point b,

$$N_{CH3OH,b} = \gamma_{MA}\left(-\nu_{A,CH3OH}\right)k_A C_{CH3OH,b} \quad [6]$$

$$i_A = \gamma_{MA} F \nu_{A,e^-} k_A C_{CH3OH,b} \quad [7]$$

At the electrodes, methanol is oxidized to carbon dioxide at anode and oxygen is reduced to water at cathode as follows;

Anode: $H_3OH + H_2O \leftrightarrows CO_2 + 6H^+ + 6e^-$ [8]

Cathode: $.5O_2 + 6H^+ + 6e^- \leftrightarrows 3H_2O$ [9]

Butler-Volmer form of rate expression is often used for methanol electro-oxidation and is adopted here

Butler-Volmer equation

For Anode

$$r_A = \vec{k}_A(T)C_{CH3OH,b}\exp\left(\frac{\nu_{\rho e^-}\alpha_A F\eta_A}{RT}\right) - \overleftarrow{k}_A(T)C_{CO2,b}\exp\left(-\frac{\nu_{\rho e^-}(1-\alpha_A)F\eta_A}{RT}\right) \quad [10]$$

For $\alpha_A = 0.5$, the pseudo-irreversible form is

$$r_A = k_A C_{CH3OH,b} \quad [11$$

where

$$k_A = k_{A,\phi_0}\left[2\sinh\left(\frac{\nu_{\rho e^-} F\eta_A}{RT}\right)\right] \quad [12]$$

Equating Eqs. 5 and 6, the concentration of methanol at b is

$$C_{CH3OH,b} = \frac{\frac{D_{ab}}{L_{ab}} C_{CH3OH,a}}{\left(-\nu_{A,CH3OH}\right)\gamma_{MA} k_A + \frac{D_{ab}}{L_{ab}}} \quad [13]$$

Substituting equation 13 into equation 7,

$$i_A = \gamma_{MA} F \nu_{A,e^-} k_A \frac{\frac{D_{ab}}{L_{ab}} C_{CH3OH,a}}{\left(-\nu_{A,CH3OH}\right)\gamma_{MA} k_A + \frac{D_{ab}}{L_{ab}}} \quad [14]$$

When the diffusion controls the rate,

$$\left(-\nu_A\right)\gamma_{MA} k_A >> \frac{D_{ab}}{L_{ab}} \quad [15]$$

Eq. 14 can be rearranged for the anode limiting current density as

$$i_{AL} = \left(-\frac{\nu_{Ae^-}}{\nu_{A,CH3OH}}\right)\left(\frac{D_{ab}}{L_{ab}}\right) F C_{CH3OH,a} \quad [16]$$

The anode exchange current density can be written similarly to Eq. 7 assuming uniform concentration of methanol as

$$i_{A0} = \gamma_{MA} F \nu_{A,e^-} \vec{k}_{A,\phi_0} C_{CH3OH,a} \quad [17]$$

Substituting Eqs. 16 and 17 into 14 and rearranging gives

$$\frac{k_A}{\vec{k}_{A,\phi_0}} = \left(\frac{i_A / i_{A0}}{1 - i_A / i_{AL}}\right) \quad [18]$$

The anode over-potential can be obtained from the Eqs. 12 and 18 as

$$\eta_A = \frac{RT}{\alpha_A F}\sinh^{-1}\left[\frac{1}{2}\left(\frac{i_A / i_{A0}}{1 - i_A / i_{AL}}\right)\right] \quad [19$$

Similarly for cathode over-potential,

$$\eta_C = -\frac{RT}{\alpha_C F}\sinh^{-1}\left[\frac{1}{2}\left(\frac{i_C / i_{CO}}{1 - i_A / i_{AL}}\right)\right] \quad [20]$$

The cathode exchange density can be written as

$$i_{C0} = \gamma_{MC} F \nu_{C,e^-} \vec{k}_{A,\phi_0} C_{O2,f} \quad [21]$$

where the cathode limiting current density is

$$i_{CL} = \frac{\nu_{C,e^-}}{-\nu_{C,O2}}\left(\frac{D_{ef}^e}{L_{ef}}\right) F C_{O2,f} \quad [22]$$

The overall cell potential of the fuel cell can be written as

$$V = V_0 + \eta_C - \eta_A - \eta_{ohmic} \quad [23]$$

where η_{ohmic} denotes the ohmic drop over the fuel cell which can be written as

$$\eta_{ohmic} = i\left(\frac{L_B}{\sigma_B}\right) + iR_I \quad [24]$$

where L_B is the thickness of the membrane, σ_B is conductivity of the membrane and R_I is the interfacial resistance.

The methanol crossover may decrease the potential of DMFC by the formation of surface carbon species at the anode and cathode. In other words, the exchange current density at anode and cathode may be written as[13]

$$i_{Ao,eff} = (1 - \theta_{CO,A})^2 i_{A0} \quad [25]$$

$$i_{Co,eff} = (1 - \theta_{CO,C})^2 i_{C0} \quad [26]$$

or more explicitly as a function of temperature and surface coverage of carbon-containing species, e.g., CO, as

$$i_{A0} = \gamma_{MA}\left(1-\theta_{CO,A}\right)^{\chi} \exp\left[-\frac{E_{A,\Phi_0}}{R}\left(\frac{1}{T}-\frac{1}{T_{ref}}\right)\right] i_{A0,ref} \qquad [27]$$

where γ_{MA} is the roughness factor, $\theta_{CO,A}$ is surface CO coverage on anode, E_{A,Φ_0} is the effective activation energy of exchange current density, R is the gas constant, $i_{A,0,ref}$ is the reference current density and χ is the affinity factor, typically 2. The surface coverage of carbon-containing species is not known for DMFC and may be estimated from the CO coverage of hydrogen fuel cell with CO containing anode feed. The surface of the cathode is assumed to be covered with carbon-containing species because of the permeated methanol. The theoretical OCV is 1.21 V, while the experimental value is 0.5-0.7 V. Therefore, there is large potential drop caused by an increase in overpotential at the anode due to undesired carbon containing intermediates on the catalyst surface, as well as by the overpotential for oxygen reduction reaction on the poisoned surface. The huge drop in fuel cell potential at low current density is a characteristic feature of DMFC as compared with hydrogen-oxygen fuel cell.

The analytical model above incorporates many of the reaction and transport details of all the compartments of DMFC. The model describes the steady state behavior of DMFC quantitatively and provides an insight for the each part of DMFC.

b) Dynamic Modeling of DMFC - A dynamic model is developed here to account for the details of the surface chemistry of the electrode. If the concentration of the key surface intermediates of the electrochemical reaction varies with time in a certain manner, the resulting current or voltage would also change with time correspondingly. The time-dependent behavior of current or voltage is often observed in many electrochemical

systems. A mathematical model for this is developed here based on the following assumptions.

1. The anode chamber is considered as being well-mixed, i.e., it is treated as a continuous stirred tank reactor.
2. The temperature of fuel cell is constant (isothermal operation).
3. Oxygen and carbon dioxide do not diffuse through the membrane.
4. Ohmic resistance in current collector and electric connections are negligible.
5. The catalyst surface is uniform.

Surface mechanism

The electrochemical oxidation of methanol at anode is a multi-step reaction involving six electrons. The oxidation of methanol on Pt is inhibited by the adsorbed CO and hydrogenated residues such as COH, HCOH, CH_2OH. The following simple scheme is adopted here.

The elementary reactions can be written as the first step of methanol adsorption and successive stripping of hydrogen atom as follow:

$$Pt + CH_3OH \leftrightarrows Pt\text{-}(CH_3OH)_{ads} \qquad r_1 \qquad [28]$$

$$Pt\text{-}(CH_3OH)_{ads} \leftrightarrows Pt\text{-}(CH_2OH)_{ads} + H^+ + e^- \qquad r_2 \qquad [29]$$

$$Pt\text{-}(CH_2OH)_{ads} \leftrightarrows Pt\text{-}(CHOH)_{ads} + H^+ + e^- \qquad r_3 \qquad [30]$$

$$Pt\text{-}(CHOH)_{ads} \leftrightarrows Pt\text{-}(CHO)_{ads} + H^+ + e^- \qquad r_4 \qquad [31]$$

$$Pt\text{-}(CHO)_{ads} \leftrightarrows Pt\text{-}(CO)_{ads} + H^+ + e^- \qquad r_5 \qquad [32]$$

$$Ru(s) + H_2O \leftrightarrows Ru\text{-}(OH)_{ads} + H^+ + e^- \qquad r_6 \qquad [33]$$

$$Pt\text{-}(CO)_{ads} + Ru\text{-}(OH)_{ads} \leftrightarrows Pt + Ru + CO_2 + H^+ + e^- \qquad r_7 \qquad [34]$$

The corresponding rate expressions using Butler-Volmer relation can be written as

$$r_1 = \vec{k}_1\theta_0 - \overleftarrow{k}_1\theta_{CH3OH} \quad [35]$$

$$r_2 = \vec{k}_2\theta_{CH3OH}\exp\left(\frac{\alpha_2 F\eta_A}{RT}\right) - \overleftarrow{k}_2\theta_{CH2OH}\exp\left(-\frac{(1-\alpha_2)F\eta_A}{RT}\right) \quad [36]$$

$$r_3 = \vec{k}_3\theta_{CH2OH}\exp\left(\frac{\alpha_3 F\eta_A}{RT}\right) - \overleftarrow{k}_3\theta_{CHOH}\exp\left(-\frac{(1-\alpha_3)F\eta_A}{RT}\right) \quad [37]$$

$$r_4 = \vec{k}_4\theta_{CHOH}\exp\left(\frac{\alpha_4 F\eta_A}{RT}\right) - \overleftarrow{k}_4\theta_{COH}\exp\left(-\frac{(1-\alpha_4)F\eta_A}{RT}\right) \quad [38]$$

$$r_5 = \vec{k}_5\theta_{COH}\exp\left(\frac{\alpha_5 F\eta_A}{RT}\right) - \overleftarrow{k}_5\theta_{CO}\exp\left(-\frac{(1-\alpha_5)F\eta_A}{RT}\right) \quad [39]$$

$$r_6 = \vec{k}_6\exp\left(\frac{\alpha_6 F\eta_A}{RT}\right) - \overleftarrow{k}_6\theta_{OH}\exp\left(-\frac{(1-\alpha_6)F\eta_A}{RT}\right) \quad [40]$$

$$r_7 = \vec{k}_7\theta_{CO}\theta_{OH}\exp\left(\frac{\alpha_7 F\eta_A}{RT}\right) - \overleftarrow{k}_7\theta_{OH}\exp\left(-\frac{(1-\alpha_7)F\eta_A}{RT}\right) \quad [41]$$

Reaction 41 may be assumed to be irreversible.

Mass balance and charge conservation

The surface coverage, θ_{COH}, θ_{OH} and θ_{COOH}, varies with time on the electrode surface and the site balance for each species are

$$F\gamma C_t^* \frac{d\theta_{CH3OH}}{dt} = r_1 - r_2 \quad [42]$$

$$F\gamma C_t^* \frac{d\theta_{CH2OH}}{dt} = r_2 - r_3 \quad [43]$$

$$F\gamma C_t^* \frac{d\theta_{CHOH}}{dt} = r_3 - r_4 \quad [44]$$

$$F\gamma C_t^* \frac{d\theta_{COH}}{dt} = r_3 - r_4 \quad [45]$$

$$F\gamma C_t^* \frac{d\theta_{CO}}{dt} = r_4 - r_5 \quad [46]$$

$$F\gamma C_t^* \frac{d\theta_{OH}}{dt} = r_5 - r_6 \quad [47]$$

Site balance among the surface coverage is

$$1 = \theta_0 + \theta_{CH3OH} + \theta_{CH2OH} + \theta_{CHOH} + \theta_{COH} + \theta_{CO} + \theta_{OH} \quad [48]$$

Assuming the anode chamber as a continuous stirred tank reactor, the mass balance for methanol is

$$V \frac{dC_{CH_3OH}}{dt} = v_0 C_{CH_3OH,0} - vC_{CH_3OH} - N_{CH_3OH} A - r_1 \quad [49]$$

where N_{CH_3OH} accounts for the methanol crossover through the membrane. It is a function of concentration gradient between anode and cathode side and also of current across the fuel cell. Since the concentration of methanol at cathode side is relatively small compared with that of anode, the flux of methanol crossover can be approximated to proportional to anode concentration if the current effect is negligible as

$$N_{CH3OH} = mC_{CH_3OH} \quad [50]$$

Besides the mass balance, the model contains charge balance. Since the total current is the sum of Faradic and capacitive current, the current and the time variation of potential can be obtained as

$$C_{dl} \frac{d\eta_A}{dt} = A\left(i - r_2 - r_3 - r_4 - r_5 - r_6 - r_7\right) \quad [51]$$

From the analysis, there are eight ordinary differential equations, Eqs. 42-47, 49 and 51 along with eight variables, θ_{CH3OH}, θ_{CH2OH}, θ_{CHOH}, θ_{COH}, θ_{CO}, θ_{OH}, C_{CH3OH} and η_A. The

simulation of the anode kinetics needs to be studied with appropriate parameters for the methanol oxidation reaction.

7-5. Experimental Current Oscillations in DMFC

The anode reaction of DMFC is the oxidation of methanol by electrochemical reaction. It may be assumed that a surface carbon species are responsible for the slow kinetics at the anode. Figure 7-7 shows the experimental data of current density as a function of time at different potentials from 0.1 V to 0.5 V. For the DMFC potential of 0.1 V, current oscillates from 0.6 to 1.4 A per 5 cm^2 MEA. Figure 7-8 shows the amplitude and period of the oscillations. At low potential, the current oscillates over wide ranges with irregular manner. This may be due to the many carbon-containing surface species react competitively. However, the amplitude of the oscillation decreases with the increase of potentials due to the one or two surface species determine the overall reaction and, thus, the current generation is rather regular. However, the periods of the oscillation remain the same at about 7.5 minutes for all the different potentials. The oscillatory behavior of electrochemical reactions has been reported for many systems,[15-20] although current oscillations are less common than potential oscillations. Current oscillations under potentiostatic conditions and potential oscillation under galvanostatic systems of HCOOH on Pt were reported.[21] Potential oscillations of methanol[22] and ethanol oxidation[23] in acid solutions have also been observed, although the mechanistic details are not well understood. The oscillations of current have not been reported yet under DMFC conditions. The reason for the current oscillation in DMFC can be attributed to the transition of the electrode surface from a poisoned to an active state. Based on the mechanism suggested above, the current oscillation with time may be adequately understood. From Eq. 50, for constant potential mode,

$$i = r_2 + r_3 + r_4 + r_5 + r_6 + r_7 \qquad [52]$$

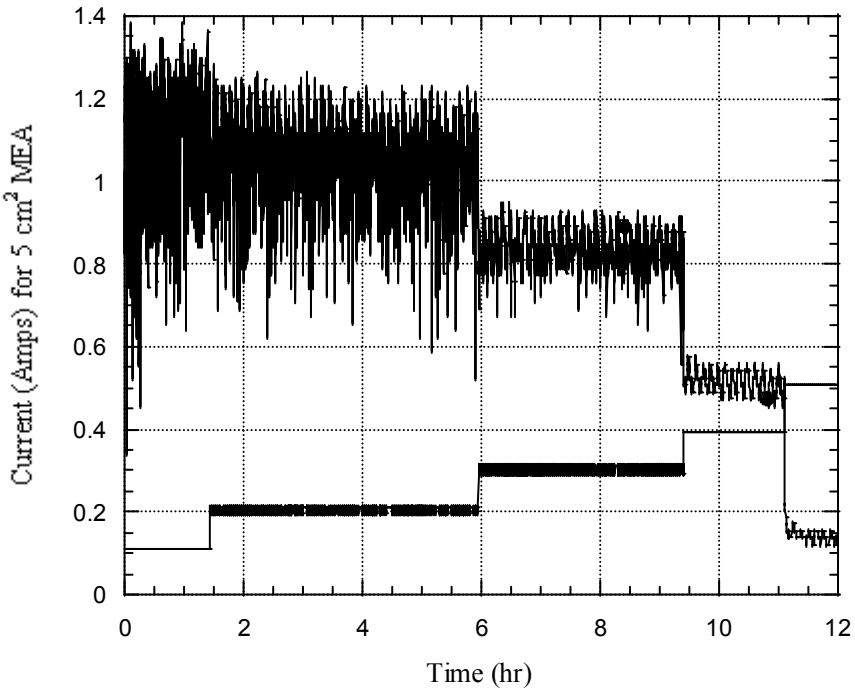

Figure 7-7. Current oscillations in DMFC (60ºC, 0 psig O_2, 1 M Methanol, 0.5 ml/min).

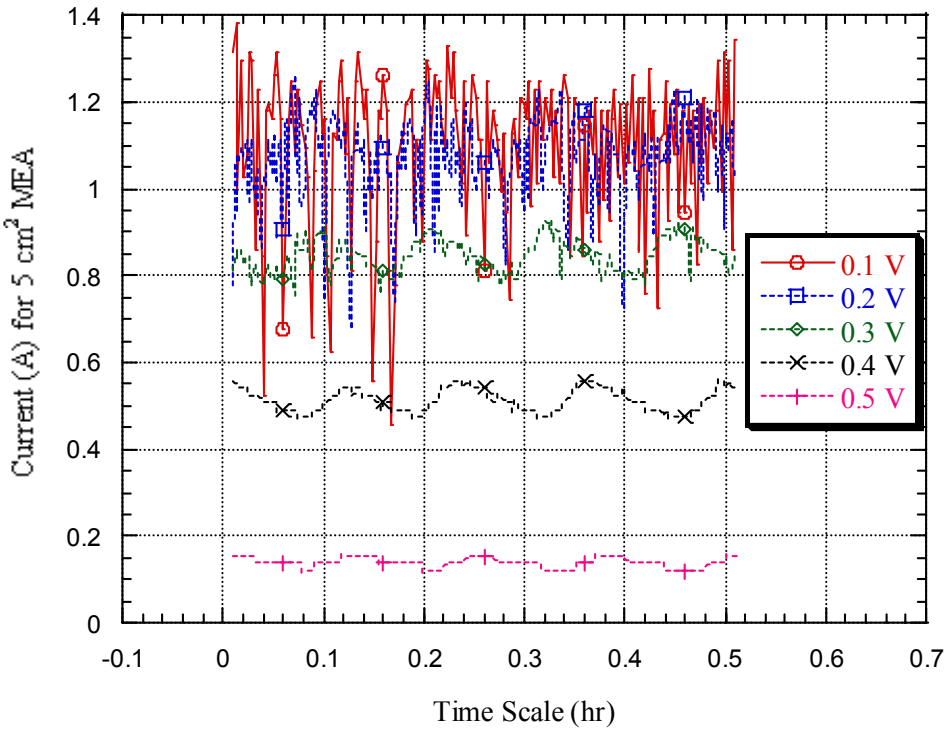

Figure 7-8. Period and amplitude of the oscillations.

where r_i are a function of surface coverages, which are function of time as given in Eq. 42-47. Therefore, the current is a function of time at constant potential mode. As the surface sites are cleaned through Eq. 34, the adsorption of methanol (Eq. 28 to 32) and water dissociation (Eq. 33) begin again, increasing the reaction rate and thus current. The current oscillations are self-sustained and can be explained by adsorption of CO and the potential dependent H_2O adsorption on the electrode surface. The current oscillations are observed for wide ranges of fuel cell temperatures, pressures, methanol concentration, and methanol feed rates. The magnitude of oscillation, of course, depends on the potential of the DMFC. The parameters for the oscillation need to be investigated further along with development of improved kinetic models for the anode methanol oxidation reaction.

7-6. Dynamic Feed Operation of DMFC

The DMFC performance is relatively low because of the poor performance of anode and cathode catalyst. The surface species on the anode electrode such as CO are stable and strongly adsorbed on the catalyst surface. This inhibits the further oxidation of methanol and results in a considerable increase of the anode overpotential. At the cathode side, the methanol diffusing through the membrane is oxidized which also involves adsorbed CO that causes significant competition for catalyst sites and concomitant drop in cathodic electrode potential. Both phenomena lead to the drop in total cell voltage. Therefore, it is desirable to develop selective catalysts that can increase the reaction rates and at the same time suppress the undesired side reactions, and better membranes that can conduct proton more efficiently while inhibiting the methanol crossover. Both of these are significant technological challenges.

Another possible way to improve the performance of DMFC is by dynamic feeding strategy of methanol solution.[24] It is based on the idea that the undesirable surface species can be oxidized and removed by feeding pure water solution periodically, instead of

methanol solution continuously, for a certain period of time until the voltage or current begins to drop appreciably due to methanol starvation. This periodic feeding of methanol solution may improve the overall kinetics of the methanol oxidation reaction and, therefore, the fuel cell performance. It will also affect the rate and amount of methanol crossover depending upon the frequency of the periodic feed. It is expected that the cell voltage will be increased by the introduction of pure water for a short period of time because it will remove surface inhibitors such as adsorbed COH and CO while maintaining current from the oxidation of these intermediates and remaining methanol via electrochemical reaction.

The success of this idea will depend on the system dynamics, i.e., how fast the system responds to the change of feed condition and the amount of intermediates accumulated on the surface. If the system reacts very fast to the change of feed composition, for example the cell voltage drops quickly when operated under constant current mode upon introduction of pure water, it would require high frequency change in feed and it may be difficult to apply this strategy. On the other hand, if the system sustains the improved voltage at constant current mode for a relatively long time, this approach could be useful in achieving high power density as well as efficient use of fuel.

In order to determine system dynamics, a response of cell voltage following a step change of methanol feed concentration was investigated. The methanol concentration was switched from 1M methanol to pure water. The flow rate of 1 M methanol solution was 0.5 ml/min and that of water introduced are 16 ml/min and 24 ml/min. The voltage was constant 0.44 V under constant current mode before the step change. When the pure water of two different flow rates was introduced at the timed 9 second in Figure 7-9, the cell voltage increased from its previous value of 0.44 V. It stayed for 2 seconds at the maximum voltage and then began to decrease. Thereupon, the voltage and current decreased with time because of the dilution of remaining methanol residue by pure water.

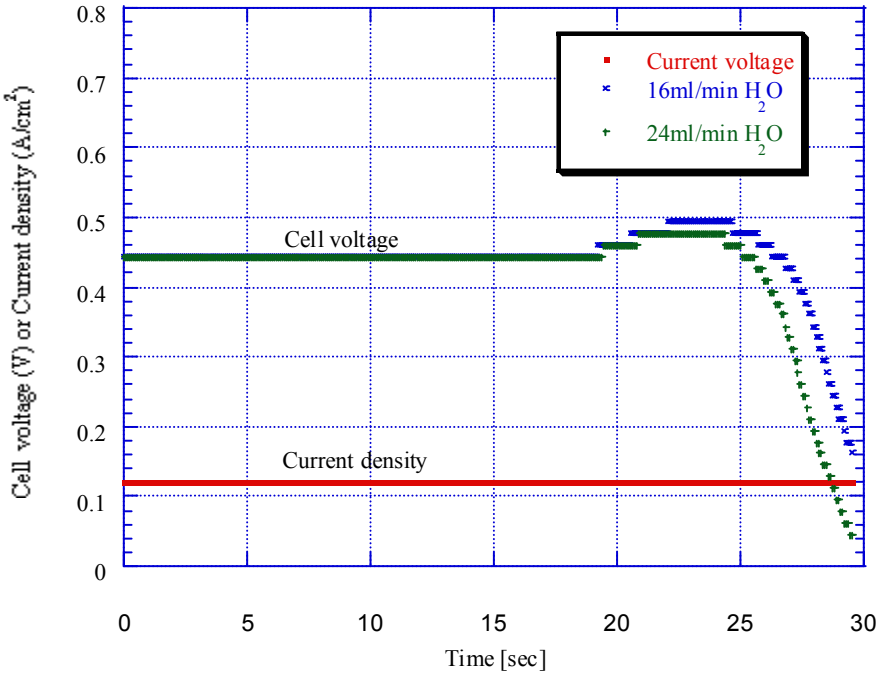

Figure 7-9. Dynamic feeding of anode methanol feed.

Therefore, clearly, there should be an advantage to using a dynamic feeding strategy with pulsed methanol concentration which may save the fuel while providing better power output. In order to sustain a higher cell voltage in a constant current mode, periodic pulsing of methanol feed is indicated in a water stream in order to achieve enhanced output of power. Alternatively, periodic pulses of pure methanol may be introduced in a steady flow stream of very dilute methanol feed. The dynamics are, of course, dependent upon the dynamics of surface and that of the anode chamber.

7-7. Impermeable PEM for DMFC

DMFC has two key technical problems. One is the slow anode kinetics discussed above and the other is methanol crossover. The methanol oxidation kinetics are inherently slower than those of the hydrogen oxidation because six electrons must be exchanged for complete oxidation in DMFC. Another key reason for the slow methanol kinetics is that the anode catalyst is poisoned by intermediates, likely CO formed during methanol electro-oxidation. Oxidation of carbon containing intermediates to carbon dioxide requires the adsorption of oxygen containing species (i.e., OH). Formation of these species does not occur readily until high overpotentials are used. Platinum is, thus, not sufficiently active for the anode catalyst and binary catalyst, e.g., Pt-Ru, has been shown to process better activity, where the Ru forms a surface oxide to promote CO oxidation in the potential range for methanol oxidation. The research for better oxidation catalyst to the successful commercialization is underway in many research groups worldwide.

The methanol crossover is the second important issue limiting performance of DMFC. It reduces OCV substantially due to mixed cathode potential and poisoning of anode and cathode as discussed in the previous chapter. The only manner in which this problem has so far been addressed is to use very dilute methanol solution (~1 M), instead of equimolar ratio of methanol and water indicated by stoichiometry, so that methanol is substantially

consumed within the anode catalyst layer, thus reducing the overall methanol flux across the proton exchange membrane to the cathode. In fact, at the concentration of methanol higher than 2 M, the cell voltage declines significantly due to poisoning of the cathode electrocatalyst by methanol that has diffused through the membrane. Further, even with dilute feeds, the fuel loss by methanol crossover can be as much as 40 % of the fuel. Therefore, this problem needs be addressed effectively before large-scale commercialization of DMFC can occur.

The use of Pd foil and the modification of PEM by sputtering have been suggested to solve methanol crossover problem.[25-28] It is proposed here that the deposition of a thin layer of Pd or Pd-containing metals within the MEA would block or substantially inhibit the transfer of methanol from the anode to cathode while allowing the transfer of protons through this metal layer. The metal chosen is palladium or its alloy because of its facile rate of permeation of hydrogen. The method of depositing Pd or Pd-alloy on the membrane is the electroless plating developed by Mardilovich. et at.[29]

DMFC Performance - The DMFC performance of Pd activated, not completely plated, membrane is shown in Figures 7-10 and 7-11 at 0 and 1 atm. gauge pressure, respectively. Compared the regular Nafion membrane, the performance is higher in the range of low current density. This is because of the inhibition of methanol crossover by the Pd existing on the surface or in the pore of the membranes. From the OCV to about 100 mA/cm^2 current density, the modified membrane shows better performance. Beyond a current density of more than 100 mA/cm^2, the modified membrane shows poorer performance than the regular PEM performance for this region likely because of higher transport resistance to protons. The low performance of the Pd activated membrane at high current density might also be caused by poor contact between the electrode and the activated membrane. During the hot pressing of the MEA, the metallic character on the surface of the modified membrane inhibits good attachment between the membrane and electrodes. The impact of

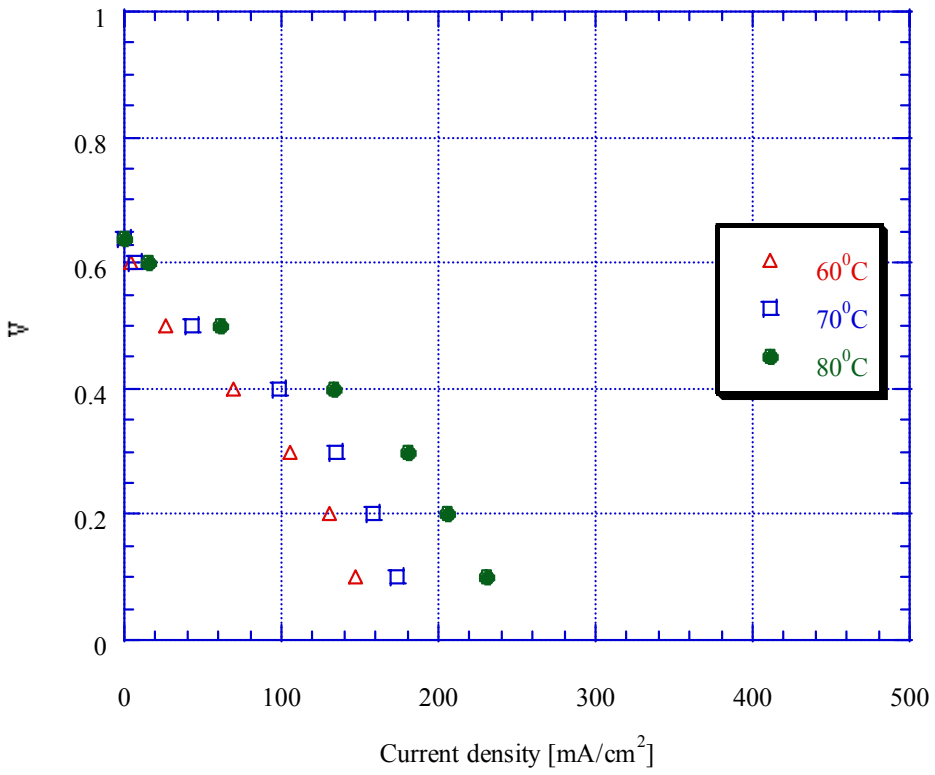

Figure 7-10. The performance of Pd plated Nafion® membrane (0 atm O_2, 1M methanol, 1 ml/min).

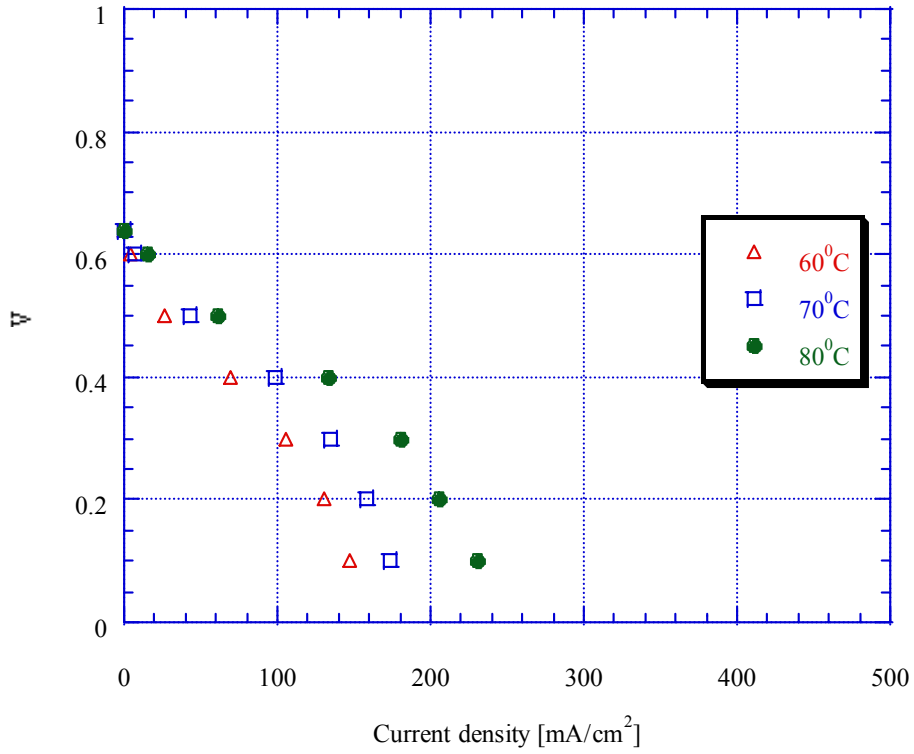

Figure 7-11. The performance of Pd plated Nafion® membrane (1 atm O_2, 1M methanol, 1 ml/min).

the Pd membranes should be more appreciable when the concentration of feed is increased. The performance at lower current densities might be better if a more uniformly plated film could be obtained.

Open Circuit Potentials - Table 7-4 shows the open circuit potentials of the modified MEAs at 2 atm gauge pressure and three different temperatures. The electroless-plated Nafion membrane loses its polymer elasticity and become brittle. Therefore, the completely Pd layered Nafion can not be used for MEA fabrication and hence only the activation steps are adopted here for only partial plating. The OCV of the modified MEAs are higher than MEA by bare Nafion except the sputtered Nafion case. The most effective procedure appears to be the deposition on the anode electrode layer itself rather than the membrane. The depositions of Pd on the anode layer showed higher open circuit potential. The use of Pd deposited PEM improved OCV and performance at low current densities. However, in higher current density region, the performance was lower than the regular PEM. The unresolved issues of this Pd deposited membranes are the poor contact of electrode and membrane, low water sorption and proton transport, and brittleness of the metal deposited membrane, etc, which should be addressed for further development of this technique. Pd film can, of course, also be sandwiched between PEM for DMFC applications.[25,28,30] However, the available Pd foils are rather thick offering substantial resistance to transport. The feasibility of this approach is discussed in the next chapter.

Table 7-4 Open circuit voltage of modified MEAs.

Temp (^{0}C)	Nafion (V)	AcNafion[1] (V)	SpNafion[2] (V)	AcAnode[3] (V)	SpAnode[4] (V)
25	0.54	0.57	0.39	0.68	0.60
50	0.61	0.65	0.41	0.69	0.67
80	0.65	0.67	0.47	0.72	0.70

[1] Nafion is activated by 3 cycles of activation procedure.
[2] Nafion is sputtered by Pd for 60 seconds.
[3] Anode is activated by 3 cycles of activation procedure.
[4] Anode is sputtered by Pd for 60 seconds.

References

1. B. D. McNicol, D. A. J. Rand and K. R. Williams, *J. Power Sources,* **83**, 15 (1999).
2. X. Ren, P. Zelenay, S. Thomas, J. Davey and S. Gottesfeld, *J. Power Sources*, **86**, 111 (2000).
3. M. W. Breiter, *J. Electroanal. Chem*., **14**, 407 (1967).
4. V. S. Vagotzsky and Y. B. Vassiliev, *Electrochim. Acta*, **11**, 1439 (1966).
5. J.O.M. Bockris and A.K.N. Reddy, *Modern Electrochemistry*, Klumer Academic/Plenum Publishers, New York, 2000.
6. A.S. Arico, S. Srinivan, and V. Antonucci, *Fuel Cells*, **1**, 133 (2001).
7. R. Dillon, S. Srinivasan, A. S. Arico and V. Antonucci, *J. Power Sources*, **127**, 112 (2004).
8. S. Wasmus and A. Küver, *J. Electroanal. Chem.,* **461**, 14 (1999).
9. A. Heinzel and V. M. Barragan, *J. Power Sources*, **84**, 70 (1999).
10. A. Hamnett, *Catalysis Today* **38**, 445 (1997).
11. H. Dohle, J. Divisek, J. Mergel, H. F. Oetjen, C. Zinger, and D. Stolten, *J. Power Sources*, **105**, 274 (2002).
12. J. Cruickshank, and K. Scott, *J. Power Sources*, **70**, 40 (1998).
13. T. Thampan, S. Malhotra, J. Zhang, and D. Datta, *Catalysis Today*, **67**, 15 (2001).
14. K. Sundmacher, T. Schultz, S. Zhou, K. Scott, M. Ginkel, and E. D. Gilles, *Chem. Eng. Sci*., **56**, 333 (2001).
15. E. W. Bohannan, L. Y. Huang, F. S. Miller, M. G. Shumsky, and J. A. Switzer, *Langmuir*, **15**, 813 (1999).
16. D. T. Bowlin, A. Scheeline, and A. Pearlstein, *Electrochim. Acta*, **43**, 417 (1998).
17. J. Lee, P. Strasser, M. Eiswirth, and G. Ertl, *Electrochim. Acta*, **47**, 501 (2001).
18. M. Krausa and W. Vielstich, *J. Electroanal. Chem.*, **339**, 7 (1995).
19. S. Sriramulu, T. D. Jarvi, and E. M. Stuve, *J. Electroanal. Chem.*, **467**, 132 (1999).

20. F. Berthier, J. P. Diard, and S. Nugues, *J. Electroanal. Chem.*, **436**, 35 (1997).

21. J. Lee, J. Christoph, P. Strasser, M. Eiswirth, and G. Etrl, *J. Chem. Phys.*, **115**, 1485 (2001).

22. J. Lee, J. Christoph, M. Eiswirth, and G. Etrl, *Electrochim. Acta*, **47**, 2297 (2002).

23. S. Chen and M. Schell, *Electrochim. Acta*, **44**, 4773 (1999).

24. S. Zhou, T. Schultz, M. Peglow, and K. Sundmacher, *Phys. Chem. Chem. Phys.*, **3**, 347 (2001).

25. C. Pu, W. Hwang, K. L. Ley, and E. S. Smotkin, *J. Electrochem. Soc.*, **142**, L119 (1995).

26. R. G. Hockday, *US Patent*, 5,759,712 (1998).

27. S. R. Yoon, G. H. Hwang, W. I. Cho, I. H. Oh, S. A. Hong, and H. Y. Ha, *J. Power Sources*, **106**, 215 (2002).

28. J. H. Shim, S. M. Song, W. K. Her, I. G. Koo, and W. M. Lee, *J. Electrochem. Soc.*, **150**, A1592 (2003).

29. P. P. Mardilovich, Y. She, Y. H. Ma, and M. H. Rei, *AIChE J.*, **44**, 310 (1998).

30. H. Dohle, V. Peinecke, I. Busenbedder, and T. Kels, *US Patent*, 6242122 B1 (2001).

Chapter 8. Fuel Cell with Pd Nonporous Anode

8-1. Introduction

A new non-porous anode has been developed which can be used effectively for Co-containing reformate feed stream in H_2/O_2 fuel cell as well as for direct methanol fuel cell (DMFC). In the hydrogen fuel cell, it is desirable to develop anode materials which have lower affinity for CO, while maintaining their activity for the oxidation of hydrogen. Platinum, the most active metal for the hydrogen oxidation reaction, is unfortunately extremely sensitive to carbon monoxide, and thus, a number of binary and ternary electro-catalysts such as Pt-Ru and Pt-Ru-Mo have been developed to obtain better performance for CO-containing anode feed. These alloys are more effective than Pt in oxidizing the adsorbed CO with dissociated water into CO_2. Here, it is proposed to develop non-porous anode capable of extracting hydrogen at low partial pressure from hydrocarbon containing feed streams. Figure 8-1 shows a schematic diagram of the non-porous anode for fuel cell. This is an interesting structure because it breaks down the process into the following distinct steps: hydrogen dissociation (Tafel step), hydrogen atom diffusion, hydrogen atom electro-oxidation into protons and electrons (Volmer step), proton diffusion through PEM and oxygen reduction at cathode.[1-3] A mathematical model has been developed for the whole fuel cell process based on the kinetics on electrode surfaces, and transport of hydrogen atom and proton through the non-porous anode and proton exchange membrane, respectively.

8-2. The Model

A model accounting mass balances, transport of reaction species and electrochemical kinetics is developed to understand the mechanisms involved in the nonporous anode

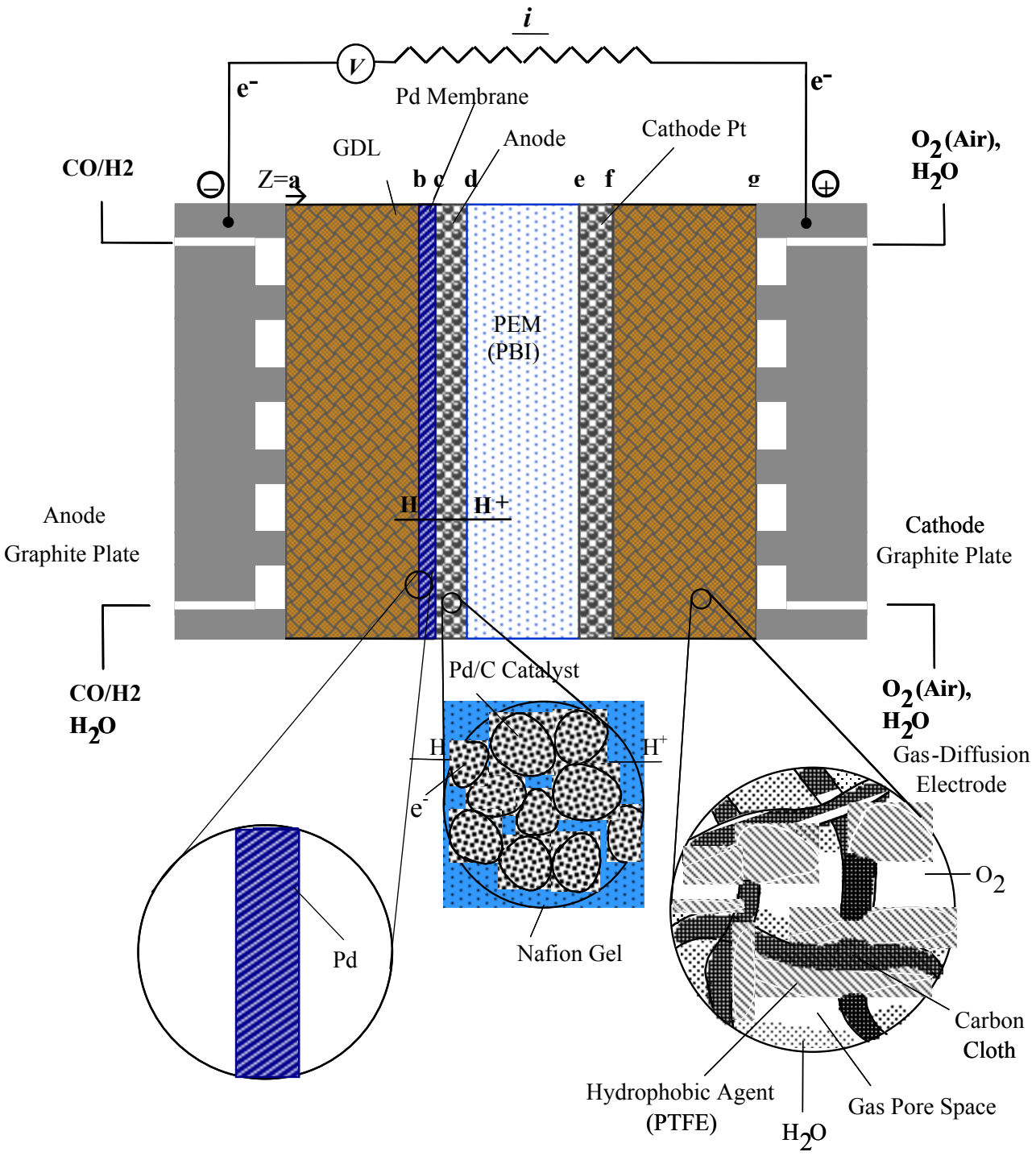

Figure 8-1. Schematic diagram of Pd nonporous anode fuel cells.

hydrogen fuel cells. The total overpotential for the MEA is the sum of the overpotentials from H_2/CO diffusion, H_2 dissociation, H atom diffusion, H_2 oxidation, H^+ transport through PEM, and O_2 reduction.

$$\eta_{Total} = \eta_{D,GDL(A)} + \eta_{K,Diss} + \eta_{D,Pd} + \eta_{K,HOR} + \eta_{D,PEM} + \eta_{K,ORR} + \eta_{D,GDL(C)} \quad [1]$$

where $\eta_{D,GDL(A)}$ is the diffusion overpotential of anode feed through GDL, η_K is the equivalent kinetic overpotential for hydrogen atom dissociation, $\eta_{D,Pd}$ is the diffusion overpotential in dense Pd film, $\eta_{K,HOR}$ is the kinetic overpotential for hydrogen oxidation reaction, $\eta_{D,PEM}$ is the diffusion overpotential for protons through PEM, $\eta_{K,ORR}$ is the kinetic overpotential for oxygen reduction reaction, and $\eta_{D,GDL(C)}$ is the diffusion overpotential for oxygen transport through GDL.

Steady State Conservation Equations

Anode Chambers (AC)

The anode feed is composed of hydrogen and carbon monoxide. Assuming that the anode chamber is a well-mixed CSTR, the mass balance can be written as

$$F_A\left(C_{Ai} - C_A\right) = N_{i,z=a} A_{GDL} \quad [2]$$

where F_A is the anode volumetric flow rate [cm^3/sec], C_{Ai} and C_A are the concentration of species i at the inlet and exit, $N_{i,z=a}$ is the molar flux of species A through the GDB layer, and A_{GDL} is the area of GDL.

Gas Diffusion Backing (GDB)

The anode gases diffuse into the GDL by the potential difference. At steady state, the diffusion flux can be written as

$$\frac{dN_i}{dz} = 0 \qquad [3]$$

$$N_{iz} = -\frac{1}{RT} D_i^e C_i \nabla_T \mu_i^e \approx \frac{D_i^e C_{i,z=a}}{L_{GDB}} \left(\frac{\mu_{i,z=a}^e - \mu_{i,z=b}^e}{RT} \right) = r_D \qquad [4]$$

where D_i^e is the effective diffusion coefficient, $C_{i,z=a}$ is the concentration of i, L_{GDB} is the thickness of GDB layer, $\mu_{i,z=a}^e$ and $\mu_{i,z=b}^e$ are the chemical potential of species i at $z = a$ and $z = b$, respectively. In terms of affinity A, chemical potential defference, Eq. 4 can be written as

$$\frac{A_D}{RT} = \frac{\mu_{i,z=a}^e - \mu_{i,z=b}^e}{RT} = \left(\frac{L_{GDB}}{D_i^e C_i} \right) r_D \qquad [5]$$

Hydrogen Atom Diffusion Electrode (HADE)

i) Dissociation of H_2

The H_2/CO mixture gas adsorbs on the surface of palladium film, which may have been catalyzed with Pt, for example,

$$H_2 + 2S \leftrightarrows 2H_{ad,b} \qquad \text{(Tafel Step)} \qquad [6]$$

where S denotes the surface active site for gas adsorption. The rate of adsorption per unit metal area can be written as

$$r_1^* = \vec{k}_1^* a_{H2} \theta_0^2 - \overleftarrow{k}_1^* \theta_H^2 = \vec{r}_1 - \overleftarrow{r}_1 \qquad [7]$$

where from the thermodynamic transition state theory

$$\vec{k}_\rho^* = \kappa \frac{k_B T}{h} \left(\frac{C_t^*}{N_{Av}} \right) \exp\left(\frac{-\Delta \vec{G}_\rho^{0,*}}{RT} \right) \qquad [8]$$

The actual reaction rate mols/cm^2 MEA) can be obtained by multiplying the roughness factor of the metal surface γ_M, i.e.,

$$r_\rho = r_\rho^* \gamma_M , \quad [9]$$

From the site balance for H_2/CO feed

$$1 = \theta_0 + \theta_H + \theta_{CO} \quad [10]$$

Let $\theta_F = 1 - \theta_{CO}$, where θ_F is the fraction of free sites not poisoned by carbon monoxide. Substitution of this into Eq. 7 gives

$$r_2 = \vec{r}_2 - \overleftarrow{r}_2 = \gamma_{M,a} \vec{k}_2 (\theta_F - \theta_H)^2 a_{H_2} - \gamma_{M,a} \overleftarrow{k}_2 \theta_{H,z=b}^2 \quad [11]$$

For elementary reactions, affinity

$$A_\rho = RT \ln \frac{\vec{r}_\rho}{\overleftarrow{r}_\rho} = RT \ln \frac{\vec{k}_\rho \prod_{i=1}^{r} a_\rho^{-\nu_{\rho i}}}{\overleftarrow{k}_\rho \prod_{i=r+1}^{n} a_\rho^{\nu_{\rho i}}} = RT \left(K_\rho \prod_{i=1}^{n} a_\rho^{-\nu_{\rho i}} \right) \quad [12]$$

and

$$r_\rho = r_{\rho,0} \left\{ \exp\left[\left(\beta_\rho \frac{A_\rho}{RT} \right) \right] - \exp\left[(\beta_\rho - 1) \frac{A_\rho}{RT} \right] \right\} \quad [13]$$

where β_ρ is transfer coefficient and $r_{\rho,0}$ is exchange rate given by $r_{\rho,0} = \vec{r}_\rho^{\,\beta_\rho} \overleftarrow{r}_\rho^{\,1-\beta_\rho}$. For $\beta = 1/2$

$$r_\rho = 2 r_{\rho,0} \sinh\left(\frac{A_\rho}{2RT} \right) \quad [14]$$

and $r_{\rho,0} = \sqrt{\vec{r}_\rho \overleftarrow{r}_\rho}$. Applying for the hydrogen dissociation reaction, affinity is given by

$$A_1 = RT \ln\left(\frac{\vec{k}_1 a_{H2} \theta_0^2}{\overleftarrow{k}_1 \theta_H^2} \right) \quad [15]$$

and $r_{1,0} = \sqrt{\vec{k}_1 \overleftarrow{k}_1} \left(\sqrt{a_H} \theta_0 \theta_H \right)$

Therefore

$$A_1 = 2RT \sinh^{-1}\left(\frac{r_1}{r_{10}}\right) = \mu^e_{H_2,z=b} - 2\mu^e_{H,z=c} \quad [16]$$

ii) H atom diffusion

The diffusion of dissociated hydrogen through the Pd film may be represented by

$$H_{ad,b} \leftrightarrows H_{ad,c} \qquad \text{(H atom diffusion)} \quad [17]$$

At steady state, the mass balance of hydrogen atom through palladium film is

$$\frac{dN_i}{dz} = 0 \quad [18]$$

along with

$$N_{iz} = -\frac{1}{RT} D^e_i C_i \nabla_T \mu^e_i \approx \frac{D^e_i C_{i,z=b}}{L_{Pd}} \left(\frac{\mu^e_{i,z=b} - \mu^e_{i,z=c}}{RT}\right) = r_2 \quad [19]$$

In terms of affinity

$$A_2 = RT\left(\mu^e_{i,z=b} - \mu^e_{i,z=c}\right) = RT\left(\frac{L_{Pd}}{D^e_i C_{i,z=b}}\right) r_2 \quad [20]$$

iii) Hydrogen Oxidation Reaction (HOR)

For the formation of a proton and electron from a hydrogen atom

$$H_{ad,c} \leftrightarrows H^+ + e^- \qquad \text{(Volmer)} \quad [21]$$

for which

$$r_3 = \vec{r}_3 - \overleftarrow{r}_3 = \gamma_c \vec{k}_3 \theta_{H,z=c} - \gamma_c \overleftarrow{k}_3 a_{H^+} \quad [22]$$

or

$$r_3 = 2r_{3,0} \sinh\left(\frac{A_3}{2RT}\right) \quad [23]$$

i.e.,

$$\frac{A_3}{RT} = 2\sinh^{-1}\left(\frac{r_3}{r_{30}}\right) = \frac{\mu^e_{H,z=c} - \mu^e_{H^+,z=c} - \mu^e_{e^-,z=c}}{RT} \quad [24]$$

The overall affinity for the anode reaction that includes adsorption, diffusion through Pd film, and hydrogen oxidation reaction can be written as

$$A_{Overall} = A_1 + 2A_2 + 2A_3 \quad [25]$$

$$A_{Overall} = \left(\mu^e_{H_2} - 2\mu^e_{H,a}\right) + 2\left(\mu^e_{H,a} - \mu^e_{H,b}\right) + 2\left(\mu^e_{H,b} - \mu^e_{H+,b} - \mu^e_{e-,b}\right) \quad [26]$$

Using the relations among the rates

$$r = r_1 = r_2 = \frac{r_3}{2} = \frac{r_4}{2} \quad [27]$$

$$\frac{A_{Overall}}{RT} = 2\sinh^{-1}\left(\frac{r}{2r_{1,0}}\right) + 4\sinh^{-1}\left(\frac{r}{2r_{3,0}}\right) + 2r\left(\frac{L_{Pd}}{C_{H,ad}D^e_H}\right) \quad [28]$$

where

$$A_{Overall} = \mu^e_{H_2} - 2\mu^e_{H+,b} - 2\mu^e_{e^-,b} \quad [29]$$

For the overall anode reaction

$$\mathrm{H_2} = 2\mathrm{H^+} + 2\mathrm{e^-} \quad [30]$$

$$\Delta G_\rho = \Delta G^0_\rho + RT\ln\prod_{i=1}^{n} a_i^{\nu_{\rho i}} = \left(\Delta G^0_{\rho,\Phi=0} - \nu_{\rho e-}F\Phi_\rho\right) + RT\ln\prod_{i=1}^{n} a_i^{\nu_{\rho i}} \quad [31]$$

Using

$$\Delta G^0_{\rho,\Phi=0} + RT\ln\prod_{i=1}^{n} a_i^{\nu_{\rho i}} = \Phi_{\rho,0}\nu_{\rho e-}F \quad [32]$$

where $\Phi_{\rho,0}$ is the equilibrium potential.

$$\Delta G_\rho = \nu_{\rho e^-}F\left(\Phi_{\rho,0} - \Phi_\rho\right) = \nu_{\rho e^-}F\eta_\rho \quad [33]$$

where $\nu_{\rho e-} = 2$ and η_ρ is the anode overpotential.

From $i_A = \nu_{\rho e^-} Fr$ where $r = [mol/cm^2/s]$, the affinity for anode reaction can be related to the

$$\frac{A_{Overall}}{RT} = \frac{\nu_{\rho e^-} F\eta_A}{RT} = \left[2\sinh^{-1}\left(\frac{i}{2i_{1,0}}\right) + \frac{L_{Pd}}{D_i^e C_{i,z=b}} \frac{i}{F} + 4\sinh^{-1}\left(\frac{i}{2i_{3,0}}\right) \right] \quad [34]$$

where $\eta_A = \eta_{K,Diss} + \eta_{D,Pd} + \eta_{K,HOR}$

Therefore, the overpotentials for hydrogen dissociation, hydrogen atom diffusion, and hydrogen oxidation reactions, are

$$\eta_A = \frac{RT}{2F}\left[2\sinh^{-1}\left(\frac{i}{i_{10}}\right) + \frac{L_{Pd}}{D_i^e C_{i,z=b}} \frac{i}{F} + 4\sinh^{-1}\left(\frac{i}{i_{30}}\right) \right] \quad [35]$$

For small argument x, $\sinh^{-1}x = x$, for low x,

$$\eta_A = \left[\frac{RT}{Fi_{20}} + \frac{RT}{2F^2} \frac{L_{Pd}}{D_i^e C_{i,z=b}} + \frac{2RT}{Fi_{40}} \right] i \quad [36]$$

The total fuel cell overepotential is obtained by η_A, $\eta_{D,GDL(A)}$, $\eta_{D,PEM}$, $\eta_{K,ORR}$, and $\eta_{D,GDL(C)}$ as shown in Eq. 1.

Further refinement of model should include details of H atom diffusion through Pd. The diffusion of hydrogen atom through Pd and Pd alloys by pressure gradient is well known and extensively studied. The rate of diffusion of hydrogen through the solid membrane is governed by the diffusion coefficient that is dependent on its chemical composition (α- phase or β-phase Pd) and to the concentration gradient across the membrane and to its thickness. Figure 8-2 shows a hypothetical concentration of hydrogen atom and phases in Pd foil. The atomic diffusion flux in Pd can be written in terms of Fick's first law as

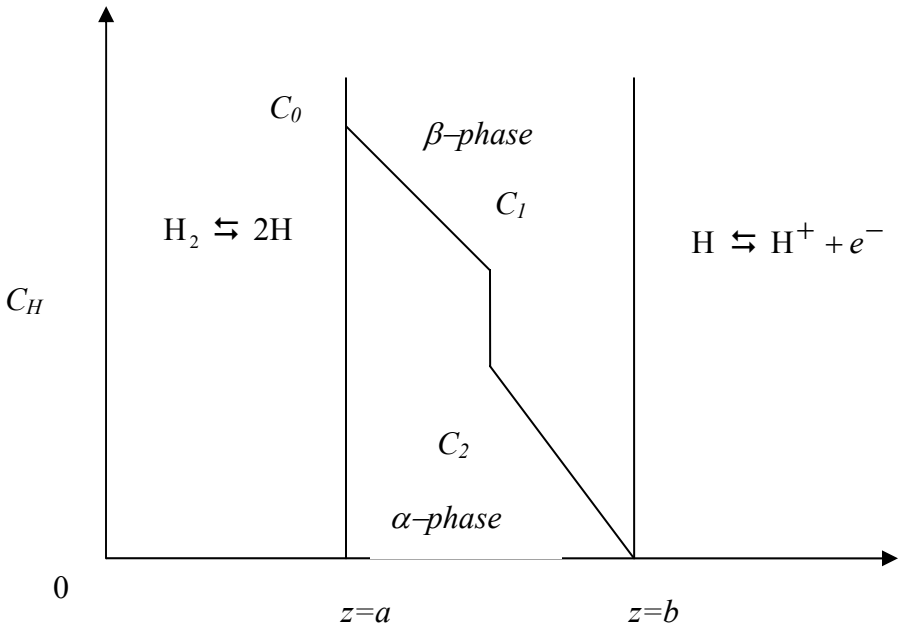

Figure 8-2. Schematic diagram of the concentration of hydrogen atom in Pd layer of hydrogen diffusion anode fuel cells.

$$N_H = N_{H\alpha} + N_{H\beta} = -D_\alpha \frac{dC_\alpha}{dz} - D_\beta \frac{dC_\beta}{dz} \quad [37]$$

The limiting current density may be approximated as

$$i_{AL} = \frac{nF}{L_{Pd}}\left[D_\beta\left(C_0 - C_1\right) + D_\alpha C_2\right] \quad [38]$$

where D_α and D_β represent the diffusion coefficient of hydrogen atom in Pd for α and β phase, respectively. The diffusion coefficients in Pd (cm^2/sec) for the phase are given as follows;

$$\alpha\text{–phase: } D_\alpha = (4.3*10^{-3})\exp(-5600/RT) \quad [39]$$

$$\beta\text{–phase: } D_\beta = (3.8*10^{-4})\exp(-2900/RT) \quad [40]$$

where the activation energy in given as cals/mole. Table 8-1 provides the diffusion coefficient calculated from the above relations. The diffusion coefficient of hydrogen atoms in β phase is higher than α phase. From the diffusion coefficients and the hydrogen atom concentration given in Table 8-2, the limiting currents for anode reaction are calculated by Eq. 38 and given in Table 8-3.

The overall performance of H_2 diffusion anode fuel cells can be theoretically understood based on the models developed here.

Table 8-1. Diffusion coefficients in α and β phase Pd at different temperature.

$T(^0C)$	30	40	50	60	70	80	200
D_α	3.9×10^{-7}	5.3×10^{-7}	7.0×10^{-7}	9.1×10^{-7}	1.16×10^{-6}	1.47×10^{-6}	1.11×10^{-5}
D_β	2.93×10^{-6}	3.42×10^{-6}	3.95×10^{-6}	4.54×10^{-6}	5.16×10^{-6}	5.83×10^{-6}	1.68×10^{-5}

Table 8-2. Data for hydrogen concentration [g H/cc Pd] where Co is the concentration of hydrogen atom in the β phase in equilibrium with 1 atm. of H_2 and C_1 is the concentration of β phase in equilibrium with C_2 in the α phase.

Temperature	C_0	C_1	C_2
30	0.0703	0.0555	0.0035
40	0.0693	0.0536	0.0040
50	0.0684	0.0531	0.0045
60	0.0674	0.0526	0.0050
70	0.0664	0.0516	0.0060
80	0.0664	0.0506	0.0070
200	0	0	0.0030

Table 8-3. Limiting current density (A/cm^2) at different temperatures for the variation of thickness of commercial Pd foil (1 atm).

Thickness	Temperature (^oC)						
	30	40	50	60	70	80	200
0.05 mm	0.8621	1.0763	1.2283	1.3830	1.6084	1.9753	0.6433
0.1 mm	0.4311	0.5382	0.6141	0.6915	0.8042	0.9877	0.3216
0.005 inch	0.3394	0.4237	0.4836	0.5445	0.6332	0.7777	0.2533
0.01 inch	0.1697	0.2119	0.2418	0.2722	0.3166	0.3888	0.1266
0.02 inch	0.0849	0.1059	0.1209	0.1361	0.1583	0.1944	0.0633

References

1. H. G. Oswin, and S. M. Chodosh, *Advances in Chemistry Series*, **47**, 61 (1965).
2. H. G. Oswin, and N. Y. Elmsford, *US Patent*, 3092517 (1963).
3. H. G. Oswin, *US Patent*, 3375140 (1968).

Chapter 9. Water Electrolysis in Regenerative Fuel Cells

9-1. Introduction

The solid polymer electrolyte (SPE) has been utilized in many energy-related fields such as fuel cell,[1] hydrogen compressor,[2] and solar cell systems.[3] Electrolysis of water using the SPE,[4-6] which serves as a solid electrolyte that conducts protons and as a separator of gases, is considered as a promising methodology for producing hydrogen as an alternative to the conventional alkaline water electrolysis. SPE electrolyzer has certain advantages over classical alkaline process in terms of its simplicity at low temperature, high energy efficiency and specific production capacity. It is also creating new options for the fuel cell system, e.g., a regenerative fuel cell which operates both as a fuel cell and as an electrolyzer.[7-9]

In principle, SPE water electrolyzer and fuel cells are basically the same device working in the opposite direction.[10] Although there are many studies on the theoretical analysis of fuel cells,[11-15] not much has been reported on the kinetics and polarization characteristics of the SPE electrolyzer. In order to design and use the SPE electrolyzer effectively, analytical models for the device are necessary so that the system can be optimized. Recently, Onda et. al.[16] have provided a voltage-current relation wherein the cell voltage is described as the sum of Nernst voltage, resistive overpotential, and anode and cathode overpotentials. However, empirical equations were utilized for the anode and cathode overpotentials as a function of temperature of the electrolytes and current density of the cell.

The objective of this study is to propose a simple but useful first-generation theoretical model to explain the current-potential characteristics of SPE electrolysis cell based on the involved charge and mass balances as well as Butler-Volmer kinetics on the electrode surfaces.

Principle of operation

Electrolysis of water is the dissociation of water molecules into hydrogen and oxygen gas. The working principle of SPE water electrolysis is shown in Figure 9-1. A potential is applied across the electrochemical cell to induce electrochemical reactions in both electrodes. Water is introduced at the anode and dissociated into oxygen, protons and electrons via the following reaction:

$$\text{At anode: } H_2O \leftrightarrows 2H^+ + 2e^- + \frac{1}{2}O_2 \qquad E^\circ(25^\circ C) = 1.23\ V \qquad [1]$$

The protons are driven through the SPE to the cathode under an electric field where they combine with the electrons arriving from the external circuit to form hydrogen gas:

$$\text{At cathode: } 2H^+ + 2e^- \leftrightarrows H_2 \qquad E^\circ(25^\circ C) = 0.00\ V \qquad [2]$$

Therefore, the net reaction in the electrolysis cell is

$$\text{Net reaction: } H_2O \leftrightarrows H_2 + \frac{1}{2}O_2 \qquad E^\circ(25^\circ C) = 1.23\ V \qquad [3]$$

The heart of the SPE water electrolyzer is of course the membrane electrode assembly. For the solid electrolyte, typically a perfluorosulfonic acid (PFSA) polymer such as Nafion, has widely been used for water electrolysis.[6-9, 16-20] For the anode, platinum shows a significant overpotential and thus platinum/ruthenium,[18] iridium[19] and platinum/iridium[16,18,20] have been investigated. The addition of Ru decreases the anode overpotential, but Pt-Ru anode is not stable and corrodes under oxygen evolution.[18] The Pt-IrO_2 based alloy catalysts are relatively stable and preferred for anode water dissociation reaction.[20] For the cathode, platinum metal is known to show best performance and commonly used for water electrolysis.[16-20]

9-2. The Model

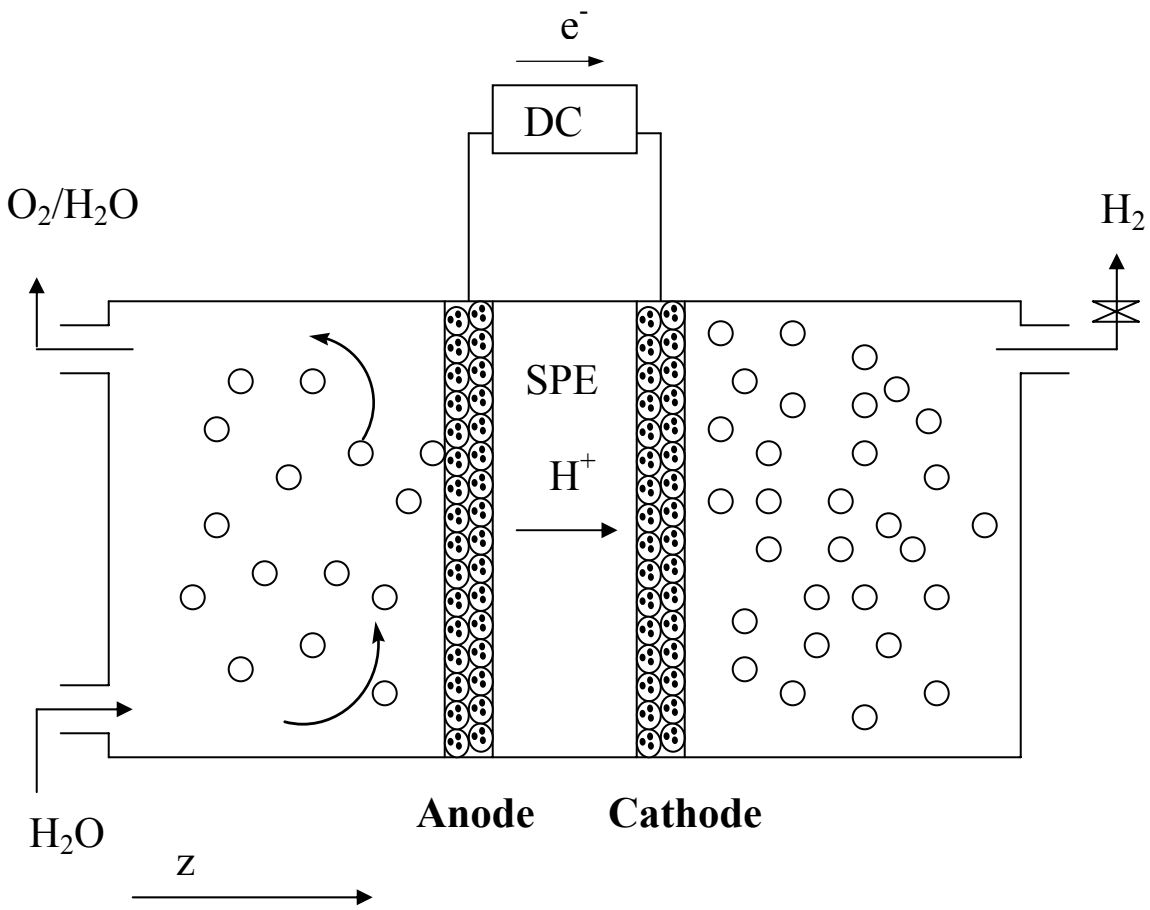

Figure 9-1. Cross-section of SPE water electrolyzer.

A simplified mathematical model is developed below based on appropriate mass balances, transport, and electrochemical kinetics applied to the SPE electrolysis cell.

Steady State Conservation Equations

Anode and Cathode Chambers

For the sake of simplicity, the anode chamber is treated as a well-mixed reactor. The mass balances of water and oxygen at the anode, and that of hydrogen at the cathode can be written as

$$\dot{N}_{H_2O,in} - \dot{N}_{H_2O,out} = \frac{iA}{2F} \quad [4]$$

$$\dot{N}_{H_2,in} - \dot{N}_{H_2,out} = -\frac{iA}{2F} \quad [5]$$

$$\dot{N}_{O_2,in} - \dot{N}_{O_2,out} = -\frac{iA}{4F} \quad [6]$$

where $\dot{N}$, i, A and F represent the molar flow rates [mol/s], current density [A/cm^2], MEA area [cm^2] and faraday's constant [96,487 C/mol], respectively.

Anode and Cathode Layers

The Butler-Volmer expression is utilized for the overall electrochemical reaction at the anode

$$i = i_{A0}\left[\exp\left(\frac{\alpha_A \nu_{e^-} F \eta_A}{RT}\right) - \exp\left(-\frac{(1-\alpha_A)\nu_{e^-} F \eta_A}{RT}\right)\right] \quad [7]$$

where i_{A0} is the anode exchange current density [A/cm^2], ν_{e^-} is the stoichiometric coefficient of electrons , α_A is the transfer coefficient and η_A is the anode overpotential. Alternatively, the anode overpotential can be written as follows in terms of current density,

assuming the effective transfer coefficient α_A = 0.5 and ν_{e^-} = 2 for the de-electronation reaction at the anode[11]

$$\eta_A = \frac{RT}{F}\sinh^{-1}\left(\frac{i}{2i_{A0}}\right) \quad [8]$$

For the cathode, if Butler-Volmer equation is assumed as well with α_C = 0.5 and ν_{e^-} = -2, the cathode overpotential is obtained similarly as

$$\eta_C = -\frac{RT}{F}\sinh^{-1}\left(\frac{i}{2i_{C0}}\right) \quad [9]$$

Here, it should be noted that the solutions are assumed to be well-mixed in the chambers and thus the surface concentrations do not differ appreciably from the bulk phase. If there is a limitation for mass transfer, e.g., oxygen diffusion from catalyst site to gas bubble across a diffusion film near electrode, limiting current density may be incorporated in Eq. 8 and 9.[11,14]

Solid Polymer Electrolyte (SPE)

At steady state, no current gradient exists across the solid polymer electrolyte, i. e.,

$$\frac{di}{dz} = 0 \text{ and } i = -\sigma\frac{d\phi}{dz} \quad [10]$$

where σ is the conductivity of the electrolyte [S/cm] and ϕ is the potential [V].

Electrochemical Potential of Electrolysis Cell

Figure 9-2 shows the equivalent circuit for electrolysis process represented by a series of resistance. The overall cell potential is composed of Nernst potential, anode and cathode overpotentials, overpotential due to membrane, and interfacial resistance as[11,14]

$$V = V_\circ + \eta_A - \eta_C + \eta_{SPE} + \eta_I \quad [11]$$

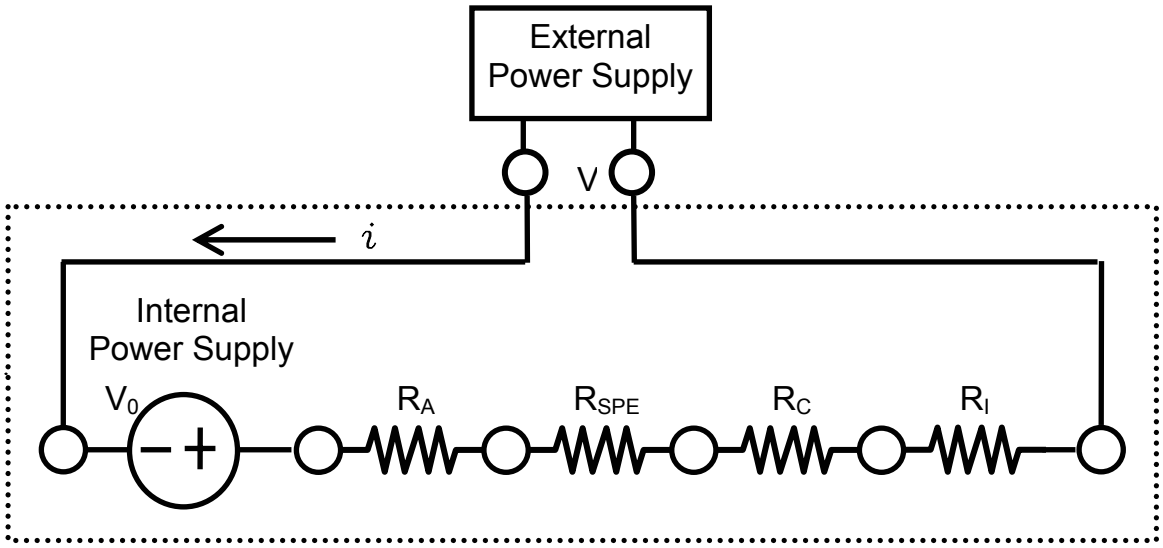

Figure 9-2. Equivalent circuit for the electrolysis process: $V_{\circ}$ = internal power supply, R_A = anode resistance, R_{SPE} = membrane resistance R_C = cathode resistance and R_I = interface resistance.

where the Nernst potential $V_\circ$ is empirically given as[21]

$$V_\circ = 1.23 - 0.9\text{x}10^{-3}(T - 298) + 2.3\frac{RT}{4F}\log\left(P_{H_2}^2 P_{O_2}\right) \quad [12]$$

The anode and cathode overpotentials in Eq. 11 are provided by Eq. 8 and 9. Integration of Eq. 10 gives overpotential due to the membrane resistance

$$\eta_{SPE} = \left(\frac{L_B}{\sigma_B}\right) i \quad [13]$$

where L_B is the thickness of SPE, σ_B is conductivity of the electrolyte. The interfacial overpotential η_I may be written in terms of interfacial resistance R_I and current density as

$$\eta_I = R_I i \quad [14]$$

Therefore, the overall cell voltage-current relation can be obtained by combining Eqs. 8, 9, 12, 13 and 14 with 11.

$$V = V_\circ + \frac{RT}{F}\sinh^{-1}\left[\frac{1}{2}\left(\frac{i}{i_{A0}}\right)\right] + \frac{RT}{F}\sinh^{-1}\left[\frac{1}{2}\left(\frac{i}{i_{C0}}\right)\right] + \left(\frac{L_B}{\sigma_B}\right) i + R_I i \quad [15]$$

Correspondingly, the required power density is obtained by $P = Vi$ as

$$P = V_\circ i + \frac{RT}{F}\sinh^{-1}\left[\frac{1}{2}\left(\frac{i}{i_{A0}}\right)\right] i + \frac{RT}{F}\sinh^{-1}\left[\frac{1}{2}\left(\frac{i}{i_{C0}}\right)\right] i + \left(\frac{L_B}{\sigma_B}\right) i^2 + R_I i^2 \quad [16]$$

9-3. Simulation

Figure 9-3 shows the simulation results obtained by using Eq. 15 based on the parameters provided in Table 9-1 along with experimental data[18,20] to validate the adequacy of this simple model. For Pt based electrodes, the exchange current density for the oxygen reduction and hydrogen oxidation reactions is reported as[22-24] 10^{-9}-10^{-12} and 10^{-4}-10^{-3} A/cm^2 respectively.[25] The exchange current density depends on the temperature at the

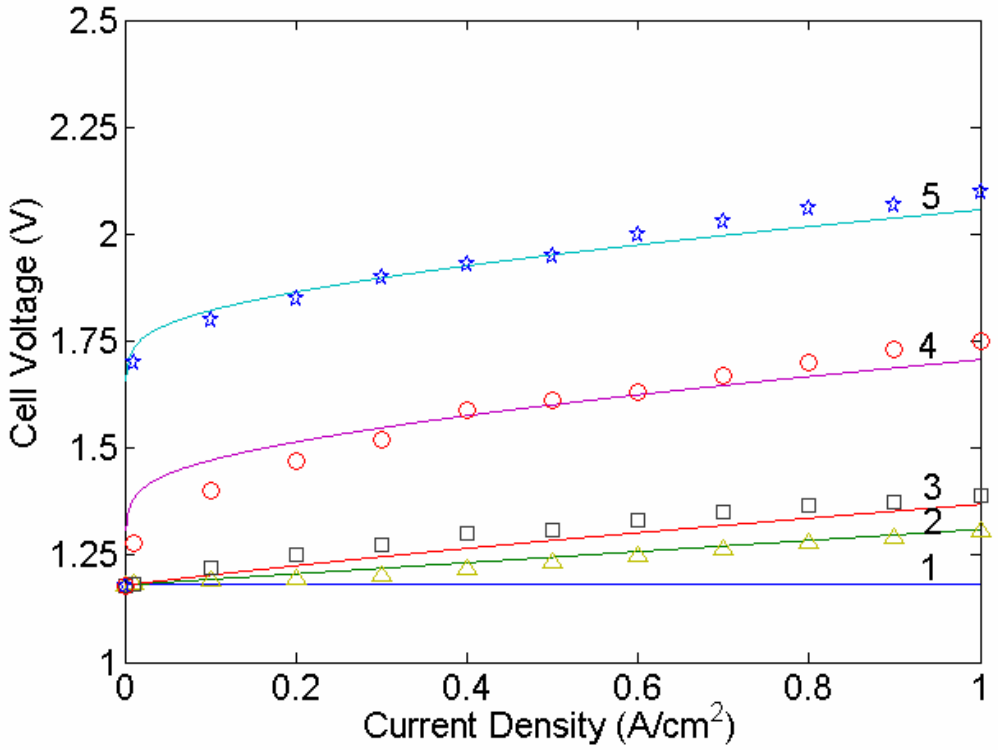

Figure 9-3.Comparison of the model with experiments at 80ºC (1: equilibrium voltage, 2: ohmic drop, 3: cathode overpotential, 4: anode overpotential on Pt-IrO_2, 5: anode overpotential on Pt). Experimental data is given by symbols.

Table 9-1. Model parameters for water electrolysis for Pt coated anode and cathode electrodes on Nafion® electrolyte.

Parameters	Values	Dimensions	Comments and references
i_{A0}	10^{-11}	A/cm^2	anode exchange current density at 25° C[8]
i_{C0}	10^{-3}	A/cm^2	cathode exchange current density at 25° C[9]
L_B	183	μm	thickness of Nafion® 117 electrolyte
σ_B	0.14	Siemens/cm	conductivity of Nafion® 117 electrolyte[10]

electrode surface and also the roughness factor,[14] which is defined as the electrochemically determined electrode area divided by the geometric area.

$$i_\circ = \gamma_M \exp\left[-\frac{E}{R}\left(\frac{1}{T}-\frac{1}{T_{ref}}\right)\right] i_\circ^{ref} \qquad [17]$$

where $i_\circ$, γ_M, E and $i_\circ^{ref}$ represent exchange current density, roughness factor, activation energy and exchange current density at reference state. The roughness factor can be determined experimentally[4,22-24] or estimated by catalyst loading, catalyst particle density and diameter.[14] Of course, the microstructure of electrodes affects the roughness factor and reported for oxygen reduction reaction as 2.7[24], 9.2,[26] 200[4] for Pt microdisk, Pt wire and Pt powder electrodes, respectively. The roughness factor for typical electrolysis cell would be 100-300[27,28] and here 150 is adopted for both electrodes in the model. The conductivity of Nafion depends on the water content in it and taken to be 0.14 S/cm at 80º C for liquid phase immersion.[29] The interface resistance R_I is assumed to be relatively small and set to zero in this model.

Figure 9-3 shows that the ohmic overpotential increases steadily and the cathode overpotential is relatively small because of the fast kinetics at the electrode surface. The anode reaction is sluggish and the overall process is limited by the oxygen evolution reaction. The anode overpotential increases rather sharply at low current density and slowly thereafter with the current density. Since the cathode reaction is relatively fast compared with the anode reaction, the potential increase of the electrolysis cell with current density is mainly attributable to the slow kinetics of water dissociation at the anode. Thus, a current density of 1 A/cm^2 is achieved for the applied voltage of 2.1 V at 80º C for the Pt anode.[18,20] In order to reduce anode polarization, iridium, which exists in oxide form under reaction conditions, has usually been added to Pt for SPE water electrolysis. Ioroi et .al.[20] reported that the mixture of high surface area IrO_2 and Pt black

(50:50 mol ratio) improved the efficiency of water electrolysis from 77 % to 95 % at 300 mA/cm^2. When IrO_2 is added to Pt, the exchange current density is increased and thus the oxygen evolution reaction at the anode occurs at lower overpotential.[22] The model predicts overpotentials quite satisfactorily over the current range of the experiment for the Pt and Pt-IrO_2 anodes.

The electrolysis process may be represented by an equivalent electrical circuit consisting of a series of resistances representing each individual steps. In analogy to the linear ohm's law, a differential resistance R_d may be defined for an electrolysis cell as[11]

$$R_d = \frac{d(V_\circ - V)}{di} \qquad [18]$$

where $V_\circ$ is the Nernst potential and may be thought of as an internal power supply for the cell to reach the equilibrium. Combining Eq. 11 with 18 provides each individual resistance associated with the different steps of the process.

$$R_d = \frac{d\eta_C}{di} - \frac{d\eta_A}{di} + \frac{d\eta_A}{di} + \frac{d\eta_A}{di} \qquad [19]$$

Differentiation of the corresponding overpotentials gives resistance separately for anode, cathode, solid polymer electrolyte and interface.

$$R_A = \frac{RT}{(2Fi_{A0})\sqrt{1+\frac{1}{4}\left(\frac{i}{i_{A0}}\right)^2}} \qquad [20]$$

$$R_C = \frac{RT}{(2Fi_{C0})\sqrt{1+\frac{1}{4}\left(\frac{i}{i_{C0}}\right)^2}} \qquad [21]$$

$$R_{SPE} = \frac{L_B}{\sigma_B} \qquad [22]$$

and of course, $R_I = R_I$. The overall resistance for membrane/electrode unit calculated for the parameters given in Table 9-1 is shown in Figure 9-4. At low current densities, i.e., at a current density less than 200 mA/cm^2, the anode resistance R_A dominates and thereafter R_{SPE} = 0.13 $\Omega\,\text{cm}^2$ becomes a significant fraction of the total resistance. If there is a limitation for mass transfer in the cell, diffusional limitation resistance would dominate at high current densities, which have been neglected in this simple analysis.

Figure 9-5 represents the power density input to the electrolysis cell using a solid polymer electrolyte with Pt-IrO_2 for oxygen electrode and Pt for hydrogen electrode. The power supply to the cell is proportional to the current density, and thus the rate of reaction. The inherent energy, or the lowest energy supply for water electrolysis, is about 1.2 W/cm^2 for 1 A/cm^2 at 80º C. It is impossible to avoid this minimum power input for water electrolysis because it comes from the Gibbs free energy change of the reaction at the experimental condition. An additional energy requirement due to anode overpotential is 0.3 W/cm^2 at 1 A/cm^2 and may be reduced by new anode electrocatalysts. For hydrogen production, the energy requirement may conceivably be reduced substantially if a methanol solution is used instead at anode because of its low equilibrium potential of 0.02 V compared with that of pure water of 1.23 V.

9-4. Conclusions

The performance of SPE water electrolysis is analyzed by means of a simple analytical model incorporating the kinetics at the electrodes surfaces and transport in the cell. The model analyzes each individual resistance associated with the different steps of the electrolysis process in the membrane/electrode unit and predicts overpotentials over a range of current densities for Pt and Pt-IrO_2 electrocatalysts. It clearly shows that the high anode overpotential is the limiting factor for the whole process and mainly responsible for

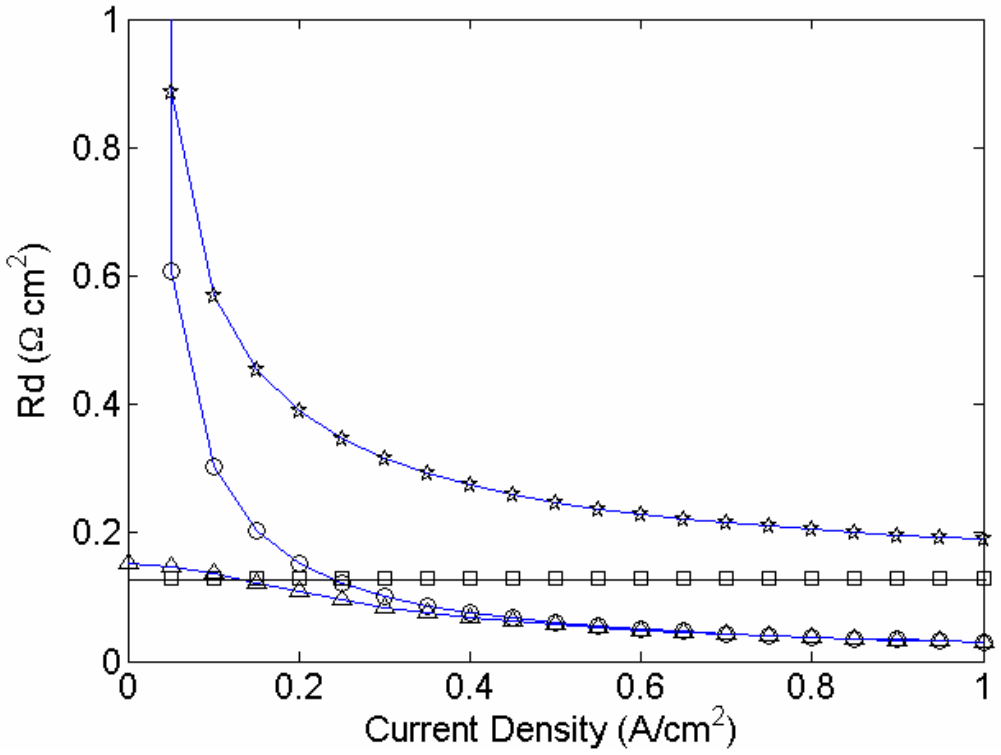

Figure 9-4. Differential resistances for water electrolysis: star = total differential resistance, circle = anode differential resistance, square = membrane differential resistance and triangle = cathode differential resistance.

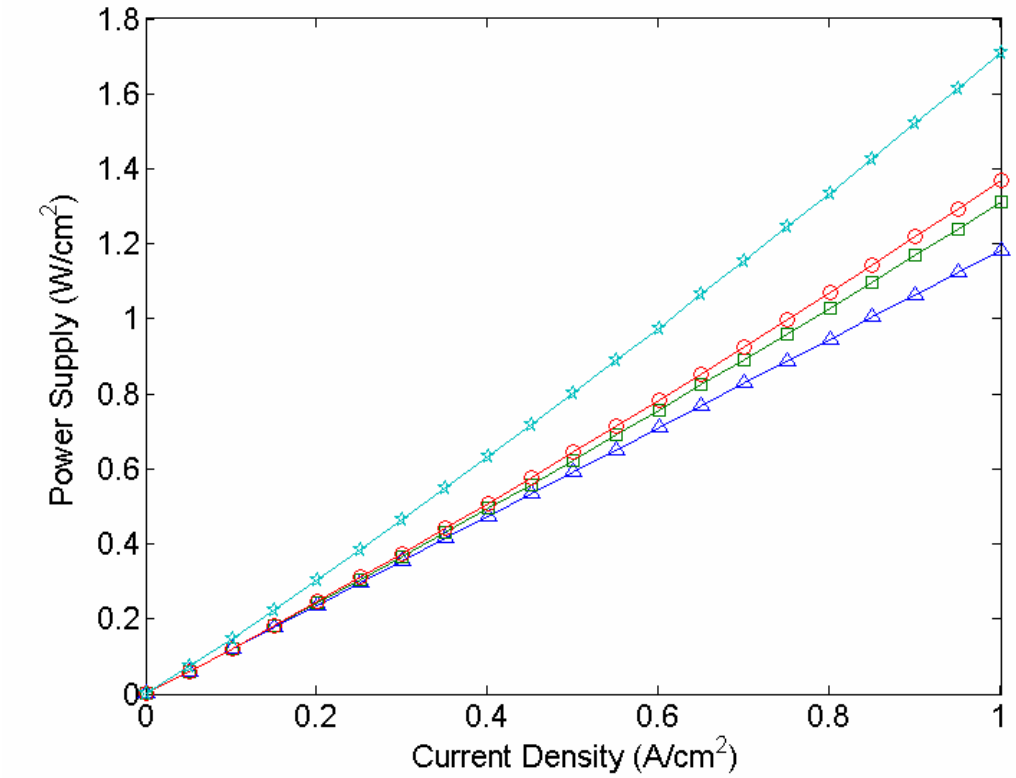

Figure 9-5. Energy input vs. current density: star = energy supply due to Pt-IrO_2 anode overpotential, circle = energy supply due to cathode overpotential, square = energy supply due to ohmic drop and triangle = inherent energy supply.

the energy supply needed in the electrolysis cell in addition to that to overcome the thermodynamic work. The model represents the experimental data satisfactorily and provides useful insights for water electrolysis by a solid polymer electrolyte cell.

References

1 C. Stone and A. E. Morrison, *Solid State Ionics,* **152-153**, 1 (2002).

2 R. Strobel, M. Oszcipok, M. Fasil, B. Rohland, L. Jorissen, and J. Garche, *J. Power Sources,* **105**, 208 (2002).

3. M. Kato, S. Maezawa and K. Sato, *Applied Energy,* **59**, 261 (1998).

4 A. Aldebert, F. Novel-Cattin, M. Pineri, P. Millet, C. Doumain, and R. Durand, *Solid State Ionics*, **35**, 3 (1989).

5. C. A. Linkous, H. R. Anderson, R. W. Kopitzke, G. L. Nelson, *Int. J. Hydrogen Energy*, **23**, 525 (1998).

6. W. Smith, *J. Power Sources*, **86**, 74 (2000).

7. A. Leonida, J. McElroy, and T. Nalette, *J. Power Sources*, **29**, 399 (1990).

8. L. L. Swette, A. B. LaConti, and S. A. McCatty, *J. Power Sources*, **47**, 343 (1994).

9. T. Ioroi, N. Kitazawa. K. Yasuda, Y. Yamamoto, H. Takenaka, *J. Electrochem. Soc.*, **147**, 2018 (2000).

10 J. O'M. Bockris, A. K. N. Reddy, Modern Electrochemistry, Kluwer Academic/Plenum Publishers, New York, 2000.

11. J. O'M. Bockris and S. Srinivasan, *Fuel Cells: Their Electrochemistry,* McGraw-Hill, New York, 1969.

12. T. Berning, D. M. Lu, and N. Djilali, *J. Power Sources,* **106**, 284 (2002).

13. K. Sundmacher, T. Schultz, S. Shou, K. Scott, M. Gunkel, and E. D. Gilles, *Chem. Eng. Sci.*, **56**, 333 (2001).

14. T. Thampan, S. Malhotra, J. Zhang, and R. Datta, *Catalysis Today,* **67**, 15 (2001).

15. N. M. Markovic and P. N. Ross, *Electrochim. Acta*, **45**, 4101 (2000).

16. K. Onda, T. Murakami, T. Hikosaka, M. Kobayashi, R. Notu, and K. Ito, *J. Electrochem. Soc*., **149**, A1069 (2002).

17. R. Holze and J. Ahn, *J. Membrane Science*, **73**, 87 (1992).

18. P. Millet, *Electrochim. Acta,* **39**, 2501 (1994).
19. K. Ledjeff, F. Mahlendorf, V. Peinecke, and A. Heinzel, *Electrochim. Acta,* **40**, 315 (1995).
20. T. Ioroi, K. Yasuda, Z. Siroma, N. Fujimara, and Y. Miyazaki, *J. Power Sources,* **112**, 583 (2002).
21. D. M. Bernardi and M. W. Verbrugge, *J. Electrochem. Soc.,* **139**, 2477 (1992).
22. A. Damjanovic, A. Dey and J. O'M. Bockris, *J. Electrochem. Soc*., **113**, 739 (1966).
23. K. Kinoshita, *Electrochemical Oxygen Technology*, Wiley, New York, 1992.
24. P. D. Beattie, V. I. Basura, and S. Holdcroft, *J. Electroanal. Chem*., **468**, 180 (1999).
25. N. M. Markovic, B. N. Grugr, and P. N. Ross, *J. Phys. Chem*., **101**, 5405 (1997).
26. A. Parthasarathy, C. R. Martin, and S. Srinivasan, *J. Electrochem. Soc.*, **138**, 916 (1992).
27. A. R. Kucernak and B. Muir, *Electrochim. Acta,* **46**, 1313 (2001).
28. O.J. Murphy, G. D. Hitchens, and D. J. Manko, *J. Power Sources,* **47**, 353 (1994).
29. K. Scott, W. Taama, and J. Cruickshank, *J. Power Sources*, **65**, 159 (1997).

PART IV.

Conclusions and

Recommendation for Future Work

Chapter 10. Conclusions and Recommendation for Future Work

"Excellence is an art won by training and habituation. We do not act rightly because we have virtue or excellence, but we rather have those because we have acted rightly. We are what we repeatedly do. Excellence, then, is not an act but a habit." *- Aristotle -*

Chapter 10. Conclusions and Recommendations for Future Work

10-1. Conclusions

This thesis deals with the theoretical aspects of PEM fuel cells in terms of thermodynamics, transport, and kinetics of different fuel cell applications. Each chapter of the thesis summarizes conclusions therein. Here, some of these results are summarized.

1. Thermodynamic models describing the sorption of water in Nafion have been developed. The models are insightful for understanding phase equilibrium in PEM-water systems and are used to predict sorption isotherms from the fundamental properties of PEM and water. The first version is based on the use of ideal molecular mixture for free solvent and involves a spring constant to describe the elastic behavior. This model provide a plausible explanation for the long unresolved phenomenon termed Schroeder's paradox, namely the difference between the amounts sorbed from a liquid solvent versus from its saturated vapor. The solvent uptake is governed by the swelling pressure caused within the membrane as a result of stretching of the polymer chains upon solvent uptake, Π_M, as well as a surface pressure, Π_σ, due to the curved vapor-liquid interface of pore liquid. The second version relaxes these assumptions and involves the Flory-Huggins model for the mixture thermodynamics and a more realistic model of polymer elasticity. The key variables for sorption are equivalent weight of ionomer, acid strength of the ionic groups, modulus of polymer elasticity, and interaction between water and polymer. The water uptake per unit mass of dry Nafion® increases with the increasing acid strength of the functional groups, decreasing Young's modulus, and decreasing equivalent weight of Nafion®. The model provides insights on the sorption and swelling behavior of ion-

exchange membranes, and this framework can be used to evaluate and design alternate proton-exchange membranes for fuel cell applications.

2. The proton transport models in PEMs have been proposed based on the understanding of the structure, thermodynamics, and various transport mechanisms in PEMs. A pore transport model describes proton diffusion at various hydration levels within Nafion® by incorporating structural effect upon water uptake and various proton transport mechanisms, namely proton hopping on pore surface, Grotthuss diffusion in pore bulk, as well as ordinary mass diffusion of hydronium ions. The diffusion coefficients are obtained *a priori* based on a comprehensive random walk framework that connects the molecular details of proton transfer to the continuum diffusion coefficients. The proton conductivity in contact with water vapor is accurately predicted as a function of relative humidity without any fitted parameters. The model is has been extended to describe proton diffusion in Nafion®/(ZrO_2/SO_4^{2-}) nanocomposite membrane designed for operation at high temperature and low relative humidity conditions. The proton conductivity in the composite membrane depends upon i) the water content, which affects structural parameters such as porosity and tortuosity, ii) diffusion coefficients at surface and bulk regions, and iii) proton concentration on the surface on the surface and in the pores. The conductivity of the membrane in contact with water vapor is accurately predicted as a function of relative humidity without any fitted parameters. Nafion®/(ZrO_2/SO_4^{2-}) composite membrane shows higher proton conductivity compared with Nafion at the same temperature and humidity conditions due to the improved water uptake and additional acid sites. The model provides a theoretical framework for understanding proton conduction in Nafion®/(ZrO_2/SO_4^{2-}) membrane and can be used to investigate performance of new composite proton exchange membranes at elevated temperatures for fuel cell applications. The results are encouraging and this polymer/inorganic membrane can be classified as a

remarkable family of proton exchange membranes which have great potential in fuel cell applications.

3. Fuel cell systems that include DMFC, hydrogen diffusion Pd anode fuel cell, and regenerative fuel cells have been investigated. A performance model along with methanol oxidation kinetic model in DMFC has been proposed. The current oscillations during DMFC operation at constant potential condition are reported. The basic reason for the oscillations is due to the transition of the anode surface from a poisoned to a free surface available for methanol oxidation reaction. Dynamic feed operation in DMFC has been tested to improve the performance as well as to save the fuel. The undesirable surface carbon species were oxidized during the operation and this strategy may be applied for improved DMFC operation. Methanol impermeable Pd deposited PEM has been developed by the electroless plating of PEMs to reduce methanol crossover problems in DMFC. The Pd deposited PEMs are beneficial for the low current region of DMFC. The use of nonporous anode has been studied and a theoretical model for the process has been developed based on the kinetics of the electrode surfaces, transport of hydrogen atoms, and protons through the nonporous anode and proton exchange membrane, respectively. Water electrolysis in a regenerative fuel cell system has been studied and a performance model has been proposed.

4. This thesis provides a theoretical framework for detail understanding of thermodynamics, transport, and kinetics of PEM fuel cell systems. This approach may be applied to various related fields. For example, the thermodynamic approach for studying water-PEM system can successfully be applied to investigate the isotherm of hydrogen-metal hydride system as well as hysterisis of sorption in both cases. Also, the understanding of proton transport in PEM by the application of the Einstein-Smoluchowski relation, which connects the microscopic details of particle motion to the macroscopic parameter of diffusion, can be used for hydrogen diffusion in metals.

10-2. Recommendations for Future Work

10-2-1. Proton Transport in PEM below Freezing Temperature

The PEM fuel cells perform optimally at around 80 ºC. If the temperature exceeds 100 ºC, drying of the membrane as well as that of the ionomer within the catalyst layer causes the performance to drop precipitously, even though these higher temperatures are desirable from the standpoint of improved CO tolerance of anode and better oxygen reduction kinetics at the cathode. During fuel cell operation, water is supplied by humidifier and also produced at cathode by oxygen reduction. When the temperature of fuel cell becomes falls below zero Celsius, as expected for automobile and outdoor applications in winter, water in the fuel cell system is expected to freeze. Clearly, the electrode kinetics at both anode and cathode are expected to be slow at these low temperatures.[1] How about the transfer of protons at temperatures at subzero temperatures? Does the membrane even conduct protons when frozen? This basic question should be addressed adequately, especially for automobile applications of fuel cells.

Both kinetics and thermodynamics (Nernst potential) of electrode reactions are strongly dependent upon temperature. Thus, temperature dependence of kinetics is given by the variation of the exchange-current density which, e.g., for cathode is given by[2]

$$i_{C,0} = \gamma_{M,C}\left(\frac{p_{O_2}}{p_{O_2,ref}}\right)\left(\frac{c_{H^+}}{c_{H^+,ref}}\right)\exp\left\{-\frac{E_{C,\Phi_0}}{R}\left(\frac{1}{T}-\frac{1}{T_{ref}}\right)\right\} i^*_{C,0,ref} \qquad [1]$$

where $i_{C,0}$ is exchange current density at cathode, $\gamma_{M,C}$ is the effective electrochemical surface area, p_{O_2} is the partial pressure of oxygen $p_{O_2,ref}$ is the partial pressure of oxygen at reference state, C_{H+} is the proton concentration at the electrode surface, $C_{H+,ref}$ is the proton concentration at a reference state (250C), E_{C,Φ_0} is the activation energy, $i_{C,0,ref}$ is the exchange current density at reference state. The activation energy for the cathode is

around 76 kJ/mol and that for anode is 18 kJ/mol. Therefore, the cathode would be more severly affected by lower temperatures. The open-circuit potential of a H_2-O_2 fuel cell is given as a function of temperature by[2]

$$V_0 = 1.23 - 0.9 \times 10^{-3}(T - 298) + \frac{RT}{4F} \ln p_{\mathrm{H}_2}^2 p_{\mathrm{O}_2} \qquad [2]$$

where V_0 is the equilibrium potential for oxygen reduction reaction, p_{H_2} is the partial pressure of hydrogen. The overall effect on the performance of the electrode at low temperatures is, however, not so clear. For example, certainly the partial pressure of oxygen p_{O_2} (in Eqs. 1 and 2) would be substantially higher due to the very low vapor pressure of water below freezing. Further, the solubility of oxygen would be different, as would the effective electrochemical surface area ($\gamma_{M,C}$), as well as the proton conductivity of the ionomer in the catalyst layer, as discussed below. Such effects and their impact on the overall electrode performance need to be carefully investigated.

The degree of water loading in this layer determines the limiting current and hence constraints the fuel cell performance under high current density conditions. The adhesion of the various layers and the contact resistance is also, to a large extent, dependent upon the degree of swelling of the PEM. It is, thus, clear that all layers of the MEA and, hence, the fuel cell performance is strongly affected by water. Operating below the freezing point would clearly, thus, be expected to have a significant impact on the fuel cell performance.

The change of conductivity of ions with temperature has been reported.[3-14] In pure ice, the proton's mobility is, however, approximately 100 times greater than it is in water. For example, at -10^0C, the concentration of protons in pure water is 2.8×10^{-8} g ion/l, while in ice it is 5×10^{-11} g ion/l. This gives proton mobility of water 3.3×10^{-3} $cm^2 s^{-1} V^{-1}$ and that of ice 1.9×10^{-1} $cm^2 s^{-1} V^{-1}$ at -10^0C.[6] As discussed in this thesis, the reason for high proton mobility in ice is due to the low proton concentration and changes in the rate-determining step (RDS) in the Grotthuss diffusion mechanism. The Grotthuss proton transfer involves

two sequential steps: i) rotation of a water molecule adjacent to a hydronium ion into a receptive orientation, and ii) the transfer of proton from the hydronium ion to the water molecule, possibly via quantum mechanical tunneling. In liquid water, the first step is the RDS, while in ice the second step may be the RDS, since water molecules in ice are likely to be frozen in a receptive orientation via hydrogen bonding, rather than being randomly oriented via thermal relaxation. Water molecules in ice rotate into the correct position, even without the help of oncoming proton, so that they offer an inviting orbital to any oncoming proton. With so few protons in ice, the waters rotate spontaneously in time for occasional oncoming proton. The conduction phenomena in Nafion at subzero temperatures have reported.[15,16] The proton mobility of frozen Nafion are expected to be higher than that when the water in the pores is in the liquid state at the same temperature, since Grotthuss diffusion is a dominant contributor (~ 80%) to proton conduction in Nafion®. A study of this phenomenon would be of fundamental interest in addition, of course, to the very practical reasons alluded above for its investigation.

The PEM conductivity at subzero temperatures can be measured by both the current interruption method and with either *in-situ* or *ex-situ* AC Impedance Spectroscopy. With the proper model, the conductivity both in the catalyst layer and membrane can be determined. Fuel cell experiments will also be performed at temperatures ranging from room temperature down to – 40 ºF. Modeling the effect of temperature on kinetics and transport and on performance of the MEA should be done along with the experiments.

10-2-2. Thermodynamics of Hydrogen Sorption in Pd

Metal hydrides have been used in a number of applications such as hydrogen storage for portable power sources and catalytic converters.[17-20] The most important property of the metal hydrides is the pressure-composition isotherm for the hydrides. Palladium hydride is in a class of metal hydrides where the interaction between the metal and

hydrogen results in the phase transformation, under increasing hydrogen pressure, from a low concentration phase of hydrogen saturated metal called α phase, to a higher concentration, defective phase of somewhat variable composition called the β phase. For some metals there is a structural phase transformation of metal lattice in passing from the α to β phase, but in palladium there is only a change in lattice constant of fcc lattice. The thermodynamic equilibrium of palladium-hydrogen systems is established between gaseous hydrogen and hydrogen in metal hydride phase. The thermodynamic properties of palladium-hydrogen system have been extensively studied.[21-31]

$$H_2 + 2M \leftrightarrows 2M - H_{ab} \quad [3]$$

The chemical potential of H_2 in the gas phase and H atom in metal phase are governed by

$$\sum_i^n \nu_{\rho i} \mu_i = 0 \quad [4]$$

Chemical potential of species *i* in phase α can generally be written as

$$\mu_{i,\alpha} = G_i^0(T, P^0) + \int_{P^0}^{p} \left(\overline{V}_{i,\alpha}\right) dP + \mathrm{RT} \ln\left(a_{i,\alpha}\right) + \Psi_i \quad [5]$$

For the gas phase H_2 and the atomic H in the metal,

$$\mu_{H_2} = \mu_{H_2}^{\circ} + \mathrm{RT} \ln a_{H_2,V} \quad [6]$$

$$\mu_H = \mu_H^{\circ} + \mathrm{RT} \ln a_{H,S} + \int_{p^{\circ}}^{p} \left(\overline{V}_{H,S}\right) dP \quad [7]$$

From the equilibrium criteria,

$$\ln\left(\frac{a_{H_2,V}}{\left(a_{H,S}\right)^2}\right) = \frac{\mu_H^{\circ} - \frac{1}{2}\mu_{H_2}^{\circ}}{RT} + \frac{1}{RT}\int_{p^{\circ}}^{p} \left(\overline{V}_{H,S}\right) dP \quad [8]$$

Substituting

$$a_{H_2,V} = p \Big/ p^{\circ} \quad [9]$$

$$a_{H,S} = \frac{x}{x_S - x} \quad [10]$$

$$\ln K = \frac{\mu_H^\circ - \frac{1}{2}\mu_{H_2}^\circ}{RT} \quad [11]$$

where x is the atomic ratio of H to Pd in Pd hydride, and x_S is the atomic ratio at saturation. Assuming constant partial molar volume over the pressure range, the Eq. can be rearranged as

$$\ln\left(p_{H_2}\left(\frac{x_S - x}{x}\right)^2 \right) = 2\ln K + \frac{2}{RT}\overline{V}_H \Pi_M \quad [12]$$

where

$$\Pi_M = p - p^\circ \quad [13]$$

The increasing pressure inside of the metal Π_M with hydrogen ingress stretches out the lattice of the metal resulting in phase transformation and an increase in its lattice constant. For example, the lattice constant of pure Pd metal increases from 3.891 Å to 3.894 Å for the absorption of hydrogen up to x = 0.025-0.003 and further absorption of hydrogen causes the formation of β phase of palladium hydride in equilibrium with the low concentration of α phase. The α phase retains the fcc metal lattice of palladium atoms. However, there occurs a discontinuous change to a new lattice parameter of 4.026 Å characteristic of a first-order phase transition. The hydrogen concentration at this phase is $x \approx 0.6$ with the hydrogens apparently randomly occupying the octahedral interstices in the lattice. The macroscopic concentration ratios 0.03 < x < 0.6 only reflect a mixture of α and β phase according to the lever rule.

The K value may be obtained by plotting the LHS of Eq. vs. x. The intercept of the plot will be 2lnK because the pressure term will be zero at no absorption of hydrogen gas. With adequate expression for Π_M, the thermodynamic isotherm can be obtained. The

lattice expansion of Pd can be correlated to the pressure Π_M by Pd metal's mechanical property such as Young's modulus of elasticity.

10-2-3. Others

Here are some research topics that I would finish in a couple of years

1. DMFC Modeling and Experiment
2. Use of nanocomposites in DMFC
3. Pulsing Studies of DMFC
4. Pd Anode Fabrication and Testing for H_2-O_2 or Methanol Fuel Cells
5. Kinetic Modeling of Current Oscillations
6. Transport of Protons in Palladium
7. Transport of Hydrogen Atom in Palladium
8. PEM Characterization by IR (ATR)
9. Transport of Water in PEM by Isotope Experiment

Some long-term research topics are

1. Transport of Protons in PEM by Molecular Dynamic Simulation
2. Design and Development of PEM
3. Design and Development of Nano-structured Electrodes

References

1. E. Cho, J. J. Ko, H. Y. Ha, S. A. Hong, K. Y. Lee, T. W. Lim, and I. H. Oh, *J. Electrochem. Soc.*, **151**, A661 (2004).
2. T. Thampan, S. Malhotra, J. X. Zhang, and R. Datta, *Catal. Today*, **67**, 15, (2001).
3. J. Johnson, *J. Am. Chem. Soc.*, **31**, 987 (1909).
4. J. Johnson, *J. Am. Chem. Soc.*, **31**, 1010 (1909).
5. A. Gierer, and K. Wirtz, *J. Chem. Phys*., **17**, 745 (1949).
6. B. E. Conway and J O'M Bockris, *J. Chem. Phys.*, **28**, 354 (1958).
7. J. O'M. Bockris and A. K. N. Reddy, *Modern Electrochemistry 1 Ionics*, Plenum Press, NY (1998).
8. M. Eigen, L de Maeyer, *Proc. Roy. Soc. Lond., A. Math. Phys. Sci*., **247**, 505 (1958).
9. Hobbs, P. V., *Ice Physics*, Clarendon Press, Oxford (1974).
10. Jaccard, C., "Transport Properties of Ice" in Horne, R. A., ed., *Water and Aqueous Solutions*, Wiley-Interscience, NY (1972).
11. N. Bjerrum, *Science*, **115**, 385 (1952).
12. M. Kunst and J. M. Warman, *J. Phys. Chem*., **87**, 4093 (1983).
13. W. B. Collier, G. Ritzhaupt, and J. P. Devlin, *J. Phys. Chem*., **88**, 363 (1984).
14. A. A. Kornshev, A. M. Kuznetsov, E. Spohr, and J. Ulstrup, *J. Phys. Chem. B*, **107**, 3351 (2003).
15. K. Uosaki, K. Okazaki, and H. Kita, *J. Electroanal. Chem.*, **287**, 163 (1990).
16. M. Cappadonia, J. W. Erning, S. M. S. Niaki, and U. Stimming, *Solid State Ionics*, **77**, 65 (1995).
17. *Transition Metal Hydrides*, edited by E. L. Muetterties, Marcel Dekker, NY (1971).
18. *Hydrogen in Metals I*, edited by G. Alefeld and J. Volkl, Springer-Verlag, Berlin (1978).
19. *Hydrogen in Metals II*, edited by G. Alefeld and J. Volkl, Springer-Verlag, Berlin

(1978).

20. Y. Fukai, *The Metal-Hydrogen System*, Springer-Verlag, Berlin (1992).
21. D. P. Smith, *Hydrogen in Metals*, University Press, Chicago (1948).
22. F. A. Lewis, *The Palladium Hydrogen System*, Academic Press, London (1967).
23. J. F. Lynch and T. B. Flanagan, *J. Chem. Soc. Faraday Trans.* I, **70**, 814 (1974).
24. C. A. Mackliet, D. J. Gillespie, A. I. Achindler, *J. Phys. Chem. Solids*, **37**, 379 (1976).
25. C. Picard, O. J. Kleppa, and G. boureau, *J. Chem. Phys.*, **65**, 5549 (1978).
26. T. Kuji, W. A. Oates, B. S. Bowerman, and T. B. Flanagan, *J. Phys. F: Met. Phys.*, **13**, 1785 (1983).
27. S. Salomons, *Phys. Rev. B*, **42**, 1183 (1990).
28. R. J. Wolf, M. W. Lee, and R. C. Davis, *Phys. Rev. B*, **48**, 12415 (1993).
29. R. J. Wolf and M. W. Lee, *Phys. Rev. Lett.*, **73**, 557 (1994).
30. F. A. Lewis, *Int. J. Hydrogen Energy*, **21**, 461 (1996).
31. V. Srivastava and R. Balasubramaniam, *Mat. Sci. Eng.*, **A304-306**, 897 (2001).

Appendix

General theory of random walk

The random walk theory can be successfully applied to the diffusion process of protons and hydrogen atoms. Here the general derivation of random walk theory and its relation to diffusion process have been described from the different point of views. Random walk means that each jump of a particle is independent of all its preceding ones, both in length and direction. The so-called Einstein-Smoluchowski equation provides a bridge between the microscopic view of random-walking of particle (or ions) and the macroscopic Fick's law.

1. Distribution Function[1]

A distribution function W (X, τ) is introduced which gives the probability that at time τ the particle will have traveled a path with projection X. It is assumed that W depends neither on x nor τ. Consider next a balance for the number of particles of the diffusing species located in the plane x at time t + τ. At time t, these particles were located in the planes $x - X$. Thus:

$$\text{c (x, t + } \tau \text{)} = \sum_X c(x-X,t) \bullet W(X,\tau) \qquad [1]$$

where c is the number of particles per unit volume, and the summation being carried out over all values of X. Expanding c to second order in x and first order in t, and dropping higher order terms:

$$\text{c (x, t)} + \tau \frac{\partial C}{\partial t} + \ldots = \sum_X \left[c(x,t) - X \frac{\partial c}{\partial x} + \frac{X^2}{2} \frac{\partial^2 c}{\partial x^2} + \ldots \right] \bullet W(X,\tau) \qquad [2]$$

where the derivatives of C are defined for the plane x at time t.

By definition of the moment X:

$$\sum_X W(X,\tau) = 1 \qquad [3]$$

$$\sum_X X^m \bullet W(X,\tau) = \left\langle X^m \right\rangle \qquad [4]$$

Eq. 3 shows that the probabilities W are normalized. Eq. 4 defines the m^{th} moment of X: the average value of X^m taken over a large number of particles. For small value of τ, the terms of omitted on LHS of Eq. 2 become negligible. Further, the function W (X, $\tau \rightarrow 0$) becomes more and more narrow around x = 0, and all terms higher than second order on the RHS can also be neglected. Thus:

$$\frac{\partial c}{\partial t} = -\frac{\left\langle X \right\rangle}{\tau}\frac{\partial c}{\partial x} + \frac{\left\langle X^2 \right\rangle}{2\tau}\frac{\partial^2 c}{\partial x^2} \qquad [5]$$

For a random walk in the absence of a driving force $\left\langle X \right\rangle = 0$:

$$\frac{\partial c}{\partial t} = \frac{\left\langle X^2 \right\rangle}{2\tau}\frac{\partial^2 c}{\partial x^2} \qquad [6]$$

Comparison with the Fick's 2nd diffusion equation gives

$$D_x = \frac{\left\langle X^2 \right\rangle}{2\tau} \qquad [7]$$

2. Statistical View of Diffusion[2]

Fick's 2nd diffusion equation is known as

$$\frac{\partial c}{\partial t} = D_x \frac{\partial^2 c}{\partial x^2} \qquad [8]$$

where c is the number density of diffusion species, c (x,t). This is second order differential equation with respect to space and a first order differential equation with respect to time. Therefore, in order to solve this equation, we need to specify two boundary conditions for the spatial dependence and a single initial condition for the time dependence. A specific

example can be made, i.e., a sugar is initially coated on the bottom of a deep beaker of water. The initial condition is that at t = 0, all c_0 particles are concentrated on the yz plane (of area A) at x = 0. The boundary conditions are i) the concentration must everywhere be finite and ii) the total number of particles present is c_0 at all times. The solution of the diffusion equation under these conditions is

$$c = \left[c_0 / A(\pi Dt)^{\frac{1}{2}} \right] e^{-x^2/4Dt} \qquad [9]$$

On the other hand, the probability that a particle will be found at distance x from the origin after time t is calculated as follows. During that time it will have taken n steps, with $n = t/\tau$. If n_R of these are steps to the right, and n_L are steps to the left (with $n_R + n_L = n$), then the net distance traveled is $x = (n_R - n_L)d$, where d is jump distance. That is, to arrive at x, we must ensure that

$$n_R = \frac{1}{2}(n+s) \text{ and } n_L = \frac{1}{2}(n-s) \qquad [10]$$

with s = x/d. The probability of being at x after n steps of length d is therefore the probability that, when n random steps are taken, the numbers to the right and the left are as give Eq. 10.

The total number of different journeys for a walk of n steps is equal to 2^n, because each step can be in either of two directions. The number of journeys in which exactly n_R steps are taken to the right is equal to the number of ways of choosing n_R objects from n possibilities irrespective of the order: this is

$$\frac{n!}{n_R!(n-n_R)!} \qquad [11]$$

Thus the probability of being at x after n steps is

P = Number of journeys with nR steps to the right/Total number of journeys

$$= \frac{[n!/n!(n-n_R)!]}{2^n}$$

$$= \frac{\left\{n!/\left[\frac{1}{2}(n+s)!\right]\left[\frac{1}{2}(n-s)!\right]\right\}}{2^n} \qquad [12]$$

Using Stirling's approximation

$$\ln N! = (N+\tfrac{1}{2})\ln N - N + \ln(2\pi)^{1/2} \qquad [13]$$

Taking logarisms of Eq. 12 provides

$$\ln P = \ln n! - \ln\left[\frac{1}{2}(n+s)\right]! - \ln\left[\frac{1}{2}(n-s)\right]! - n\ln 2$$

$$= \ln(2/\pi n)^{1/2} - \frac{1}{2}(n+s+1)\ln(1+s/n) - \frac{1}{2}(n-s+1)\ln(1-s/n) \qquad [14]$$

So long as s/n <<1 (which is equivalent to x not being at great distance from the origin) we can use the approximation ln (1+z) $\approx$ z, and obtain

$$\ln P = \ln(2/\pi n)^{1/2} - s^2/2n \text{, or } P = (2/\pi n)^{1/2} e^{-s^2/2n} \qquad [15]$$

Finally replace s by x/d and n by t/τ, and obtain

$$P = (2\tau/\pi t)^{1/2} e^{-x^2\tau/2td^2} \qquad [16]$$

Comparison of Eq. 9 and 16 provides

$$D = d^2/2\tau \qquad [17]$$

3. Use of Mean Square Distance[3]

Consider unit area of reference plane normal to the x direction. There is a random walk of particles across this plane both from left to right and from the right to left. This reference plane is termed the transit plane. On either side of the transit plane, one can imagine two planes L and R which are parallel to the transit plane and situated at a distance

$\sqrt{< X^2 >}$ from it. In other words, the region under consideration has been divided into left and right compartments in which the concentrations of particles are different and designated by c_L and c_R, respectively.

In a time t sec, a random walking particle covers a mean square distance of $<X^2>$. Thus, by choosing the plane L to be at a distance $\sqrt{< X^2 >}$ from the transit plane, one has insured that all the particles in the left compartment will cross the transit plane in a time t provided they are moving in left→ right direction. The number of particles in left compartment is the volume $\sqrt{< X^2 >}$ of this compartment times the concentration c_L of particles. Due to the random walk, one half of the particles move to the right. The number of moles of particles making left to right crossing in 1 sec is thus $\frac{1}{2}\left(\sqrt{< x^2 >}/t\right)c_L$. Similarly the number of moles of particles making the right to left crossing in 1 sec is $\frac{1}{2}\left(\sqrt{< x^2 >}/t\right)c_R$. Thus the diffusion flux of particles across the transit plane , i.e., the net number of moles of particles crossing unit area of the transit plane per second from left to right is given by

$$J = \frac{1}{2}\frac{\sqrt{< x^2 >}}{t}(c_L - c_R) \qquad [18]$$

Now, the concentration gradient *dc/dx* in the left to right direction can be written as

$$\frac{dc}{dx} = \frac{c_R - c_V}{\sqrt{< x^2 >}} = -\frac{c_L - c_R}{\sqrt{< x^2 >}} \qquad [19]$$

or

$$c_L - c_R = -\sqrt{< x^2 >}\frac{dc}{dx} \qquad [20]$$

The result for $c_L - c_R$ in Eq. 20 is substituted to Eq. 18

$$J = -\frac{1}{2}\frac{< x^2 >}{t}\frac{dc}{dx} \quad [21]$$

By equating the coefficients of this equation with that of Fick's first law, one has

$$D = \frac{< x^2 >}{2t} \quad [22]$$

Three different derivations provide the same results on the relation between the diffusion coefficients and mean square jump distance.

For two dimensional diffusion,

$<X^2> = <Y^2>$ and $<L^2> = <X^2> + <Y^2>$, whence:

$$D_{2D} = \frac{< L^2 >}{4t} \quad [23]$$

and for three-dimensional isotropic diffusion

$<X^2> = <Y^2> = <Z^2>$ and $<R^2> = <X^2> + <Y^2> + <Z^2>$,

$$D_{3D} = \frac{< R^2 >}{6t} \quad [24]$$

References

1. J. Philibert, *Atom Movements Diffusion and Mass Transport in Solids*, p. 37, Les Editions de Physique, Les Ulis, (1991).
2. P. W. Atkins, *Physical Chemistry* 3rd ed., Chap. 27, W. H. Freeman and Company, NY (1986).
3. J. O'M. Bockris and A. K. N. Reddy, *Modern Electrochemistry*, p. 304, Plenum Press, NY (1970).